Winter March 2015

Search for Contact Interactions and Large Extra Dimensions in Dimuon Events from pp Collisions at √s = 8 TeV with the ATLAS Detector

TÜLİN VAROL
University of Massachusetts - Amherst

SEARCH FOR CONTACT INTERACTIONS AND LARGE EXTRA DIMENSIONS IN DIMUON EVENTS FROM pp COLLISIONS AT $\sqrt{s} = 8$ TEV WITH THE ATLAS DETECTOR

A Dissertation Presented

by

TÜLİN VAROL

Submitted to the Graduate School of the
University of Massachusetts Amherst in partial fulfillment
of the requirements for the degree of

DOCTOR OF PHILOSOPHY

February 2015

Physics

SEARCH FOR CONTACT INTERACTIONS AND LARGE EXTRA DIMENSIONS IN DIMUON EVENTS FROM pp COLLISIONS AT $\sqrt{s} = 8$ TEV WITH THE ATLAS DETECTOR

A Dissertation Presented

by

TÜLİN VAROL

Approved as to style and content by:

Stéphane Willocq, Chair

Carlo Dallapiccola, Member

John Donoghue, Member

Grant Wilson, Member

Rory Miskimen, Department Chair
Physics

To my parents, my sister and my brothers.

ACKNOWLEDGEMENT

Foremost, I would like to offer my sincerest gratitude to my advisor Prof. Stéphane Willocq for his excellent guidance, patience, motivation and encouragement. He always provided insightful answers to my questions and has been an inspiring role model for me. I have been extremely lucky to benefit from his expertise and vast knowledge while his student.

I would also like to thank my doctorate committee members, Prof. Carlo Dallapiccola, Prof. John Donoghue and Prof. Grant Wilson for their precious comments and suggestions about my thesis.

I would like to extend my sincerest appreciation to the rest of the UMass ATLAS Group, Prof. Ben Brau, Dr. Rozmin Daya, Dr. Edward Moyse, Dr. Massimiliano Bellomo, Nathan Bernard, who accompanied me in my doctorate journey with their valuable advice, discussions and friendship. Special thanks to Preema Pais, for being an amazing friend and for the countless coffee breaks and lunches at CERN. She has been like a sister to me ever since we met. Also, I would like to take this opportunity to thank Dr. Emily Thompson, the mother of contact interaction analysis, who has been a great friend and helped me a lot throughout my graduate study. I am thankful to Dr. German Colon for his help, friendship and enjoyable sarcasm. I would like to express my heartfelt gratitude to Dr. Niels Van Eldik for teaching me a lot about the ATLAS muon system and programming.

I am indebted to Physics Department secretary Jane Knapp for taking care of all my official transactions while I was away from UMass and for all the joyful lunches we had together in Amherst.

I am immensely grateful to my dear friend Engin Abat who was an ATLAS member and introduced me the wonders of experimental high energy physics. He was an amazing friend and I was always so impressed by his excitement. I also would like to thank Prof. Engin Arık. It was privilege to know her during my undergraduate study. They both had an impact on me in choosing this area and sadly passed away in the same airplane crash. They will never be forgotten.

I would like to thank the Exotics Non-Resonant Group, Dr. Tracey Berry, Dr. Daniel Hayden, Dr. Liam Duguid, Graham Savage and Marc Cano Bret for their great cooperation, kindness and friendship. I enjoyed learning from each of them and had a great time working in this team of brilliant people.

Special thanks to my Turkish friends, Dr. Aytül Adıgüzel, Dr. Kadri Özdemir, İlknur Hoş and Emine Gürpınar, who have supported me and cheered me up during my time at CERN.

I would like to express my gratitude to Dr. Alaettin Serhan Mete for his endless help throughout my PhD, and also for the happiness, peace and light he brings to my heart. He has always been a great supporter and a second pair of eyes on my work.

I would like to express my greatest gratitude to my family. I would like to thank my dear parents Affet Varol and Fahreddin Varol for their unconditional and unlimited love. There is no single word to express how grateful I am for their invaluable care and the sacrifices they have made. I would like to thank my twin sister, *canım kadişim*, Tülay Flamand. Having her has been the most beautiful thing that ever happened in my life. Special thanks to my dear brothers, Tunay Varol and Tayfun Varol for their love, caring and support. I would also like to thank my in-laws Joseph Flamand, Işılay Varol and Hacer Varol for their support and love. Thanks to my nephew Bora and my nieces Feride, Hatice, Beren who have been the joy in my life and always put a smile on my face.

ABSTRACT

SEARCH FOR CONTACT INTERACTIONS AND LARGE EXTRA DIMENSIONS IN DIMUON EVENTS FROM pp COLLISIONS AT $\sqrt{s} = 8$ TEV WITH THE ATLAS DETECTOR

FEBRUARY 2015

TÜLİN VAROL

B.Sc., BOĞAZİÇİ UNIVERSITY, ISTANBUL, TURKEY

Ph.D., UNIVERSITY OF MASSACHUSETTS, AMHERST

Directed by: Professor Stéphane Willocq

A search is conducted for non-resonant new phenomena in the dimuon final states, originating from either contact interactions or large extra spatial dimensions. The proton-proton collision data recorded by the ATLAS detector at the LHC in 2012 at $\sqrt{s} = 8$ TeV, corresponding to an integrated luminosity of 20.5 fb^{-1}, is used. The dimuon invariant mass spectrum is a discriminating variable in both searches, with the contact interaction search additionally utilizing the dimuon forward-backward asymmetry. No significant deviations from the Standard Model expectation are observed. Lower limits are set on the new physics parameters of interest at 95% credibility level. For $qq\mu\mu$ contact interactions, lower limits are set on the contact interaction scale Λ between 11.8 and 20.5 TeV. Lower limits are also set on the string scale M_{S} for large extra spatial dimensions, from 2.8 TeV to 4.4 TeV. Results from the muon channel are combined with the electron channel to further extend the range of the lower limits

on the contact interaction scale Λ to 15.4-26.3 TeV and the range of the lower limits on the string scale M_S to 3.2-5.0 TeV. The lower limits both on Λ and M_S are the most stringent limits to date.

TABLE OF CONTENTS

LIST OF TABLES

LIST OF FIGURES

Figure **Page**

INTRODUCTION

The Standard Model has been successful in explaining the experimental observations in particle physics so far. However, the Standard Model is not the ultimate theory and suffers from many deficiencies since it offers no explanation for puzzles such as the hierarchy problem, the matter/antimatter asymmetry, the origin of the free parameters of the Standard Model, the number of quark/lepton families, etc. These important shortcomings are the motivation to explore physics beyond the Standard Model. In pursuit of that, contact interactions and Arkani-Hamed, Dimopoulos and Dvali large extra dimensions model are considered as effective frameworks for new physics searches.

This thesis presents a search for four-fermion contact interactions and large extra dimensions in the dimuon channel ($qq\mu\mu$), based on the data collected with the ATLAS detector in 2012. The first chapter describes the Standard Model, mostly focusing on the electroweak interaction. The theoretical motivations for the proposed models are also discussed here which is followed by the discussion of the parton distribution functions. The design and layout of the experimental setup is given in Chapter 2. It begins with the description of the LHC and continues with the detailed description of the ATLAS detector, focusing on the Muon Spectrometer. The discussion of muon reconstruction algorithms as well as the discussion of the muon reconstruction performance are also given. Data taking with the ATLAS detector is included at the end of the chapter. Chapter 3 begins with the discussion of Monte Carlo simulation strategies and event reconstruction in ATLAS. The 2012 data, background and signal MC samples used in this analysis are listed here. Then the corrections made to simulated samples are discussed. Chapter 4 is devoted to the description of the selection

criteria applied to select muons and dimuon events in this analysis. Event yields and kinematic distributions are shown. Chapter 5 presents the theoretical and experimental uncertainties that are considered in this analysis in detail. Chapter 6 begins with the introduction of the Bayes' Theorem. It is then followed by the discussion of the methods that are used to check consistency between data and the SM expectation. Since no significant excess of data is observed above the SM background, the thesis proceeds with a discussion of the expected and observed limit setting procedures using a Bayesian approach. Chapter 7 presents the resulting limits for the contact interaction and ADD large extra dimension searches. The combination of limits with the electron channel is also discussed. Finally, the conclusion is given in Chapter 8.

CHAPTER 1

THEORETICAL BACKGROUND

This chapter begins with the introduction of the Standard Model of particle physics. It is followed by the discussion of the physics beyond the Standard Model including contact interactions and large extra dimensions. Finally, parton distribution functions are introduced.

1.1 Standard Model

The Standard Model (SM) is a gauge theory that characterizes all of the known fundamental particles and describes the electromagnetic, strong and weak interactions between them. By using the gauge symmetry group $SU(3)_C$ x $SU(2)_L$ x $U(1)_Y$ and the concepts of a relativistic quantum field theory (QFT) in which the particles are represented by fields, the SM incorporates quantum chromodynamics (the theory of the strong interaction) and electroweak interactions. The SM has been tested in many experiments and the predictions of the SM are verified with high precision.

1.1.1 Fundamental Particles

The fundamental particles of the SM are categorized as fermions (with half-integer spin: $\frac{1}{2},\ \frac{3}{2},\ \frac{5}{2}, ...$) and bosons (with integer spin: $0, 1, 2, ...$).

Fermions with spin-$\frac{1}{2}$ are the fundamental constituents of matter and the interactions between them are mediated by gauge bosons with integer spin. Each particle from the fermion group has an antiparticle counterpart with the same mass and spin but opposite electric charge. Fermions are categorized into three generations (or

families) of quarks (q) and leptons (charged: ℓ, neutral: ν). The first generation of quarks and charged leptons is composed of the lightest and most stable particles, whereas the heavier and less stable particles belong to the second and third generations. Since heavier particles quickly decay to the next most stable level, the first generation particles make all stable matter in the universe.

Leptons: There are six leptons in total, each with their antilepton counterpart. Electrons (e^-) are the lightest charged leptons and belong to the first generation. Muons from the second generation (μ^-) are heavier with mass 200 times greater than the mass of electrons. The third generation particles, taus (τ^-) are 3700 times more massive than electrons. Each charged lepton has an associated neutral partner, or *neutrino*; electron-neutrino (ν_e), muon-neutrino (ν_μ), and tau-neutrino (ν_τ). Antilepton counterparts of $e^-, \mu^-, \tau^-, \nu_e, \nu_\mu, \nu_\tau$ are $e^+, \mu^+, \tau^+, \bar{\nu_e}, \bar{\nu_\mu}, \bar{\nu_\tau}$.

Quarks: There are six "flavors" of quarks that are paired in three generations. The first generation is formed by up (u) and down (d) quarks, the second generation is followed by the charm (c) and strange (s) quarks, then the third generation is made up by the top (t) and bottom (or beauty) (b) quarks. Each quark carries a fractional value of the electron charge; u, c, t (collectively referred as up-type quarks) have a charge of +2/3, while d, s, b (down-type quarks) have -1/3.

Antiparticles of quarks are called antiquarks, and are denoted by a bar over the symbol for the corresponding quark, $\bar{u}, \bar{d}, \bar{c}, \bar{s}, \bar{t}, \bar{b}$. Antiquarks have the opposite charge to their corresponding quarks; up-type antiquarks have charges of -2/3 and down-type antiquarks have charges of +1/3.

Quarks experience the strong force. In order to describe the strong interaction, a new quantum number called *color* charge is introduced. Each quark has one of three possible colors: red, blue, green. Antiquarks carry an anticolor: anti-red, anti-blue or anti-green.

Bosons: The fundamental particles such as photons (γ), gluons (g), W and Z bosons are the force-carrying gauge bosons of the Standard Model. The only scalar boson is the Higgs boson (H). There is also the graviton (G) which is a hypothetical particle and not incorporated in the SM but if it exists, it must be a boson. These particles are explained in the next section in more detail.

Elementary particles of the SM with their mass, spin and charge are shown in Fig. 1.1.

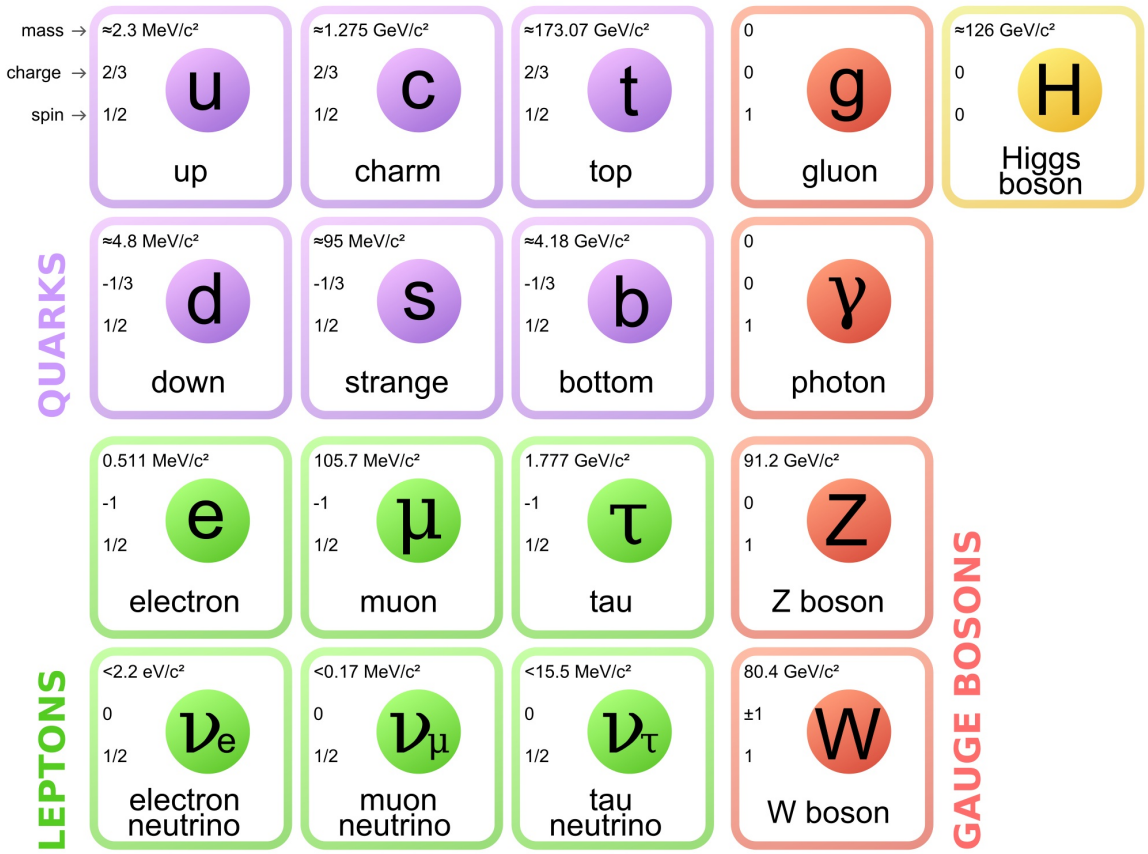

Figure 1.1: Elementary particles of the Standard Model.

1.1.2 Fundamental Interactions

The universe is governed by four fundamental interactions: the strong interaction, the electromagnetic interaction, the weak interaction, and the gravitational interaction. They work over different ranges and have different strengths. The first three

interactions occur via exchange of spin-1 particles, namely bosons. The gravitational interaction, postulated to be carried by a spin-2 *graviton*, has not been integrated into the theoretical framework of the SM yet.

1.1.2.1 The Electromagnetic Interaction

The electromagnetic interaction acts only on charged particles. It holds electrons and protons together in atoms and also allows atoms to bond together to form molecules. The theory that describes the electromagnetic interaction is called quantum electrodynamics (QED). The electromagnetic interaction is mediated by massless photons. In QED, all electromagnetic fields are associated with photons, and the interaction between charged particles occurs when one charged particle emits a virtual photon that is then absorbed by another charged particle. The photon has to be a virtual photon, because emission of a real photon would violate energy and momentum conservation. According to the Heisenberg uncertainty relation $\Delta E \Delta t \sim \hbar$, if a system is observed in a time interval Δt, the energy of the system can not be known better than to within an uncertainty ΔE. Thus, the photon can have energy ΔE for a time interval $\Delta t \sim \hbar/\Delta E$, without anybody being able to know if energy conservation is violated. As long as the photon is reabsorbed quickly enough, there is no measurable violation of energy conservation. Although these virtual photons can not be observed directly, they contribute to the probabilities of observable events.

Some calculations in QED can lead to infinities. In order to avoid mathematical inconsistencies and correct unphysical results, the technique of renormalization is used. Renormalization can remove infinities from the theory by absorbing the infinities into available free parameters without violating known principles of physics. Mathematically, QED is an abelian gauge theory with the symmetry group U(1).

Like gravity, the electromagnetic interaction is effective in an infinite range and obeys the inverse square law. The strength of the electromagnetic force is set by the

coupling constant:

$$g_e = \sqrt{4\pi\alpha}, \tag{1.1}$$

where α is the fine structure constant and can be written as:

$$\alpha = \frac{e^2}{\hbar c} \simeq \frac{1}{137}. \tag{1.2}$$

The electromagnetic current can be written as:

$$J^{\mu}_{em} = \sum_f q_f \bar{\psi}_f \gamma^{\mu} \psi_f, \tag{1.3}$$

where q_f is the charge of the fermion, γ^{μ} is the Dirac matrices operator, and ψ_f is the spinor field with its adjoint spinor $\bar{\psi}_f$.

1.1.2.2 The Strong Interaction

The strong interaction originates from the color charge of quarks and acts only at very short distances. The strong interaction binds quarks together to make nucleons and binds nucleons together to make nuclei. The force between two quarks is mediated by the exchange of massless gluons that carry one color and one anticolor. Color is conserved at each quark-quark-gluon vertex as well as three-gluon and four-gluon vertices. For example, a blue quark can turn into a red quark by emitting a gluon with blue and anti-red color. Only colored particles can emit or absorb a gluon. Leptons and the other gauge bosons are colorless. Neither quarks nor gluons can appear in isolation but they can only exist within colorless (color-neutral) composite states, which is known as "*color confinement*".

Quarks combine to form colorless composite particles called *hadrons*. There are two types of hadrons, *baryons* which consists of three quarks (e.g. the proton or neutron) or *mesons* which consist of a quark-antiquark pair (e.g. the pion). Baryons are fermions since they have half-integer spin values whereas mesons are bosons that

have an integer spin. The quarks which determine the quantum numbers of hadrons are called *valence* quarks. Within a hadron, there is also an indefinite number of *virtual* (or *sea*) quarks, antiquarks, and gluons, which do not influence its quantum numbers but can play a role in high energy collisions. Baryons are usually confined within nuclei. If not inside the nucleus, they are unstable and decay. The exception to this is the proton which is essentially stable in free space.

Colorless configurations can also be made out of gluons alone, which means that gluons can couple directly to other gluons (bound states of interacting gluons, *glueball*).

A special unitary group $SU(3)_C$ describes the color symmetry of strong interactions. It has eight generators[1] corresponding to eight color state massless gluons.

The theory of strong forces is called Quantum Chromodynamics (QCD). The strength of the chromodynamic force is set by the "strong" coupling constant:

$$g_s = \sqrt{4\pi\alpha_s}. \tag{1.4}$$

In this theory, the number that plays the role of coupling "constant" is in fact not constant at all, but depends on the separation distance between the interacting particles. It is a so-called *running* coupling constant. At relatively large distances the strong force between quarks becomes stronger and at very short distances (less than size of a proton), it becomes quite small. This phenomenon is known as *asymptotic freedom* that means within a hadron, quarks bounce around without interacting much and behaving like independent particles. This behavior can be explained qualitatively as follows.

A charge $q > 0$ that is embedded in a dielectric medium causes the negative end of each molecular dipole to attract toward q and positive end to repel away. Hence a

[1] A special unitary group of SU(N) has N^2 -1 generators.

"halo" of negative charge is formed around q which partially cancels its field. Then in the presence of the dielectric, the effective charge can be written as:

$$q_{eff} = \frac{q}{\epsilon}, \tag{1.5}$$

where ϵ the dielectric constant of the material. In a distance that is closer than the nearest molecule, there is no screening effect. Thus, the effective charge increases at very small distances. In quantum electrodynamics, the vacuum behaves like a dielectric medium. Thus, screening is created by vacuum polarization. Again, in a distance too close to q, there is no screening. Thus, one expects the interaction to become stronger in a small distance. However, in QCD there is an important factor; in addition to quark-quark-gluon vertex, there is also the direct gluon-gluon vertices. The effect of gluon loops is the opposite; causing the interaction to become weaker at small distances. In QCD, there are two contributions affecting the coupling strength: the quark polarization diagrams that drive α_S up and gluon polarization that drives it down. The overall effect from both depends on the number of flavors (for quarks) and the number of colors (for gluons).

In order to get rid of ultraviolet divergences that appear in the perturbative calculation of the QCD theory, renormalization is required. After subtraction of UV divergences, all renormalized quantities and renormalisation constant become functions of the renormalisation scale μ. The development of the coupling constant with changing momentum and renormalization scale is determined by the so-called β-function, which is defined as:

$$\mu\frac{\partial\alpha}{\partial\mu} = -\frac{\beta_0}{2\pi}\alpha_S^2 - \frac{\beta_1}{4\pi^2}\alpha_S^3 - ....., \tag{1.6}$$

where two coefficients β_0 and β_1 are independent of the renormalisation scheme. In order to solve this equation, a constant μ_0 is introduced. This is one of the constants

in QCD theory and needs to be determined from experiments. Without going in any details of calculation, α_S that is derived from β-function is written below:

$$\alpha_S(Q^2) = \frac{\alpha_S(\mu^2)}{1 + \frac{\alpha_S(\mu^2)}{12\pi}(11c - 2n_f)ln(\frac{Q^2}{\mu^2})}, \tag{1.7}$$

where Q is the momentum transfer in the interaction, c is the number of colors and n_f is the number of flavors. This equation can also be written in terms of "cutoff" parameter Λ_{QCD}:

$$\alpha_S(Q^2) = \frac{12\pi}{(11c - 2n_f)ln(Q^2/\Lambda)}. \tag{1.8}$$

The critical parameter is $11c - 2n_f$. If this is negative then the effective coupling increases at short distances and if it is positive then it decreases [1]. In the SM, there are 6 flavors and 3 colors which gives $11c - 2n_f = 21$. Therefore, QCD coupling decreases at short distances. The cutoff parameter Λ_{QCD} defines spatial regions to which quarks are required to be confined. The value of this parameter is $\Lambda_{QCD} \approx$ 200 MeV or $\approx$ 1 fm. At this distance and larger, the strong interaction is very strong and leads to permanent confinement of quarks inside colorless hadrons. At a distance smaller than this value, quarks are asymptotically free.

1.1.2.3 The Weak Interaction

The weak interaction acts upon all quarks and leptons, including those with no electric charge. There are two kinds of weak interactions: the charged interaction that is mediated by the W bosons and the neutral interaction that is mediated by the Z boson. The weak interaction is the only interaction that can change the flavor of a quark. The weak interaction is distinguished from other interactions by some characteristic properties like lifetimes, strength of coupling, cross sections and violation of symmetries. Historically, the first weak decay discovered was the β-decay, that allows protons to transmute into neutrons and vice versa.

The fundamental interactions are listed in Table 1.1.

Table 1.1: Fundamental interactions.

Force	**Theory**	**Mediator**	**Range**
Strong	Chromodynamics	Gluon (g)	10^{-15} m
Electromagnetic	Electrodynamics	Photon (γ)	∞
Weak	Flavordynamics	$W^{\pm}, Z$	10^{-18} m
Gravity	Geometrodynamics	Graviton (G)	∞

1.1.3 A Closer Look At the Weak Interaction

1.1.3.1 The Fermi Interaction

The process of β-decay ($n \rightarrow p + e^-$) occurs since the daughter nucleus has less mass than the parent, and therefore the decay is energetically favored. By Einstein's $E = mc^2$, an electron is expected to carry of the difference in masses in the form of kinetic energy. However, experiments showed that the electron carries less energy than expected. Also, instead of all electrons having the same energy, there was a continuous distribution. This result was unexpected since that would violate the energy conservation. In December 1930, Wolfgang Pauli proposed the existence of a light neutral particle of spin 1/2 emitted in addition to the electron in β-decay [2]. Only with the emission of a third particle could momentum and energy be conserved. The available energy is split between the electron and the undetected neutral particle, thus, explains the continuous spectrum. Pauli gave the name "neutron" to this new particle. However, it was renamed "neutrino" later by Fermi.

Fermi incorporated the neutrino into his theory of β-decay [3] ($n \rightarrow p + e^- + \bar{\nu}_e$), published in 1934. He described the interaction as a four-fermion process that happens at a single point in space-time. His idea of β-decay is shown in Fig 1.2.

In analogy to the electromagnetic interaction, Fermi proposed the following matrix element:

$$M = \frac{G_F}{\sqrt{2}}[\bar{u}_p \gamma^\mu u_N][\bar{u}_e \gamma^\nu u_\nu], \tag{1.9}$$

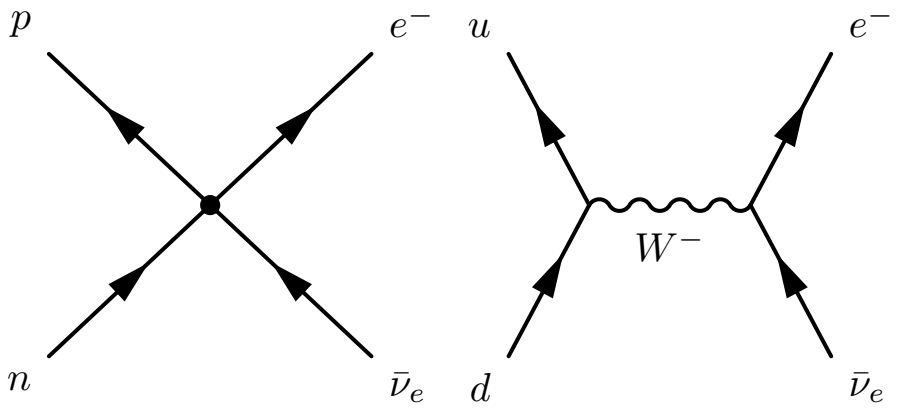

Figure 1.2: Fermi's 4-point interaction describing nuclear β-decay (left) and the nuclear β-decay via the emission of a virtual W^- boson (right).

where G_F is a coupling factor, also known as the Fermi constant and u_P, u_N, u_e, u_ν are the proton, neutron, electron and neutrino wave functions.

The Fermi constant G_F is equal to 1.166 $\times 10^{-5}$ GeV^2. Fermi postulated that the weak coupling factor is the same for all weak vertices without any dependence on the lepton flavor. This is called *universality*. In this process, the hadronic current has $\Delta Q = +1$ whereas the lepton current has ΔQ = -1. This is called a *charged current* interaction since there is a net charge transferred from the hadronic to the lepton current. Also, there is no propagator in this description. In analogy to the electromagnetic interaction, the currents have a vector character.

The intrinsic coupling at high energy can be estimated by assuming that the Fermi theory is the low energy limit of the weak interaction. For the weak interaction, the propagator term for the massive $W^\pm$ and Z bosons is $\frac{1}{M^2_{W,Z}-q^2}$. This reduces to $\frac{1}{M^2_W}$ at low energies ($M^2_{W,Z} \gg q^2$). In the Fermi limit, the coupling factor is $\frac{G_F}{\sqrt{2}}$. Hence the strength of weak interaction can be defined by G_F:

$$\frac{G_F}{\sqrt{2}} = \frac{g_w^2}{8M_W^2}, \tag{1.10}$$

where g_w is the weak coupling. Substituting the values for the W boson mass (80.4 GeV) and the Fermi constant (1.66 $\times 10^{-5}$ GeV^{-2}) into Eq. (1.10), the weak coupling

g_w is found to be 0.65. The weak fine structure constant is then:

$$\alpha_W = \frac{g_W^2}{4\pi} = \frac{1}{30}. \tag{1.11}$$

Comparing this to the fine structure constant of the electromagnetic interaction (1/137), one can say that the weak interaction is four times stronger than the electromagnetic interaction. What makes the weak interaction feeble is not the intrinsic coupling but the mediators being so massive. In fact at very high energies ($q^2 \sim M_W^2$), the strength of weak interaction is comparable to the electromagnetic interaction.

1.1.3.2 Parity Violation and the V-A Interaction

Prior to 1956, it was believed that the laws of physics were invariant under parity transformations which reverse spatial coordinates as:

$$x \to -x \qquad y \to -y \qquad z \to -z.$$

Parity conservation implies that the probability of one interaction happening in this world is the same as the probability of its mirror image occurring.

In 1956, T.D. Lee and C.N. Yang realized that past experiments on the weak interaction offered no evidence of the parity conservation after making a careful study of all known experiments involving weak interactions. They were actually trying to find an answer to a very puzzling problem which was known as the $\tau - \theta$ puzzle. Two strange mesons, called τ and θ at the time (it was found later that these are both charged kaons), were found to be identical in every respect; same mass, same spin, same charge, etc. However, τ was observed to decay into three pions $\pi^+\pi^+\pi^-$ or $\pi^+\pi^0\pi^0$ leading to an odd parity state, whereas θ was observed to decay into two pions $\pi^+\pi^0$ with even parity state [4]. Even though it was considered that the two particles were the same, that seemed impossible then since they have different parity states. Also, the lifetime of τ meson was found to be longer than that of the θ meson.

Later that year, C. S. Wu set up an experiment to test the possibility of parity violation in β-decay. In her famous experiment, she aligned radioactive Co^{60} nuclei in a magnetic field, so their spins pointed in the same direction, chosen as upwards in the z direction. Atoms of Co^{60} decay into Ni^{60} via an electron emission. Hence, Wu recorded the direction of the emitted electrons. If the mirror image of the same process is considered, the nucleus rotates in the opposite direction. That means in the mirror process, spins of Co^{60} atoms point downwards (see Fig. 1.3). However, electrons in the mirror image are still emitted in the same direction as in the real world. In the real world process, while electrons are emitted in the direction of the nuclear spin, in the mirror process they are emitted in the direction opposite to the nuclear spin. Parity conservation requires both processes occurs at equal probabilities. However, Wu observed the emission of electrons "maximally" in the direction of the nuclear spin. That implies parity is violated and it is not limited to β-decay in cobalt. Parity violation is practically the signature of the weak interaction. Therefore, Fermi's theory needs to be revised to incorporate parity violation.

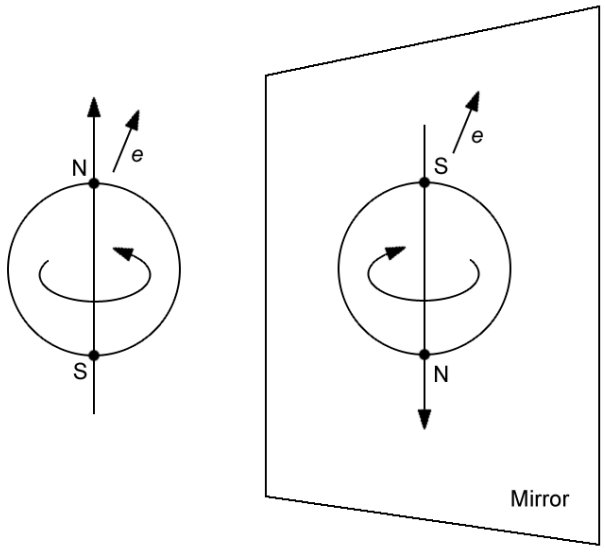

Figure 1.3: Parity Violation in β-decay of Co^{60} nuclei.

By convention, the z axis is chosen as the axis of quantization for the angular momentum. The orientation of the z axis is arbitrary. If one is dealing with a particle traveling through the laboratory, choosing the direction of motion as the z axis would be a natural choice. The *helicity* of a particle is defined as the projection of the spin onto the direction of momentum. It can also be expressed as m_s/s. If the particle spin direction is the same as the direction of motion, the particle is said to be right-handed. The helicity is +1 for right-handed particles (i.e: $s = 1/2$ and $m_s = 1/2$, $m_s/s = +1$). If the spin projection is in the opposite direction to the direction of motion, it is called as left-handed. The helicity is -1 for left-handed particles (i.e: $s = 1/2$ and m_s = -1/2). Handedness is explained in Fig. 1.4.

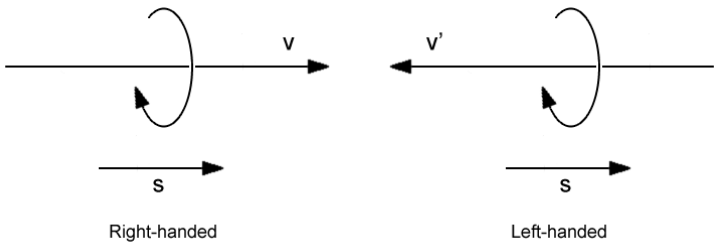

Figure 1.4: The cartoon depicts the concept of handedness. When the spin of the particle is aligned with its direct of flight (left) it's called right-handed, if they are anti-aligned (right) left-handed.

When talking about parity transformations, instead of using the concept of *reflection* in the mirror, the concept of *inversion* is used. For the reflection in the x-z plane, the spatial coordinates transform as (x, y, z) $\rightarrow$ (x, -y, z). For the inversion, they transform as (x, y, z) $\rightarrow$ (-x, -y, -z), which represents a reflection followed by a 180° rotation about the y axis.

Under parity transformations, the wave functions transform as

$$\psi \rightarrow \hat{P}\psi = \pm\gamma^0\psi. \tag{1.12}$$

If the parity operator is applied twice, the original wave function is obtained ($\hat{P}^2 = \gamma^{0\,2} = 1$). Therefore, the eigenvalues of the parity operator are $\pm$ 1. According to Quantum Field Theory, the parity of a fermion is opposite that of the anti-fermion, whereas the parity of a boson is the same as its antiparticle. Positive parity is also known as "even" intrinsic parity whereas negative parity is known as "odd" intrinsic parity.

Behavior of scalars and vectors under the parity transformation is different. The behavior of four independent bilinear covariant expressions is given below.

Scalar	P(s) = s
Pseudoscalar	P(p) = -p
Vector (or Polar Vector)	P(**v**) = -**v**
Pseudovector (or Axial Vector)	P(**a**) = **a**

Defining the current responsible for the weak interaction requires a combination for which the charged weak interaction only couples to left-handed particles. Using the left-handed projection operator introduced as $P_L = \frac{1}{2}(1-\gamma^5)$, the current can be written as:

$$\bar{\psi}\gamma^\mu \frac{1}{2}(1-\gamma^5)\psi, \tag{1.13}$$

where ψ is a fermionic field. If this is expanded:

$$\underbrace{\frac{1}{2}\bar{\psi}\gamma^\mu\psi}_{\text{vector current}} - \underbrace{\frac{1}{2}\bar{\psi}\gamma^\mu\gamma^5\psi}_{\text{axial vector current}} . \tag{1.14}$$

This is the famous **V-A** form [5] that is responsible for the parity violating nature of the weak interaction. This theory modifies the Fermi's theory which was represented by the vector current, by subtracting the axial vector current term. Parity violation comes from the fact that the behavior of the vector and axial vector currents under a parity transformation is different. As shown above, there is a charge flip in

the vector current under parity whereas the axial vector current stays the same. The interference between these two terms creates the parity violation. Considering the fact that what we observe is usually the square of the amplitude and assuming the amplitude is pure V-A, one can write [6]:

$$\begin{aligned} |M|^2 &\sim (V-A)(V-A) \\ &= VV - 2AV + AA. \end{aligned} \tag{1.15}$$

When applying a parity transformation, the sign of the V term flips, but the sign of the A term doesn't.

$$\begin{aligned} \hat{P}\{|M|^2\} &\sim \hat{P}\{(V-A)(V-A)\} \\ &= \hat{P}\{VV - 2AV + AA\} \\ &= (-V)(-V) + AA - 2A(-V) \\ &= VV + AA + 2AV. \end{aligned} \tag{1.16}$$

Comparing the $|M|^2$ and $\hat{P}\{|M|^2\}$ we see a difference from -2AV to +2AV. This cross term, AV, including currents with opposite parity behaviors, introduces a parity violation. Without this term, $|M|^2$ would be equal to $\hat{P}\{|M|^2\}$ and no parity violation would be observed.

The parity violation occurs maximally when both currents have the same strength. The current including different V and A weights can be written as:

$$\frac{1}{2}\bar{\psi}\gamma^{\mu}(c_V - c_A\gamma^5)\psi. \tag{1.17}$$

It is observed that the parity is violated in all charged weak interactions and experimentally it is found that $c_V = c_A = 1$. Therefore, the weak charged current

can be written as:

$$J^{CC}_{weak} = \frac{g_w}{\sqrt{2}}\bar{u}\gamma^\mu\frac{1}{2}(1-\gamma^5)u. \tag{1.18}$$

where u is the fermion wave function.

The charged current weak interaction is mediated by W bosons. The coupling factor for a charged weak vertex is

$$\frac{g_w}{2\sqrt{2}}\gamma^\mu(1-\gamma^5). \tag{1.19}$$

There is also a neutral current interaction, mediated by the Z boson. The fermion flavor is not changed in a neutral current interaction. As opposed to that W boson only couples to the left-handed fermions, the Z boson couples also to right-handed fermions. The coupling factor depends on what the Z is interacting with and can be written as:

$$\frac{g_z}{2}\gamma^\mu(c^f_V - c^f_A\gamma^5), \tag{1.20}$$

where g_z is the neutral current coupling constant and coefficients c^f_V and c^f_A depend on the flavor of fermion (f) involved. A full list of coefficients is shown below.

Table 1.2: Neutral vector and axial vector couplings in the GWS model.

Fermion	c^f_V	c^f_A
ν_e, ν_μ, ν_τ	$\frac{1}{2}$	$\frac{1}{2}$
e^-, μ^-, τ^-	$-\frac{1}{2} + 2\sin\theta_W$	$-\frac{1}{2}$
u, c, t	$\frac{1}{2} - \frac{4}{3}\sin^2\theta_W$	$\frac{1}{2}$
d, s, b	$-\frac{1}{2} + \frac{2}{3}\sin^2\theta_W$	$-\frac{1}{2}$

As seen from the table, these coefficients depend on the weak mixing angle (θ_W), also known as Weinberg angle, which relates the weak, neutral and electromagnetic coupling strengths

$$g_w = \frac{g_e}{\sin\theta_W}, \qquad\qquad g_z = \frac{g_e}{\sin\theta_W \cos\theta_W}. \tag{1.21}$$

The mass of the W and Z bosons can also be related using θ_W:

$$M_W = M_Z \cos\theta_W. \tag{1.22}$$

The value of θ_W is determined experimentally and $\sin^2\theta_W$ is measured as 0.23.

After the parity violation was revealed, most physicists still believed that the parity along with the charge conjugation would still be conserved (CP-symmetry) where the charge conjugation, C, converts each particle into its antiparticle. It was found later that CP is also violated. This was first shown by J. Cronin and V. Fitch in 1964. They expected to see short-lived K mesons always decay into two pions and long-lived K mesons decay into three pions. However, they observed that long-lived K mesons also decay into two pions (45 two-pion events in a total of 22700 decays). This observation confirmed CP violation in weak interaction although it is very rare. It means that there is a difference in the laws of nature in our world and in the mirror world.

1.1.4 Forward-Backward Asymmetry

Because there is a parity violation in weak interactions, processes that involve weak interactions can exhibit asymmetries in the distribution of particles in their final states. As opposed to the fact that the charged weak interactions couple only to left-handed fermions or right-handed antifermions, the neutral weak interaction can couple to right-handed fermions. However, there is still a preference to couple to

left-handed fermions mostly which gives rise to a forward-backward asymmetry, as described below.

The Drell-Yan (DY) process in which lepton pair production occurs via an electromagnetic or a weak interaction ($q\bar{q} \to \gamma^*/Z \to \ell^+\ell^-$), as shown in Fig. 3.2, is one of the processes that display asymmetries in the final state. This process is explained by S. D. Drell and T. M. Yan in 1970 [7]. The DY process is the most important SM background for new physics searches with dilepton final states.

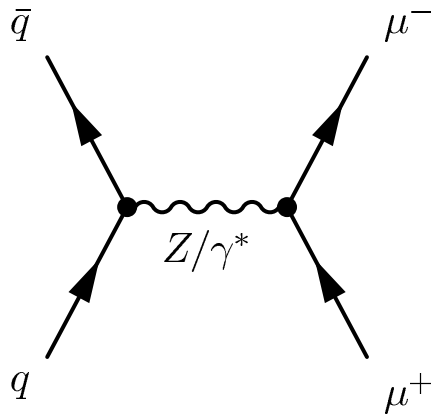

Figure 1.5: The Drell-Yan process with a dimuon final state.

The other source of the forward-backward asymmetry in the DY process is the interference between photon and Z boson exchange. The differential cross section for the fermion production via the DY process can be written as [8]:

$$\begin{aligned}\frac{d\sigma(q\bar{q} \to \mu^+\mu^-)}{d\cos\theta^*} = C\frac{\pi\alpha^2}{2\hat{s}}[&Q_\mu^2 Q_q^2(1+\cos^2\theta^*) \\ &+ Q_\mu Q_q Re(\chi(\hat{s}))(2g_V^q g_A^\mu(1+\cos^2\theta^*) + 4g_A^q g_A^\mu \cos\theta^*) \\ &+ |\chi(\hat{s})|^2((g_V^{q\,2}+g_A^{q\,2})(g_V^{\mu\,2}+g_A^{\mu\,2})(1+\cos^2\theta^*) + 8g_V^q g_A^q g_V^\mu g_A^\mu \cos\theta^*)],\end{aligned} \tag{1.23}$$

where $C = 1/9$ which is the color factor for qq interaction, Q is the charge of a muon or a quark, θ^* is the angle between the lepton (antilepton) and the quark (antiquark) directions in the rest frame of the lepton pair, as shown in Fig. 1.6, and

$$\chi(\hat{s}) = \frac{1}{\cos^2\theta_W \sin^2\theta_W} \frac{\hat{s}}{\hat{s} - M_Z^2 + i\Gamma_Z M_Z}, \tag{1.24}$$

where $\hat{s}$ is the momentum transfer in the interaction, M_Z and Γ_Z are the mass and the width of the Z boson, respectively.

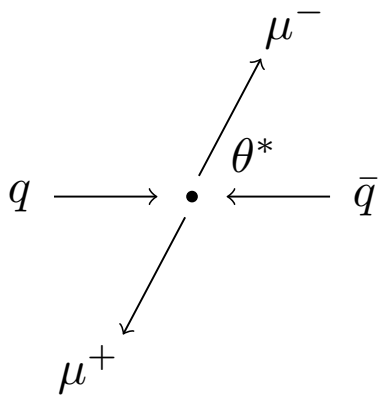

Figure 1.6: Lepton decay angle θ^*.

The first and third terms in Eq. (1.23) correspond to the pure γ^* and Z exchange respectively while the second term stands for the Z/γ^* interference. The various terms either depend on $\cos\theta^*$ or $(1 + \cos^2\theta^*)$. It can be clearly seen when the Eq. (1.23) is written in a simplified form:

$$\frac{d\sigma}{d\cos\theta^*} = A(1 + \cos^2\theta^*) + B\cos\theta^*, \tag{1.25}$$

where A and B are functions that depend on the weak isospin, the charge of the incoming fermions and also the momentum transfer in the interaction. The functions A and B can be written as:

$$A = Q_\mu^2 Q_q^2 + 2Q_\mu Q_q g_V^q g_V^\mu Re(\chi(\hat{s})) + (g_V^{\mu\,2} + g_A^{\mu\,2})(g_V^{q\,2} + g_A^{q\,2})|\chi(\hat{s})|^2, \tag{1.26}$$

$$B = \frac{3}{2} g_A^q g_A^\mu (Q_\mu Q_q Re(\chi(\hat{s})) + 2g_V^q g_V^\mu |\chi(\hat{s})|^2). \tag{1.27}$$

Events with $\cos\theta^* > 0$ are called forward events and events with $\cos\theta^* < 0$ are called backward events. The integrated cross section for the forward events is $\sigma_F = \int_0^1 \frac{d\sigma}{d\cos\theta^*} d\cos\theta^*$ and the integrated cross section for the backward events is $\sigma_B = \int_{-1}^0 \frac{d\sigma}{d\cos\theta^*} d\cos\theta^*$. The forward-backward asymmetry A_{FB} can be written as:

$$\begin{aligned} A_{FB} &= \frac{\sigma_F - \sigma_B}{\sigma_F + \sigma_B}, \\ &= \frac{B}{A}, \\ &= \frac{\frac{3}{2} g_A^q g_A^\mu (Q_\mu Q_q Re(\chi(\hat{s})) + 2 g_V^q g_V^\mu |\chi(\hat{s})|^2)}{Q_\mu^2 Q_q^2 + 2 Q_\mu Q_q g_V^q g_V^\mu Re(\chi(\hat{s})) + ({g_V^\mu}^2 + {g_A^\mu}^2)({g_V^q}^2 + {g_A^q}^2)|\chi(\hat{s})|^2}. \end{aligned} \tag{1.28}$$

1.1.5 Charged Current Coupling to Quarks

The charged weak interaction only couples to leptons within a particular generation ($e^- \to \nu_e + W^-, \mu^- \to \nu_\mu + W^-, \tau \to \nu_\tau + W^-$). One might expect that is also true for coupling to quarks (i.e the up quark will couple to the down quark, the charm quark to the strange and the top quark to the bottom quark). However, the kaon decay process, $K^+ \to \mu^+ \nu_\mu$, shows that this is not true. Since K^+ includes an up quark and anti-strange quark, the W boson couples to the up quark from the first generation and anti-strange quark from the second generation. The other problem is that the lifetime for the strangeness-changing process is 20 times longer than the strangeness-conserving one, which leads to the strangeness-changing process to be 20 times weaker than the strangeness-conserving one.

In 1963, Nicola Cabibbo proposed that the weak interaction acts on a linear combination of the down and strange quarks [9], which is denoted by d'. Thus, he introduced the Cabibbo angle (θ_C) in order to preserve the universality of the weak interaction. Using the Cabibbo angle, a rotated state is given as:

$$d' = d\cos\theta_C + s\sin\theta_C. \tag{1.29}$$

Experimentally, $\theta_C = 13°$. Hence, if the interaction is reduced to the down quark, the vertex factor is smaller by a factor of $\cos\theta_C$. If it is reduced to the strange quark, then the vertex factor is smaller by a factor of $\sin\theta_C$ which has a value around 0.22. Then the probability that the W boson scatter off a strange quark is $\sin^2\theta_C \sim 0.05$, solving the lifetime discrepancy problem. Therefore, in Cabibbo's theory, the first generation of quarks that the weak interaction sees can be written as:

$$\begin{pmatrix} u \\ d' \end{pmatrix} = \begin{pmatrix} u \\ d\cos\theta_C + s\sin\theta_C \end{pmatrix}. \tag{1.30}$$

Although Cabibbo's theory was successful to explain many decay rates, there was still a remaining problem which comes from the process $K^0 \to \mu^+\mu^-$. This is a flavor-changing neutral-current process (FCNC) in which a strange quarks turns into a down quark and a virtual Z boson. The amplitude should be proportional to $\sin\theta_C\cos\theta_C$. Thus, the decay rate of this process should be comparable to the one for the process $K^+ \to \mu^+\nu_\mu$. However, experiments show that it is much less than the calculated value.

$$\frac{\Gamma(K^0 \to \mu^+\mu^-)}{\Gamma(K^+ \to \mu^+\nu_\mu)} \sim 10^{-8}. \tag{1.31}$$

In attempt to solve this problem, S. Glashow, J. Iliopoulos and L. Maiani (GIM) proposed the existence of a new quark, the charm c, whose couplings to the strange and down quarks carry factors of $\cos\theta_C$ and -$\sin\theta_C$, respectively [10]. Thus, the amplitude is proportional to -$\sin\theta_C\cos\theta_C$ and cancels the term with $\sin\theta_C\cos\theta_C$ in the lagrangian. Therefore, adding a fourth quark actually explains the very small branching ratio of decays involving a FCNC. Thus, Cabibbo's theory is extended by adding another rotated state:

$$s' = s\cos\theta_C - d\sin\theta_C. \tag{1.32}$$

Then the coupling to the physical particles are given by:

$$\begin{pmatrix} c \\ s' \end{pmatrix} = \begin{pmatrix} c \\ s\cos\theta_C - d\sin\theta_C \end{pmatrix}. \tag{1.33}$$

The two rules given in Eqs. (1.29) and (1.32) are combined in the matrix equation:

$$\begin{bmatrix} \cos\theta_C & \sin\theta_C \\ -\sin\theta_C & \cos\theta_C \end{bmatrix} \begin{bmatrix} d \\ s \end{bmatrix} = \begin{bmatrix} d' \\ s' \end{bmatrix}. \tag{1.34}$$

The vector $\left(\begin{smallmatrix} d \\ s \end{smallmatrix}\right)$ is rotated into the vector $\left(\begin{smallmatrix} d' \\ s' \end{smallmatrix}\right)$ by the transition matrix.

$$\begin{bmatrix} U_{ud} & U_{us} \\ U_{cd} & U_{cs} \end{bmatrix} = \begin{bmatrix} \cos\theta_C & \sin\theta_C \\ -\sin\theta_C & \cos\theta_C \end{bmatrix}. \tag{1.35}$$

The GIM mechanism was confirmed in 1974 by the discovery of a charm quark observed in the $c\bar{c}$ bound state denoted as J/ψ [11]. M. Kobayashi and T. Maskawa wanted to explain CP violation within the Cabibbo-GIM scheme. They realized that in a four-quark model, this is not possible. Hence, before the second generation of quarks were found, they proposed a third quark generation and generalized the Cabibbo matrix into the Cabibbo-Kobayashi-Maskawa matrix (or CKM matrix) [12] to handle three generation of quarks:

$$\begin{bmatrix} d' \\ s' \\ b' \end{bmatrix} = \begin{bmatrix} U_{ud} & U_{us} & U_{ub} \\ U_{cd} & U_{cs} & U_{cb} \\ U_{td} & U_{ts} & U_{tb} \end{bmatrix} \begin{bmatrix} d \\ s \\ b \end{bmatrix}, \tag{1.36}$$

where weak interaction quark generations are given by:

$$\begin{pmatrix} u \\ d' \end{pmatrix}, \quad \begin{pmatrix} c \\ s' \end{pmatrix}, \quad \begin{pmatrix} t \\ b' \end{pmatrix} \tag{1.37}$$

The entries in the matrix are not all independent and can be reduced to four independent terms. They are free parameters of the SM and need to be measured experimentally [13].

The matrix element describing Fermi's beta decay now becomes:

$$\begin{aligned} M &= \left[\frac{g_w}{\sqrt{2}}\bar{u_e}\frac{1}{2}\gamma^\mu(1-\gamma^5)v_{\nu_e}\right]\frac{1}{M_W^2-q^2}\left[U_{ud}\frac{g_w}{\sqrt{2}}\bar{u}_u\frac{1}{2}\gamma^\mu(1-\gamma^5)u_d\right] \\ &= U_{ud}\frac{g_w^2}{8}\frac{1}{M_W^2-q^2}\left[\bar{u}_e\gamma^\mu(1-\gamma^5)v_{\nu_e}\right]\left[\bar{u}_e\gamma^\mu(1-\gamma^5)u_d\right]. \end{aligned} \tag{1.38}$$

Comparing this matrix element to Fermi's original matrix element given in Eq. (1.9) at high energies ($q \gg M_W$), the coupling equation is obtained again:

$$\frac{G_F}{\sqrt{2}} = \frac{g_w^2}{8M_W^2}. \tag{1.39}$$

The problem with the theory of intermediate vector bosons is that it is not renormalizable. This is due to the huge masses of the intermediate particles. One solution may be to find a gauge theory that describes the weak interaction. However, this causes a problem since no mass term is allowed in the Lagrangian for the gauge bosons. The solution to this problem requires a unified theory of the weak and electromagnetic interactions. Then the bosons acquire their masses in the process of spontaneous symmetry breaking (EWSB) via the "Higgs mechanism".

1.1.6 Electroweak Unification

Between 1961 and 1967, Sheldon Lee Glashow, Abdus Salam and Steven Weinberg proposed the theory of electroweak interactions, which predicted the existence of vector bosons with huge masses (∼100 GeV). The unification of the electromagnetic and weak interactions is accomplished under an $SU(2)_L$ x $U(1)_Y$ gauge group. The weak interaction is described by the $SU(2)_L$ group where subscript "L" implies that it acts only on the left-handed particles. The conserved quantity in $SU(2)_L$ is the weak

isospin[2] $\vec{I}$ whereas in the $U(1)_Y$ group, the conserved quantity is weak hypercharge Y. Their relation to the electromagnetic charge Q is given by $Q = I_3 + \frac{Y}{2}$ where I_3 is the third component of the weak isospin.

Initially four massless bosons are required by the requirement of local gauge invariance: three $SU(2)_L$ gauge bosons (W^1, W^2, W^3) and one $U(1)_Y$ gauge boson (B^0). The spontaneous symmetry breaking via the Brout-Englert-Higgs mechanism results in the four physical bosons: W^+, W^-, Z^0, and γ bosons that are linear superpositions of the W^1, W^2, W^3, and B^0 bosons.

The Z^0 and γ can be written in terms of the initial bosons by using the relation:

$$\begin{bmatrix} Z^0 \\ \gamma \end{bmatrix} = \begin{bmatrix} \cos\theta_W & -\sin\theta_W \\ \sin\theta_W & \cos\theta_W \end{bmatrix} \begin{bmatrix} W^3 \\ B^0 \end{bmatrix}. \tag{1.40}$$

The spontaneous symmetry breaking leads to a mass term appearing in the neutral weak field, while the mass term for the photon field cancels out. Thus, the photon is massless.

In 1983, the W and Z bosons were discovered by the UA1 and UA2 collaborations at the Super Proton Synchrotron at CERN. The Higgs boson that is the quantized state of the Higgs field had been the last missing piece of the SM until 2012. The discovery of the boson that is consistent with the Higgs boson and at a mass around 126 GeV was announced by the ATLAS and CMS collaborations at the LHC at CERN on the 4^{th} of July 2012. It will take further work to determine whether or not it is the Higgs boson predicted by the Standard Model.

---

[2]Weak isospin is a quantum number and parallels the idea of isospin under the strong interaction. The weak isospin of a particle describes how the electroweak force transforms under the $SU(2)_L$ group.

1.2 Beyond the Standard Model

The Standard Model has been the most successful theory of particle physics to date. However, it is not a complete theory. There are still lots of questions that the SM offers no explanation for. For example, it does not explain why the amount of matter and antimatter is not the same in the universe. There is also no explanation for the number of quark and lepton families. Moreover, even though neutrinos are massless in the SM, neutrino oscillation experiments have shown that neutrinos do have mass. The origin of free parameters of the SM is another unanswered question.

In order to address these imperfections, theories including various extensions of the SM, "new physics", are proposed. Models for physics beyond the SM include supersymmetry, extra dimensions, quark/lepton compositeness, etc.

1.2.1 Contact Interactions

One approach to address the open questions of the SM is to search for a contact interaction that would result from new phenomena such as quark and lepton compositeness. Moreover, the energy scale that the LHC provides may not be high enough for the direct observation of a new gauge boson mediating a new interaction. This approach is very similar to the one that Fermi used to explain nuclear β-decay before the discovery of the W boson. Hence, without knowing the intermediate process, one can still write the Lagrangian by describing it as a four-fermion contact interaction (CI) between two incoming quarks and two final state leptons [14]:

$$\begin{aligned} \mathcal{L} &= \frac{g^2}{\Lambda^2} \left[\eta_{LL} \left(\bar{\psi}_L \gamma^\mu \psi_L\right) \left(\bar{\psi}'_L \gamma_\mu \psi'_L\right) + \eta_{RR} \left(\bar{\psi}_R \gamma^\mu \psi_R\right) \left(\bar{\psi}'_R \gamma_\mu \psi'_R\right) \right. \\ &+ \left. \eta_{LR} \left(\bar{\psi}_L \gamma^\mu \psi_L\right) \left(\bar{\psi}'_R \gamma_\mu \psi'_R\right) + \eta_{RL} \left(\bar{\psi}_R \gamma^\mu \psi_R\right) \left(\bar{\psi}'_L \gamma_\mu \psi'_L\right) \right] , \end{aligned} \tag{1.41}$$

where g is a coupling constant chosen as $g^2/4\pi = 1$, $\psi_{L,R}$ and $\psi'_{L,R}$ are the incoming and outgoing left and right fermionic fields. The energy scale of the new interaction

is given by Λ. It may have different interpretations depending on the model proposed. For instance, in the quark and lepton compositeness model, Λ is the energy scale below which the fermion constituents are bound together. The parameters $\eta_{i,j}$ where the indices i,j are L or R (left or right) determine the chiral structure of the new interaction and may have values of -1, 0, +1 by convention. By choosing the appropriate combinations of these values, different chirality models are built:

- The left-left contact interaction model: $\eta_{LL} = \pm 1$ and $\eta_{LR} = \eta_{RL} = \eta_{RR} = 0$, which is often considered as a benchmark model for the contact interaction searches.
- The right-right contact interaction model: $\eta_{RR} = \pm 1$ and $\eta_{LL} = \eta_{LR} = \eta_{RL} = 0$.
- The left-right/right-left contact interaction model: $\eta_{LR} = \eta_{RL} = \pm 1$ and $\eta_{LL} = \eta_{RR} = 0$.

In this study, the last choice is referred to as left-right contact interaction model.

The Lagrangian can be written particularly for the process $q\bar{q} \to \mu^+\mu^-$ as:

$$\begin{aligned} \mathcal{L} &= \frac{g^2}{\Lambda^2} \left[\eta_{LL} \left(\bar{q}_L \gamma^\mu q_L\right) \left(\bar{\mu}_L \gamma_\mu \mu_L\right) + \eta_{RR} \left(\bar{q}_R \gamma^\mu q_R\right) \left(\bar{\mu}_R \gamma_\mu \mu_R\right) \right. \\ &+ \left. \eta_{LR} \left(\bar{q}_L \gamma^\mu q_L\right) \left(\bar{\mu}_R \gamma_\mu \mu_R\right) + \eta_{RL} \left(\bar{q}_R \gamma^\mu q_R\right) \left(\bar{\mu}_L \gamma_\mu \mu_L\right) \right] , \end{aligned} \tag{1.42}$$

The signature of the new interaction would appear as an excess in the tail of the dimuon mass distribution of the SM DY production as well as in the lepton angular distribution.

The differential cross section for the process $q\,\bar{q} \to \mu^+\mu^-$ with the addition of the new interaction (see Fig. 1.7) can be written as

$$\frac{d\sigma}{dm_{\mu\mu}} = \frac{d\sigma_{DY}}{dm_{\mu\mu}} - \eta_{ij} \frac{F_I}{\Lambda^2} + \frac{F_C}{\Lambda^4} , \tag{1.43}$$

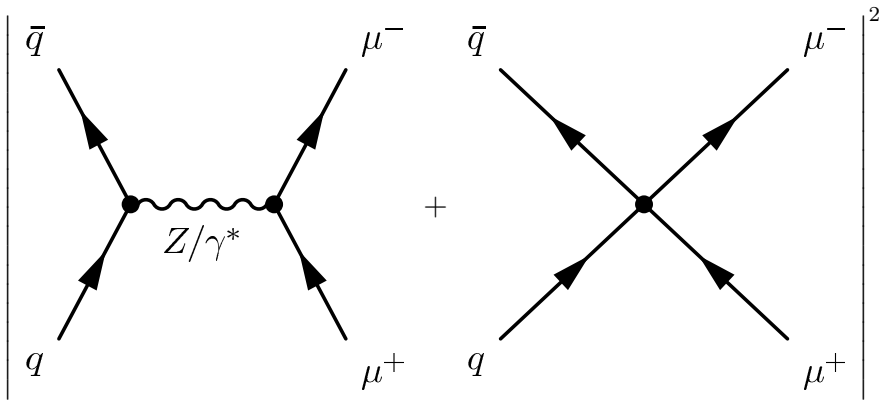

Figure 1.7: Leading order production mechanism for Drell-Yan with additional contact term with scale Λ in the dimuon final state.

which includes the SM DY term, the pure contact interaction term (F_C) and the DY-CI interference term (F_I), in terms of the dilepton mass $m_{\mu\mu}$. Depending on the value of η_{ij}, the interference between SM and new physics processes may occur constructively ($\eta_{ij} = -1$) or destructively ($\eta_{ij} = +1$).

1.2.1.1 Quark and Lepton Compositeness

The SM fails to explain the variety of observed quark and lepton flavors and their masses. Also, there is no obvious logical reason why these particles fall into a pattern of three families. One possible explanation is that quarks and leptons could be made of more fundamental constituents, often called *preons* [15], tightly bound together. The preons interact via a new gauge interaction named *metacolor*. In this model, the scale of compositeness is defined as the characteristic energy scale below which the metacolor interaction becomes strong and binds the preons to form metacolor-singlet states like the quarks and leptons. If the collision energy goes beyond the energy scale Λ then the multiple production processes would dominate over the two-body parton scattering processes. In other words, unconventional events such as multijets, jets with leptons and multileptons will dominate standard model processes. The cross section for these allowed inelastic processes of the order of $4\pi/\Lambda^2$, would be different than the

SM cross section, which is of the order of $\pi\alpha^2/\hat{s}$ where α is the fine structure constant and $\hat{s}$ is the partonic center of mass energy. However, if the collision energy does not reach the compositeness scale, even though the direct evidence is imperceptible, compositeness might be visible through deviations in the cross section, the angular distribution or the dilepton mass tail. At this energy scale, the quark and lepton compositeness can be described as a four-fermion contact interaction.

1.2.2 Large Extra Dimensions

One of the deficiencies of the SM is the hierarchy problem. The enormous gap between the electroweak scale and the Planck mass scale (∼16 orders of magnitude) remains unexplained to date. Also, the weakness of gravity as compared to the other three interactions of the SM is another intriguing question waiting to be answered. Arkani-Hamed, Dimopoulos and Dvali (ADD) [16] postulated the existence of large extra dimensions to address these issues. This model anticipates the existence of n extra spatial dimensions compactified to a radius R. In accordance to this scenario, gravitons propagate freely in the bulk of 4+n dimensions while the other known forces are constrained to the brane of 3+1 space-time dimensions, which leads to a relative dilution of gravity on the 4-D membrane. The mass M_D is introduced as the fundamental Planck scale in the "fixed-brane" scenario, expected to be of the order of a few TeVs which is achieved by requiring the volume of the extra dimensions to be large. It can be formulated as:

$$M_{Pl}^2 = M_D^{n+2} R^n, \tag{1.44}$$

which is calculated by integrating out the extra dimensional degrees of freedom from the 4+n Einstein-Hilbert action which depends on the parameter M_D. This action is compared to the four dimensional effective action which includes the parameter M_{Pl}, the Planck mass scale ($M_{Pl} \sim 1$ x 10^{16} TeV) to obtain the relation given in Eq. (1.44).

The propagation of gravity in the large extra dimensions results in Kaluza-Klein (KK) modes of the graviton. The mass splitting of these modes for each n dimension is $1/R$. KK modes have small spacings since the extra dimensions are required to be large to resolve the hierarchy problem. This leads to an almost continuous spectrum of the KK graviton states and an expected non-resonant broad excess over the SM prediction.

The production of dimuons via virtual KK graviton exchange involves a sum over many KK modes that needs to be cut off at some value. In this analysis, the ultraviolet cutoff is chosen to be the string scale M_{S}. This scale is related to M_D via the Gamma function, Γ, by;

$$M_{\mathrm{S}} = 2\sqrt{\pi}\Big[\Gamma\left(\frac{n}{2}\right)\Big]^{1/(n+2)} M_D. \tag{1.45}$$

Leading order virtual graviton exchange occurs via two processes, a $q\bar{q}$ initiated process which is similar to the SM DY process, and a gluon initiated process which does not have a SM analog. The Feynman diagrams for these processes are shown in Fig. 1.8.

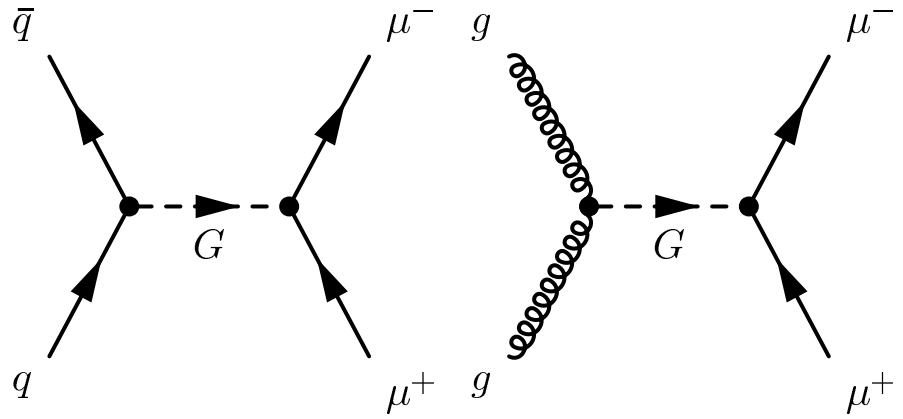

Figure 1.8: Virtual graviton exchange via $q\bar{q}$ initiated process on the left and a gluon initiated process on the right.

The differential cross section for the $q\bar{q}/gg \to \mu^+\mu^-$ process is:

$$\frac{d\sigma}{dm_{\mu\mu}} = \frac{d\sigma_{DY}}{dm_{\mu\mu}} + \frac{F_{int}}{M_S^4} + \frac{F_G}{M_S^8} \ , \tag{1.46}$$

which includes the SM DY term, the interference term F_{int} and the pure graviton exchange term F_G, in terms of the dimuon mass $m_{\mu\mu}$.

There are three different formalisms for this model depending on the way of performing the summation over the tower of KK modes: Giudice-Rattazzi-Wells (GRW) [17], Hewett [18], and Han-Lykken-Zhang (HLZ) [19]. In the presence of extra dimensions, the strength of gravity can be parameterized as $\mathcal{F}/M_{\rm S}^4$, where $\mathcal{F}$ is a dimensionless parameter that encodes the dependence of the virtual KK graviton exchange on the number of extra dimensions. The definition of $\mathcal{F}$ depends on each formalism:

$$\begin{aligned}
\mathcal{F} &= 1, \quad \text{(GRW)} \\
\mathcal{F} &= \frac{2\lambda}{\pi} = \frac{\pm 2}{\pi}, \quad \text{(Hewett)} \\
\mathcal{F} &= \log\left(\frac{M_S^2}{s}\right) \text{ for } n = 2, \quad \text{(HLZ)} \\
\mathcal{F} &= \frac{2}{n-2} \text{ for } n > 2. \quad \text{(HLZ)}
\end{aligned} \tag{1.47}$$

As opposed to the HLZ formalism, GRW and Hewett have no explicit dependence on the number of extra dimensions. While gravitational effects interfere constructively with the SM processes in the GRW and HLZ formalisms, the interference may occur constructively or destructively in the Hewett formalism. The sign of λ determines if it is a constructive interference (λ = +1) or a destructive interference (λ = -1). Interference effects between the DY and virtual KK graviton processes are small due to dimuon production by virtual KK gravitons being predominantly gluon-induced rather than quark-induced.

1.2.3 Review of Previous Searches

Previous searches for quark and lepton compositeness include studies from the Neutrinos at the Tevatron (NuTeV) [20], the Stanford Linear Accelerator Center (SLAC) [21], the Large Electron-Positron Collider (LEP) [22–26], the Hadron Electron Ring Accelerator (HERA) [27, 28], the Tevatron [29–33], and recently from ATLAS (A Toroidal LHC ApparatuS) [34–36] and CMS (Compact Muon Solenoid) [37] experiments at the LHC. Thus, quark and lepton compositeness searches have been performed in neutrino-nucleus and electron-electron scattering and at electron-positron, electron-proton, and hadron colliders. All of these studies have resulted in exclusion lower limits on the compositeness energy scale and the searches have been carried out in dilepton and dijet final states.

The SLAC E158 collaboration used the measurement of a parity violating asymmetry to set limits on Λ in the LL model for the *eeee* interaction. The DELPHI collaboration at the LEP set the limits for *eebb* interaction, using the measurements of R_b (defined as $\sigma_{b\bar{b}}/\sigma_{q\bar{q}}$) and A^b_{FB}. The fits of R_b and A^b_{FB} as a function of $\sqrt{s}$ are compared to the SM predictions. The other collaboration at the LEP, the ALEPH collaboration, also set limits on Λ for generic hadronic final states by performing fits to the hadronic cross sections assuming that the contact interaction affects all flavors with equal strength. The OPAL collaboration derived the limits for the same interaction but in the specific case of first generation quarks. At HERA experiment, the H1 collaboration investigated contact interactions by searching for deviations in the neutral current differential cross section $d\sigma/dQ^2$ from the SM expectation at high Q^2 for the *eeqq* interaction. The limit is also set on the light quark radius; $R_q < 0.65 \times 10^{-18}$ m. The CDF collaboration from the Tevatron used $\cos\theta^*$ as a discriminating variable to set limits on Λ.

At the LHC, the CMS collaboration conducted the contact interaction search in the dimuon channel with the 2011 data at $\sqrt{s} = 7$ TeV, corresponding to an

integrated luminosity of 5.3 fb^{-1}. The best published limits in the case of $qq\mu\mu$ contact interactions come from the ATLAS analysis of 2011 data corresponding to 5 fb^{-1} for which only the dilepton invariant mass was used as a discriminating variable. Both collaborations only investigated the LL CI model with the 2011 data. The most stringent limits on $qqqq$ contact interactions are obtained by using the inclusive jet p_T distribution [38].

The list of previous limits from the experiments mentioned above is shown in Table 1.3.

The most recent limits from the CMS collaboration are not included in the table. For the recent results [39], the 2012 data at $\sqrt{s} = 8$ TeV, corresponding to an integrated luminosity of 20.6 (19.7) fb^{-1} for the dimuon (dielectron) channel is used. The limits are $\Lambda^- < 15.2$ TeV ($\Lambda^- < 18.3$ TeV) for constructive case and $\Lambda^+ < 12.0$ TeV ($\Lambda^+ < 13.5$ TeV) for destructive case for the $qq\mu\mu$ ($qqee$) interaction. These limits can be directly compared to the results of this analysis which shows that the limits obtained in this analysis are the most stringent to date.

Table 1.3: Previous limits on the contact interaction scale Λ.

Previous Limits on Λ (TeV)						
Experiment	Collaboration	Proces	Λ^-_{LL}	Λ^-_{LL}	Λ^-_{RR}	Λ^-_{RR}
SLAC	E158	$eeee$	16	7	-	-
LEP	DELPHI	$eebb$	10.2	8.4	2.2	5.7
LEP	ALEPH	$eeqq$	7.2	12.9	5.3	10.2
LEP	OPAL	$eeqq$	9.1	8.6	-	-
HERA	H1	$eeqq$	4	4.2	3.9	4.4
TEVATRON	CDF	$qqee$	5.9	3.7	5.6	3.9
LHC	CMS	$qq\mu\mu$	13.1	9.5	-	-
		$qqqq$	14.6	10.6		
LHC	ATLAS	$qq\mu\mu$	12.7	9.9	-	-
		$qqee$	13.8	10.4	-	-

Previous searches for large extra dimensions in the context of the ADD model have been carried out at LEP [40–45] , HERA [46], the Tevatron [47, 48], and the LHC. The D0 experiment at the Tevatron, using proton-anti-proton collisions, performed the extra dimension searches in dimuon, dielectron, dijet and diphoton channels.

At the LHC, both ATLAS [49, 50] and CMS [51–53] have searched in dimuon, dielectron and diphoton channels. The observed lower limits that ATLAS produced by using the 2011 data at $\sqrt{s} = 7$ TeV, corresponding to an integrated luminosity of 4.9 (5.0) fb^{-1} are $M_S > 2.83$ TeV and $M_S > 2.73$ TeV for the dimuon and dielectron channels, respectively, for the GRW formalism. The observed limit from the combination of these channels is 2.85 TeV which is then further combined with the limits from the diphoton channel resulting $M_S > 3.22$ TeV. The CMS limit obtained with the 2011 data at $\sqrt{s} = 7$ TeV, corresponding to an integrated luminosity of 2 fb^{-1} is

$M_S > 2.8$ TeV both for the dimuon and dielectron channels. The combined limit is $M_S > 3.1$ TeV.

The most recent results that the CMS recently released are obtained using the 2012 data at $\sqrt{s} = 8$ TeV, corresponding to an integrated luminosity of 20.6 (19.6) fb^{-1} for the dimuon (dielectron) channel [54, 55]. The observed (expected) limits are $M_S > 3.64$ TeV (3.65 TeV) for the dimuon channel, $M_S > 3.90$ TeV (3.89 TeV) for the dielectron channel and $M_S > 4.01$ TeV (4.00 TeV) for the combined dilepton channel. These limits can be directly compared to the results of this analysis which shows that the limits obtained in this analysis are the most stringent to date.

1.3 Parton Distribution Functions

The idea of quarks and antiquarks as the building blocks of hadrons was proposed in 1964 by Gell-Man and independently by Zweig. Five years later, in 1969, Richard Feynman proposed that when a hadron moves with a speed close to that of light, it appears as a collection of infinite number of point-like constituents called "partons" with a wide-spread momentum distribution.

The partonic structure of a nucleon is best probed in scattering processes like Deep Inelastic Scattering (DIS) of leptons (electrons, muons or neutrinos) off nucleons where the square of the 4-momentum transferred between the electron and nucleus, Q^2, is large. The nucleon was found to have substructure at electron-proton DIS experiment at SLAC in 1966. Jerome Friedman, Henry Kendall and Richard Taylor were awarded by the Nobel Prize in 1990 for performing this experiment.

The three-quark model assuming that a proton or a neutron is made of three free non-interacting quarks is too simple. Those valence quarks are actually imbedded in a sea of virtual quark-antiquark pairs generated by the gluons which hold the quarks together in the nucleon. Valence quarks, sea quarks and gluons are all called partons.

The momentum distribution functions of the partons within the nucleon are called Parton Distribution Functions (PDFs). They represent the probability densities to find a parton carrying a momentum fraction x at a squared energy scale Q^2 ($f(x, Q^2)$). The behavior of PDFs are different at low and high Q^2. At low Q^2, three valence quarks become more dominant in the nucleon. At high Q^2, there are more sea quarks with low momentum fraction x. It was found in DIS experiments that only the half of the nucleon momentum is carried by quarks and antiquarks. The remainder is carried by gluons.

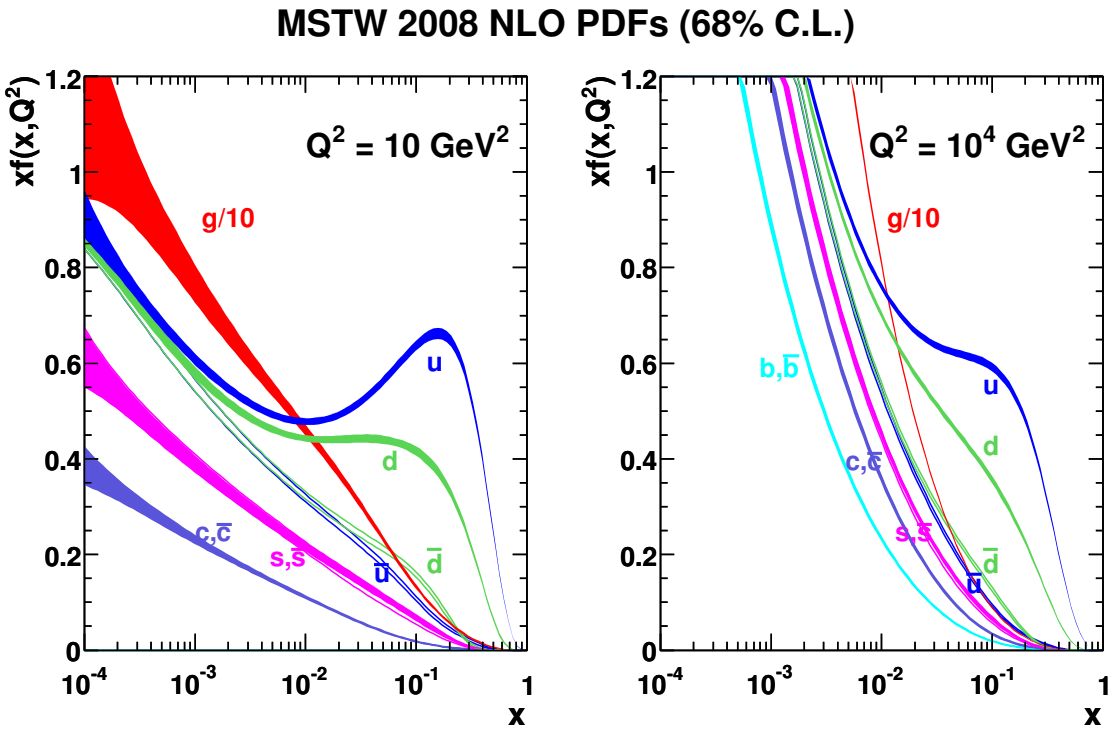

Figure 1.9: Next-to-leading order parton distribution functions as a function of momentum fraction x, taken from MSTW2008NLO PDF set, for a momentum transfer of 10 GeV^2 (left) and 1000 GeV^2 (right).

This behavior is encoded in the QCD evolution equations for parton densities called DGLAP (Dokshitzer-Gribov-Lipatov-Altarelli-Parisi) equations. These are the consequence of the asymptotic freedom which implies that at high energy partons

behave as free particles, emitting color radiation whereas at low energy their interaction with the gluon field increases in strength. The equations are formulated relative to different powers of $\alpha_s(Q^2)$ in the perturbative development. They give the Q^2 dependence but not the prediction of the x dependence of the parton distributions at given Q^2. Thus, this needs to be extracted from the data.

Hadronic collisions which involve a hard scattering can also be described by the parton model. Assuming that A and B are incoming partons which are confined in protons. The longitudinal momentum fraction of parton a in proton A is denoted by x_a and the parton density of a in A by $f_{a/A}(x_a)$. The cross section for producing a quark or lepton c in the inclusive reaction is obtained by multiplying the subprocess cross section $\hat{\sigma}$ by $dx_a f_{a/A}(x_a)$ and $dx_b f_{b/B}(x_b)$. It needs to be summed over parton and antiparton types a, b and integrated over x_a and x_b. Also, an average must be made over the colors of a and b. The resulting cross section is shown as:

$$\sigma(AB \to cX) = \sum_{a,b} C_{ab} \int dx_a dx_b [f_{a/A}(x_a) f_{b/B}(x_b) + (A \leftrightarrow B \text{ if } a \neq b)] \hat{\sigma}(ab \to cX). \tag{1.48}$$

where C_{ab} is the initial color-averaging factor. Also, $\hat{\sigma}$ is summed over initial and final colors. The color-average factors for quarks and gluons are

$$C_{qq} = C_{q\bar{q}} = \frac{1}{9}, \qquad C_{qg} = \frac{1}{24}, \qquad C_{gg} = \frac{1}{64}. \tag{1.49}$$

Here X denotes all other interactions in a proton-proton collision apart from the hard scattering between the two partons including initial and final state radiation (ISR and FSR), parton showering, hadronization, etc.

In DY production at a proton-proton collider, in the case of *initial state radiation*, one of the incoming fermions emit a photon or a gluon before the interaction with other particles. For *final state radiation*, the leptons produced after the hard scattering emit a photon.

In a proton-proton collision, since the incoming and outgoing partons of the hard scattering have a color, they radiate gluons which in turn can split up in gluon-gluon or quark-antiquark pairs. The resulting partons will generally radiate further, hence producing more pairs. This leads to a cascade of partons. This process is called *parton showering*. The quarks are then combined into colorless hadrons, which is called *hadronization*. Resulting unstable hadrons then subsequently decay into stable particles that can be detected.

Therefore, the resulting event after the proton-proton collision in which a hard scattering occurs contains particles that originate from the two outgoing partons (plus initial and final state radiation). It also includes particles that are left over after a parton is knocked out of each of the initial protons, which are called *beam-beam remnants*. Particles other than the two outgoing particles from the hard scattering process are referred to as the *underlying event*. This set of particles includes contributions from the beam-beam remnants as well as initial and final state radiation.

These physics processes are simulated by dedicated software tools. As a first step, the interaction between partons that originate from the colliding protons is simulated. The partonic composition of colliding protons is modeled by PDF sets. The hard parton-parton scattering cross section is calculated by using the matrix element. The power of a coupling constant that is used in this calculation determines the order of the generator. The lowest order of a given process is called leading order (LO). Calculations for higher order QCD effects for the hard scattering are notoriously difficult and generally not included in the matrix element calculation. Thus, effects of some interactions such as parton showering are added in the next stage of the simulation. However, there is a difference between the calculation for gluon radiation in the matrix element and the calculation of gluon radiation in the parton shower. Because in the matrix element calculation, spin interactions and interference effects are taken into account. Next stage of the simulation is hadronization which is then

followed by the simulation of interactions between beam-beam remnants. Different generators have different approaches to account for these processes:

- PYTHIA [56] is a general purpose LO event generator, both in QCD and QED diagrams. The matrix elements for the hard process are evaluated at LO. Corrections are applied due to beam remnants, parton showering and hadronization. In order to account for final state radiation, PYTHIA can be interfaced with the program PHOTOS [57].

- HERWIG [58] is a general purpose event generator similar to PYTHIA. It provides initial and final state radiation via its parton shower algorithm. The implementation of the simulation of hadronization is the major difference with respect to PYTHIA. Its hadronization algorithm is referred to as "cluster fragmentation" which determines whether a hadron will decay based on its mass.

- POWHEG [59] is a next-to-leading order (NLO) event generator. The hard process is evaluated at NLO in QCD. For parton showering and hadronization, POWHEG has its own algorithms but it can also be interfaced with PYTHIA in order to simulate these effects.

- MC@NLO [60] calculates the hard processes, including real gluon or quark emissions and virtual particle loops, at NLO in QCD. However, the calculations for electroweak diagrams are performed in LO. It is interfaced with HERWIG for parton showering and hadronization.

- SHERPA [61] is a multi-purpose generator which contains a very flexible LO matrix-element generator for the calculation of hard scattering processes within the SM and various new physics models. The initial and final state QCD radiation is described through a parton shower model. For hadronization, it uses the cluster model.

CHAPTER 2

EXPERIMENTAL SETUP

This chapter describes the design and layout of the experimental setup. Section 2.1 gives an overview of the LHC technologies. Section 2.2 focuses on the ATLAS detector, by describing its subdetectors, each optimized for a specific task. Due to its importance for this study, special attention is given to the Muon Spectrometer. Detailed description of the muon reconstruction algorithms and a discussion of the muon reconstruction performance are also included in this section. In the last section, data taking with the ATLAS detector is discussed.

2.1 Large Hadron Collider

The Large Hadron Collider (LHC) [62] is a proton-proton (pp), lead-lead (Pb-Pb) and proton-lead (p-Pb) collider, operated by the European Organization for Nuclear Research (CERN). The main accelerator ring has a circumference of about 27 km. It is situated underground in the former Large Electron-Positron (LEP) collider tunnel at a depth that varies between 50 and 150 m. The collider goes around the neighborhood of the city of Geneva and crosses the border between France and Switzerland. The ultimate design center of mass energy ($\sqrt{s}$) for pp collisions is 14 TeV.

2.1.1 Choice of a Circular Hadron Collider

There are two fundamental shapes of colliders: linear colliders and circular colliders. These colliders generally collect particles into bunches and these bunches are then set to collide. However, only a small fraction of the particles in each bunch

actually collide. In circular colliders, the remaining particles keep circulating and are used for future collisions whereas they are lost and cannot be re-used in linear colliders. Hence, using a circular design enables a high rate of collisions and facilitates collecting a large amount of data which is important for precision measurements and observing rare processes. However, the beam energy is limited due to synchrotron radiation, which is electromagnetic radiation emitted when charged particles accelerate in a curved path. That, on the other hand, is not an issue for a linear collider since particles are accelerated along a straight line and do not suffer from the synchrotron radiation.

Energy loss due to the synchrotron radiation is directly proportional to the energy of a particle (E) and inversely proportional to its mass (m), as well as the radius of the curvature of its trajectory. The relation is given by:

$$\frac{dE}{dt} \propto \frac{E^4}{m^4 R}. \tag{2.1}$$

Since the mass of a proton is 2000 times larger than the mass of an electron, with the same energy and the same collider dimensions, an electron loses more energy than a proton by the amount of $(m_p/m_e)^4 \sim 10^{13}$. On that account, it is more advantageous to use heavy hadrons such as protons for circular colliders.

2.1.2 LHC Parameters

For colliders, the instantaneous luminosity $\mathcal{L}$ is a measure of the number of particles in the beam, e.g protons, that pass through a surface of unit area per unit time. The instantaneous luminosity is measured in units of $\mathrm{cm}^{-2}\mathrm{s}^{-1}$. The number of events generated per second in the LHC collisions is correlated to a cross section (σ_{event}) for a given physical process and the instantaneous luminosity by:

$$N_{event} = \mathcal{L}\sigma_{event}. \tag{2.2}$$

The cross section depends on the type of particles involved in the collision as well as the considered processes, whereas the instantaneous luminosity depends on the properties of the colliding beams and can be written as:

$$\mathcal{L} = \frac{N_b^2 n_b f_r \gamma_r}{4\pi\epsilon_n \beta^*} F, \tag{2.3}$$

where N_b is the number of protons per bunch, n_b is the number of bunches per beam, f_{rev} is the revolution frequency, γ_r is the relativistic gamma factor, ϵ_n is the normalized transverse beam emittance[1], β^* is the beta function[2] at the collision point and F is the geometric luminosity reduction factor due to the crossing angle at the interaction point.

For a fixed center-of-mass energy, the size of the instantaneous luminosity represents the amount of data collected per unit time. The luminosity integrated over time, $\mathcal{L}_{int} = \int \mathcal{L} dt$, is a measure for the total number of events.

The design value of the instantaneous luminosity at a center of mass energy of 14 TeV is $\mathcal{L} = 10^{34}$ cm^{-2}s^{-1}. The beam structure is composed of bunches of protons, where each bunch is made up of about 10^{11} protons. The design number of bunches is 2808. The bunches are organized into "trains" in which they follow each other at separation of about 7.5 cm in length or 25 ns in time. That means two proton beams collide 40 million times per second (collision rate $\approx$ 40 MHz).

2.1.3 Accelerator Chain

The primary source of the protons for the CERN accelerator complex is a "duoplasmatron" source that has a cathode (tungsten) filament emitting electrons into

[1]The transverse emittance is a measure of the beam size in the transverse plane. The nominal normalized transverse emittance for the LHC is $\epsilon_n = 3.75$ μm.

[2]The beta function is a measure of how focused the beam is. Reducing the beta function decreases the beam size at the collision point and results in a more focused beam. The nominal design value of the beta function at the LHC is $\beta^* = 0.55$ m.

hydrogen gas. The filament is surrounded by a solenoidal coil that produces a magnetic field. That causes the emitted electrons to spiral around the field lines, which increases the distance they travel, which in turn increases their probability of colliding with a hydrogen molecule. These collisions free additional electrons. The process can be simplified as the following:

$$H_2 + e^- \rightarrow H_2^+ + 2e^-$$
$$H_2^+ + e^- \rightarrow H^+ + H + e^-,$$
$$H + e^- \rightarrow H^+ + 2e^-$$

The protons extracted from duoplasmatron source are sent through a linear accelerator (LINAC2) after traveling less than a meter through a radiofrequency quadrupole (RFQ2) where they are accelerated to 750 keV and divided into bunches.

In LINAC2, positively and negatively charged conductors are arranged successively along 30 meter distance so the protons pass through them pushed by the conductor behind and pulled by the one ahead, which in turn accelerates the protons. At the end of the line they gain an energy of 50 MeV.

The journey of protons continues in a series of synchrotrons that use magnets to bend the protons into a closed path. Since the energy gain of particles in synchrotrons is limited by the strength of their magnets, particles need to be transported to another ring with a larger radius.

The Proton Synchrotron Booster (PSB) is the first circular accelerator that the protons are injected into. It is composed of four rings, stacked on each other. Three of these rings are filled with a single bunch that is accelerated to 1.4 GeV.

Three proton bunches accelerated in PSB are sent into the Proton Synchrotron (PS), the oldest machine in the chain. Since two revolutions of the PSB correspond to one revolution of the PS, a total of 6 bunches are fed into the PS. Each of the 6 bunches are then further split into 3 bunches, giving a total of 18 bunches which are accelerated to 26 GeV. These 18 bunches are again split into 2, resulting in a total of 36 bunches which is called a "bunch train". Injecting protons at once in a form of bunch train to the next machine is a time saving process and allows to keep more bunches in the ring.

The next accelerator in the chain, the Super Proton Synchrotron (SPS), collects between 1 and 4 bunch trains coming from the PS and accelerates them to 450 GeV.

Finally, all bunches are transferred to the LHC. The SPS sends bunch trains to the LHC through two different lines to allow for collisions of two beams of protons circulating in opposite directions. From LINAC2 up to this step takes approximately 17 seconds and injecting all bunches to the LHC takes 20 minutes. When all bunches are collected by the LHC, they are accelerated to 4 TeV. This "ramp-up" process takes around 11 minutes. The bunches are kept circulating for 6 more minutes until beams are "stable". After a 5-minute "squeezing" process to focus the beams, they are circulated for 10 more minutes to prepare for physics collisions. A run started for data collection typically lasts between 10-20 hours. After 20 hours, since half of the luminosity is lost, the beam is dumped.

The acceleration chain of the lead ion is slightly different. They are first accelerated by the linear accelerator 3 (LINAC3) before being collected and accelerated by Low Energy Ion Ring (LEIR). Then the ions are further accelerated by the PS, the SPS and the LHC in sequence. A layout of CERN accelerator complex is shown in Fig. 2.1.

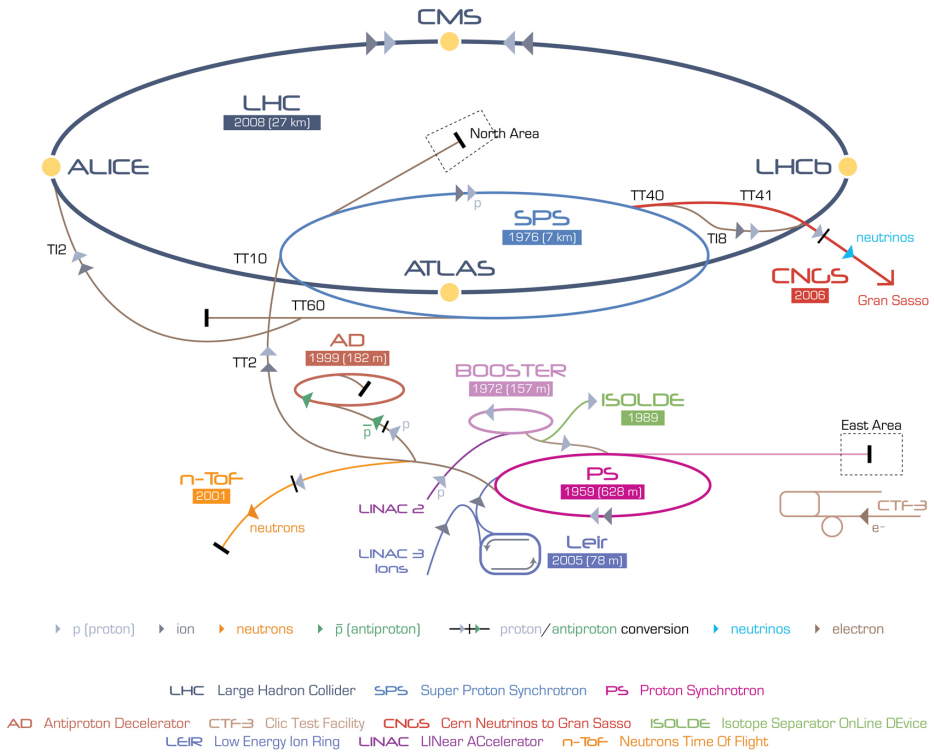

Figure 2.1: CERN accelerator complex.

2.1.4 LHC Status

On 10 September 2008, the LHC started its operations by successfully circulating proton beams in opposite directions without a collision. Unfortunately, on 19 September 2008, a fault occurred in the electrical bus connection in the region between a dipole and a quadrupole during powering tests of the main dipole circuit in Sector 3-4 of the LHC, resulting in mechanical damage of 53 superconducting magnets and release of several tons of helium gas into the tunnel [63]. In order to repair the damage and consolidate the machine, the further operations were delayed by 14 months.

On November 20, 2009 proton beams were successfully circulated again. Three days later, the first proton-proton collisions at $\sqrt{s} = 900$ GeV were recorded. By increasing the center of mass energy to 2.36 TeV on 16 December 2009, the LHC set a new world record for the highest-energy particle accelerator by beating the Tevatron's previous record of 0.98 TeV per beam. On 30 March 2010, the proton-

proton collisions were recorded at $\sqrt{s} = 7$ TeV and the LHC began its planned research program. During the running period in 2010, an integrated luminosity of 48.9 pb^{-1} was delivered by the LHC and an instantaneous luminosity of 2.1×10^{32} s^{-1}cm^{-2} was reached.

In 2011, the collisions continued at the same center of mass energy. The luminosity delivered by the LHC corresponds to an integrated luminosity of 5.61 fb^{-1}, with a peak instantaneous luminosity of 3.65×10^{33} s^{-1}cm^{-2}.

The collisions at $\sqrt{s} = 8$ TeV started on 5 April 2012 and a total of 23.3 fb^{-1} of pp collision data was delivered. During the 2012 run, a maximum instantaneous luminosity of 7.73×10^{33} s^{-1}cm^{-2} was reached, which is very close to the design luminosity of 10^{34} s^{-1}cm^{-2}.

The 2012 proton-proton running period was ended on 16 December 2012. After lead-lead running period between 20 January-14 February in 2013 , the LHC was shut down until 2015 to prepare the machine to operate at its design center of mass energy of 14 TeV with a peak instantaneous luminosity of 10^{34} s^{-1}cm^{-2} and with 25 ns between bunches.

2.1.5 Experiments at the LHC

Two proton beams are circulated in opposite directions and are set to collide at four interaction points. There are four main experiments built around each of these collision points: **ATLAS** (**A** **T**oroidal **L**HC **A**pparatu**S**), **CMS** (**C**ompact **M**uon **S**olenoid), **ALICE** (**A** **L**arge **I**on **C**ollider **E**xperiment) and **LHCb** (**LHC** **b**eauty).

ATLAS and CMS are general purpose detectors, designed to understand the SM and search for the physics beyond the SM, as well as the Higgs boson. The purpose of LHCb is to explore the properties of hadrons containing bottom quarks at high energy. ALICE is a heavy ion collision detector and specially designed for observing a new likely phase of matter, namely a quark-gluon plasma.

Two rather small experiments operating at the LHC are the **LHCf** (**LHC f**orward) and the **TOTEM** (**TOT**al **E**lastic and diffractive cross section **M**easurement). They are situated close to ALICE and CMS respectively and are specialized to study very forward physics that is not accessible to the general purpose detectors.

LHCf uses the high energy particles thrown forward by collisions as a source to simulate cosmic rays in laboratory conditions in order to understand the reaction chains induced by cosmic rays in the atmosphere. TOTEM is built to study the structure and interactions of the proton and to calibrate the luminosity at great accuracy.

2.2 ATLAS Detector

ATLAS [64] is one of two general purpose detectors at the LHC, designed to measure high-p_{T} objects such as electrons, muons, photons, jets, etc. with high precision for the general physics studies including the measurement of the SM parameters, searching for the Higgs boson and physics beyond the SM.

The ATLAS detector is located 92.5 m underground at interaction point 1 of the LHC tunnel. It was constructed between 2003 and 2008. The ATLAS detector is the biggest particle detector ever built with the outer dimensions of 44 m in length, 25 m in height and weighs about 7000 tons ($\sim$ weight of a hundred 747 jets). The overall layout of the detector is shown in Fig 2.2.

ATLAS is comprised of layered concentric subdetectors situated around the beam line, each optimized for a specific task. All subdetectors have a central part called "*barrel*" and a forward section on each side, called "*end-cap*". The ATLAS detector has four major components:

- **Inner Detector (ID)** finds vertices[3] and measures the momenta of the charged particles,
- **Calorimeter** measures the energy of the particles,
- **Muon Spectrometer (MS)** identifies and measures the momenta of muons
- **Magnet System** bends charged particles for momentum measurements

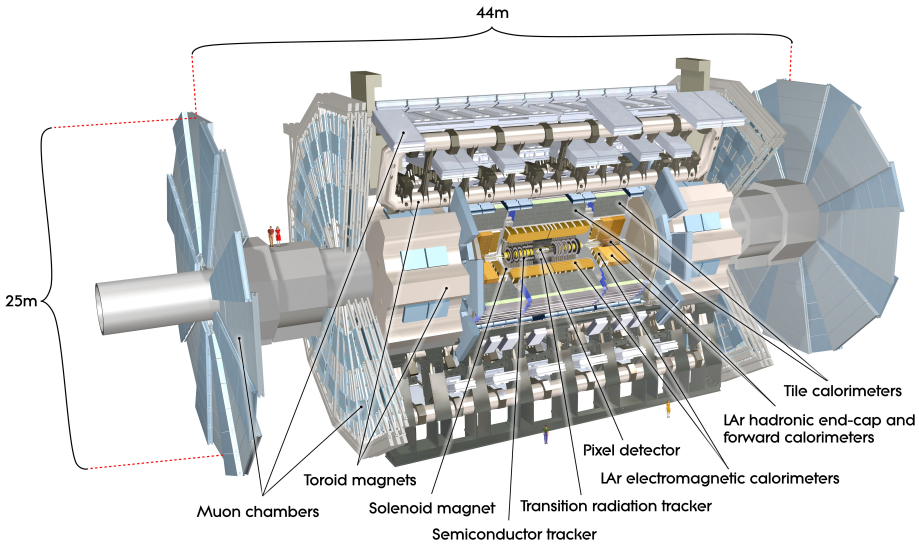

Figure 2.2: A detailed computer-generated image of the ATLAS detector and its systems.

The ATLAS collaboration was formed in 1992. Now it consists of about 3000 physicists from more than 177 universities and laboratories in 38 countries.

2.2.1 Coordinate System and Conventions

The ATLAS coordinate system is a right-handed coordinate system with the z-axis directed along the beam pipe. The x-axis points to the center of the LHC ring and

[3]Vertices are the positions of interesting physics interactions, such as proton collisions and particle decays.

the y-axis points upwards, towards the surface. The azimuthal angle ϕ is measured in the x-y plane around the beam axis and $\phi = 0$ corresponds to the positive x-axis. It can be written in terms of linear coordinates as:

$$\phi = \arctan\left(\frac{y}{x}\right). \tag{2.4}$$

The polar angle θ is measured relative to the positive z-axis and shown as:

$$\theta = \arctan\left(\frac{\sqrt{x^2 + y^2}}{z}\right). \tag{2.5}$$

In this context, the pseudo-rapidity is defined as:

$$\eta = -\ln\left(\tan\frac{\theta}{2}\right). \tag{2.6}$$

For cases where the particle is massless or $E \gg m$, the pseudorapidity approximates the rapidity, defined as:

$$y = \frac{1}{2}\ln\left(\frac{E + p_z}{E - p_z}\right). \tag{2.7}$$

The radial distance to the interaction point in the x-y plane is denoted by r and defined as $r = \sqrt{x^2 + y^2}$. A distance in $\eta - \phi$ space is shown by ΔR that can be written as $\Delta R = \sqrt{\Delta\eta^2 + \Delta\phi^2}$. Furthermore, the parameters given with a subscript "T" such as p_T, E_T, E_T^{miss} are the parameters projected on the transverse (x-y) plane.

The track of a particle with charge q can be represented by five main parameters; inverse momentum (q/p), ϕ, θ, transverse impact parameter (d_0) and longitudinal impact parameter (z_0). The impact parameter d_0 (z_0) is defined as the transverse (longitudinal) distance to a given reference point which is generally the collision point.

2.2.2 Inner Detector

The ID is the innermost system of the ATLAS detector, designed to provide a precise measurement of charged particle trajectories in a dense track environment.

The ID tracks are reconstructed within the pseudo-rapidity range $|\eta| < 2.5$. It is immersed in a solenoidal magnetic field of 2 T and its overall dimensions are 2.1 m in diameter and 6.2 m in length. A computer-generated image of the ID can be seen in Fig. 2.3. The ID exploits three types of detectors, covering different radial distances from the interaction point (IP): the Pixel detector, the Semi-Conductor Tracker (SCT), and the Transition Radiation Tracker (TRT).

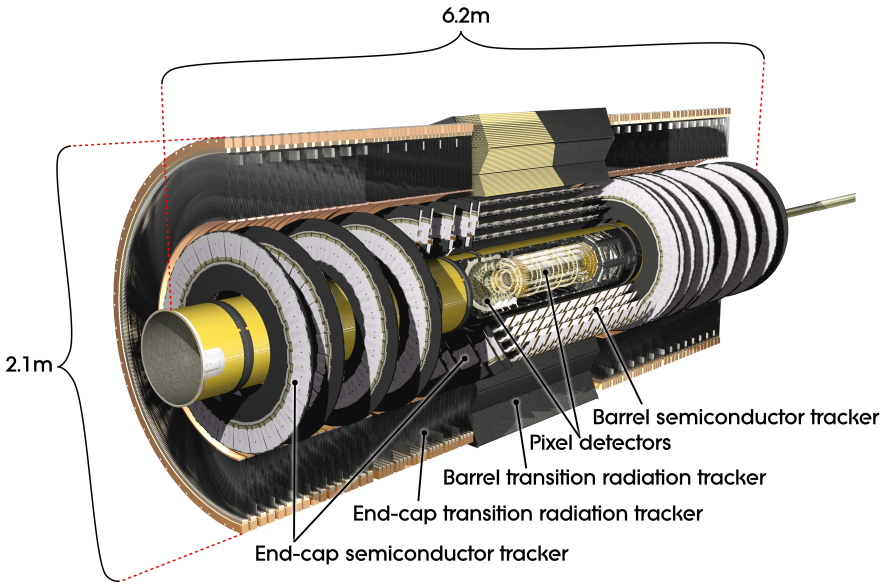

Figure 2.3: Cut-away image of the ATLAS Inner Detector.

The Pixel Detector is directly built onto the beryllium beam pipe to provide the best possible primary vertex (PV)[4] and secondary vertex[5] resolution. It consists of three layers in the barrel and three disks in each of the two end-caps. With over 80 million pixels, it has 90% of the total number of ATLAS readout channels. The nominal pixel size is 50 µm by 400 µm, while about 10% have the dimensions of 50 µm

[4]The primary vertex is the one that has the largest $\sum p_{\mathrm{T}}^2$ of the associated tracks.

[5]The secondary vertex is the position where relatively long lived particles like τ-leptons and b-hadrons coming from the PV decay.

by 600 µm. The pixel detector operates at ∼150 V and suffers from intense radiation since it is very close to the collision point.

The pixel detector consists of semiconducting silicon elements. The working principle of the pixel detector is very similar to the one of a camera which has an array of 6 million silicon pixels. A camera is designed to capture light coming from one particular direction. When a photon passes through the silicon material of the pixel, it knocks out an electron in the silicon so creates a *hole*. Similar to a camera, the pixel detector is interested in the particles coming from one particular direction; interaction point. In order to achieve that, it is built very close to the beam line covering radii from 5 cm to 15 cm. Instead of a photon with an energy of a few eV passing through a pixel of a camera, the interesting particles passing through the pixel detector have energies in GeV or TeV scales. One particle passes through the detector knocks loose a bunch of electron-hole pairs. Electrons and holes are then pulled in the opposite directions by the electric field. The charge built on a pixel produces a current that flows to the read-out electronics. Since each pixel has a separate circuit and electronics, the pixel that sends the signal is known. That provides a precise position measurement of the original particle.

The Semi-Conductor Tracker is located outside of the pixel detector, covering radii up to 52 cm. It is similar to the pixel detector but instead of the pixels, it consists of long silicon microstrips with a size of 80 µm by 12.6 cm, that are placed parallel to the beam line in the barrel and radially in the end-cap, thus providing a precision measurement in r - ϕ. The silicon strip tracker is arranged in four concentric cylinders for the barrel and in six end-cap disks on both sides of the IP. The SCT, together with the pixel detector, allows impact parameter measurements and vertex reconstruction. They ensure an accurate particle momentum measurement.

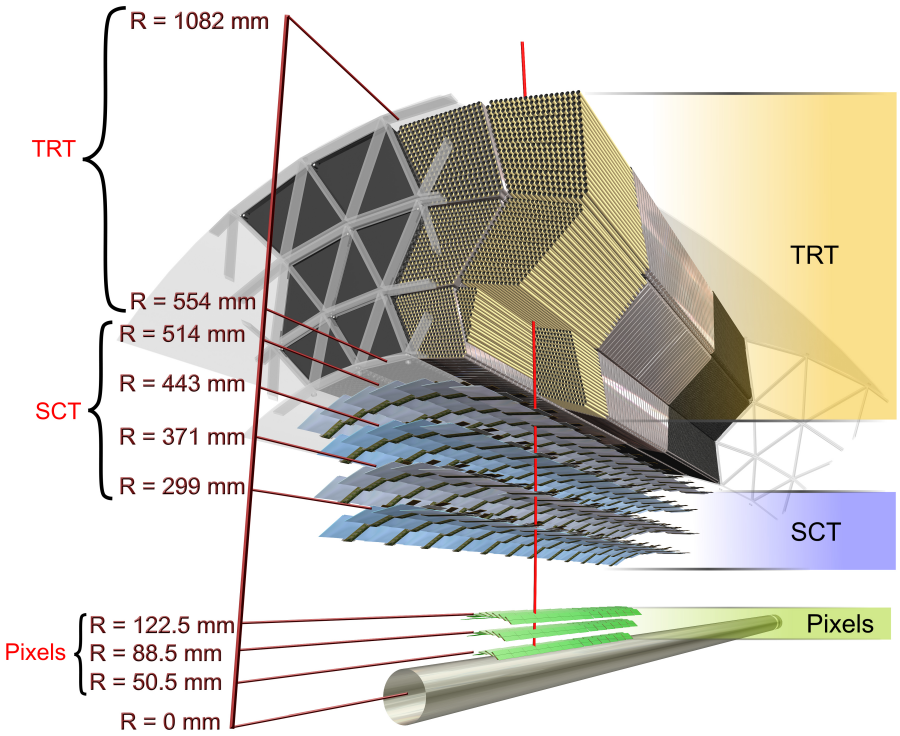

Figure 2.4: Scheme of the ATLAS inner detector barrel being crossed by one high-energy particle (shown by red line).

In order to reduce the leakage current that increases linearly with the integrated radiation dose, both the pixel detector and the SCT are cooled down to operate in the temperature of -5°C to -10°C.

The Transition Radiation Tracker surrounding the SCT is comprised of 4 mm diameter and 1.44 m long straw tubes filled with a gaseous mixture of xenon (70%), carbon dioxide (27%) and oxygen (3%). The tubes are placed parallel to the beam in the barrel region and radially in wheels in the end-cap region, providing a measurement in r - ϕ. The TRT covers a pseudorapidity region of $|\eta| < 0.7$ in the barrel and of $0.7 < |\eta| < 2.5$ in the end-cap.

The space between the layers of straw tubes are filled with radiators (polypropylene foils or fibres). A charged particle traveling through the radiator leads to a transition radiation which is an electromagnetic radiation emitted when a relativistic particle passes through an inhomogenous media, such as the boundary of two materials. Hence, when a charged particle passes through the material between the tubes, photons are produced. Within the tube, the particle ionizes the gas. Also, the accompanied radiated photons interact with the molecules of xenon and free more electrons. The signal amplitude produced as a result of the photon interaction is much larger than the ionization signal itself. Since, a 30 µm diameter gold-plated tungsten wire in the center of the straw (kept at the ground potential) acts as an anode and each straw (kept at -1530 V) acts as a cathode, a voltage difference is created in a tube. Hence, liberated electrons move towards the wire at the center of the tube. A gas mixture inside a straw helps increasing the electron drift velocity (max 45 ns) and photon-quenching.

In the TRT, transition radiation is used to distinguish between electrons and pions. If the initial particle is an electron far more photons are radiated than if it is a charged pion so more negative charges are measured on the wire. Because an electron is much lighter than a pion, an energy needed to create transition radiation is much less than a pion needed.

2.2.3 Calorimeter

The ATLAS calorimeter system includes two main calorimeter types; the Electromagnetic (EM) Calorimeter and the Hadronic (Had) Calorimeter. It is composed of six subsystems divided into three groups depending on their position in barrel, extended barrel and end-cap regions. The barrel includes an electromagnetic **L**iquid **Ar**gon (**LAr**) calorimeter and a hadronic **Tile Cal**orimeter (**TileCal**). The end-cap region is comprised of **E**lectro**M**agnetic **E**nd-**C**ap (**EMEC**), the **H**adronic **E**nd-**C**ap

(**HEC**) and the **F**orward **CAL**orimeter (FCAL). The hadronic calorimeter in the extended barrel region surrounds the end-cap calorimeters. A computer generated image of ATLAS calorimeters can be seen in Fig. 2.5.

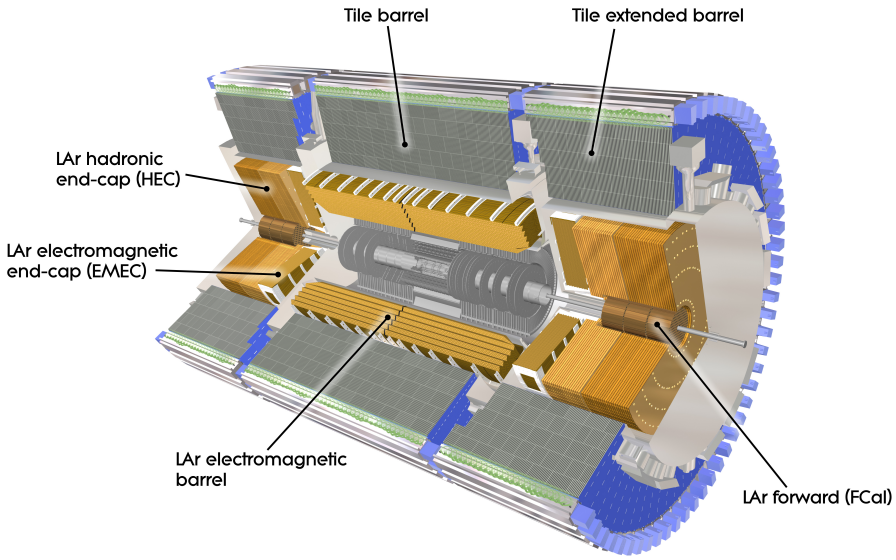

Figure 2.5: Overview of ATLAS calorimeters.

The LAr Electromagnetic Calorimeter is optimized to measure the energy of electrons and photons as well as their positions. Also, it provides electron and photon identification.

The LAr EM calorimeter has a coverage up to $|\eta|$=3.2. The two halves of the LAr EM calorimeter in the barrel region are separated by a small gap (4 mm) at z=0 and together spans up the pseudorapidity range of $|\eta| < 1.475$. In the end-cap region, two coaxial wheels cover a pseudorapidity range of $1.375 \leq |\eta| < 2.5$ and $2.5 \leq |\eta| < 3.2$. Between the barrel and the end-cap regions, in a coverage over $1.375 \leq |\eta| < 1.52$, a *crack* region exists in order to accommodate instrumentation and cooling infrastructure to the inner detector. A region with dead material in front of the EM calorimeter leads to energy loss. In the region, $0 < |\eta| < 1.8$ the electromagnetic calorimeters are

complemented by a **P**re**S**ampler (**PS**), an instrumented argon layer, which provides a measurement of the energy loss in front of the electromagnetic calorimeters.

In order to ensure the maximum azimuthal coverage and allow for fast read-out, the EM Calorimeter was designed with an accordion geometry. Its accordion shape structure consists of many layers of lead and steel that serve as absorber materials. Between them is liquid argon cooled down to -185°C. Liquid argon is used as an active material since it has an intrinsic linear behavior and its response over time is stable. Immersed in a liquid argon is a copper grid which acts as an electrode.

When an electron passing through the EM calorimeter meets the lead layer, it interacts with the material and produces a shower of low energy electrons, positrons and photons. A high energy electron that passes through several layers of absorber material creates a large shower before it eventually stops. The shower of low energy particles then passes into a liquid argon and ionizes the atoms creating more negatively charged electrons and positively charged ions. The negative charge is attracted towards the copper electrode. From the amount of charge deposited on the electrodes along its path, it is possible to measure the energy possessed by the original electron or photon when it entered the EM calorimeter.

The depth of the EM calorimeter is defined in terms of *radiation lengths* (X_0). A radiation length corresponds to the distance after which an electron (or positron) loses $(1 - 1/e)$ of its initial energy. The total thickness of the EM calorimeter is greater than $22X_0$ in the barrel, as seen in Fig. 2.6, and $24X_0$ in the end-cap.

The Hadronic Tile Calorimeter uses steel as an absorber material and scintillating tiles as an active material. It provides energy measurements of hadrons that includes neutrons, protons and mesons. The hadronic calorimeter also provides jet energy measurements.

The hadronic tile calorimeter is comprised of three parts; one in a center barrel region covering the pseudorapidity range of $|\eta| < 0.8$, two in the extended barrel

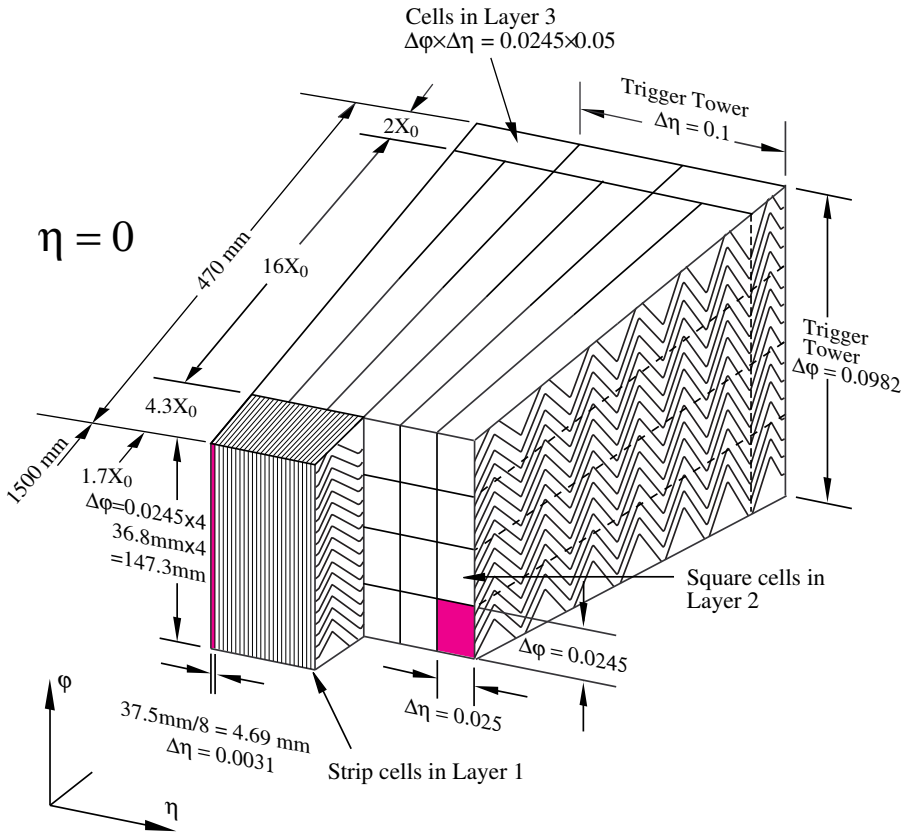

Figure 2.6: Sketch of a barrel module of the EM calorimeter.

region giving coverage over $0.8 < |\eta| < 1.7$. There is a vertical gap between these two regions that provides some space for cables and is partially instrumented with the **I**ntermediate **T**ile **C**alorimeter (**ITC**).

When a high energy hadron like a proton passes through the steel, it interacts with an atomic nuclei. These nuclear reactions lead to the production of more particles which initiate further interactions leading to a shower of particles. The particle shower passing through layers of scintillating[6] tiles produce light in these tiles. Long fibers located at the edge of the steel-tile sheet then carry the light to devices where the light intensity from many tiles is measured and converted to an electric current. Using

[6]A scintillator is a material which radiates light when struck by a charged particle.

the intensity of the light collected, it is possible to measure the energy possessed by the high energy hadron which entered the hadronic calorimeter.

For the hadronic calorimeters, the depth is expressed in terms of an *interaction length* (λ) which is the average distance a hadronic particle travels inside the material before any inelastic interaction occurs. The total thickness of the active calorimeter material in the barrel region is 9.7 λ and 11 λ in the end-cap region. The thickness of the hadronic calorimeter is good enough to provide good resolution for high energy jets and also to limit the energy leakage into the muon spectrometer.

Forward Calorimeters are the hadronic calorimeters placed in the forward region (HEC and FCAL) and due to the large radiation environment in this region, they all use LAr as an active material rather than scintillating tiles. As an absorber material, instead of lead, HEC and one section of FCAL use copper and the remaining two sections of FCAL uses tungsten in order to cope with the high radiation. The HEC covers a pseudorapidity range of $1.5 < |\eta| < 3.2$ whereas the range $3.1 < |\eta| < 4.9$ is covered by the FCAL.

2.2.4 Muon Spectrometer

The MS [65] is the outermost component of the ATLAS detector. It allows for precise momentum measurements independently of the inner tracking detector and provides identification and reconstruction of muons. It is comprised of two main parts; a barrel region within the pseudorapidity range of $|\eta| < 1.0$ and the end-cap region covering over $1.0 < |\eta| < 2.7$. A barrel toroid and two end-cap toroids produce a toroidal magnetic field of approximately 0.5 T and 1 T for the muon detectors in the central and end-cap regions, respectively. The layout of the MS with its subdetectors is shown in Fig. 2.7.

In the barrel region, precision tracking chambers are located between and on the eight coils of the toroid whereas in the end-cap they are placed behind and in front of

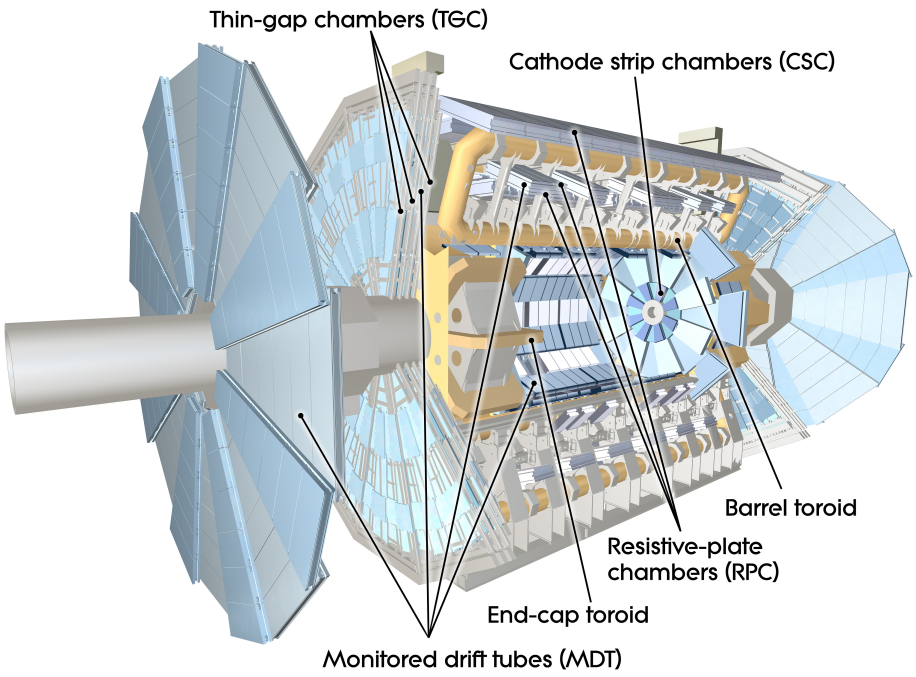

Figure 2.7: Overview of the Muon Spectrometer.

two end-cap toroids. Eight-fold symmetry of the MS toroids reflected in the structure of the muon chamber system as a sixteen-fold symmetry since each octant is divided into two parts in the azimuthal direction, including small sectors (aligned with the coils) and large sectors (aligned between the coils). These sectors are designed to have a small overlap in ϕ in order to minimize gaps between the detector parts and achieve maximum coverage.

The chambers are placed into layers. There are three layers called as "Inner", "Middle" and "Outer", with increasing distance from the IP. The naming convention of the MS chambers is based on their location (in the Barrel (B) or End-cap (E)), their layer type (Inner (I), Middle (M), Outer (O), Extra (E)), and also the sector type (Small (S) or Large (L)). For instance, BIS (Barrel, Inner, Small) is located in a small sector of the barrel in the inner layer whereas EML (End-cap, Middle, Large) lies in the large sector of the middle layer of the end-cap.

In the barrel region, precision measurements are done by the **M**onitored **D**rift **T**ubes (**MDT**), placed in a form of three concentric cylinders around the beam axis, in combination with **C**athode **S**trip **C**hambers (**CSC**). The inner layer is located inside the barrel toroid coils and arranged at a radius of ∼5 m from the beam axis (BIS and BIL chambers). The BIL chambers next to the rails[7] cannot have the same dimensions as in the other sectors and are therefore narrowed. Since this would introduce an unacceptable loss in coverage, this is recovered by placing BIR (R for rails) chambers below the rails. Encompassing the inner layer, the middle layer is located in the middle of the coils and at a radius of 7.5 m from the beam axis (BMS and BML chambers). The outer layer is placed outside the coils at a radius of ∼10 m (BOS and BOL chambers). In order to reduce the acceptance losses due to the ATLAS support system, special chambers (BOF and BMF chambers) are placed in this region called as the *feet* region. Fig. 2.8 shows the transverse view of the barrel part of the MS.

In the end-cap region, the muon chambers are located perpendicular to the z axis. The inner layer, in other words *small wheel* including EIS and EIL chambers are located inside the end-cap toroids at distances of z = ±7.4 m from the IP. The middle layer or *large wheel* including EMS and EML chambers is placed outside the end-cap toroid at a distance of z = ±14 m. The outer layer including EOS and EOL chambers is located on the cavern walls at z = ± 21.5 m. There are additional chambers, namely EES and EEL chambers, which are placed in the magnetic transition region between the barrel and end-cap's magnetic fields covering a pseudorapidity range of $1.0 < |\eta| < 1.4$. The other special chambers are the BEE (Barrel,End-Cap, Extra) chambers that are located in the castellations of the end-cap toroid cryostats. Although labelled barrel chambers, the BEE are used in the measurement of tracks

[7]The muon end-caps and calorimeters have been placed on the rail support system so they can be moved out of position in order to have access to every part of the ATLAS detector.

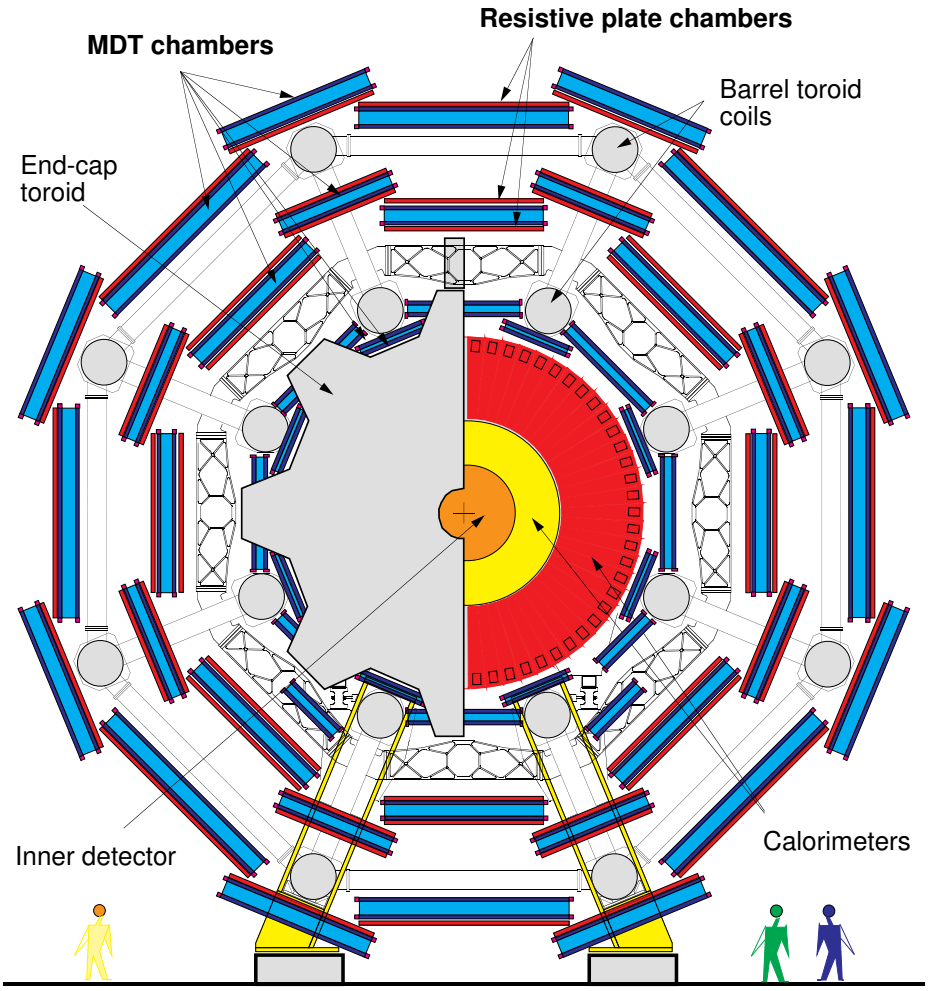

Figure 2.8: Transverse view of the muon spectrometer.

passing from the barrel to the end-cap. The BEE chambers consist of a single multi-layer of four tube layers.

There are also trigger chambers that serve a three-fold purpose: to help muon transverse momentum measurement, to provide high-speed timing to assist in bunch-crossing identification and to measure the muon coordinate in the non-bending ϕ projection to complement the MDT measurement. For these purposes, **R**esistive **P**late **C**hambers (**RPCs**) are used in the barrel and **T**hin-**G**ap **C**hambers (**TGCs**) are used in the end-cap.

Monitored Drift Tube chambers consist of three to eight layers of drift tubes and provide a precise measurement of the muon momentum in $|\eta| < 2.7$ (except in the innermost end-cap layer where their coverage is limited to $|\eta| < 2$ and CSCs are used instead of MDTs for the region of $2 < |\eta| < 2.7$) and measure the position in the bending plane, namely η. An average resolution of 80 µm per tube or 35 µm per chamber is achieved.

Each tube is made out of 400 µm thick aluminum with a diameter of 29.970 mm. It is filled with a gas mixture of argon (93%) and carbon dioxide (7%) and pressurized to operate at an absolute pressure of 3 bars. At the center of the tube, a tungsten-rhenium wire with a diameter of 50 µm is placed to collect the electrons produced as a result of ionization of the gas when a charged particle passes through. The tubes are arranged into layers. Each layer then stick onto each other by an epoxy glue to form 3 or 4 tube layers, so called *multi-layers*. A regular MDT chamber consists of two multi-layers separated by a mechanical spacer. Thus, the chambers in the middle and outer layer of the muon detector include 2×3 tube layers while the inner layer chambers (BI, EI) consist of 2×4 tube layers in order to enhance the pattern recognition performance. The shape and the dimensions of the chambers are optimized to achieve the maximum solid angle coverage possible permitted by the magnet coils and support structures. The chambers are rectangular in the barrel and trapezoidal in the end-cap, and are mounted on a rigid support structure. Despite the solid construction of the MDT chambers, there may be deformations and displacements occurring over time due to temperature gradients. In order to monitor these, the alignment system is implemented in the chamber. It is composed of four optical alignment rays; two of them are running parallel to the tube direction, two are placed in a diagonal direction, as shown in Fig. 2.9.

In the middle of the chamber light ray lenses are located whereas CCD cameras and LEDs are placed in the outer spacer. This system can record deformations of a few

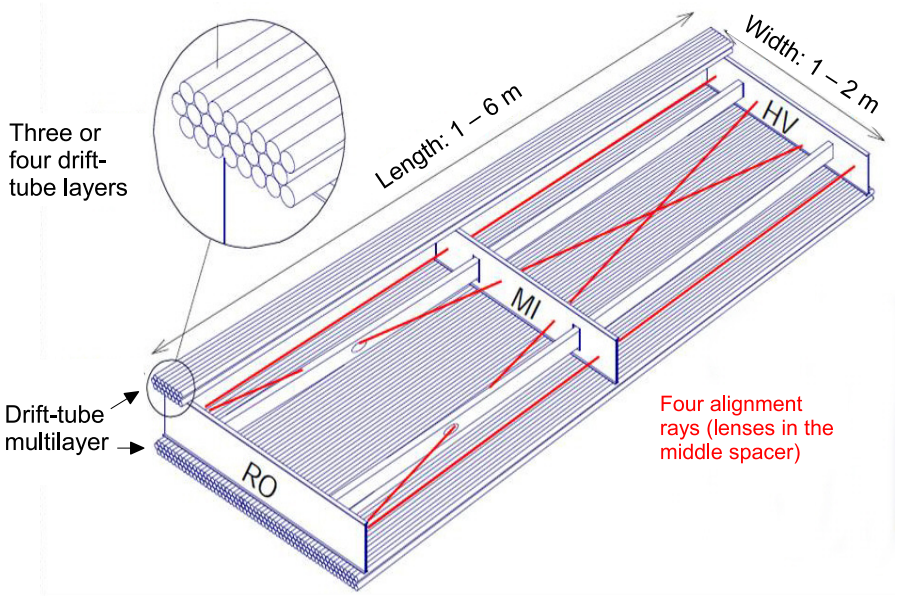

Figure 2.9: Mechanical structure of a MDT chamber.

µm. Using the in-plane system as reference, deformations can be corrected with a precision of about 10 µm.

There is also the projective alignment system which gives the chamber position within a tower. The MDT and CSC chambers are installed with a precision of 5 mm. However, in order to achieve the required momentum resolution, the position of the chambers should be known with a precision less than 30 µm. On that account, an alignment system was built which relates the position of each chamber to that of its neighbors, both within an MDT layer and along r-z trajectories within MDT towers. Fig. 2.10 shows a schematic representation of the alignment system in small and large sectors.

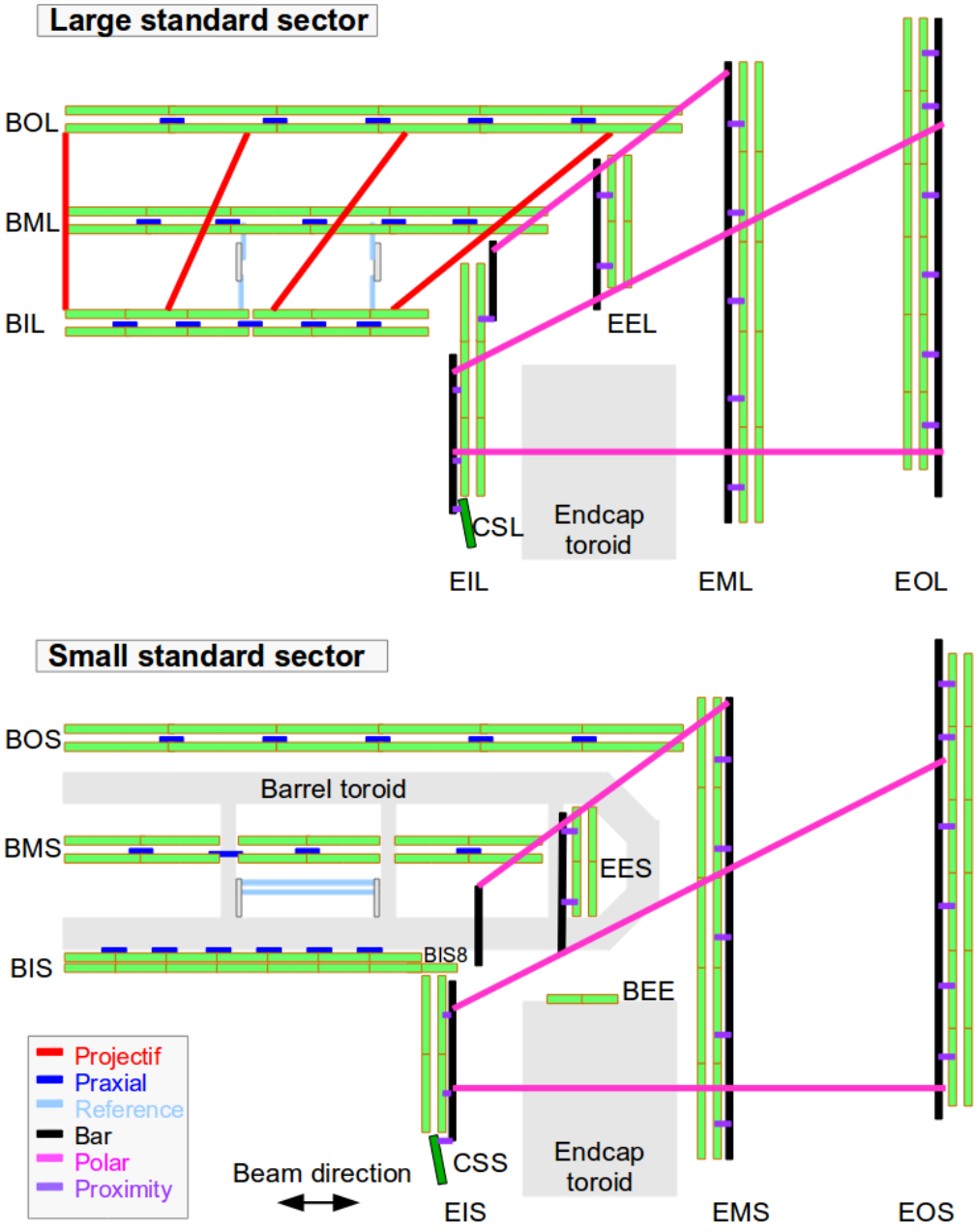

Figure 2.10: A schematic representation of the alignment system in small and large sectors in the r-z plane.

Cathode Strip Chambers are located at about 7 m from the interaction point covering a pseudorapidity region of $2 < |\eta| < 2.7$ in the first layer of the end-cap.

The particle fluxes and muon track density are the highest in this region so the limit for the safe operation of MDT chambers (at counting rates of 150 Hz/cm^2) would be exceeded. However, for CSCs, operation at counting rates up to 1000 Hz/cm^2 is considered safe so CSCs are used instead of MDTs in this specific region. The other characteristics that make CSC convenient for the regions with high particle densities are small electron drift times (max. 30 ns), good time resolution (7 ns), low neutron sensitivity due to the absence of hydrogen gas in the chamber gas and good two-track resolution.

CSCs are multiwire proportional chambers with cathode strip readout. The anode-cathode spacing is equal to the anode wire pitch. CSCs are arranged in 2×4 layers, a similar configuration like in the multi-layer of the MDT system in the end-cap, but with much finer granularity. A segmented cathode with the strips oriented orthogonal to the wires provides the measurements in the bending plane, namely η and the other cathode strip placed parallel to the wires provides measurements in the non-bending plane, namely ϕ. Thus, both coordinates are measured from the charge induced on the cathode strips due to the charge avalanche formed by the ionization trail of a muon in the anode wire. The position of the track is obtained by interpolation between the charges induced on neighboring cathode strips. The resolution of 60 µm is achieved in the bending plane and about 5 mm in the non-bending plane. The difference in resolution between different planes is due to the larger spacing of the readout strips in the bending plane.

Resistive Plate Chambers are used as a trigger system in the barrel region. There are three layers of RPCs; one layer is attached to the inside and one attached to the outside of the middle layer (BM) while the third layer is placed on the outside of the outer layer (BO), as shown in Fig. 2.11. They are referred to as three trigger stations. The large distance between the inner and outer RPCs allows the trigger to select high-p_{T} muon tracks in the p_{T} range of 9-35 GeV. Two chambers around

the middle layer provide the trigger for low-p_{T} muons in the p_{T} range of 6-9 GeV. Each station includes two independent detector layers which in turn provide the measurements in η and in ϕ, giving a total of six measurements.

RPC consists of two bakelite plates placed parallel to each other and separated by 2 mm. The plates are interleaved with insulating polycarbonate spacers. A gas mixture of tetrafluoroethane (97%) and isobutane (3%) between the plates allows for a relatively low operating voltage. The outside of the plates are coated with a layer of graphite and then connected to the voltage supply. The resulting electric field of 4.9 kV/mm between the plates multiplies the primary ionization electrons into avalanches giving a pulses of 0.5 pC. The signal is read out by the capacitively-coupled strips outside of the two plates.

There is no wire in the structure of RPC, which leads to a simple structure and manufacture. Each chamber is made from two detector layers and four readout strip panels.

Thin Gap Chambers are multiwire proportional chambers, providing bunch crossing identification with an efficiency greater than 99% and participating in muon triggering. TGCs are arranged as seven layers in the end-cap middle layer (EM) and two layers on the support structures of the barrel toroid in the end-cap inner layer (EI), as shown in Fig. 2.11.

TGCs consists of anode wires, cathode planes, cathode strips and honeycomb support structures. Anode wires are used as readouts for trigger and cathode strips provide measurements of the second coordinate. High electron field and small wire-to-wire distance (1.8 mm) lead to good time resolution for most of the muon tracks. TGCs are filled with a gas mixture of 55% carbon dioxide and 45% n-pentane. The highly quenching nature of the gas mixture prevents streamers to occur.

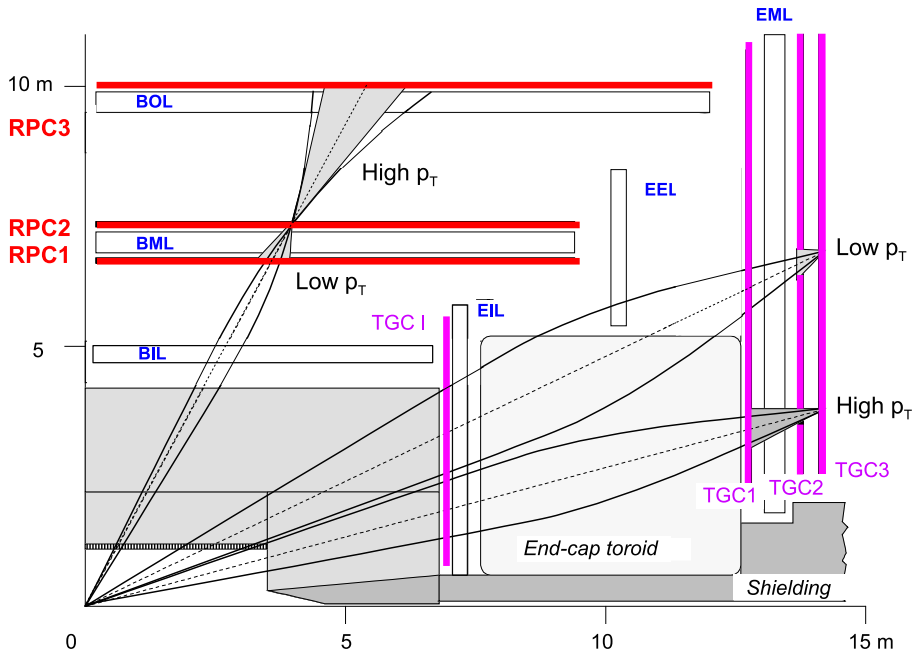

Figure 2.11: Schematics of the muon trigger system with the typical trajectories of low-p_{T} and high-p_{T} muons.

2.2.5 Magnet System

The magnet system that generates the bending power for the momentum measurement of charged particles is an essential part of a detector. In the ATLAS detector, this is achieved by two different magnet systems; a central solenoid and outer toroid system.

The ATLAS Central Solenoid (CS) [66] is a 5.3 m long cylinder with inner and outer radii of 2.44 m and 2.63 m, respectively. It surrounds the inner detector and is designed to provide an axial magnetic field of 2 T, with a peak magnetic field of 2.6 T at the boundary of the CS. The magnetic field deflects each charged particle coming from the collision. Since the LAr EM calorimeter is situated just outside the solenoid, the material thickness of the magnet should be minimized to be transparent enough for the particles to traverse. In order to achieve that, the CS is installed in a common cryostat with the LAr EM calorimeter. It does not have a cryostat of its own. The CS uses NbTi/Cu Rutherford superconducting cables in a pure aluminum

sheath, that carry the current generating magnetic fields. Since they operate at a temperature of 4.5 K, the cooling of the cables is needed. The pipes with aluminum coating contain circulating liquid helium and are in a good thermal contact with the cables. Thus, the cooling is provided indirectly by liquid helium.

The ATLAS Toroid System [67] is comprised of the Barrel Toroid (BT) and two End-Cap Toroids (ECTs) to generate the external toroidal magnetic field in the MS for tracking, shown in Fig. 2.12. As in the CS, NbTi/Cu Rutherford superconducting cables are used and cooled by liquid helium indirectly.

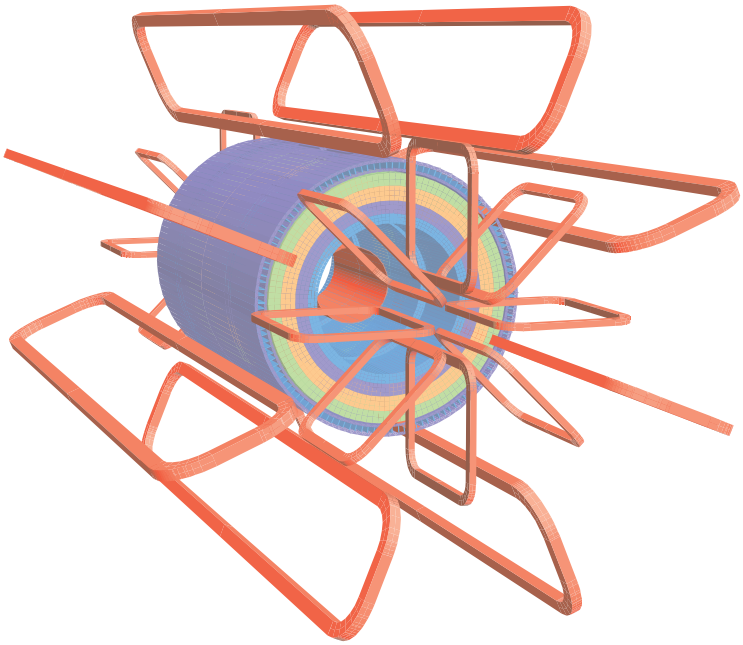

Figure 2.12: The ATLAS Toroid System, showing 8 coils of the barrel toroid and 8 coils of each end-cap toroid.

The BT consists of eight flat racetrack coils. Each coil has an axial length of 25.3 m and extends radially from 9.4 m to 20.1 m. The superconducting cables are arranged as two "pancakes", each with two layers of cables inside the coil. Each coil has its own cryogenic system. The peak field provided by the BT is 3.9 T in the inner surface of the coils. Because of the spacing between the coils, the magnetic field is around 0.6 T throughout the BT, in the region $|\eta| < 1.4$.

The ECT design is based on eight superconducting, racetrack type coils with two double-pancakes of superconducting cables. This design is very similar to that of the BT's. However, the ECTs are much smaller and therefore assembled as two single cold masses each in a vacuum vessel. Each coil has an axial length of 5 m and extends radially from 1.65 m to 10.7 m. The peak magnetic field provided is 4.1 T, that gives an average of ∼1 T throughout the ECTs, in the region $1.6 < |\eta| < 2.7$. The ECT coils are rotated by an angle of 22.5° with respect to the BT coils in order to provide the radial overlap.

The "magnetic transition region" where the magnetic fields of the barrel and end-cap toroids overlap covers a pseudorapidity range of $1.4 < |\eta| < 1.6$ and leads to an irregular magnetic field. In this region, the particle track is mostly straight, as in the case of high-p_{T} muons, due to the complex geometry of the magnetic field. That makes muon reconstruction more difficult. Bending power $\int$Bdl of the ATLAS toroid system is shown as a function of $|\eta|$ in Fig. 2.13.

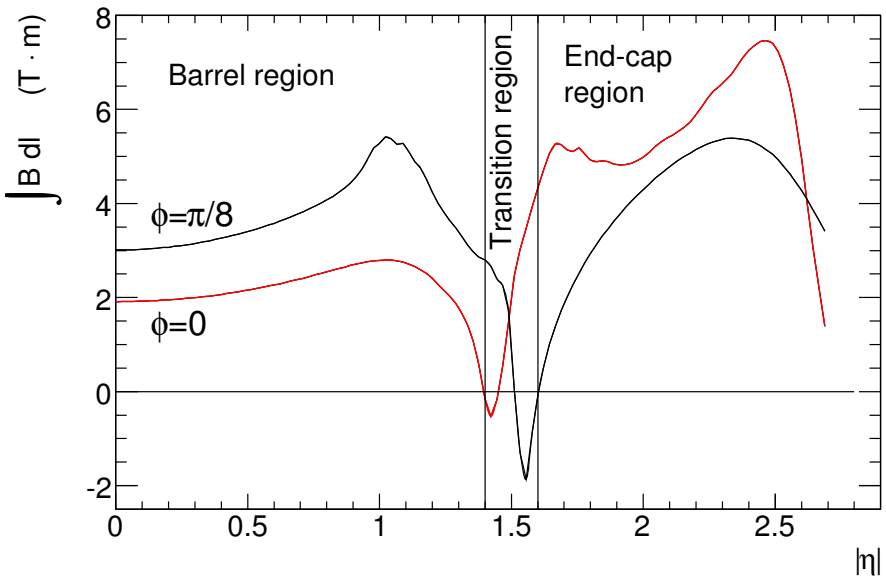

Figure 2.13: Predicted field integral as a function of $|\eta|$ from the innermost to the outermost MDT layer in one toroid octant, for infinite momentum muons. The curves correspond to the azimuthal angles $\phi = 0$ (red) and $\phi = \pi/8$ (black).

2.2.6 Trigger System

The proton-proton collision rate at the LHC reaches 40 MHz. Considering that one event has a size of about 1.5 MB, the collision rate provides too much data to store. However, not all of these events are interesting. *Minimum bias* events including elastic scattering or soft collisions can be filtered. In order to perform preselection and reduce the total data-flow without losing interesting physics, a three-level trigger system has been developed: Level 1 (LVL1), Level 2 (LVL2) and Event Filter (EF). Each level of the trigger refines the previous decision by using more advanced algorithms and more amount of information from the subdetectors.

The LVL1 is a hardware based trigger and uses coarse-granularity data from the calorimeter and the muon spectrometer. It reduces the event rate of ∼20 MHz (40 MHz by design) to a rate of ∼65 kHz (75 kHz by design). The corresponding output is reduced to ∼100 GB/s. Decision time or *latency* is 2 µs for LVL1. The LVL1 muon trigger system consists of low-p_{T} and high-p_{T} triggers. The momentum cut-off for the low-p_{T} trigger is 6 GeV and it uses information from the middle layer RPC stations in the barrel, two outer layers of TGC in the end-cap. The high-p_{T} trigger, on the other hand, uses information from all trigger stations and applies a cut-off momentum of 20 GeV. LVL1 defines a **R**egion **o**f **I**nterest (**RoI**) for LVL2 to use. Once the decision is made by LVL1, the data is passed to LVL2.

The LVL2 is a software trigger and works on full-granularity RoI data from LVL1. The fast software algorithms are used for track matching and tightening the requirements on the objects. In order to improve momentum estimate, the LVL2 trigger also uses information from the precision chambers. It reduces the event rate from ∼65 Hz (75 kHz by design) to ∼5 kHz (3 kHz by design), which corresponds to data output of ∼7.5 GB/s. Decision time for LVL2 is 60 ms. Until the decision is made in LVL2, full detector data is kept in Read-out Buffers (ROBs). Then, if selected, the data is passed to the final trigger or if not, it is discarded.

The EF is the third and final level trigger that uses full event information from all detector systems. It runs advanced reconstruction algorithms, also in offline reconstruction, to enable full reconstruction of the events. It runs on a computer farm located at CERN. The latency for the EF is about 1 second and it reduces the event rate from ∼5 kHz (3 kHz by design) to ∼400 Hz (200 Hz by design). Final data output is ∼600 MB/s. After processing in the EF, the data is written to ATLAS data storage and made available for further offline analysis.

2.3 Data Taking with the ATLAS Detector

The Run I can be divided into three main data taking periods corresponding to the years 2010, 2011 and 2012.

In 2010, the LHC delivered pp collisions at $\sqrt{s} = 7$ TeV corresponding to a total integrated luminosity of 48.9 pb^{-1} where ATLAS recorded 45 pb^{-1} with an uncertainty of 3.4%.

In 2011, the collision energy remained the same but the total delivered luminosity increased to 5.61 fb^{-1}. During this period, ATLAS recorded an integrated luminosity of 5.25 fb^{-1} with an uncertainty of 3.7%.

In 2012, the collision energy is increased to $\sqrt{s} = 8$ TeV and a total integrated luminosity of 21.7 fb^{-1} is recorded by ATLAS with an uncertainty of 2.8% out of the delivered 23.3 fb^{-1}.

Cumulative luminosity versus day delivered to ATLAS and also cumulative luminosity versus time delivered to and recorded by ATLAS during stable beams can be seen in Fig. 2.14.

ATLAS online data taking is divided into subperiods. The time interval during which the luminosity is supposed to remain constant is called "Luminosity Block" (LB or lbn) and is roughly 2 min. A "run" is a collection of luminosity blocks and its duration depends on the beam conditions. Status and functionality of all subdetectors

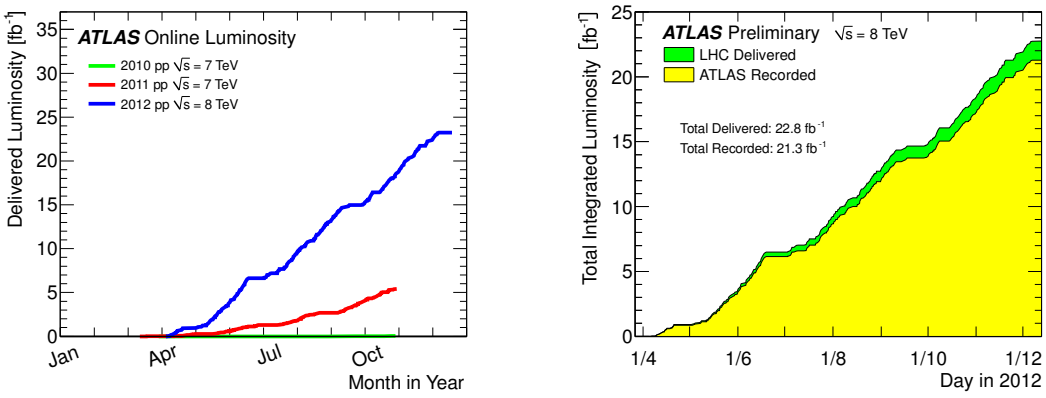

Figure 2.14: **Left:** Cumulative luminosity versus day delivered to ATLAS during stable beams and for *pp* collisions. This is shown for 2010 (green), 2011 (red) and 2012 (blue) running. **Right:** Cumulative luminosity versus time delivered to (green) and recorded by ATLAS (yellow) during stable beams and for *pp* collisions at $\sqrt{s} = 8$ TeV.

are known for each lbn in each run. Thus, each analysis is required to use data from "good" luminosity blocks in each run. For this purpose, a "Good Run List" (GRL) is prepared and used to determine the integrated luminosity for a given analysis. The total luminosity used in the analysis presented in this thesis is 20.5 fb^{-1}, recorded with the ATLAS detector during the year 2012 with $\sqrt{s} = 8$ TeV and with a time interval of 50 ns between bunches.

2.3.1 Pile-up

The high instantaneous luminosity and short bunch spacing introduces some challenges for the ATLAS detector and its subsystems during data taking. Multiple interactions per event, called "pile-up", are directly correlated with the instantaneous luminosity. The parameter μ is defined as the average number of particle interactions per bunch crossing. If the multiple interactions occur in the same bunch crossing, the pile-up is referred to as "in-time". There are also overlapping signals in the detector from other neighboring bunch crossings, so called "out-of-time" pile-up. This occurs due to the existence of electronic signals from previous bunch crossings. Considering that the signal length of LAr calorimeters is ∼500 ns whereas the bunch spacing is

50 ns, out-of-time pileup is highly possible to occur. In order to account for that, μ is averaged over all bunches in the collider in a given lbn ($<\mu>$) and used as a measure of pile-up. Average number of interactions per bunch crossing for 2012 data is shown in Fig. 2.15.

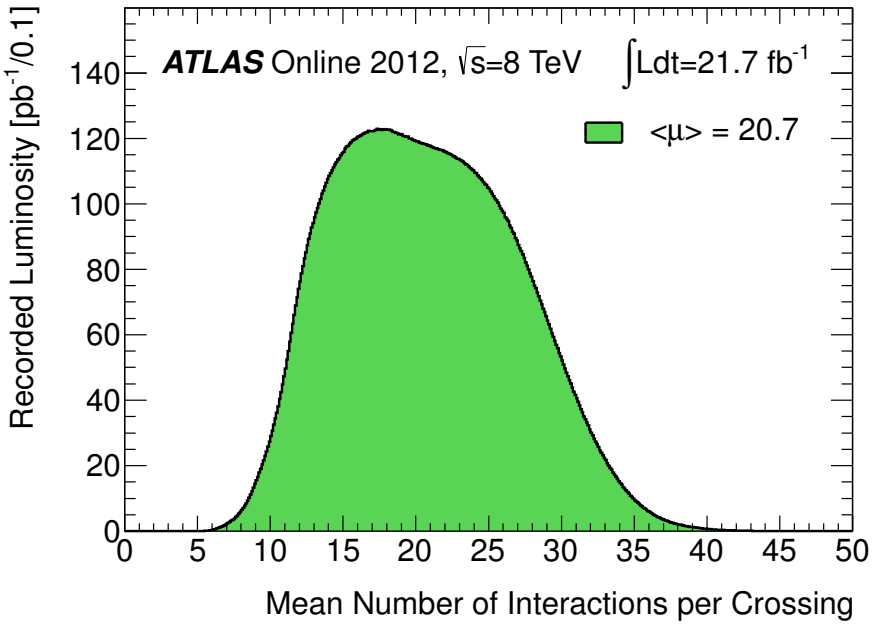

Figure 2.15: The luminosity-weighted distribution of the mean number of interactions per crossing for 2012 data.

2.4 Muon Reconstruction

2.4.1 Muon Reconstruction Algorithms

In ATLAS, four kinds of muon candidates are distinguished depending on the way they are reconstructed; stand-alone (SA) muon, combined muon (CB), segment tagged (ST) muon and calorimeter tagged (Calo) muon. Several independent algorithms have been developed to implement different muon reconstructions. The algorithms are grouped into *collections*, also known as *chains*. The STACO [68] and Muid [69] collections are two main collections including standalone, combined

and tagging algorithms. The third collection, CaloMuonTag, consists of calorimeter based muon tagging algorithms. The analysis presented in this thesis uses the muons reconstructed by Muid.

2.4.1.1 Standalone Muon

For the standalone muon reconstruction, only the information from the MS is used. The track is entirely reconstructed in the MS and then extrapolated back to the beam line in order to determine the track parameters of the muon at the interaction point. The muon momentum measured in the MS is corrected for the parametrized energy loss in the calorimeter.

- **Muid Standalone Algorithms:**
  - **The MOORE** (**M**uon **O**bject **O**riented **RE**construction) uses hit information in the MS to build segments. Segments are built by pattern recognition algorithms. First, "regions of activity" (ROA) are identified in the muon system, through the trigger chambers. Then, in each muon station of these ROA, "local straight track segments" are reconstructed. Track segments constructed in ϕ and in R-z planes are approximated to be straight due to the minimal bending of toroids in the ϕ plane and negligible bending power of toroids over a distance of one single precision layer. Constructed track segments from each plane are matched to form a *road*. Finally, the global fit of hits along the road is performed. An energy correction is applied to account for energy loss upstream the material as well as that arises from multiple scattering in the MS. The track parameters are expressed at the entrance of the MS.
  - **The MuidStandalone** extrapolates tracks from MOORE back to the interaction point by taking energy loss in the calorimeter into account. Thus, track parameters are expressed at the primary vertex.

- **STACO Standalone Algorithms:**

  – **The Muonboy** uses hit information to create segments in the MS. Pattern recognition algorithms provides segment finding. ROA is identified through the trigger chambers and then, in each muon station of these ROA, "local straight track segments" are reconstructed, as similar to MOORE strategy. These track segments of different muon stations are used to form track candidates. A global track fit of the muon track candidates is performed through the full system. Tracks are extrapolated to the primary vertex and the momentum is corrected using an energy loss parametrization. Track parameters are expressed at the primary vertex. This algorithm is very similar to the MuidSA algorithm in the Muid collection.

2.4.1.2 Combined Muon

The combination of independent measurements from the ID and MS is performed to reconstruct a combined muon. Energy losses in the calorimeter are taken into account using parametrization and possibly calorimeter measurements. This reconstruction strategy provides the most precise measurement of the momentum and position of a muon. The combined algorithms Muid and STACO perform a matching between pairs of inner detector and muon spectrometer tracks, both by calculating a χ^2_{match}. It is defined as the difference between the track parameter vectors ($\mathbf{T}$) weighted by their combined covariance matrix ($\mathbf{C}$) and can be shown as:

$$\chi^2_{match} = (\mathbf{T_{MS}} - \mathbf{T_{ID}})^{\mathbf{T}}(\mathbf{C_{ID}} + \mathbf{C_{MS}})^{-\mathbf{1}}(\mathbf{T_{MS}} - \mathbf{T_{ID}}). \tag{2.8}$$

The value of χ^2_{match} decides whether the match is successful and the inner detector track is identified as a muon. The Muid and STACO combined algorithms follow a different approach to obtain combined track parameters.

- **Muid Combined Algorithms:**

  - **Muid Combined** muons are reconstructed by refitting the tracks which are obtained according to χ^2_{match} and by using the measurements and scatterers from the inner detector, calorimeter and muon spectrometer systems. The full hit information in the ID and MS is also used to perform a refit. The matches with a satisfactory combined fit are identified as combined muons. Reconstruction efficiency for Muid CB muons as a function of η for muons with p_{T} >20 GeV is shown in Fig. 2.16.

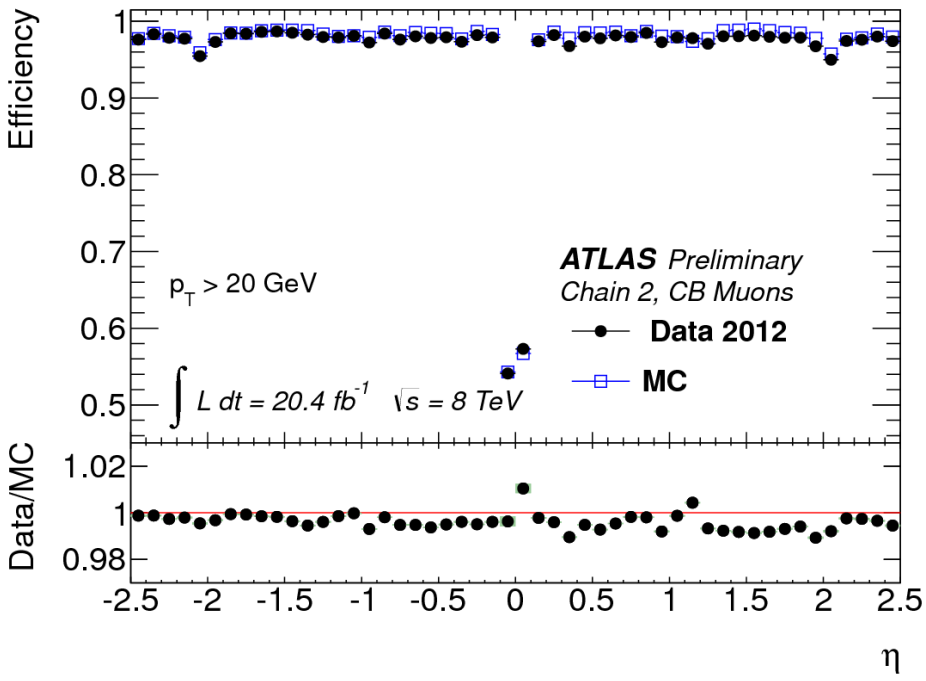

Figure 2.16: Reconstruction efficiency for Muid combined muons with $p_{\mathrm{T}} > 20$ GeV [70].

- **STACO Combined Algorithms:**

  - **STACO Combined** muons are reconstructed by a statistical combination between the ID tracks and the Muonboy MS tracks. This statistical combination is defined as:

$$\mathbf{T} = (\mathbf{C_{ID}}^{-1} + \mathbf{C_{MS}}^{-1})^{-1}(\mathbf{C_{ID}}^{-1}\mathbf{T_{ID}} + \mathbf{C_{MS}}^{-1}\mathbf{T_{MS}}). \tag{2.9}$$

    The value of χ^2_{match} of the global fit is required to be below a maximum value chosen. If there are more than one ID tracks matching an MS track, only the pair giving the best combined χ^2_{match} (or the minimum χ^2_{match}) is kept and defined as a combined muon candidate.

2.4.1.3 Segment Tagged Muon

Segment tagged muons consist of ID tracks with an additional information from the MS. If a track in the ID, extrapolated to the MS, is associated with straight track segments in the precision muon chambers, it is identified as a muon. This provides efficiency recovery in regions with low MS detector coverage. Besides that, tagging muons increase the identification efficiency for low-p_{T} muons. These muons may be absorbed in the calorimeter or even if they reach the MS, they only hit few stations due to their large curvature. Thus, tracks are not reconstructed in the MS but the segments are available for muon tagging.

- **Muid Tagging Algorithms:**

  - **The MuGirl** algorithm extrapolates the ID tracks to the inner and middle layer of the MS and performs a matching at hit level. It uses artificial neural networks to define a matching discriminant. The ID tracks and the matched muon hits are combined by performing a refit. If the MS information is not enough to perform combined muon reconstruction, then

an ID track with an associated muon segment in the MS is "tagged" as a muon.

– **The MuTagIMO** (**MU**on **TAG**ged **I**nner-**M**iddle-**O**uter) algorithm extrapolates ID tracks to the all stations in the MS. It searches for MOORE segments and performs a χ^2 based match. There may be multiple segments associated with the ID tracks.

- **STACO Tagging Algorithms:**

  – **MuTag** complements the combined muon algorithm by using the segments that do not share any hits with the muons reconstructed by STACO. It extrapolates the ID tracks to the inner layer of the MS and searches for Muonboy segments. Matching to the segments is performed based on the value of χ^2. This algorithm recovers low-p_{T} muons and also the muons from the regions with poor MS coverage.

2.4.1.4 Calorimeter Tagged Muon

An ID track with an energy deposition in calorimeters compatible with a minimum ionizing particle is identified as a muon. This algorithm recovers the muon identification efficiency in the region around $|\eta| = 0$ where there is a large acceptance gap in the MS for services of the ID and the calorimeters.

- **CaloMuon Tagging Algorithms:**

  – **The CaloMuonTag** algorithm extrapolated ID tracks to calorimeters, collecting the energy measurements in the cells closest to the extrapolated track.

Table 2.1: A summary of the muon reconstruction collections.

Muon Type	Muid Collection	Staco Collection	CaloMuon Collection
Standalone	MOORE	Muonboy	-
Combined	Muid	STACO	-
Tagged	MuGirl, MuTagIMO	MuTag	CaloMuonTag

2.4.2 Muon Reconstruction Performance

The designed resolution of the MS is $\Delta p_{\mathrm{T}}/p_{\mathrm{T}} = 10\%$ for muons with $p_{\mathrm{T}} = 1$ TeV. The momentum resolution of muons depends on the detector geometry, magnetic field and material effects. The $\eta - \phi$ map of ten detector regions is shown in Fig. 2.17.

Contributions to the momentum resolution for muons reconstructed in the MS as a function of transverse momentum for $|\eta| < 1.5$ is shown in Fig. 2.18. Dominant contributions to the muon momentum resolution in the detector depend on the muon momentum. Those can be categorized into three main groups:

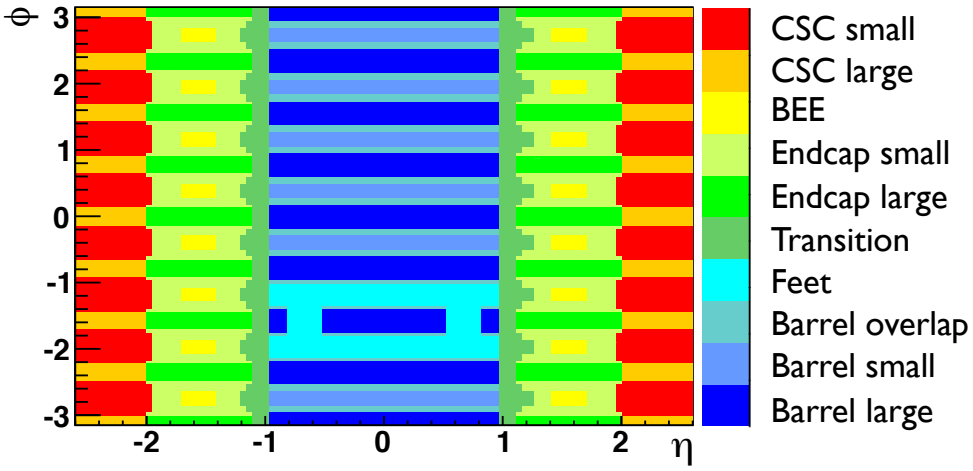

Figure 2.17: Muon spectrometer detector regions.

- The momentum resolution of muons with $p_{\mathrm{T}} < 30$ GeV is determined by the energy loss in the calorimeter.

- For the muons in a p_{T} range of $30 < p_{\mathrm{T}} < 100$ GeV, the momentum resolution is dominated by multiple scattering.

- The single tube resolution, precision of the calibration and the alignment becomes more important for the momentum resolution when the muon p_{T} is above 100 GeV. Radiative losses become the dominant energy loss mechanism for muons with $p_{\mathrm{T}} > 300$ GeV so showers resulting from bremsstrahlung make the muon reconstruction more difficult.

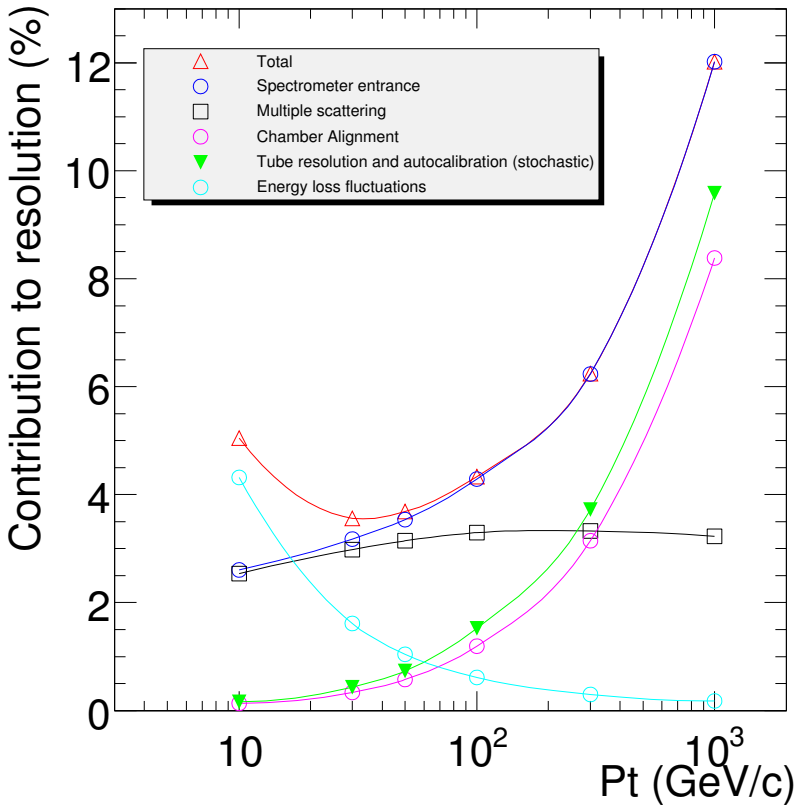

Figure 2.18: Contributions to the momentum resolution for muons reconstructed in the muon spectrometer as a function of transverse momentum for $|\eta| < 1.5$. The alignment curve is for an uncertainty of 30 µm in the chamber positions.

CHAPTER 3

DATA AND MONTE CARLO SAMPLES

This chapter begins with the discussion of Monte Carlo simulation strategies and event reconstruction in ATLAS. It is followed by the description of the 2012 data, MC samples representing SM backgrounds and signal samples, used in this analysis. The final section focuses on corrections made to simulated samples to better model the data.

3.1 Monte Carlo Simulation Strategies and Event Reconstruction

Simulation tools are important for the design of a detector and for the development of the reconstruction algorithms. In order to make a comparison between recorded and simulated data, a common output format should be used. In ATLAS, production of Monte Carlo event samples consists of four steps; Event generation, physics and detector response, digitization and reconstruction (detailed in the ATLAS Computing TDR [71]). The output of digitization has the same format as the data retrieved from the ATLAS detector. Thus, the reconstruction step is common both for recorded and simulated data.

3.1.1 Event Generation

Event generation is performed with a variety of event generators. Each event from the event generator contains particles from a single interaction vertex at (0,0,0). Particle type and four-momenta of these particles are also included in the event record.

The events can either be written to a file for further processing, or passed directly into the further simulation stages.

3.1.2 Physics and Detector Response

The second stage of the simulation process is the simulation of the passage of particles through the detector material. A description of the full ATLAS detector, including misalignments and material distortions, has been made available in the full simulation. ATLAS detector simulation methods can be categorized into two groups: full simulation and fast simulation.

The full simulation in ATLAS is based on the GEANT4 [72] simulation toolkit. GEANT4 provides functionalities including the propagation of particles through the detector and the description of the material. It has a high precision capacity. The only downside is its long processing time. Thus, for the generation of samples with very high statistics, GEANT4 is not very convenient to use due to a great amount of time needed. For this purpose, fast simulation, mostly based on ATLFAST-II or ATLFAST-IIF, is developed.

ATLFAST-II is a parametrized simulation based on GEANT4. It reduces the processing time by using a fast calorimeter simulator (FastCaloSim). Since 95% of the detector simulation is spent in the calorimeter simulation, a fast simulation makes the process a factor of 10 faster. Thus, by using ATLFAST-II, the inner detector and the muon spectrometer simulation are performed by GEANT4 whereas FastCaloSim is responsible for the calorimeter simulation. ATLFAST-IIF, on the other hand, uses fast ATLAS Tracking Simulation (Fatras) for the inner detector and muon spectrometer simulations. Detector simulation produces "*hits*" as output, which are records of the interactions of particles in the detector.

3.1.3 Digitization

The hits produced by the detector simulation need to be translated into the output actually produced by the ATLAS detectors. Thus, in the digitization stage, the response of each subdetector element is simulated in appropriate detail. The final output of the digitization step is in the form of Raw Data Objects (RDOs) equivalent to those from the read-out drivers of the real experiment.

3.1.4 Reconstruction

After the RDO output format is produced, the next step both in the simulation chain and the real detector data chain is to perform pattern recognition to identify the trajectories of particles, to measure momentum and energy and to identify individual particles. In order to ease the usage of a vast amount of data produced for physics analysis, the reconstruction step is divided into different stages, each of which requires a different type of dataset. The following are the available datasets in ATLAS, listed in decreasing order of their sizes:

- **Byte-stream Data** is reflecting the format in which data are delivered from the detector, rather than in any object-oriented representation. Events coming from the Event Filter are in byte-stream format.

- **Raw Data Object** is a C++ object representation of the byte-stream information. Hence, the initial stage in the reconstruction pipeline is to convert the byte-stream information into RDOs which are then used for subsequent reconstruction.

- **Event Summary Data (ESD)** is produced from the raw data, containing the detailed output of the detector reconstruction. It includes sufficient information for particle identification, track re-fitting, jet calibration, etc. The design of the ESD is intended to make access to raw data unnecessary.

- **Analysis Object Data (AOD)** is an event representation with reduced information for physics analysis, derived from ESD. It contains physics objects such as electrons, muons, etc. and other elements of analysis interest.

- **Derived Physics Data (DPD)** is a data representation for end-user analysis. It is a suitable format for direct physics analysis. Examples of DPD formats are dESD (derived from ESD, for performance groups), dAOD (derived from AOD, for physics groups), or NTUP (ROOT n-tuples, both for physics groups and end-users).

- **TAG** is a format holding event-level metadata. Event tags provide a summary of some general features of events, allowing a particular event selection and quick access of the required events.

The summary of the derived data types is shown in Fig. 3.1.

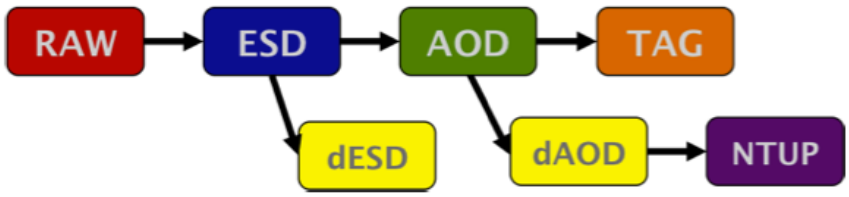

Figure 3.1: Schematic view of ATLAS raw and derived data types and associated workflows [73].

Events produced from simulated datasets have an additional "truth" component which allows a detailed comparison to be made between the results of reconstruction and the original event.

3.2 2012 Data

The data used in this analysis consist of the full 2012 dataset collected during pp collisions at $\sqrt{s} = 8$ TeV. This corresponds to 20.5 fb^{-1} of data (after quality

conditions have been applied) in the muon channel. Events are required to be collected with stable beam conditions and operational inner detector and muon spectrometer.

3.3 Standard Model Backgrounds

The analysis is performed using D3PDs designed for use in Standard Model group analyses. The ATLAS Detector response was simulated with GEANT4 and all MC events were reconstructed with the same software as for the data. The SM background to a non-resonant dilepton search consists of an irreducible component due to Drell-Yan ($q\bar{q} \to Z/\gamma^* \to \ell^+\ell^-$) as well as photon-induced events ($\gamma\gamma/\gamma q/\gamma\bar{q} \to \ell^+\ell^-$, through $\hat{t}$ and $\hat{u}$ channel processes), and reducible non-negligible components originating from $t\bar{t}$ and diboson production.

3.3.1 Drell–Yan Process

The largest and irreducible background in this analysis is the DY process that is shown in Fig. 3.2. The expected contribution from this process is simulated with POWHEG in conjunction with PYTHIA 8 for parton showering and hadronization. The CT10 PDF (The Coordinated Theoretical-Experimental Project on QCD Parton Distribution Function) [74] set is used for the event generation. To ensure an adequate number of events throughout the distributions of interest (such as dilepton invariant mass), 13 mass-binned samples were created with true dilepton invariant masses ranging between 250 GeV and 4500 GeV. To cover the region below 250 GeV an inclusive sample (all SM decays switched on, with no mass-binning) was generated above ∼60 GeV. This "unbinned" DY sample is stitched to the mass-binned DY samples at 250 GeV. Since the inclusive sample also includes events above 250 GeV, to avoid double-counting events in this region, an upper limit of 250 GeV is applied on the true dilepton invariant mass. This inclusive sample has small statistical uncer-

tainties and is important for use in the data/MC normalization region between the dilepton invariant mass of 80 GeV and 120 GeV.

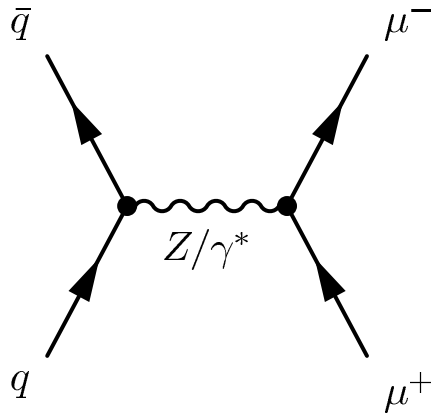

Figure 3.2: The Drell-Yan process with a dimuon final state.

The DY process is generated using next-to-leading order (NLO) matrix elements. Next-to-next-to-leading order (NNLO) generation of this process with POWHEG is not available. Thus, NNLO QCD and EW corrections are derived by using the FEWZ 3.1 (Fully Exclusive W and Z Production) program [75] with the MSTW2008 NNLO PDF [76, 77] in order to normalize the DY cross section at NLO to NNLO. More details on the DY samples used in the analysis are included in Table A.1 of Appendix A.

3.3.2 Photon-Induced Process

There is also a contribution to DY from Photon-Induced (PI) events, which are not taken into account in the samples produced with the POWHEG event generator. The PI process arises from initial state $\gamma\gamma, \gamma q$ or $\gamma\bar{q}$. Examples of born-level diagrams of PI processes can be found in Fig. 3.3. Even though a derived PI K-factor is available to correct DY cross section to account for PI processes, the dedicated PI MC samples are used in the analysis since the inclusion of these samples leads to a better description of the lepton angular distribution. The PI processes are simulated with PYTHIA 8 at LO using the MRST2004QED PDF [78]. To ensure adequate

statistics, PI samples are generated in 4 mass bins, covering true dimuon invariant mass 60-200 GeV, 200-600 GeV, 600-1500 GeV and 1500-2500 GeV.

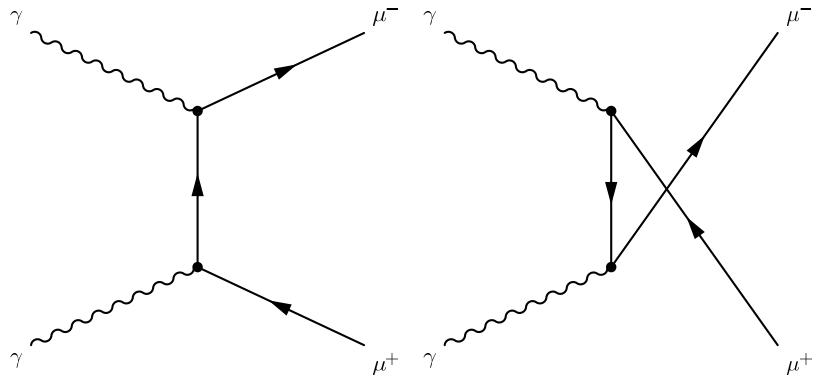

Figure 3.3: Born-level production of photon-induced processes.

3.3.3 Diboson Production

The diboson processes (WW, WZ, ZZ) can lead to a dilepton final state if the W and Z boson decay leptonically. One of these processes is shown in Fig. 3.4. These processes are generated with Herwig 6.510 at LO with the CTEQ6L1 [79] PDF. To increase the statistics at higher invariant masses, two mass-binned samples per diboson process is generated; one covering true dilepton mass in the range between 400 GeV and 1000 GeV and one above 1000 GeV. For these samples, events are required to have at least two same flavor leptons with $p_T > 10$ GeV, $|\eta| < 2.8$. Inclusive samples for each diboson process is also created to cover the mass range below 400 GeV. In order to stitch unbinned and binned samples properly, only the events with true dilepton invariant mass below 400 GeV are kept in the inclusive samples.

The LO diboson background description is scaled to NLO in a mass-independent way as described in Reference [80]. This mass-independent scaling is allowed as long as one of the bosons is always on-shell, which was found to hold in the range used for this search. More details on diboson samples used in this analysis can be found in Table A.2 of Appendix A.

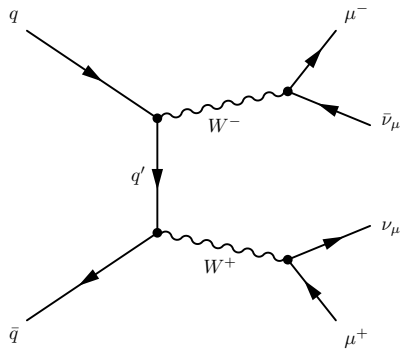

Figure 3.4: Diboson production that leads to a dimuon final state.

3.3.4 Top-quark Production

The "Top" background includes $t\bar{t}$ and Wt (a single top is produced in association with a W boson) processes. Top quark decays into a W boson and a bottom quark. Hence, if a W boson resulting from top quark decay further decays into a muon and a neutrino, that leads to a dimuon final state for $t\bar{t}$, as shown in Fig. 3.5. The $t\bar{t}$ background is simulated with MC@NLO 4.06 with the CT10 PDF to generate the matrix elements. Multiple parton interactions are described by JIMMY 4.31 [81] and HERWIG is used to describe the remaining underlying event and parton showers. The simulated $t\bar{t}$ events are generated for a top quark mass of 172.5 GeV/c^2. The Wt background is also simulated with MC@NLO and JIMMY.

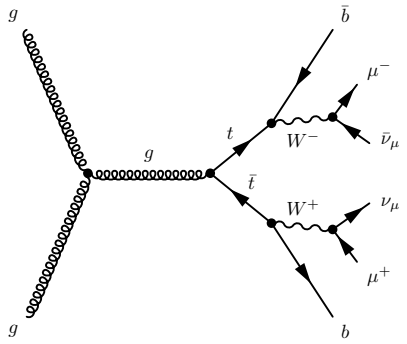

Figure 3.5: $t\bar{t}$ production that leads to a dimuon final state.

The cross sections of the $t\bar{t}$ and Wt processes are calculated at NLO with MC@NLO. Higher-order corrections are computed with Top++ 2.0 [82–87] to derive a K-factor

which brings this background description from NLO to NNLO in QCD, including resummation of next-to-next-to-leading logarithmic (NNLL) soft gluon terms. Each process is scaled to its calculated cross section and then two processes are combined to have one single "Top" background. More details on $t\bar{t}$ and Wt samples can be found in Table A.3 of Appendix A.

Due to the lack of statistics at high invariant mass, a binned χ^2 fit is performed. The choice of a fitting function is made depending on both the stability of the function with variation of fit range, and the χ^2 fit probability in the optimal fit range. Two fitting functions are explored and the function chosen to perform the fit is the so-called *dijet* function:

$$a \cdot x^b \cdot x^{c \cdot ln(x)}. \tag{3.1}$$

The fit range is from the dimuon invariant mass of 191.5 GeV to 733.9 GeV. The fit result is converted into a binned histogram. The top background estimate is taken from scaled $t\bar{t}$ and Wt samples up to 561 GeV (stitching point) and for the mass region greater than 561 GeV, results from the fit are used. Both statistical and systematic uncertainties are quantified for the fit. The statistical uncertainty for the fit stems from the errors on the number of entries in each bin extrapolated from the fit. This is taken from the fit's covariance matrix and errors returned on the fit parameters. Two systematic uncertainties are considered; first by examining the effect of using a different fit function and secondly by varying the fit range. The other fit function used to quantify systematic uncertainty is the inverse monomial function:

$$\frac{a}{(x+b)^c}. \tag{3.2}$$

The difference between the dijet and inverse monomial fit functions is taken as the first source of systematic uncertainty for the fit extrapolation. The second systematic error is calculated by varying the upper and lower boundaries of the dijet fit range,

which gives a total of 25 different fits. The maximum difference between these fits and the central fit is taken as the systematic uncertainty. Systematic uncertainties calculated for the top background are added to the statistical uncertainty in quadrature. The resulting uncertainty is assessed as the statistical uncertainty on the top background. In other words, systematic uncertainties are included in the statistical uncertainty. The top background fit and resulting final distribution are shown in Fig. 3.6. Since the analysis is performed not only in different mass bins but also in two different $\cos\theta^*$ bins, top background fits are also provided separately for forward and backward events, as shown in Fig. 3.7 and Fig. 3.8.

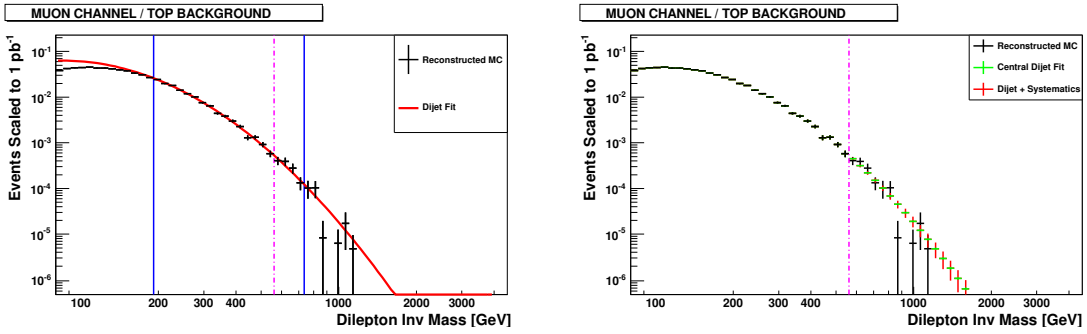

Figure 3.6: Dimuon mass distribution for $t\bar{t}$ and single-top MC events. **Left:** The nominal (dijet) fit to the top background is shown by the red curve. Black histogram shows the simulated top background including statistical errors, blue lines show the fit range and the dashed pink line shows the stitching point. **Right:** The final distribution is shown with statistical errors (green) and combined errors (red).

3.4 Signal Samples

The contact interaction signal processes are generated using PYTHIA 8.165 at LO with the MSTW2008LO PDF. The detector response is simulated with ATLFAST-II. These samples are produced at five benchmark Λ values (7 TeV, 10 TeV, 14 TeV, 20 TeV, 28 TeV) for each of three CI models (Left-Left, Left-Right, Right-Right chirality models), in both constructive and destructive interference scenarios. To ensure an adequate number of events to maintain a relatively small statistical uncertainty, three

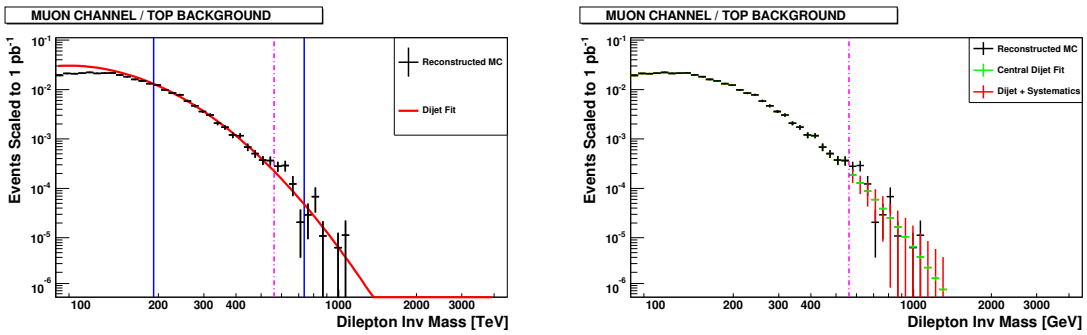

Figure 3.7: Dimuon mass distribution for $t\bar{t}$ and single-top forward MC events. **Left:** The nominal (dijet) fit to the top background is shown by the red curve. Black histogram shows the simulated top background including statistical errors, blue lines show the fit range and the dashed pink line shows the stitching point. **Right:** The final distribution is shown with statistical errors (green) and combined errors (red).

mass binned samples are created, covering the true dimuon invariant mass range 300-600 GeV, 600-1200 GeV and $>$ 1200 GeV. The CI signal needs to be generated with the SM DY background in order to provide the correct DY-CI interference description. Thus, CI samples include the SM DY background, the pure CI signal and the DY-CI interference contribution. Table 3.1 shows the relative contributions of DY only, DY-CI interference, and pure CI terms to the total production cross section under the LL scheme. As seen from this table, the pure CI contribution increases with increasing dimuon invariant mass, and more so for lower Λ values than higher values. In cases where higher than 100% of the cross-section is reported for the pure CI fraction, the destructive CI-DY interference fraction is always large enough to bring the sum of the pure and interference terms below 100% of the total cross-section as would be expected. More details on LL, LR and RR CI samples can be found in Table A.4, Table A.5 and Table A.6 of Appendix A, respectively.

As discussed in the previous chapter, the dominant DY background is generated with POWHEG, although the DY contribution in the signal samples is generated with PYTHIA. It is important to generate the main background at NLO with POWHEG since that accounts for higher order effects and model the DY background more

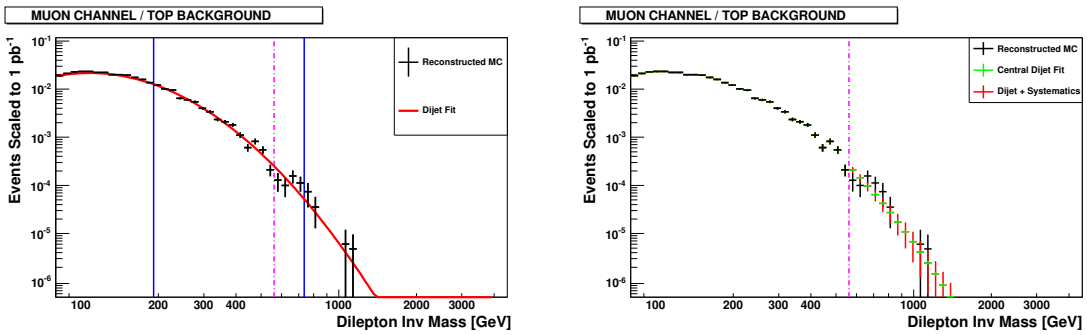

Figure 3.8: Dimuon mass distribution for $t\bar{t}$ and single-top backward MC events. **Left:** The nominal (dijet) fit to the top background is shown by the red curve. Black histogram shows the simulated top background including statistical errors, blue lines show the fit range and the dashed pink line shows the stitching point. **Right:** The final distribution is shown with statistical errors (green) and combined errors (red).

accurately. The CI signal samples are generated at LO with Pythia 8 as this is the only current generator in which the process is implemented. To scale the Pythia 8 CI and DY samples to the same order as the main Powheg Drell-Yan background, a LO to NNLO QCD+EW K-factor is calculated using the FEWZ NNLO estimate. K-factor is explained in more detail in Section 3.5.1.

The ADD signal samples are generated with Sherpa 1.3.1 at LO using multi-leg matrix elements and the CTEQ6L1. The generation includes the production of up to one jet and implements a UV cut-off on the dilepton invariant mass set equal to M_S, as the model becomes a quantum theory and so is no longer valid beyond that scale. The full simulation is available for the simulation of ADD model events in the GRW formalism. The results obtained with the GRW formalism can be converted into the Hewett and HLZ formalisms. However, this conversion does not work for the HLZ n=2 case because of the additional dependence on the dilepton mass. Therefore, the HLZ n=2 formalism is also simulated and the results for this formalism is presented for the first time in ATLAS.

The ADD signal samples are created for seven benchmark values of M_S (2.5 TeV, 3 TeV, 3.25 TeV, 3.5 TeV, 3.75 TeV, 4 TeV, 4.75 TeV), in three mass bins covering

Table 3.1: Relative contribution of DY-CI Interference (term depending on F_I) and CI (term depending on F_C) to the total cross section ($\sigma \times B(X \to \mu\mu)$) in the LL model as a function of benchmark Λ values for different true $m_{\mu\mu}$ ranges for constructive ($\eta = -1$) and destructive ($\eta = +1$) interference. Specifically the terms in the table can be read as: $\mathrm{X}_I = -\eta(F_I/\Lambda^2)/\sigma_{DY+CI}$, and $\mathrm{X}_C = (F_C/\Lambda^4)/\sigma_{DY+CI}$.

Λ [TeV]	True $m_{\mu\mu}$ range [GeV]		
	300 – 600	600 – 1200	> 1200
	X_I, X_C	X_I, X_C	X_I, X_C
Constructive Interference: $\eta = -1$			
7	10.5%, 6.15%	23.7%, 39.4%	15.3%, 79.5%
10	5.7%, 1.64%	20%, 16.3%	23.5%, 60%
14	3.03%, 0.445%	13.1%, 5.44%	27.2%, 35.4%
20	1.51%, 0.109%	7.17%, 1.46%	22.6%, 14.4%
28	0.678%, 0.0217%	3.36%, 0.305%	13.2%, 3.73%
Destructive Interference: $\eta = +1$			
7	-12.5%, 8.46%	-32.2%, 69.3%	-19.2%, 112%
10	-6.15%, 2.03%	-24.7%, 26.1%	-38.2%, 109%
14	-3.09%, 0.521%	-13.6%, 7.32%	-51%, 74.3%
20	-1.5%, 0.124%	-6.57%, 1.73%	-35.9%, 25.6%
28	-0.66%, 0.0243%	-2.86%, 0.335%	-16.1%, 5.09%

true dimuon invariant mass range 300-600 GeV, 600-1200 GeV and > 1200 GeV. As with the CI generation, both DY and ADD signal are produced as a single process. The pure DY contribution has been estimated by setting $M_{\mathrm{S}} = 50$ TeV because no SHERPA fully simulated DY was available. Low values of M_{S} yield more signal-like event samples and, thus, setting $M_{\mathrm{S}} = 50$ TeV allows one to produce an essentially pure SM DY spectrum.

A summary of MC samples for signal and background processes used in this search can be found in Table 3.2.

Table 3.2: Summary of MC sample information for signal and background processes used in this search. The columns from left to right give the process of interest, generator, matrix element order, parton shower program, and PDF utilized.

Process	Generator	Order	Parton Shower	PDF
$q\bar{q} \to Z/\gamma^* \to \ell^+\ell^-$	POWHEG [59]	NLO	PYTHIA 8.165 [56]	CT10 [74]
$\gamma\gamma/\gamma q/\gamma\bar{q} \to \ell^+\ell^-$	PYTHIA 8.165 [56]	LO	PYTHIA 8.165 [56]	MRST2004QED [78]
$t\bar{t} \to \ell X, Wt \to X$	MC@NLO 4.06 [60]	NLO	JIMMY 4.31 [81] + HERWIG 6.510 [58]	CT10 [74]
$WW, WZ, ZZ \to \ell X/\ell\nu/\ell\ell$	HERWIG 6.510 [58]	LO	HERWIG 6.510 [58]	CTEQ6L1 [79]
CI: $q\bar{q} \to \ell^+\ell^-$	PYTHIA 8.165 [56]	LO	PYTHIA 8.165 [56]	MSTW2008LO [76, 77]
ADD: $q\bar{q}/gg \to G^* \to \ell^+\ell^-$	SHERPA 1.3.1 [61]	LO (multi-leg)	SHERPA 1.3.1 [61]	CTEQ6L1 [79]

3.5 Corrections to the Simulated Samples

Due to imperfect modeling of some characteristics of data in simulation, MC samples need to be corrected. Thus, in order to ensure a fair comparison between data and MC, data derived corrections are applied to the MC where required. In this analysis, higher order corrections are made to the DY cross section and corrections to the muon momentum are applied to account for differences in resolution between data and MC simulation. The average number of interactions per bunch crossing is also corrected in MC to have a better match to data.

3.5.1 Higher Order Cross Section Corrections

Higher order corrections are applied to the simulated samples on an event-by-event basis to account for additional diagrams to the DY process that are not included in the MC generation. There are two main types of higher order corrections; QCD and EW corrections. The QCD corrections account for gluon radiation or quark/gluon loops, which only affect initial state quarks. The EW corrections have contributions from initial state photon radiation, final state photon radiation and electroweak loop corrections. Some examples of higher-order diagrams are shown in Fig 3.9.

The DY process is simulated at NLO in QCD and LO in EW with POWHEG. Since the DY has the largest contribution in the background of this analysis, its precise modeling is important. Hence, higher order corrections are calculated with

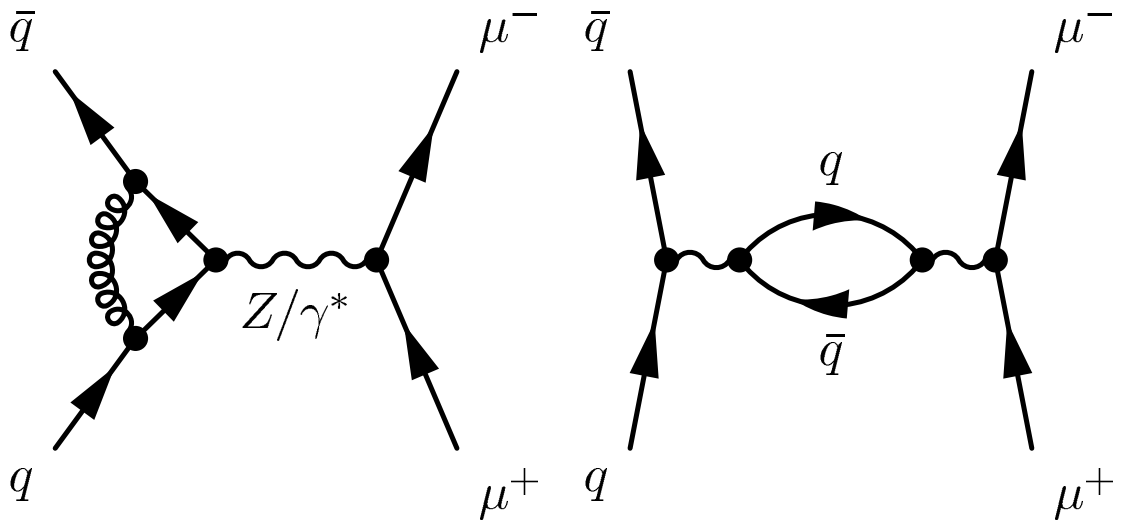

Figure 3.9: Examples of higher-order diagrams in DY production. The left diagram shows the vertex correction. The correction to the propagator is shown on the right diagram.

FEWZ at NNLO in QCD and NLO in EW. The final state QED radiation, which is the dominant part of EW corrections, is simulated with PHOTOS and included in the MC simulation. On that account, FSR corrections are excluded from the higher order (HO) EW corrections. NNLO QCD and HO EW corrections (except FSR) are calculated simultaneously in order to have a consistent EW parameter scheme. An overall K-factor per invariant mass bin is introduced as:

$$\sigma_{\text{best}}(m_{\ell\ell}) = K(m_{\ell\ell}) \times \sigma_{\text{MC}}(m_{\ell\ell}), \tag{3.3}$$

$$K(m_{\ell\ell}) = \frac{\sigma_{\text{best}}(m_{\ell\ell})}{\sigma_{\text{MC}}(m_{\ell\ell})}, \tag{3.4}$$

where "best" refers to an external NNLO QCD calculations and NLO EW calculations.

Higher-order corrections to the POWHEG DY samples are made with the following mass-dependent function:

$$K_{QCD,EW}^{POWHEG}(m_{\mu\mu}) = \begin{cases} 1.04 & - (1.49 \times 10^{-4}) \times m_{\mu\mu} & + (3.08 \times 10^{-7}) \times m_{\mu\mu}^2 \\ & - (3.44 \times 10^{-10}) \times m_{\mu\mu}^3 & + (2.02 \times 10^{-13}) \times m_{\mu\mu}^4 \\ & - (6.27 \times 10^{-17}) \times m_{\mu\mu}^5 & + (9.78 \times 10^{-21}) \times m_{\mu\mu}^6 \\ & - (6.04 \times 10^{-25}) \times m_{\mu\mu}^7 & \end{cases} . \tag{3.5}$$

where $m_{\mu\mu}$ is given in GeV.

As discussed in Section 3.4, CI signal samples also have a DY contribution which is simulated with PYTHIA at LO. Thus, higher order corrections are applied to normalize the cross section to NNLO, the same order as the main POWHEG DY background estimate. Since the higher-order QCD contributions are expected to be the same for signal and background processes, QCD corrections should also be applied to the signal samples. Because the intermediate process is unknown in the CI model, it is not clear whether EW corrections should also be included. However, EW corrections are also applied to CI signal samples in order to be conservative. The K-factor for Pythia samples, applied to CI signal samples, is given by:

$$K_{QCD,EW}^{PYTHIA}(m_{\mu\mu}) = \begin{cases} 1.29 & & \text{for } m_{\mu\mu} \leq 116 \text{ GeV} \\ 1.26 & +(1.50 \times 10^{-4}) \times m_{\mu\mu} & \text{for } m_{\mu\mu} > 116 \text{ GeV} \\ & -(4.88 \times 10^{-07}) \times m_{\mu\mu}^2 & \\ & +(3.59 \times 10^{-10}) \times m_{\mu\mu}^3 & \\ & -(1.26 \times 10^{-13}) \times m_{\mu\mu}^4 & \\ & +(2.22 \times 10^{-17}) \times m_{\mu\mu}^5 & \\ & -(1.59 \times 10^{-21}) \times m_{\mu\mu}^6 & \end{cases} . \tag{3.6}$$

where $m_{\mu\mu}$ is given in GeV. The K-factor functions given above numerically are shown in Fig. 3.10.

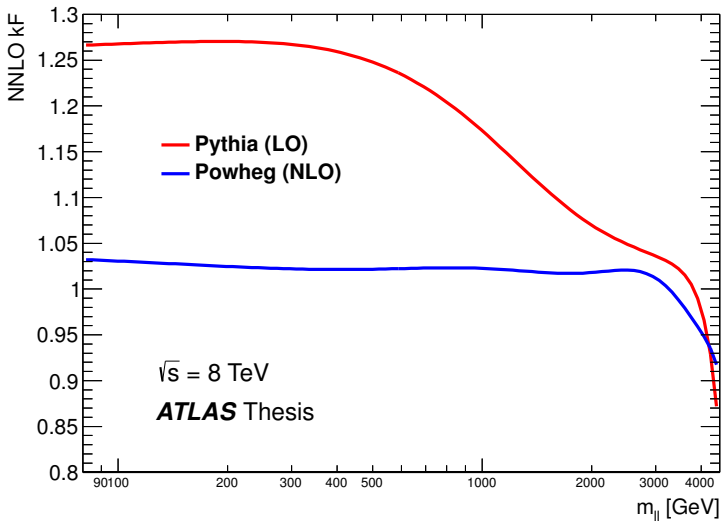

Figure 3.10: SM Drell-Yan NNLO QCD+EW K-factor derived using the FEWZ NNLO differential cross-section calculation with MSTW2008NNLO PDF. Shown are both the Pythia 8 (MSTW2008LO) LO to NNLO QCD+EW K-factor and the Powheg+Pythia 8 (CT10) NLO to NNLO QCD+EW K-factor.

3.5.2 Muon Momentum Resolution

In this analysis, muons are reconstructed as combined muons using the Muid algorithm. The momentum resolution is measured separately for each track in the ID and MS systems. That leads to the higher statistical sensitivity of the momentum resolution and higher momentum resolution than each of the individual tracks could achieve.

As discussed in Section 2.4.2, the muon momentum resolution is affected by the limited knowledge of the magnetic field, the uncertainty in the energy loss of muons and the alignment of the muon spectrometer.

The uncertainty in the bending power of the toroidal fields can be translated into an uncertainty in the momentum measurement. However, this is much smaller than the uncertainties due to the multiple scattering and the impact of misalignments. Therefore, its effect is neglected.

Another source limiting the momentum resolution is the energy loss of muons in the calorimeter. Muons with energy below 100 GeV lose an average of 3 GeV of their transverse momentum traversing the calorimeter. The amount of material muons pass through has an uncertainty of 5% which which translates into a 5% uncertainty in the energy loss.. The contribution due to energy loss in the calorimeter is strongly suppressed above $\approx$ 20 GeV and completely negligible for high-p_T muons.

For high-p_T muons, the dominant contribution to the momentum resolution is the intrinsic resolution caused by the spatial resolution of the detector components and any residual misalignments. The best estimate of the initial alignment accuracy is obtained by studying straight muon tracks from cosmic ray events and the collision data from the dedicated runs with toroidal magnetic field off. The analysis of the measurements of the optical alignment sensors also provides information on the MS detector misalignment. The MS misalignment is modeled more realistically in the 2012 simulation since the measurements of the misalignment is taken from the 2011 data. By taking the impact of realistic misalignment into account, the resolution for muons of 1 TeV of energy, reaches 13% in the barrel of the MS, 17% in the end-cap of the MS and 15% in the region covered by the CSC ($2 < |\eta| < 2.7$).

For a given value of η, the resolution in the MS can be parameterized as a function of p_T [89]:

$$\frac{\sigma(p_T)}{p_T} = \frac{p_0^{MS}}{p_T} \oplus p_1^{MS} \oplus p_2^{MS} \cdot p_T, \tag{3.7}$$

where p_0^{MS} is related to the energy loss in the calorimeter material; p_1^{MS} describes the multiple scattering; p_2^{MS} is the intrinsic resolution term.

The resolution in the ID is expressed by a similar parametrization. The curvature measurement depends on the distance that muons traverse in the ID. Hence, reduced track length close to the edge of the TRT fiducial volume ($|\eta| \sim 1.9$) leads to a uniform response in the central part and a rapid worsening beyond this region. The approximate parametrization of resolution in the ID can be written as:

$$\frac{\sigma(p_{\mathrm{T}})}{p_{\mathrm{T}}} = p_1^{ID} \oplus p_2^{ID} \cdot p_{\mathrm{T}}, \qquad \text{for } |\eta| < 1.9 \tag{3.8}$$

$$\frac{\sigma(p_{\mathrm{T}})}{p_{\mathrm{T}}} = p_1^{ID} \oplus p_2^{ID} \cdot p_{\mathrm{T}} \frac{1}{\tan^2\theta}, \qquad \text{for } |\eta| > 1.9 \tag{3.9}$$

where p_1^{ID} and p_2^{ID} are coefficients related to multiple scattering and the intrinsic resolution terms, respectively.

Muon momentum resolution studies are performed by the Muon Combined Performance group in the ATLAS collaboration. In order to determine muon momentum resolution and scale, $Z \to \mu\mu$ decays are used. The most recent study [90] is performed with the 2012 data sample. Events are required to include two isolated CB muons of opposite charge, with $p_{\mathrm{T}} > 25$ GeV. To select muons from Z decay, the $\mu^+\mu^-$ mass is required to be within 15 GeV of the Z boson mass (91.2 GeV). $Z \to \mu\mu$ MC events are generated with POWHEG. The resolution is the width of the Gaussian which is convoluted with the Breit-Wigner shape in $Z \to \mu\mu$ decays at generator level. To study low-p_{T} muons, dimuon decays of J/ψ and Υ are also used.

Due to imperfect modeling of the muon momentum resolution in MC samples, the simulation needs to be corrected in order to match the measured resolution in data. Thus, the reconstructed simulated muon momenta must be smeared and shifted. The first term corrects the multiple scattering contribution and second term corrects the intrinsic resolution. Also a momentum scale correction (s) that accounts for a shift in the momentum, is applied to the simulation. The left part of Fig. 3.11 shows that the measured Z $\to \mu\mu$ mass spectrum for the experimental data has a slight shift and larger spread with respect to the simulated one.

For the overall momentum resolution measurement, two quantities are used:

- The width of the reconstructed dimuon invariant mass peak at the Z pole.
- The difference between ID and MS momentum measurements weighted by the muon electric charge (q/$p_{\mathrm{T}}{}^{ID}$ - q/$p_{\mathrm{T}}{}^{MS}$). The weighting by the electric charge

reduces systematic effects of the curvature due to local misalignments, which reduces the bias on the estimation of the resolution and correction parameters.

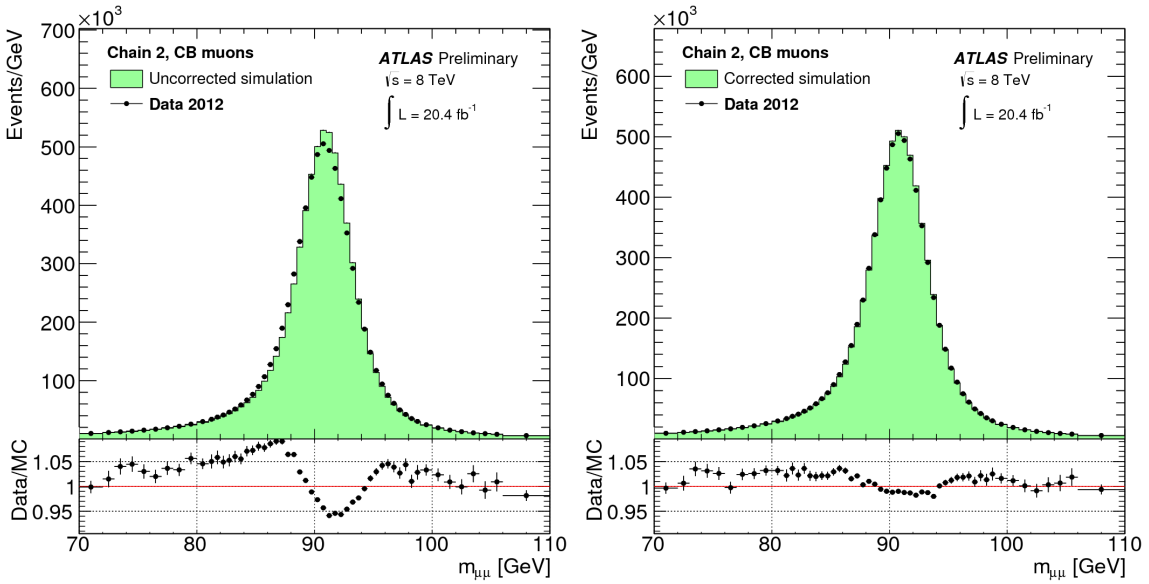

Figure 3.11: Dimuon mass distribution for Chain 2 (Muid Chain), CB muons, isolated and with $p_{\mathrm{T}} > 25$ GeV [90]. **Left:** No smearing and scale corrections are applied on the plot. **Right:** Smearing and scale corrections are applied to the MC simulation.

A corrected momentum measurement ${p_{\mathrm{T}}}^{Cor}$can be written in terms of the simulated momentum reconstruction ${p_{\mathrm{T}}}^{MC}$, the scale correction factor $s(\eta)$ and the correction parameters $\Delta p_1(\eta)$ and $\Delta p_2(\eta)$ as follows:

$$p_{\mathrm{T}}^{Cor,det} = p_{\mathrm{T}}^{MC,det} \cdot s^{det}(\eta)(1 + \Delta p_1^{det}(\eta)G(0,1) + \Delta p_2^{det}(\eta)G(0,1)), \tag{3.10}$$

whereas det = MS, ID and G(0,1) is a normally distributed random variable with mean 0 and width 1. For the ID momentum correction, the above formula is valid for the region $|\eta| < 1.9$. For the region $|\eta|$ >1.9, the term with $\Delta p_2(\eta)$ is multiplied with $1/\tan^2\theta$. Smearing parameters and scale factors calculated with the 2012 data are shown in Fig. 3.12 and Fig. 3.13, respectively.

The corrections are applied separately to ID and MS momentum measurements. The correction to the CB muon momentum is computed as the average of the ID

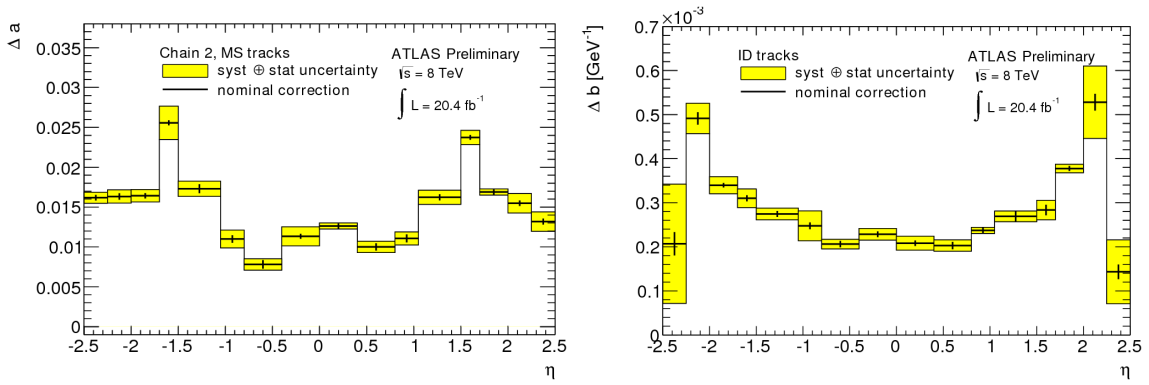

Figure 3.12: Δa (Δp_1) resolution correction term for the MS (left plot), and Δb (Δp_2) resolution correction term for the ID (right plot) for MC, derived from Z $\rightarrow \mu\mu$ data for the Muid reconstruction chain. The systematic uncertainty on the correction is shown in yellow.

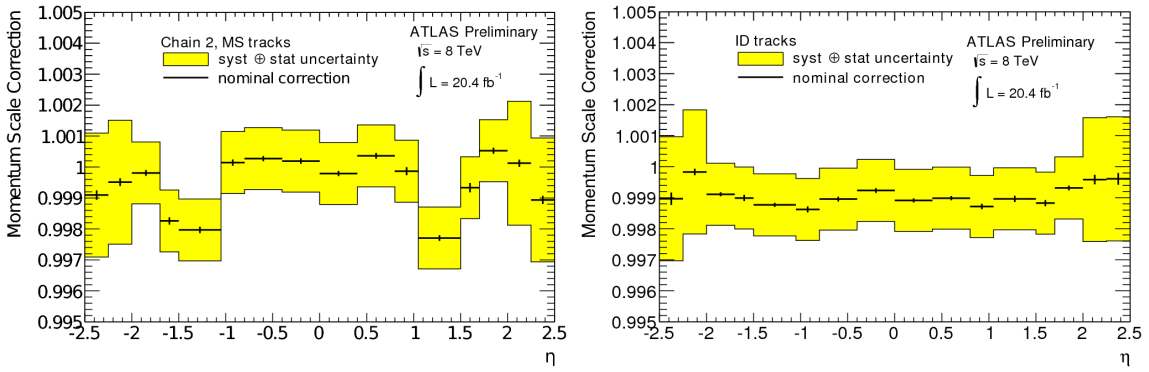

Figure 3.13: MS (left plot) and ID (right plot) momentum scale correction, for MC, derived from Z $\rightarrow \mu\mu$ data for the Muid chain reconstruction. The systematic uncertainty on the correction is shown in yellow.

and MS momentum corrections weighted by the inverse square of the ID and MS resolutions, shown as:

$$p_{\mathrm{T}}^{Cor,CB} = p_{\mathrm{T}}^{MC,CB}\left[1 + \frac{\frac{\Delta(MS)}{\sigma^2(MS)} + \frac{\Delta(ID)}{\sigma^2(ID)}}{\frac{1}{\sigma^2(MS)} + \frac{1}{\sigma^2(ID)}}\right] \tag{3.11}$$

where Δ(MS,ID) is the overall correction applied to the simulated MS and ID p_{T} and σ(MS,ID) is the resolution in the simulation at ${p_{\mathrm{T}}}^{MC}$.

The correction (smearing) parameters are the quadratic differences in the resolution parameters between data and simulation. These are derived in 16 different η regions using a MC template technique. By applying smearing to the simulation according to Eq. (3.10) many times by varying the correction parameters, a set of dimuon invariant mass distributions are derived. Then a binned likelihood fit is performed to find the best-match to the data mass spectrum. The template fitting is iterated across 16 η regions defined for the detector. Firstly, the fit is performed by requiring two muons from Z decay to be in a same η bin. The following fit allows one of the muons to be in the previous eta bin. After all η bins are analyzed, the fit is iterated again, in order to ensure the stability of the results.

The combined dimuon mass resolution obtained from the fit performed in the mass window $m_{\mu\mu} \in$ [75 GeV, 105 GeV] is shown in Fig. 3.14. Error bars are the sum of the statistical error and the absolute value of the change of the resolution when the fit range is reduced to $m_{\mu\mu} \in$ [82 GeV, 100 GeV] from $m_{\mu\mu} \in$ [75 GeV, 105 GeV].

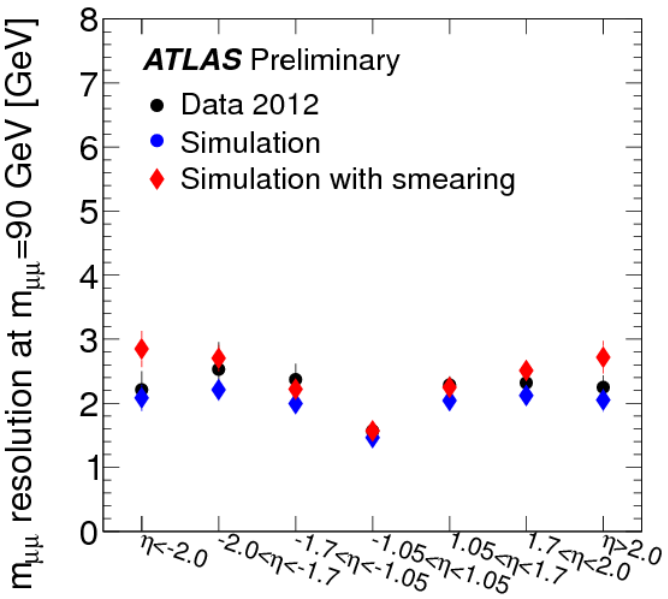

Figure 3.14: Combined dimuon mass resolution near the Z peak [91].

In the analysis, muon momentum resolution corrections are applied using the tool provided by the MCP group; MuonMomentumCorrections-00-09-08.

3.5.3 Muon Identification Efficiency

Combined muons use independent measurements from the ID and MS. Hence, the muon reconstruction efficiency is the product of the ID reconstruction efficiency (ϵ_{ID}), the extrapolated MS track reconstruction efficiency (ϵ_{MS}) and the matching efficiency between the MS and ID measurements (ϵ_{match}), shown as:

$$\epsilon_{CB} = \epsilon_{ID} \times \epsilon_{MS} \times \epsilon_{match}. \tag{3.12}$$

The muon reconstruction efficiency calculations are based on the tag-and-probe method since it provides a clean sample of muon candidates. In the study performed with the 2012 data, the tag-and-probe method selects events using $Z \to \mu\mu$ decays with one well reconstructed CB muon, the *tag*, and one opposite-charge track, the *probe*. The probe must be an "MS track" (SA or CB muon) if the ID reconstruction efficiency is to be measured. When measuring ϵ_{MS} and ϵ_{match}, ID tracks are used as probe. Therefore, ϵ_{ID} can be defined as the fraction of MS track probes which can be associated to an ID track.

In order to study the muon reconstruction efficiency, events are selected by requiring two oppositely charged isolated muons with $p_{\mathrm{T}} > 20$ GeV and dimuon invariant mass within 10 GeV of the Z pole mass. The tag and the probe in a selected pair need to have the same charge and to be close in the $\eta - \phi$ plane ($\Delta R < 0.01$ for ID probes, $\Delta R < 0.05$ for MS probes) for the match to be successful.

In the study performed with the 2012 data, CaloTag muons are used as probe instead of ID tracks since CaloTag muons reduce the background in the $Z \to \mu\mu$ sample without biasing the efficiency measurements.

The efficiencies measured with experimental data using muon pairs produced in the decays of Z bosons are compared with muon reconstruction efficiencies predicted by the MC simulation. A scale factor (SF) is then derived to correct the simulation to have a better agreement with data and can be written as:

$$SF = \frac{\epsilon_{data}}{\epsilon_{MC}}. \tag{3.13}$$

The difference between SFs calculated using CaloTag and ID tracks as probes is assigned as a systematic uncertainty. Also, the efficiency for low-p_{T} muons is measured separately in $Z \to \mu\mu$ and $J/\psi \to \mu\mu$ decays, and the 2% difference between these measurements is assigned as a systematic uncertainty.

3.5.4 Pile-up

In order to account for in-time and out-of-time pile-up conditions present during the 2012 run, as discussed in Section 2.3, MC samples are also simulated with these conditions. However, the distribution of the number of interactions per bunch crossing in MC samples is not exactly the same as in data. Thus, events from the simulation need to be corrected to data. This is applied using the official pileup reweighting tool [92] (PileupReweighting-00-02-12) on all MC12, using the final 2012 Run I recommendations. The Pile-up reweighting is done by comparing the average number of interactions per bunch crossing as measured in the collected data, to that in the generated MC sample. Figure 3.15 shows these distributions for data (dots) and MC before the correction is applied (shaded red). The MC distribution after the correction applied is also shown (green).

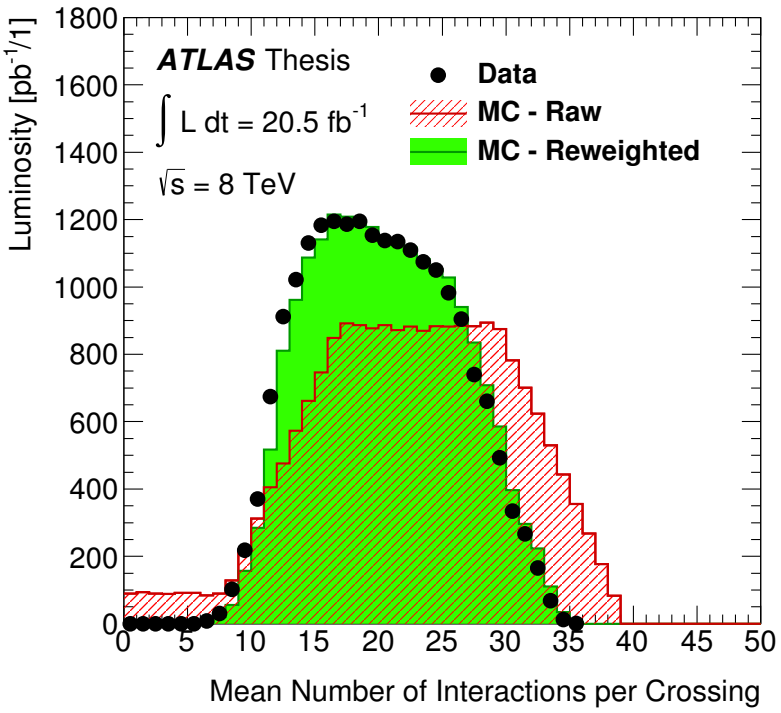

Figure 3.15: Average number of interactions per bunch crossing as measured in data (dots), DY MC before pile-up reweighting (red) and after pile-up reweighting (green) applied.

CHAPTER 4

EVENT SELECTION

This chapter discusses the selection criteria applied to select muons and dimuon events in this analysis. Background estimation is also discussed, which is followed by kinematic and angular distributions.

4.1 Event Level Selection

A series of selection criteria are applied in order to select the events with a dimuon pair. These are chosen to preserve the efficiency of potential signals, while minimizing background processes. The following criteria show the event-level selection requirements which are applied in the order listed.

- Events are required to have the luminosity blocks that belong to the Good Runs List (GRL) to assure that data are collected with the best detector operations so having a good quality of data.

- Events are required to pass *coreFlags* which is a flag for "incomplete events". In 2012 data taking, in order to recover certain detector busy conditions, a restart of a relevant subdetector, so-called TTC restart, without a run-restart is developed. A TTC restart may result in incomplete events where some detector information is missing from the event. Thus, these events are removed from the analysis.

- Events are required to pass the single-muon triggers with p_{T} thresholds of 24 GeV (EF_mu24i_tight) which is the primary trigger or 36 GeV (EF_mu36_tight),

the secondary trigger. The primary trigger requires muon isolation at the online level. Inefficiencies arising from muon isolation with low threshold trigger requirements are removed by the second complementary trigger with the higher threshold.

- Events are required to have at least 1 PV with at least 3 tracks and with longitudinal distance from the center of the detector (z_{PV}) less than 200 mm. This suppresses non-collision backgrounds such as cosmic-ray muons and ensures that the event is the result of a hard process.

4.2 Muon Level Selection

After events are selected by applying event-level selection criteria listed in the previous section, each event is required to have at least 2 MUID combined muons. The object-level selection criteria applied on each muon in the event are listed below.

- Muons are required to have $p_{\mathrm{T}} > 25$ GeV.
- Muons are required to pass the ID hit requirements determined by the MCP group in order to provide the best ID reconstruction:
  - At least 1 B-Layer hit, if one is to be expected. When track is outside of the B-Layer region or passes through dead sensors, this selection is not imposed.
  - At least 1 Pixel hit, including Pixel dead sensors crossed.
  - At least 5 SCT hits, including SCT dead sensors crossed.
  - No more than 2 missing hits on the track in Pixel or SCT.
  - If $0.1 < |\eta| < 1.9$, at least 6 TRT hits, including TRT outliers, with outlier fraction < 0.9.

- If $|\eta| \leq 0.1$ or $|\eta| \geq 1.9$, if at least 6 TRT hits, including TRT outliers, are observed, then require the outlier fraction to be < 0.9.

- Muons are required to have a muon transverse distance to the beam axis (transverse impact parameter of muon; d_0) less than 0.2 mm. This requirement suppresses the backgrounds from cosmic-ray muons and ensures muons come from the hard process (See Fig. 4.1).

- Muons are required to have longitudinal impact parameter relative to the PV less than 1 mm: $|z_0 - z_{PV}| < 1$ mm. That suppress the backgrounds from cosmic-ray muons and ensures muons come from the hard process (See Fig. 4.2).

- Muons are required to be isolated, i.e., the p_{T} sum of all ID tracks, except the muon itself, in a cone of size $\Delta R < 0.3$ relative to the muon combined p_{T} must be less than 0.05; $\sum_{p_{\mathrm{T}}}(\Delta R < 0.3)/p_{\mathrm{T}}^{\mu} < 0.05$. That suppresses background from hadronic decays. Fig. 4.3 shows the distribution of relative track isolation for single muons after all selection criteria are imposed except the one on relative track isolation. The discrepancy between the data and the expected background in the tail is due to the missing contribution from heavy flavor decays in the latter. After the isolation selection, this absence becomes irrelevant and has no effect on the final results.

- Muons are required to pass stringent MS hit requirements. The quality of the muon momentum measurement is important for the non-resonant dilepton analysis since mismeasured DY events could give rise to an excess of events at high invariant mass and mimic a signal. Hence, only 3 station muons are used for this analysis. MS hit requirements are listed as:

  - One of the following criteria must be satisfied:

    * At least 3 hits in each of the BI, BM, BO MDT precision layers.

* At least 3 hits in each of the EI, EE, EM MDT precision layers.
* At least 3 hits in each of the EI, EM, EO MDT precision layers.
* At least 3 hits in each of the EM and EO MDT precision layers, along with at least 2 CSC unspoiled eta hits.

  (See Fig. 4.4 for the distribution of hits in the inner, middle and outer precision layers.)

– At least 1 ϕ hit in two different RPC/TGC/CSC layers.

– No hit in the BEE, BIS7 or BIS8 MDT chambers since these chambers have poor alignment.

– The independent ID and MS track q/p_T must agree within 5σ of the standalone measurement uncertainties added in quadrature.

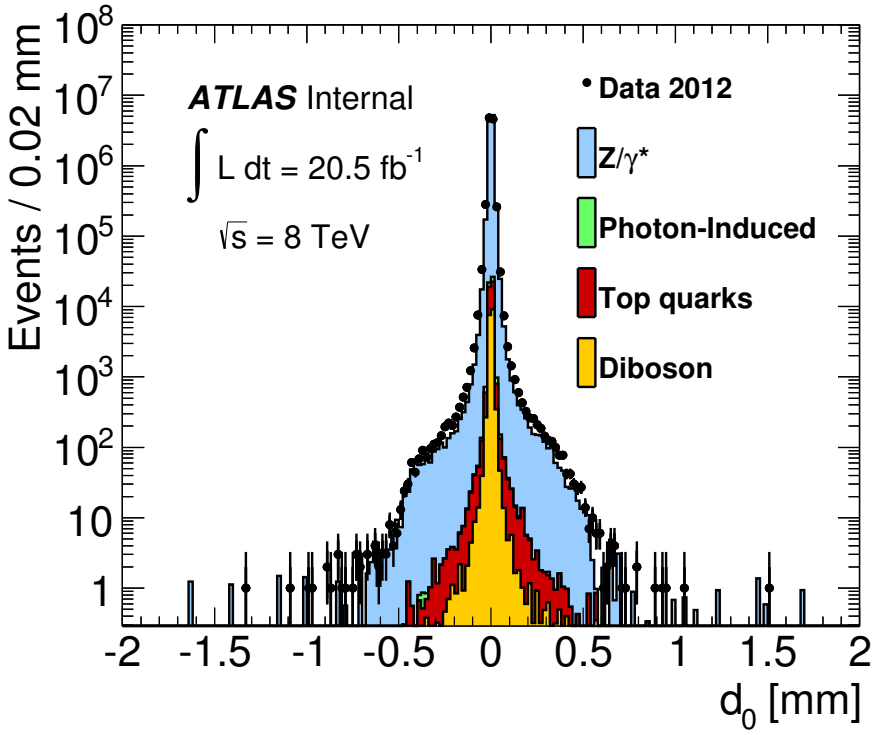

Figure 4.1: Muon transverse distance (d_0) from the primary vertex after all selection criteria are imposed except the one on d_0. The number of events in simulation is normalized to the data.

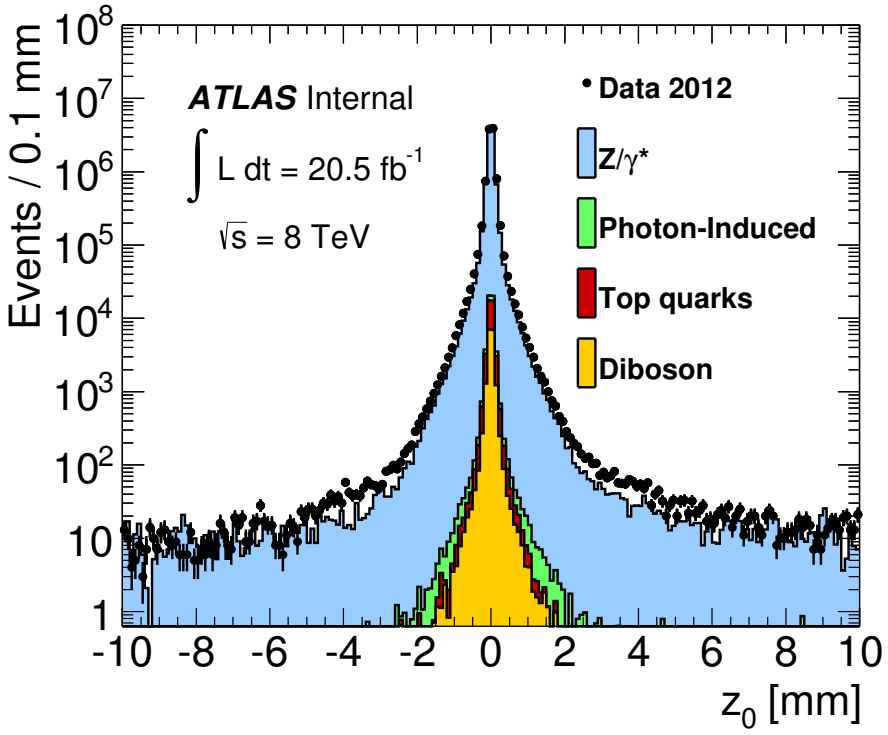

Figure 4.2: Muon longitudinal distance (z_0) from the primary vertex after all selection criteria are imposed except the one on z_0. The number of events in simulation is normalized to the data.

4.3 Dimuon Pair Selection

After applying the requirements listed in the previous section on each muon candidate, events are required to have at least two such muons to be retained. Then dimuon selection criteria as detailed below are imposed on muon pairs.

- Muons in dimuon pair are required to have opposite-sign charges.
- If there are more than one dimuon pair with opposite-sign charge in an event, the pair of oppositely charged muons with the highest scalar sum of p_{T} ($\Sigma|p_{\mathrm{T}}|$) is selected.
- The invariant mass of the muon pair is required to be greater than 80 GeV; $m_{\mu\mu} > 80$ GeV.

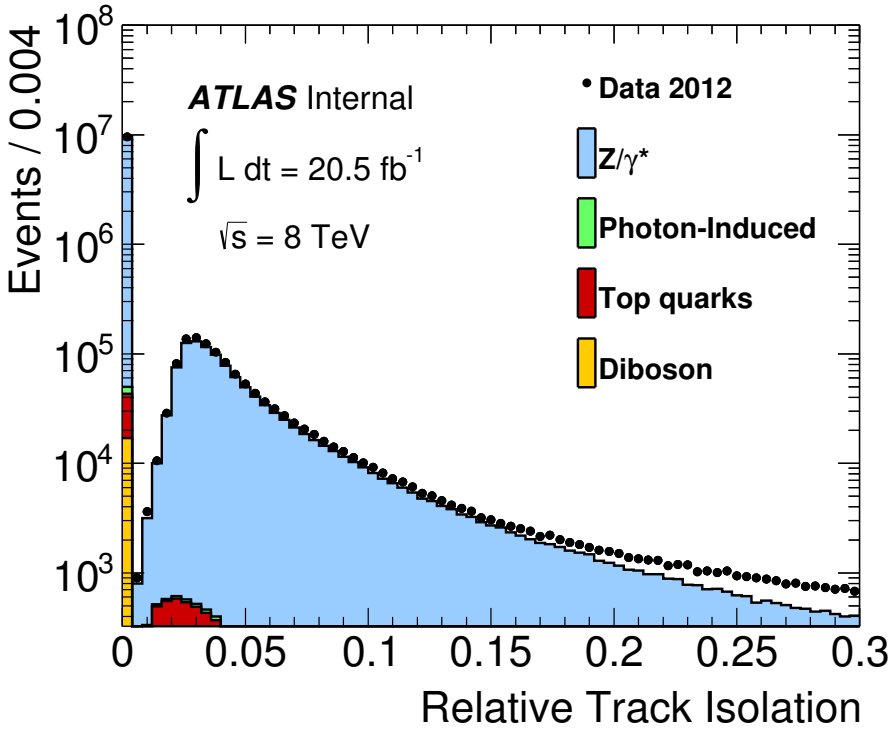

Figure 4.3: Distribution of relative track isolation for single muons after all selection criteria are imposed except the one on relative track isolation. Here the number of events in simulation is normalized to the data.

The event- and object-level selection criteria detailed above are applied to the data and all MC background samples. A total of 5193313 events are found with $m_{\mu\mu} > 80$ GeV in the 2012 dataset. The acceptance times efficiency for DY events with dimuon mass of 1 TeV (2 TeV) is found to be 47% (45%). The relative and cumulative efficiencies are given for DY events with dimuon mass of 1 and 2 TeV in Table 4.1 after each successive selection is applied. The selection criterion shown by "Object Quality" in the table includes the requirements on the impact parameters (d_0, z_0) and ID hits.

4.4 Background Estimation

Monte Carlo simulation is used to estimate the Standard Model contribution from processes which have two real muons that pass the event selection criteria

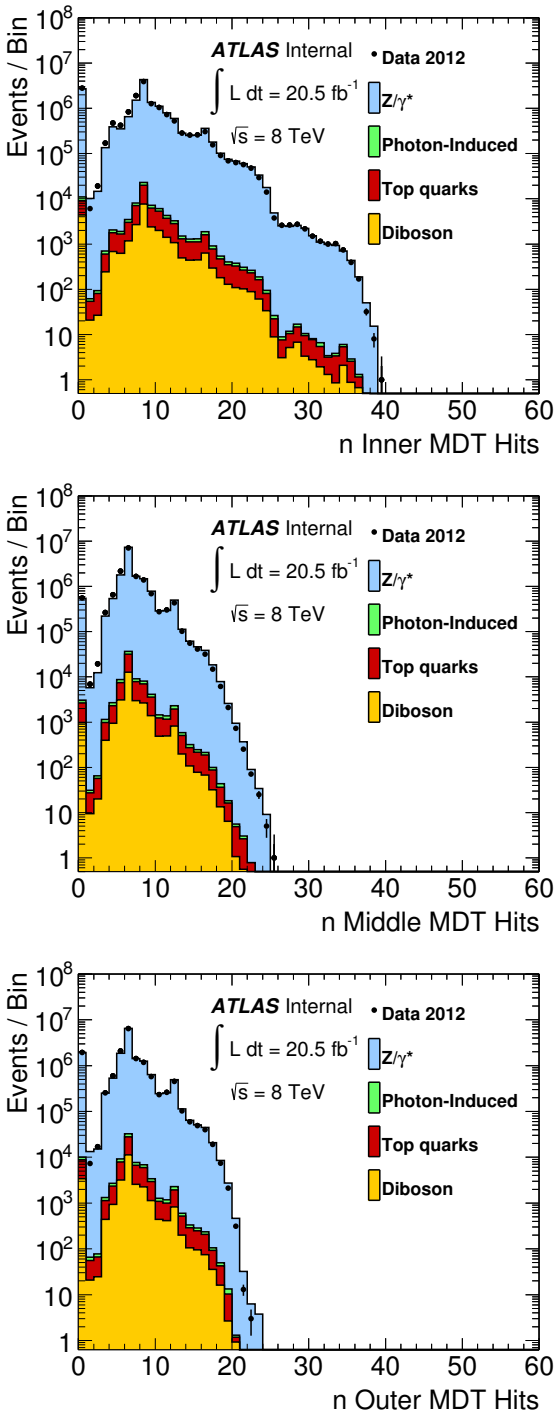

Figure 4.4: Distributions of precision hits in the inner, middle and outer stations (top, middle and bottom, respectively) after all selection criteria are imposed except the MS hit requirements. Here the number of events in simulation is normalized to the data.

Table 4.1: Dimuon channel cutflow table, presenting the relative and cumulative efficiencies for each important criterion in the non-resonant dilepton analysis. These values are given for the dominant Drell-Yan background at dimuon masses near 1 and 2 TeV. Binomial errors are quoted for each value.

Criterion	Relative Eff [%]		Cumulative Eff [%]	
	1 TeV	2 TeV	1 TeV	2 TeV
Trigger	89.77 ± 0.10	89.21 ± 0.10	89.77 ± 0.10	89.21 ± 0.10
≥ 2 Combined Muons	88.80 ± 0.11	88.77 ± 0.11	79.71 ± 0.13	79.20 ± 0.13
p_T	98.21 ± 0.05	98.28 ± 0.05	78.30 ± 0.13	77.84 ± 0.13
Object Quality	98.56 ± 0.04	98.41 ± 0.05	77.16 ± 0.13	76.60 ± 0.13
Isolation	97.47 ± 0.06	97.82 ± 0.05	75.20 ± 0.14	74.93 ± 0.14
3 Station Muons	63.10 ± 0.18	62.10 ± 0.18	47.44 ± 0.16	46.52 ± 0.16
Charge	99.97 ± 0.01	96.62 ± 0.08	47.43 ± 0.16	44.95 ± 0.16

and present a non-negligible background to the signal processes under investigation. The dominant background is from the DY process, followed by $t\bar{t}$, PI and diboson (WW, WZ, ZZ) processes. There are also other background contributions coming from the QCD multijet, W+jets processes and cosmic rays. The multijet and W+jets background is defined as events which contain a maximum of one real lepton, and one or more jets which fake a lepton. The QCD multi jet background in the muon channel is due to $b\bar{b}$ and $c\bar{c}$ production and subsequent decay to muons. These muons tend to be non-isolated and the isolation requirement strongly suppresses this source of background. Therefore, this background is excluded from the SM background estimate. The background coming from a W boson associated with a number of jets are suppressed mostly by requiring two combined muons with $p_{\mathrm{T}} > 25$ GeV. It is further suppressed by the isolation requirement. The final contribution from this background is found negligible. The cosmic background is not predicted in the Monte Carlo simulation and has to be measured directly from the data. The estimation of cosmic background is performed with the 2011 data and found to be negligible. Since then, data have been collected at higher instantaneous luminosity in 2012, therefore reducing exposure time to cosmic rays relative to integrated luminosity.

After applying event and object level selections on each MC simulation sample representing SM backgrounds, each of these samples is subsequently scaled to the same integrated luminosity (1 pb^{-1}). These separate background contributions are then summed together into a total MC background estimate. The dimuon invariant mass region between 80 GeV and 120 GeV is used as a normalization region in this analysis. Hence, the total MC background estimate is normalized to data in this region. This normalization protects the analysis against any mass-independent systematic uncertainties, e.g., the uncertainty in the integrated luminosity or the overall muon efficiency, leaving only mass-dependent systematic uncertainties to be considered. The ratio of data and MC background estimate in this region gives a value of the would-be integrated luminosity, to which all MC samples are scaled. Comparison of this value to the integrated luminosity of the data (20.5 fb^{-1}) yields a ratio of 1.002, and is therefore well within the luminosity uncertainty of $\pm 2.8\%$ [93].

After estimating all SM contributions using MC simulation, data and MC distributions are compared to search for a non-resonant signal-like excess. In the control region, from the dimuon invariant mass of 120 GeV to 400 GeV, good agreement is found between data and the MC background estimate. Until the event selection is finalized, all studies are performed in the control region and the data is kept *blinded* in the signal region.

4.5 Signal Search

This analysis searches for non-resonant new physics signatures in events with two same flavor opposite-sign leptons. The signal would be seen as an excess in the tail of the dimuon mass spectrum. For the contact interaction search, the signal region is chosen to consist of six invariant mass bins (in GeV): 400-550, 550-800, 800-1200, 1200-1800, 1800-3000, 3000-4500. The ADD search is conducted only in one single

mass bin in the range 1900-4500 GeV where the lower mass boundary is optimized based on the strongest expected exclusion limit.

Dimuon mass distributions for data and the predicted background are shown in Fig. 4.5 along with a few benchmark CI (left) and ADD (right) signals overlaid.

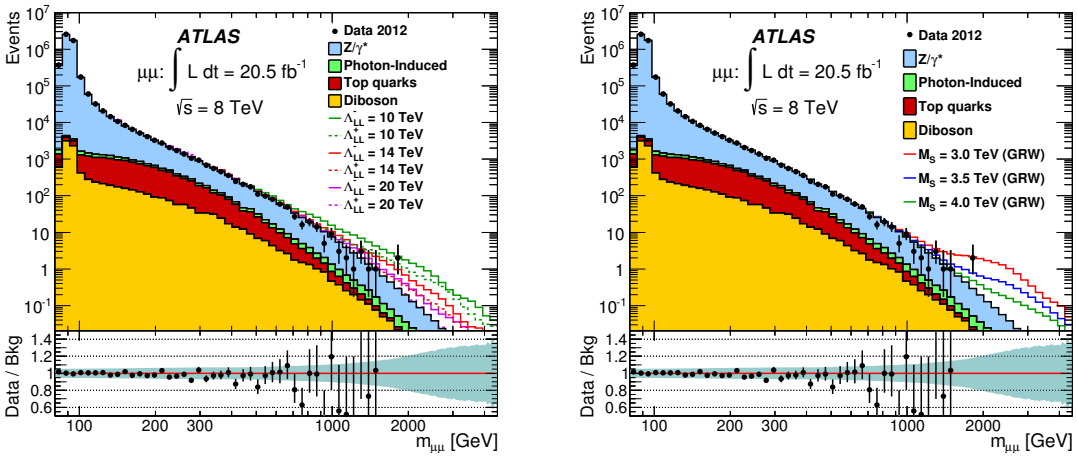

Figure 4.5: Reconstructed dimuon invariant mass distributions for data and the SM background estimate. Also shown are the predictions for a benchmark Λ value in the LL contact interaction model (left) and benchmark M_S value in the GRW ADD model (right). The distribution bin width is constant in $\log(m_{\mu\mu})$. The ratio is presented with the total systematic uncertainty overlaid as a band.

4.5.1 Using Angular Distributions as a Search Variable

In addition to the dimuon invariant mass, the distribution of $\cos\theta^*$, where θ^* is the dimuon decay angle, would also be modified by the new physics interactions at large mass scales so it is important especially for the non-resonant searches. Thus, $\cos\theta^*$ is also used as an additional discriminating variable for the CI search.

When the incoming quarks has no transverse momentum relative to their parent protons, θ^* can be determined from the four-momenta of the particles calculating the angle between the incoming quark and the outgoing muon in the center-of-mass frame of the muon pair. However, if either of the incoming quarks has significant transverse momentum, that leads to an ambiguity in the four-momenta of the incoming quarks in the frame of the dimuon pair. In order to minimize the effect of the transverse

momentum of the incoming quarks, θ^* is defined in the Collins-Soper (CS) frame [94]. The CS frame is constructed with the z-axis bisecting the angle between the incoming parton momentums, and the x-axis perpendicular to this.

$$\cos\theta^* = \frac{p_z(\mu^+\mu^-)}{|p_z(\mu^+\mu^-)|}\frac{2(p_1^+p_2^- - p_1^-p_2^+)}{m(\mu^+\mu^-)\sqrt{m(\mu^+\mu^-)^2 + p_T(\mu^+\mu^-)^2}} \tag{4.1}$$

where p_n^+ (p_n^-) denotes $(E+p_z)/\sqrt{2}$ $((E-p_z)/\sqrt{2})$, and the subscript 1 or 2 describes whether the particle is the μ^+ or μ^- respectively.

In order to determine the sign of $\cos\theta^*$, the direction of the incoming quark has to be known. In pp collisions, which one of the beams contributed the quark to the collision and which one the anti-quark is unknown. Thus, the boost direction of the combined dimuon pair is used as the incoming quark (as opposed to anti-quark) direction. This introduces a "dilution" of the asymmetry in the reconstructed spectrum as compared to theory. This dilution effect is suppressed at higher dimuon rapidity where the probability of the incoming quark direction being aligned with that of the dimuon system increases. This is due to the fact that in the parton distribution functions the regions at high fractional momentum x are dominated by valence quarks.

From $\cos\theta^*$, a forward-backward asymmetry, which is sensitive to the chiral structure of the interaction, is defined as follows:

$$A_{FB} = \frac{N_F - N_B}{N_F + N_B} \tag{4.2}$$

where N_F is the number of events with $\cos\theta^* > 0$ (forward events) and N_B is the number of events with $\cos\theta^* < 0$ (backward events).

Fig. 4.6 makes it clear how the discriminating nature of the angular distribution comes about, and why this discriminates against the SM DY background. It is seen from this figure that the existence of interference modifies the A_{FB} distribution. The

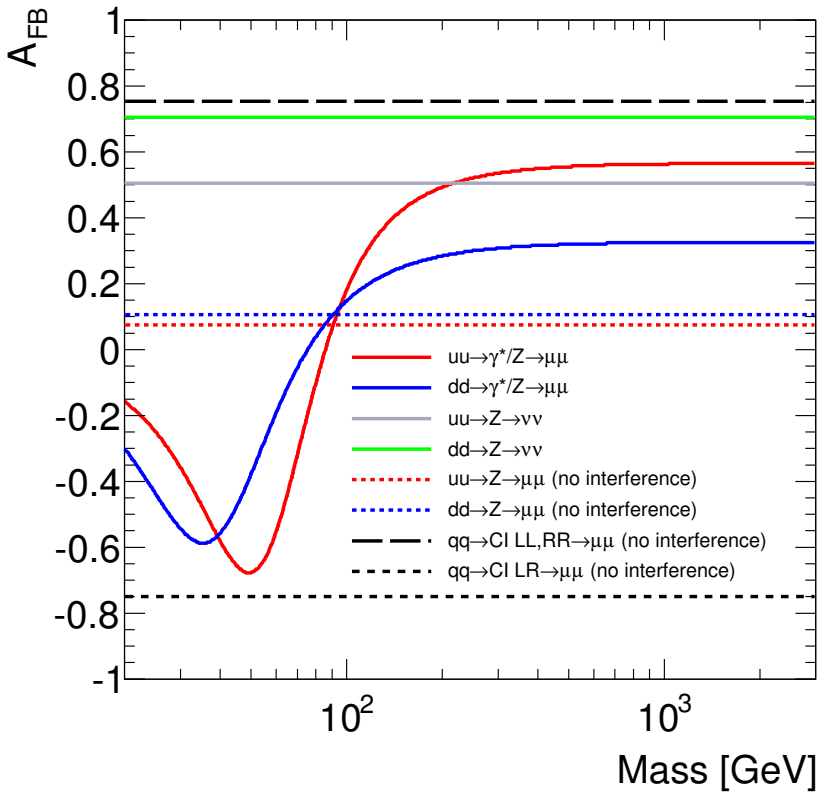

Figure 4.6: Forward-backward asymmetry as a function of dimuon invariant mass for different processes. The red and blue solid curves show processes that includes γ^*/Z interference. If only the pure Z contribution is considered and no interference is assumed, the red and blue dashed lines are obtained. Other processes which only have the pure Z contribution are shown by the light purple and green solid lines. The dashed black lines show the distributions for the CI processes for LL, LR, and RR chirality models. These CI processes correspond to pure CI contribution ignoring γ and Z.

red and blue solid curves showing the processes with Z/γ^* interference turn into red and blue dashed lines when no interference is assumed and only the contribution from the pure Z is considered. By comparing these dashed and solid lines, it is seen clearly how the existence of interference alters the distribution. The processes shown by the light purple and green solid lines can only occur via Z exchange since there are neutrinos in the final state. Thus, there is no interference for these processes and A_{FB} is constant throughout the dimuon invariant mass. The CI processes shown by black dashed lines, correspond to pure CI contribution ignoring any interference with

γ and Z. Thus, A_{FB} is constant and has the same magnitude for the LL, LR and RR CI models. However, there is a sign flip in the asymmetry for the LR model.

The discrimination power between the SM and the new physics of A_{FB} is studied with the LL, LR and RR CI models. Fig. 4.7 compares the forward-backward asymmetry as a function of dimuon mass for different chirality structures at the truth level. As can be seen in the figure, LL and RR models are very SM-like. However, a slight positive (negative) deviation relative to the SM is observed in constructive (destructive) case. The largest discrimination power is seen for LR chirality model for both destructive and constructive cases. The reason of seeing a larger deviation for the LR CI model is due to a sign flip in A_{FB}. The different DY A_{FB} shown in Figs. 4.6 and 4.7 is explained by the dilution.

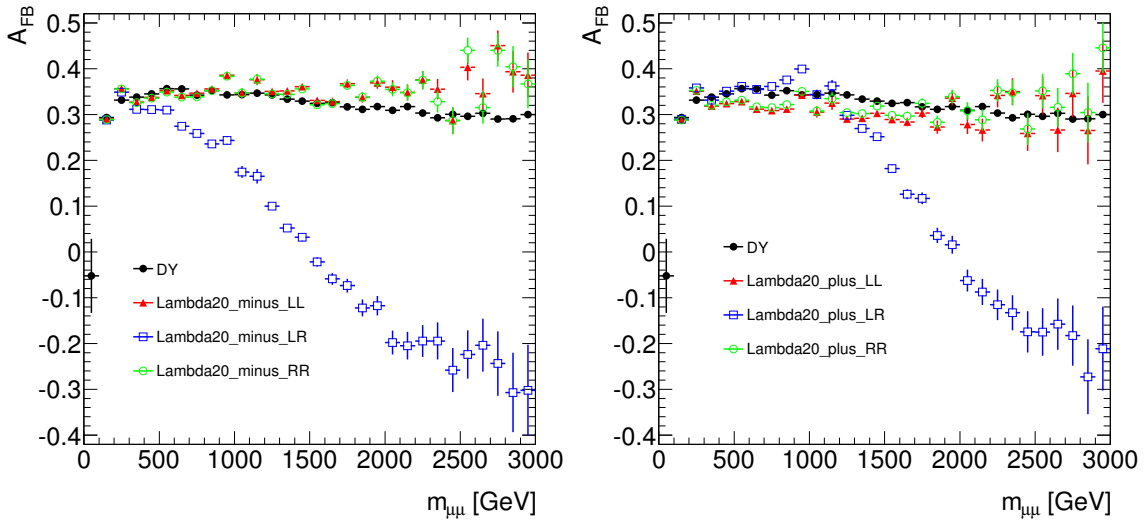

Figure 4.7: Forward backward symmetry (A_{FB}) versus true dimuon invariant mass distribution for Standard Model Drell-Yan and for three contact interaction helicity models at $\Lambda = 20$ TeV for constructive (left) and destructive (right) cases.

In order to use $\cos\theta^*$ as a discriminating variable in the CI search, each dimuon mass bin is further divided into forward and backward events for the statistical interpretation of the results. Since for each of six mass bins there are two $\cos\theta^*$ bins defined, as a total of 12 search bins are used in the contact interaction analysis. The

$\cos\theta^*$ distributions of data and background in the control region and in the signal region are presented in Fig. 4.8. The distribution in the signal region also display CI signal predictions.

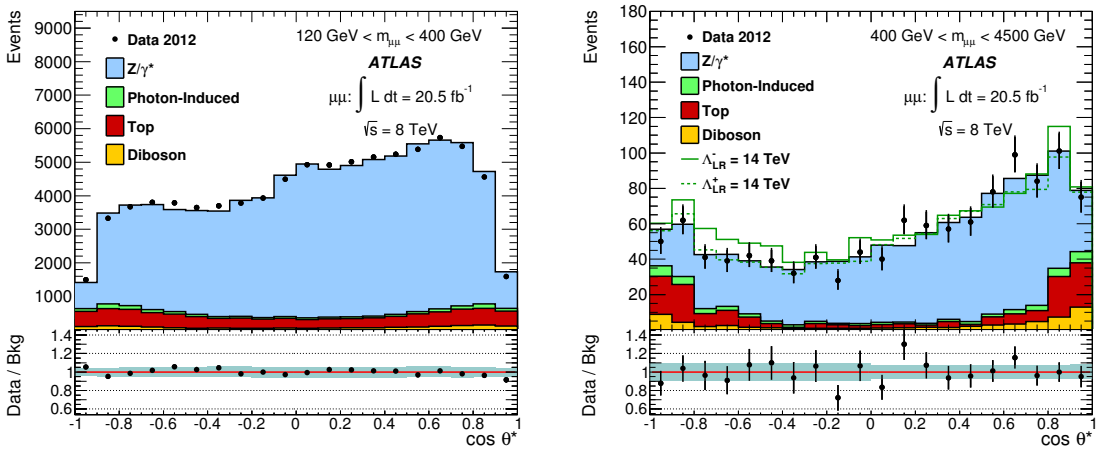

Figure 4.8: Reconstructed dimuon $\cos\theta^*$ distribution for data and SM background estimate in the control region (120 GeV $< m_{\mu\mu} <$ 400 GeV) (left), and in the signal region (400 GeV $< m_{\mu\mu} <$ 4500 GeV) (right).

Table 4.2 shows the total number of expected and observed events in the control region. A good agreement between data and the SM expectation is observed. Table 4.3 and Table 4.4 show the total number of expected and observed events in the signal region mass binning and it is also shown in presence of contact interactions for a few benchmark Λ values for the LL chirality model. As seen from these tables, the CI contribution to the total number of expected events increases by increasing invariant mass. The total number of expected events in each mass bin is also shown graphically in Fig. 4.9.

Similarly, Table 4.5 presents the observed events in data, the total number of expected events from the Standard Model, and in the additional presence of different M_S values under the ADD model.

The Fig. 4.10 shows the expected and observed A_{FB} distribution as a function of reconstructed dimuon invariant mass. This plot is particularly interesting as it

clearly presents the data/MC agreement and how data would diverge from the SM expectation if the LR model was present in nature.

Data/MC comparisons are also shown for muon η, ϕ, and p_T distributions in Figure 4.11. A gap in chamber coverage left open to allow for services to magnets, calorimeters and the ID can be clearly seen in the η distribution around $|\eta| \approx 1$ and 1.2. The structure in ϕ is mostly due to the fact that we are using three station muons and the muon spectrometer is eight-fold symmetric. It's not always possible to have three station muons everywhere in ϕ since we don't use hits from some of the chambers (i.e BIS7 or BIS8). Also, there may be muons which have hits in the MS but only leave track in two stations so are not selected. In this distribution, the structure around $\phi \approx$ -1 and -2 is the result of the detector feet in that region. Dimuon p_{T} and rapidity distributions are shown in Figure 4.12.

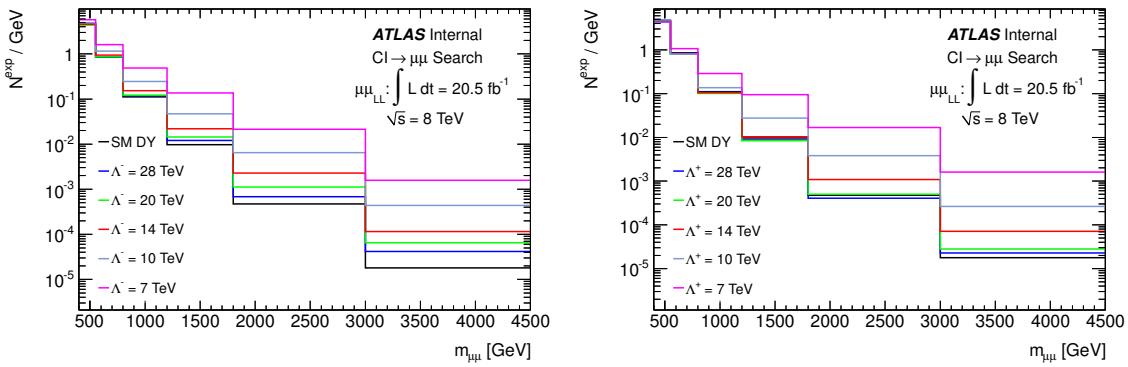

Figure 4.9: Normalized number of expected events as a function of invariant mass for the LL CI model with constructive (left) and destructive (right) interference.

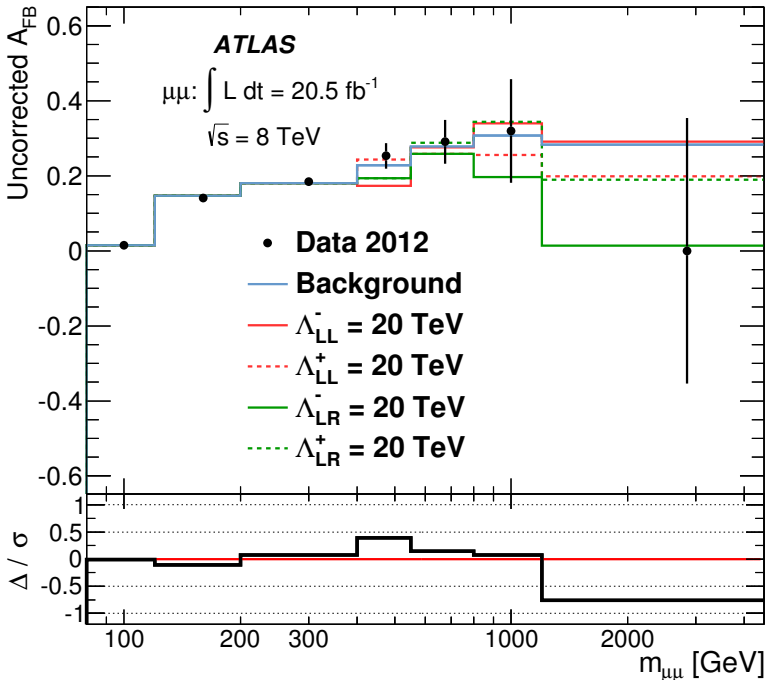

Figure 4.10: Reconstructed A_{FB} distributions for data and the SM background estimate as a function of dimuon invariant mass. Also shown are the predictions of different benchmark Λ values for the LL and LR contact interaction model (the RR model is very similar to the LL case). The ratio displays the background-subtracted data (Δ) divided by the total uncertainty (σ) in each bin.

Table 4.2: Table presenting the expected and observed number of events for contact interactions within the control region between 120 and 400 GeV. No signal contribution is expected in this region, therefore signal lines are excluded for this table. The errors quoted originate from both MC statistical and systematic uncertainties. The first column of the table for each mass bin shows all events, where as the second and third columns show the number of events in the forward and backward region respectively.

Process	$m_{\mu\mu}$ [GeV]					
	120 – 200			200 – 400		
	All	Forward	Backward	All	Forward	Backward
Drell-Yan	64000 ± 4000	37000 ± 2300	26600 ± 1500	10100 ± 700	6200 ± 400	3860 ± 270
Top	5400 ± 330	2670 ± 160	2740 ± 170	2170 ± 130	1060 ± 70	1110 ± 70
Dibosons	1170 ± 60	630 ± 34	543 ± 29	488 ± 27	274 ± 16	214 ± 13
Photon-Induced	1100 ± 1100	600 ± 600	600 ± 600	400 ± 400	190 ± 190	190 ± 190
Total SM	71000 ± 4000	40800 ± 2400	30400 ± 1600	13100 ± 800	7800 ± 500	5380 ± 330
Data	70724	40341	30383	12912	7647	5265

Table 4.3: Table presenting the expected and observed number of events search for contact interactions within the search region between 400 and 1800 GeV. Benchmark LL model parameter of interest values are given for both constructive (Λ^-) and destructive (Λ^+) interference, which are summed with the total background estimate on the signal lines. The errors quoted originate from both MC statistical and systematic uncertainties. The first column of the table for each mass bin shows all events, whereas the second and third columns show the number of events in the forward and backward region respectively.

Process	$m_{\mu\mu}$ [GeV]					
	400 – 550			550 – 800		
	All	Forward	Backward	All	Forward	Backward
Drell-Yan	670 ± 50	435 ± 29	239 ± 20	217 ± 18	142 ± 11	75 ± 7
Top	128 ± 10	61 ± 6	66 ± 7	16.3 ± 1.4	6.8 ± 1.0	6.7 ± 0.9
Dibosons	47.6 ± 2.7	28.7 ± 1.8	18.9 ± 1.3	15.3 ± 0.9	9.7 ± 0.6	5.7 ± 0.4
Photon-Induced	34 ± 34	17 ± 17	17 ± 17	13 ± 13	6 ± 6	6 ± 6
Total SM	880 ± 60	543 ± 35	341 ± 27	261 ± 22	165 ± 13	94 ± 10
Data	814	510	304	265	171	94
SM+CI ($\Lambda^- = 7$ TeV)	1070 ± 60	660 ± 40	411 ± 30	452 ± 26	293 ± 16	157 ± 12
SM+CI ($\Lambda^- = 10$ TeV)	950 ± 60	590 ± 40	357 ± 29	339 ± 24	216 ± 14	120 ± 11
SM+CI ($\Lambda^- = 14$ TeV)	900 ± 60	550 ± 40	346 ± 29	285 ± 23	177 ± 14	105 ± 11
SM+CI ($\Lambda^- = 20$ TeV)	870 ± 60	520 ± 40	352 ± 29	265 ± 23	168 ± 14	94 ± 11
SM+CI ($\Lambda^- = 28$ TeV)	910 ± 60	540 ± 40	363 ± 29	265 ± 23	168 ± 14	93 ± 11
SM+CI ($\Lambda^+ = 7$ TeV)	860 ± 60	510 ± 40	348 ± 29	313 ± 23	187 ± 14	123 ± 11
SM+CI ($\Lambda^+ = 10$ TeV)	850 ± 60	510 ± 40	338 ± 29	248 ± 23	156 ± 14	89 ± 10
SM+CI ($\Lambda^+ = 14$ TeV)	870 ± 60	530 ± 40	340 ± 29	252 ± 23	152 ± 14	97 ± 11
SM+CI ($\Lambda^+ = 20$ TeV)	890 ± 60	560 ± 40	330 ± 29	247 ± 23	155 ± 14	89 ± 11
SM+CI ($\Lambda^+ = 28$ TeV)	920 ± 60	560 ± 40	363 ± 29	257 ± 23	157 ± 14	96 ± 11

Process	$m_{\mu\mu}$ [GeV]					
	800 – 1200			1200 – 1800		
	All	Forward	Backward	All	Forward	Backward
Drell-Yan	45 ± 4	29.6 ± 2.7	15.4 ± 1.9	5.9 ± 0.8	3.9 ± 0.5	2.1 ± 0.4
Top	1.66 ± 0.11	0.44 ± 0.09	0.58 ± 0.07	0.103 ± 0.007	0.018 ± 0.011	0.026 ± 0.003
Dibosons	3.75 ± 0.26	2.54 ± 0.19	1.21 ± 0.12	0.556 ± 0.030	0.372 ± 0.021	0.184 ± 0.011
Photon-Induced	3.3 ± 3.3	1.6 ± 1.6	1.7 ± 1.7	0.5 ± 0.5	0.27 ± 0.27	0.28 ± 0.28
Total SM	54 ± 6	34.2 ± 3.2	18.8 ± 2.5	7.2 ± 1.0	4.5 ± 0.5	2.5 ± 0.5
Data	47	31	16	7	3	4
SM+CI ($\Lambda^- = 7$ TeV)	203 ± 12	138 ± 8	64 ± 5	83 ± 7	58 ± 5	25.1 ± 2.2
SM+CI ($\Lambda^- = 10$ TeV)	108 ± 7	71 ± 5	35.9 ± 3.2	29.4 ± 2.2	20.2 ± 1.5	9.2 ± 0.8
SM+CI ($\Lambda^- = 14$ TeV)	70 ± 6	48 ± 4	22.0 ± 2.8	14.4 ± 1.2	9.8 ± 0.8	4.5 ± 0.6
SM+CI ($\Lambda^- = 20$ TeV)	58 ± 6	38.7 ± 3.5	18.9 ± 2.7	10.0 ± 1.1	6.4 ± 0.6	3.5 ± 0.5
SM+CI ($\Lambda^- = 28$ TeV)	57 ± 6	36.4 ± 3.4	20.0 ± 2.7	8.6 ± 1.0	5.7 ± 0.6	2.8 ± 0.5
SM+CI ($\Lambda^+ = 7$ TeV)	125 ± 8	79 ± 5	44.6 ± 3.5	58 ± 5	37.9 ± 3.0	20.3 ± 1.7
SM+CI ($\Lambda^+ = 10$ TeV)	64 ± 6	40.2 ± 3.5	22.7 ± 2.7	18.0 ± 1.4	11.6 ± 0.9	6.4 ± 0.6
SM+CI ($\Lambda^+ = 14$ TeV)	51 ± 6	32.1 ± 3.4	18.5 ± 2.7	7.5 ± 1.0	4.8 ± 0.6	2.6 ± 0.5
SM+CI ($\Lambda^+ = 20$ TeV)	50 ± 6	30.9 ± 3.4	18.1 ± 2.7	6.4 ± 1.0	3.8 ± 0.6	2.5 ± 0.5
SM+CI ($\Lambda^+ = 28$ TeV)	52 ± 6	34.1 ± 3.4	17.5 ± 2.7	6.6 ± 1.0	4.3 ± 0.6	2.2 ± 0.5

Table 4.4: Table presenting the expected and observed number of events in muon channel search for contact interactions within the search region between 1800 and 4500 GeV. Benchmark LL model parameter of interest values are given for both constructive (Λ^-) and destructive (Λ^+) interference, which are summed with the total background estimate on the signal lines. The errors quoted originate from both MC statistical and systematic uncertainties. The first column of the table for each mass-bin shows all events, where as the second and third columns show the number of events in the forward and backward region respectively.

Process	$m_{\mu\mu}$ [GeV]					
	1800 – 3000			3000 – 4500		
	All	Forward	Backward	All	Forward	Backward
Drell-Yan	0.58 ± 0.12	0.38 ± 0.07	0.21 ± 0.06	0.027 ± 0.008	0.016 ± 0.005	0.011 ± 0.004
Top	< 0.005	< 0.002	< 0.001	< 0.001	< 0.001	< 0.001
Dibosons	0.056 ± 0.005	0.038 ± 0.004	0.018 ± 0.002	< 0.003	< 0.002	< 0.002
Photon-Induced	0.07 ± 0.07	0.033 ± 0.033	0.035 ± 0.035	0.003 ± 0.003	0.002 ± 0.002	0.002 ± 0.002
Total SM	0.71 ± 0.14	0.45 ± 0.08	0.26 ± 0.07	0.032 ± 0.009	0.019 ± 0.005	0.013 ± 0.004
Data	1	1	0	0	0	0
SM+CI ($\Lambda^- = 7$ TeV)	25.8 ± 3.2	17.3 ± 2.2	8.4 ± 1.1	2.4 ± 0.5	1.53 ± 0.32	0.83 ± 0.22
SM+CI ($\Lambda^- = 10$ TeV)	7.9 ± 0.9	5.3 ± 0.6	2.60 ± 0.34	0.66 ± 0.14	0.44 ± 0.10	0.22 ± 0.06
SM+CI ($\Lambda^- = 14$ TeV)	2.89 ± 0.33	1.8 ± 0.2	1.08 ± 0.16	0.18 ± 0.04	0.137 ± 0.033	0.040 ± 0.014
SM+CI ($\Lambda^- = 20$ TeV)	1.49 ± 0.18	1.00 ± 0.11	0.49 ± 0.08	0.103 ± 0.022	0.059 ± 0.015	0.044 ± 0.012
SM+CI ($\Lambda^- = 28$ TeV)	0.96 ± 0.15	0.62 ± 0.09	0.34 ± 0.07	0.068 ± 0.016	0.041 ± 0.011	0.027 ± 0.009
SM+CI ($\Lambda^+ = 7$ TeV)	20.3 ± 2.5	13.5 ± 1.7	6.7 ± 0.9	2.4 ± 0.5	1.64 ± 0.33	0.79 ± 0.18
SM+CI ($\Lambda^+ = 10$ TeV)	4.8 ± 0.6	3.3 ± 0.4	1.45 ± 0.19	0.40 ± 0.08	0.26 ± 0.06	0.14 ± 0.04
SM+CI ($\Lambda^+ = 14$ TeV)	1.45 ± 0.18	0.97 ± 0.11	0.48 ± 0.08	0.113 ± 0.023	0.078 ± 0.017	0.035 ± 0.010
SM+CI ($\Lambda^+ = 20$ TeV)	0.74 ± 0.15	0.42 ± 0.08	0.32 ± 0.07	0.048 ± 0.013	0.027 ± 0.008	0.021 ± 0.007
SM+CI ($\Lambda^+ = 28$ TeV)	0.63 ± 0.14	0.40 ± 0.08	0.23 ± 0.07	0.040 ± 0.011	0.029 ± 0.009	0.010 ± 0.005

Table 4.5: Table presenting the expected and observed number of events in the signal region for the ADD model. Benchmark ADD model parameter of interest values are given for the GRW formalism. The errors quoted originate from both MC statistical and systematic uncertainties.

Process	$1900 \leq m_{\mu\mu} \leq 4500$ GeV
Drell-Yan	0.44 ± 0.09
Top	$0.005 < 0.001$
Diboson	0.047 ± 0.005
Photon-Induced	0.05 ± 0.05
Total SM	0.54 ± 0.09
Data	0
SM+ADD ($M_S = 3.25$ TeV)	6.4 ± 0.7
SM+ADD ($M_S = 3.50$ TeV)	3.9 ± 0.4
SM+ADD ($M_S = 3.75$ TeV)	2.4 ± 0.2
SM+ADD ($M_S = 4.00$ TeV)	1.7 ± 0.1
SM+ADD ($M_S = 4.75$ TeV)	0.8 ± 0.1

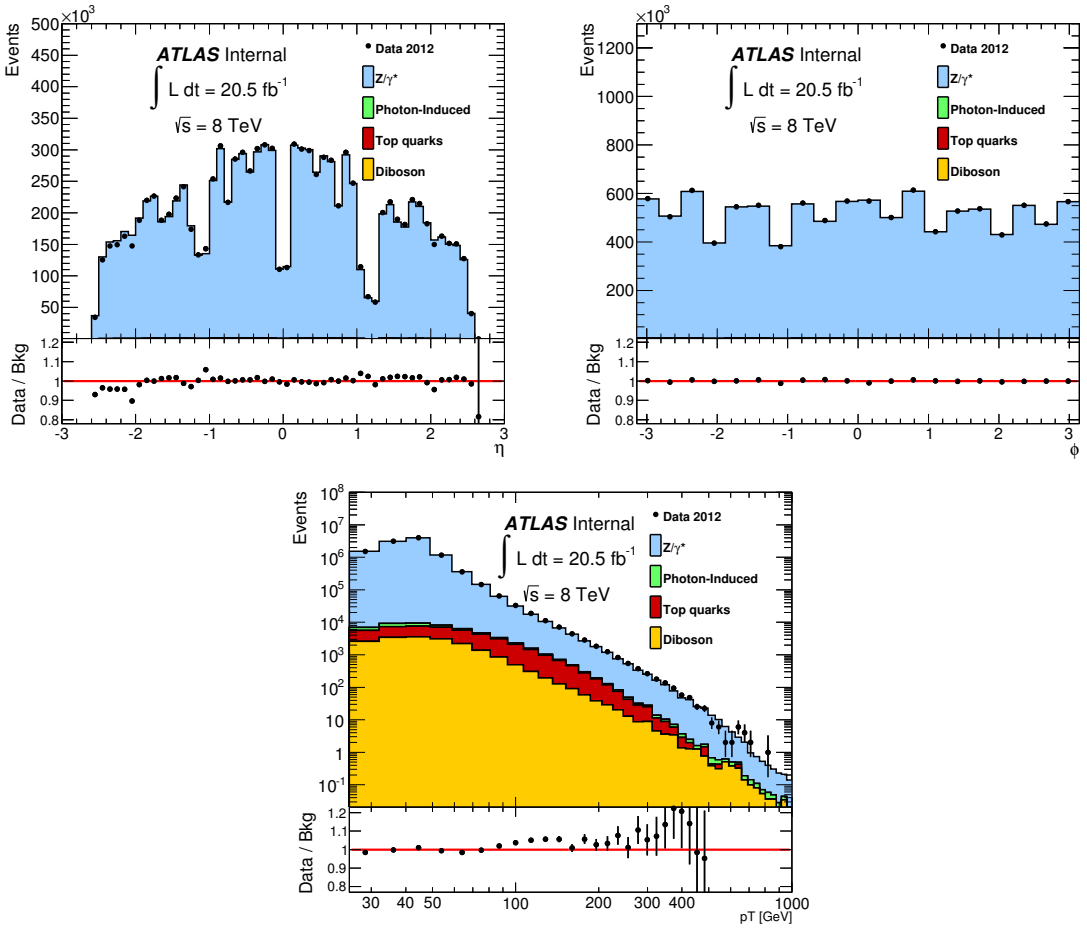

Figure 4.11: Reconstructed muon η (top left), ϕ (top right), and p_T (bottom) distributions for data and the SM background estimate.

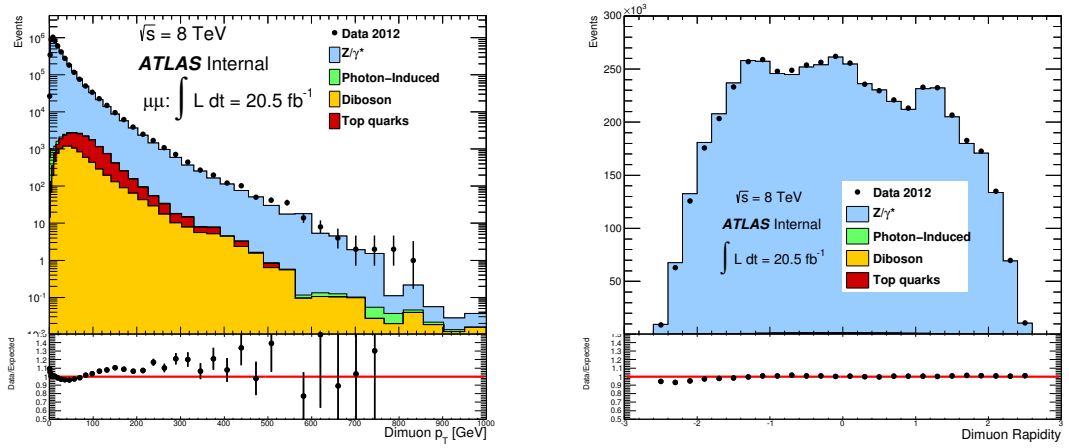

Figure 4.12: Reconstructed dimuon p_T (left), and rapidity (right), distribution comparisons between data and the SM background estimate.

CHAPTER 5

SYSTEMATIC UNCERTAINTIES

This chapter is devoted to the detailed discussion of the theoretical and experimental uncertainties that are considered in this analysis.

Systematic uncertainties generally stem from limited knowledge of the detector response and assumptions made in the analysis. To ensure a fair comparison between data and MC simulation, data derived corrections are applied to the MC simulation where required. These corrections have uncertainties that need to be considered in this analysis.

Normalizing the total background estimate to data in the dimuon invariant mass region from 80 GeV to 120 GeV protects the analysis against mass independent systematic uncertainties as any overall constant scale factors cancel out. However, mass dependent systematic uncertainties still need to be considered since the shape of the discrimination variables is affected by these uncertainties.

The sources of systematic uncertainties are categorized as theoretical and experimental, as listed below.

Theoretical systematic uncertainties:

- PDF variation.
- PDF choice.
- PDF α_s scale.
- Higher order electroweak corrections.

- Photon-induced process.
- Z/γ^* production cross section.

Experimental systematic uncertainties:

- Muon reconstruction efficiency.
- Muon momentum scale and resolution.
- Beam energy scale.
- Monte Carlo statistics.

All these systematic uncertainties (detailed below) are accounted for in the CI and ADD searches. Systematic uncertainties are calculated as a function of true dimuon invariant mass, for both signal and background estimates where relevant. Additionally, for the CI search, systematic uncertainties are assessed as a function of true dimuon invariant mass for forward ($\cos\theta^* > 0$) and backward ($\cos\theta^* < 0$) events separately. Thus, any variation in the uncertainty that might affect the expected asymmetry is taken into account. Most of systematic uncertainties are found to have a negligible dependence on $\cos\theta^*$, except for uncertainties on the PDF and photon-induced processes. These uncertainties with non-negligible variation with $\cos\theta^*$ are then considered as a function of true dimuon invariant mass in two different $\cos\theta^*$ regions.

Signal systematic uncertainties are taken into account as a function of the corresponding model's parameter of interest, in addition to invariant mass. The incorporation of these systematic uncertainties in the statistical treatment is explained in Section 6.3.3.

Systematic uncertainties that are relevant for the SM background are only applied to the DY process. Since the contribution of top and diboson backgrounds to the

overall background is small (∼11% and ∼5% of the total background, respectively), uncertainties in their rate have a negligible impact on this analysis.

5.1 Theoretical Uncertainties

Theoretical systematic uncertainties are only applied to the expected SM background except for the Z/γ^* production cross section uncertainty in the normalization region. As standard ATLAS Exotics procedure, theoretical uncertainties are not applied to the signal processes but their effects on signal acceptance times efficiency are investigated. The systematic uncertainties are calculated as a function of true dimuon invariant mass (except for the flat Z/γ^* cross section uncertainty and uncertainty on the PI effect).

5.1.1 Uncertainties Due to PDF Variation

The biggest theoretical uncertainty in this analysis is due to the uncertainty in the proton structure (parton distribution functions (PDFs)). Varying the PDFs can change the DY cross section as a function of dilepton invariant mass $m_{\ell\ell}$ (or Q^2). Each PDF has a set of independent parameters, in the parton function space, known as "eigenvectors". Systematic uncertainties associated with the PDF variation are quantified by varying these eigenvectors in orthogonal directions.

In this analysis, the nominal PDF set used is MSTW2008NNLO with 20 eigenvectors. The DY cross section at NNLO is calculated as a function of $m_{\ell\ell}$ using the VRAP program [95] by varying each of the eigenvectors at 90% C.L. Results are compared to the nominal values. The difference between them is quantified as the systematic uncertainty on the cross section for a given eigenvector. These asymmetric uncertainties are shown for each PDF eigenvector in Fig. B.1, B.2, B.3 of Appendix B. As a result of this method, there should be an associated systematic nuisance parameter for each eigenvector. However, incorporating every single parameter in the

likelihood for a limit calculation requires huge amount of computing power in the statistical analysis framework. As a solution to this problem, in the previous round of the analysis, systematic uncertainties were added in quadrature in order to obtain one single nuisance parameter for the PDF variation. However, it has been observed that using a single nuisance parameter for the uncertainty due to PDFs can lead to an over-constraint. Since eigenvectors dominating the low mass region are different from the ones dominating the high mass region, they should be treated as uncorrelated. Therefore, PDF eigenvectors are grouped into four bundles (denoted A-D) depending on the invariant mass region in which they dominate. The eigenvectors for each group are listed below. A minus sign means that the definition is inverted such that the upward eigenvector variation is exchanged with the downward one or vice versa, whereas the eigenvectors with a plus sign are taken as they are. This procedure results in all eigenvectors in a given group behaving in a similar way.

- Group A consists of eigenvectors 2+, 13+, 14-, 17-, 18+ and 20+. It is dominant nowhere, but its contribution is not negligible.
- Group B consists of eigenvectors 3-, 4-, 9+ and 11+. It is dominant for $m_{\ell\ell}$ <400 GeV.
- Group C consists of eigenvectors 1+, 5+, 7+, and 8-. It is dominant in the range 400 GeV $< m_{\ell\ell} <$ 1500 GeV.
- Group D consists of eigenvectors 10+, 12+, 15-, 16- and 19+. It is dominant for $m_{\ell\ell} >$ 1500 GeV.

The remaining eigenvector 6 does not fit any of these groups and its uncertainty contribution is negligible.

Within each group, uncertainties from constituent eigenvectors are combined in order to calculate the total asymmetric uncertainty at each mass point. The combination of uncertainties is performed according to the following:

$$\Delta\sigma_G^+ = sign_G \sqrt{\left| \sum_{i=1}^{n_G} sign(\sigma_i^+ - \sigma_0) \cdot (\sigma_i^+ - \sigma_0)^2 \right|}, \tag{5.1}$$

$$\Delta\sigma_G^- = sign_G \sqrt{\left| \sum_{i=1}^{n_G} sign(\sigma_i^- - \sigma_0) \cdot (\sigma_i^- - \sigma_0)^2 \right|}, \tag{5.2}$$

where the sum is over the PDF eigenvectors in a given group G, σ_i^+ is the cross section for the upward variation of the i^{th} PDF eigenvector (downward variation, if inverted), σ_i^- is the cross section for the downward variation of the i^{th} PDF eigenvector (upward variation, if inverted), σ_0 is the cross section for the central value PDF, and $sign_G$ is the sign of the sum inside the square root.

The total symmetric uncertainty that is obtained by adding total asymmetric uncertainties of each bundle in quadrature, is also calculated by using FEWZ for a cross check. A good agreement is found between the uncertainties obtained with FEWZ and VRAP; within 0.35% below 3.5 TeV and under 1% below 4.5 TeV.

Systematic uncertainties are studied as a function of dimuon invariant mass. Since uncertainties due to PDF variations have a dependence on forward and backward events, it is needed to look into forward and backward events separately. However, uncertainty calculations with FEWZ or VRAP cannot easily split up into separated forward and backward components. Therefore, instead of using FEWZ or VRAP for systematic uncertainty calculations, the LHAPDF (Les Houches Accord PDF) tool [96] with the MSTW2008NNLO PDF set is used. Evolution codes within the LHAPDF produce the PDF at any desired Q^2 at the user's request, using the external files of parameters that describe distributions of the parton momentum fraction x at the relevant Q^2. In order to perform uncertainty calculations, on an event-by-event basis, using the parton momentum fraction x of incoming partons, the up and down variation of each eigenvector for the PDF is determined. The difference

between the central value of the CT10 PDF which is the base PDF of the LHAPDF, and the central value from MSTW2008NNLO is also accounted for. Hence, bundle histograms for A, B, C and D, which contained all of the variations for the respective bundles of eigenvectors, are filled. Comparing these shifted histograms to the nominal ones (produced by using the central values) a systematic variation for each bundle is calculated. As a first step, these uncertainties are studied only as a function of true dilepton invariant mass, as shown in Fig. 5.1. These results are compared to the ones from FEWZ to check the consistency. Agreement within a few percent on average is found between calculations using FEWZ and LHAPDF. Then the study is extended to look at forward and backward events using LHAPDF.

The programs FEWZ and VRAP are still used for the PDF scale, α_s uncertainties, which are explained in more detail in the next part, because these are not expected to vary much with $\cos\theta^*$.

The effect of the uncertainty, that is obtained by merging different bundle uncertainties, on the reconstructed dimuon invariant mass is shown in Fig. 5.2. The mass-only dependent result for each bundle separately can be found in Fig. B.4 of Appendix B.

Signal PDF variation systematics were also studied for each model. As standard ATLAS Exotics procedure, theoretical uncertainties do not directly apply to the signal. In other words, signal yields are not directly shifted by the uncertainties. However, if uncertainties have a significant impact on the signal acceptance times efficiency, then they are taken into account. Hence, signal events are weighted by the PDF variation uncertainty and then compared to the nominal acceptance. The difference is found to be less than 0.1%, so negligible for CI processes. In the ADD search, a single high threshold mass bin is used between 1900 and 4500 GeV, therefore this study is repeated taking into account the total acceptance times efficiency, including the signal excluded. This can give a different result from the first study performed for

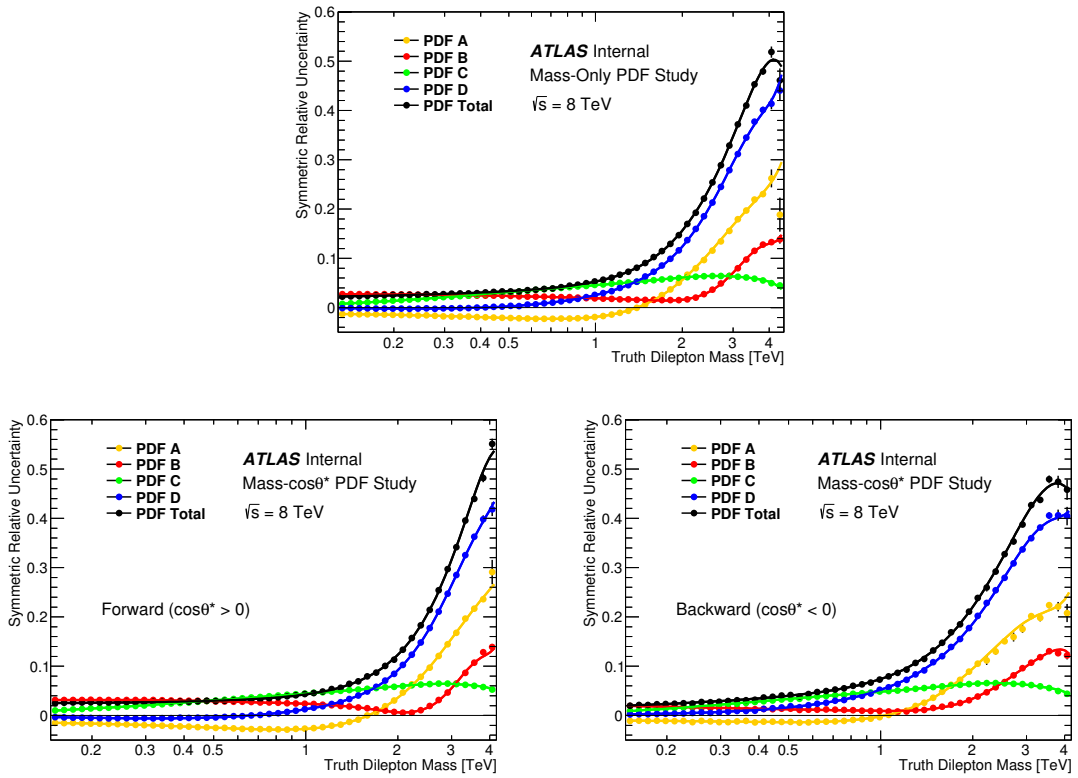

Figure 5.1: PDF uncertainty study using Drell-Yan events with MSTW2008NNLO PDF eigenvector variations (bundled into like groups A – D) to assess shape change. (Top) shows the mass-only dependent result of the PDF uncertainty, while (bottom left) and (bottom right) show the mass-cos θ^* dependent study for "forward" and "backward" events separately.

the CI search, because the PDF uncertainties no longer cancel in both the numerator and denominator of the calculation. Therefore, a larger systematic uncertainty of $\approx$3% is observed for the ADD model, as shown in Fig. 5.3, at an almost constant value versus the parameter of interest of M_S. Thus, the effect of the PDF variation is included in the acceptance times efficiency of the ADD signal. This approach is taken to avoid signal bias introduced via the specific theoretical uncertainty choices.

5.1.2 Uncertainties Due to PDF Choice, Scale and α_S

In addition to parton contributions to the proton structure, there are contributions to PDF from the strength of the strong coupling (α_S) and the renormalization (μ_R)

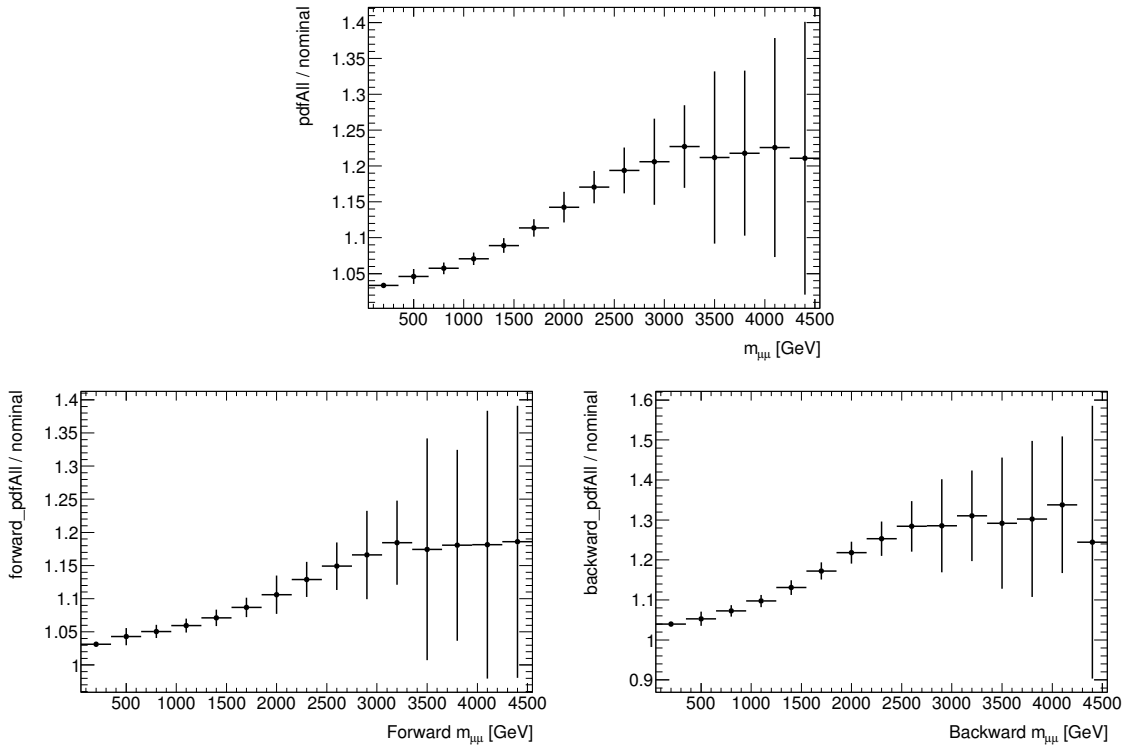

Figure 5.2: The effect of the uncertainty due to the PDF variation on the reconstructed dimuon mass. The mass-only dependent result is shown by the top plot, while bottom left and bottom right show the mass-$\cos\theta^*$ dependent study for "forward" and "backward" events separately.

and factorization (μ_F) scales. Thus, uncertainties associated with these quantities need to be evaluated. Also, DY cross section calculations are performed using different PDF sets in order to study the impact of PDF set choice.

In order to quantify the uncertainties due to α_S, DY cross sections are calculated for α_S values between 0.11365 and 0.12044 (the 90% C.L α_S limits of MSTW) as a function of $m_{\ell\ell}$, using VRAP. The calculated cross sections are compared to the ones from the calculations with nominal PDF set. The maximum difference is assessed as the asymmetric systematic uncertainty due to α_S.

Uncertainties on the QCD corrections are quantified by varying the μ_R and μ_F scales up and down by a factor of two simultaneously. The largest deviation of the

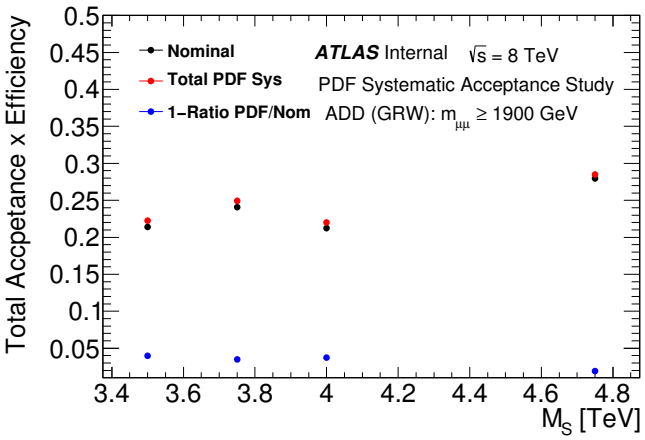

Figure 5.3: The change in acceptance times efficiency due to PDF variation for the ADD search.

calculated cross sections from the nominal cross section is taken as the symmetric uncertainty.

Potential differences in the underlying theoretical framework between the modern PDF fit collaborations are also studied by comparing nominal MSTW2008NNLO with four other PDF sets: CT10NNLO [97], NNPDF2.3 [98], ABM11 [99] and HERAPDF1.5 [100].

The cross section as a function of $m_{\ell\ell}$ is calculated for each of these PDF sets by using their central values. The deviation of these cross sections from the one calculated using the nominal MSTW2008NNLO PDF set is compared to the MSTW2008NNLO PDF uncertainty at the 90% C.L. for the same μ_R and μ_F scales, and value of $\alpha_S = 0.11707$. Cross section values obtained for the different PDF sets, except ABM11, are found to be within the MSTW2008NNLO 90% C.L uncertainty. Therefore, the deviation in the cross section obtained with the ABM11 PDF set is included as an additional systematic uncertainty due to the PDF choice.

5.1.3 Uncertainties Due to Higher Order Electroweak Corrections

As stated in the previous sections, an EW K-factor is applied to the DY samples in order to account for the effects of virtual gauge bosons and real gauge boson emissions.

The higher order EW corrections are calculated both using SANC and FEWZ. Thus, a systematic uncertainty on the EW corrections corresponds to the difference in the theoretical calculations between these two programs. Systematic uncertainties due to the higher order EW corrections as a function of true dilepton invariant mass are shown in Fig. 5.4.

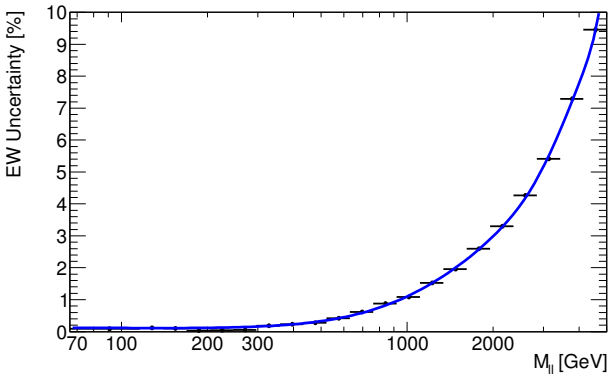

Figure 5.4: Systematic uncertainties due to the higher order EW corrections as a function of true dilepton invariant mass.

5.1.4 Uncertainties Due to the Photon-Induced Process

In this analysis, the photon-induced background is used due to the better description at high $|\cos\theta^*|$. In order to assess the systematic uncertainty due to PI contributions, the ratio between PI+DY and DY MC samples is investigated. The ratio is provided as a function of dimuon invariant mass, also for forward and backward events separately. These distributions are shown in Fig. 5.5. An arbitrary choice is made to vary the PI contribution by 100% to assess the uncertainty which is based on the expectation that the MC sample we use already corresponds to an overestimate of the effect.

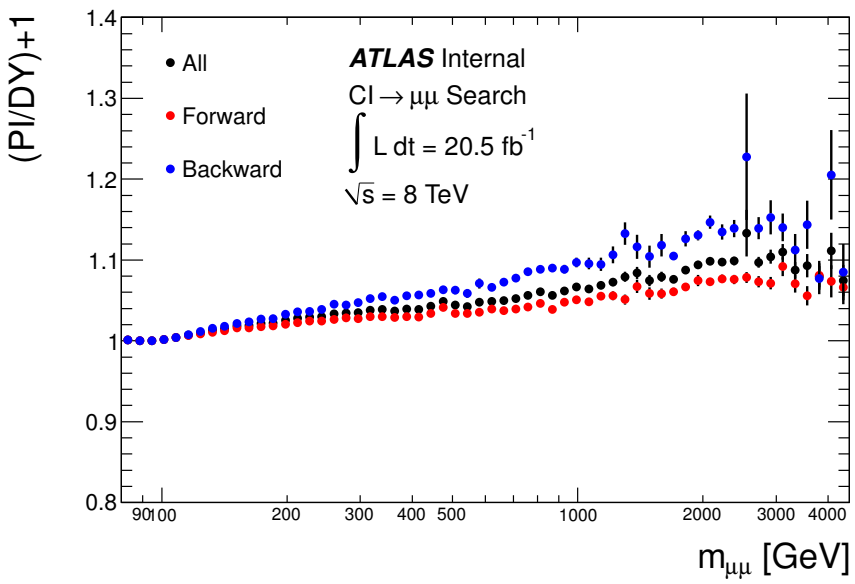

Figure 5.5: The effect of including the photon-induced MC in the dimuon non-resonant search, as a function of mass-only (black), and mass-cos θ^* for forward (red) and backward (blue) events.

5.1.5 Uncertainties Due to Z/γ^* Production Cross Section

A uniform uncertainty of 4%, due to the uncertainty on the Z/γ^* NNLO cross section in the normalization region is applied to the signal yield since it affects the signal normalization. This flat uncertainty is due to uncertainties in PDF variation, scale and α_S. These are obtained from the 90% C.L. MSTW2008NNLO PDF error set and by using VRAP for the calculation of the NNLO DY cross section in the normalization region.

5.2 Experimental Uncertainties

Experimental systematic uncertainties are applied both to the expected SM background and to the signal processes.

5.2.1 Uncertainties Due to Muon Reconstruction Efficiency

At p_{T} values above 300 GeV, the energy loss mostly comes from radiative loss (bremsstrahlung). That makes pattern recognition in the muon spectrometer difficult if an electromagnetic shower produced is sufficiently large and close to the muon spectrometer. This may result in mis-measuring the MS track parameters if some of the hits from the shower are wrongly associated with the muon tracks. This radiation affects the muon reconstruction efficiency and needs to be considered as a systematic uncertainty in the analysis. This issue becomes more relevant as the muon p_{T} increases.

5.2.2 Uncertainties Due to Muon Momentum Resolution

Since at high p_{T} the muon tracks are almost straight, any misalignment of the muon spectrometer chambers can lead to a mis-measurement of p_{T}. Hence, the biggest contribution to muon momentum resolution for high-p_{T} muons comes from the intrinsic resolution. The muon momentum resolution is discussed in detail in Section 3.5.2.

Corrections applied to the simulation to account for the differences in the description of the muon momentum resolution between data and MC are parametrized as shown in Eq. (3.11). Correction (smearing) parameters, which are basically the quadratic differences in the resolution parameters between data and simulation, have uncertainties associated with them. In order to investigate the effect of the muon momentum resolution uncertainty on background and signal expectations, two different methods are used. In both methods, the ratio between oversmeared (smearing parameters are shifted upwards by their uncertainty) and smeared dimuon mass distributions is used to determine the systematic uncertainty. In order to produce oversmeared distributions, extra smearing is applied on muons on top of the nominal

smearing performed using the official tool. The extra smearing is provided in two different ways.

The first method utilizes the specialized functions provided by the official MCP tool: `MuonMomentumCorrections-00-09-08`. The second directly applies a uniform extra 0.1 TeV^{-1} smearing to barrel muons and 0.2 TeV^{-1} to end-cap muons in addition to the nominal smearing provided by the official tool. The systematic uncertainty on the DY background is shown in Fig. 5.6 for the combined resolution systematic uncertainty obtained from the two different methods.

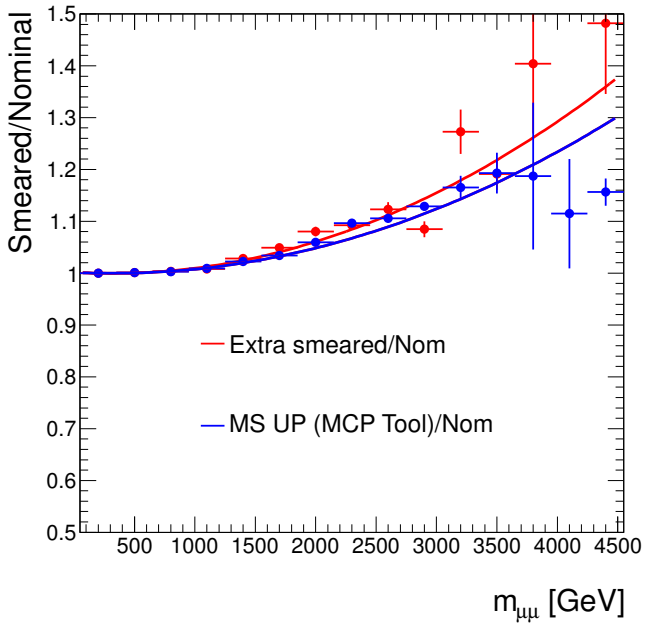

Figure 5.6: The ratio of extra smeared and nominal smeared invariant mass distributions. Additional flat smearing is shown with the red curve whereas additional smearing with the official tool is shown with the blue curve.

The impact of the muon momentum resolution uncertainty on the ADD signal estimate is shown in Figure 5.7.

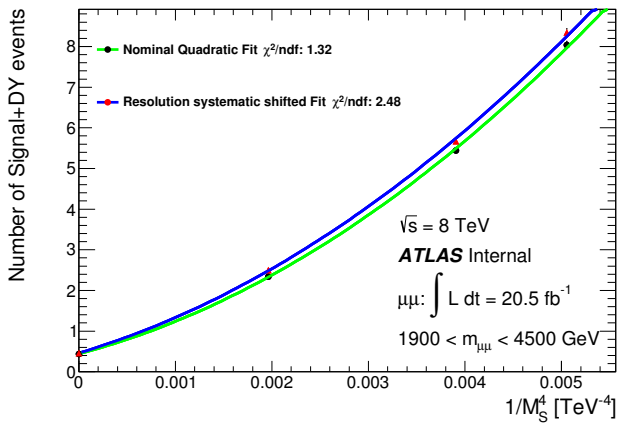

Figure 5.7: Uncertainty on the ADD signal estimate due to the muon resolution as a function of $1/M_s^4$.

5.2.3 Uncertainties Due to Muon Charge Misidentification

After the selection criteria are applied on each muon in the event, a dimuon pair is selected by requiring muons in the pair to be oppositely charged. If the charge of one of the muons is misidentified, the muons in the pair end up with the same charge and the opposite-sign charge requirement is not satisfied. This results in a decrease in the event selection efficiency. The percentage of misidentified muons is expected to be small since combined muons use independent measurement from the ID and MS. In order to quantify the impact of the systematic uncertainty due to muon charge misidentification, the study is performed by following the steps below:

- The object selection criteria are applied on muons in each event.
- Before selecting a muon pair in an event, truth matching is performed in order to find the associated true muon for a selected reconstructed muon.
- The charge of the reconstructed muon is compared to the charge of the corresponding true muon to check if the muon has a charge flip.
- The event rejection probability which is defined as the probability of one of the muons to have a charge flip so the event is rejected as a result of having

a same sign pair, is shown in Fig. 5.9 (left plot). It shows the ratio between number of events with one of the muons has a charge flip and the total number of events. It is as a function of the "truth" invariant mass in order to make a comparison between the relative efficiencies we have from mass binned DY samples generated in different true mass regions. The plot on the right shows 1-rejection probability, in other words, selection efficiency, which can be directly compared to the numbers in Table 5.1.

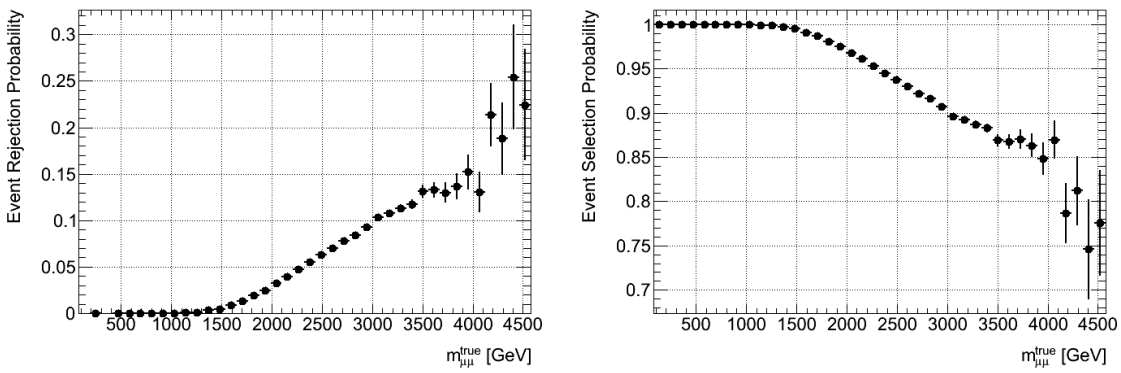

Figure 5.8: Event rejection probability (left) and event selection probability (right) due to muon charge misidentification.

- Dimuon invariant mass distribution of the DY process is produced as a function of true invariant mass by assigning 20% of the rejection probability as a systematic uncertainty. This distribution is then compared to the nominal distribution. Muon charge misidentification uncertainty is estimated to be $< 0.1\%$, $< 0.5\%$, and 1% for true dimuon mass of 1, 2, and 3 TeV, respectively, as seen from Fig. 5.9.

The systematic uncertainty due to muon charge misidentification is not taken into account since this uncertainty is folded into the uncertainty due to muon momentum resolution. As discussed above, extra smearing is applied on muons in order to quantify the muon momentum resolution uncertainty. Since q/p_{T} is smeared instead of p_{T},

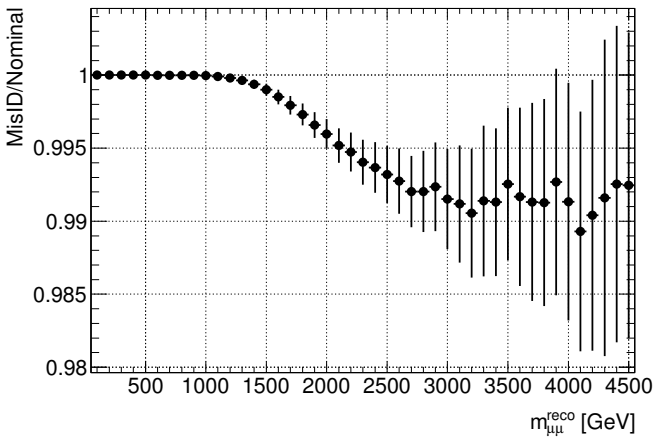

Figure 5.9: Muon charge identification efficiency as a function of reconstructed dimuon mass.

Table 5.1: The relative efficiencies due to the opposite-sign charge requirement calculated using mass binned DY samples.

$m_{\ell\ell}$ [GeV]	Relative Efficiency [%]
1000 – 1250	99.96
1250 – 1500	99.77
1500 – 1750	99.13
1750 – 2000	98.07
2000 – 2250	96.61
2250 – 2500	95.06
2500 – 2750	93.34
2750 – 3000	91.77
$\geq$ 3000	88.96

a charge flip is taken into account. Therefore, the possibility of a charge flip is covered by the muon momentum resolution uncertainty and not applied as a separate systematic uncertainty in the analysis.

5.2.4 Uncertainties Due to Beam Energy Scale

A beam energy at 4 TeV at the LHC is measured as $E_{4TeV} = 3988 \pm 5$ (stat) $\pm$ 26 (syst) GeV which shows that a systematic uncertainty on the LHC beam energy is

0.65%. This uncertainty mostly originates from an unexplained drift in measurements. The production cross section is calculated using VRAP by varying the beam energy up and down by its uncertainties. Then the ratio between the varied and nominal invariant mass distributions, shown in Fig. 5.10, are used to quantify the systematic uncertainty for signal and background. It can be as high as 5% at 3 TeV dilepton masses whereas the effect of this uncertainty for the signals on acceptance times efficiency is very small ($< 1\%$).

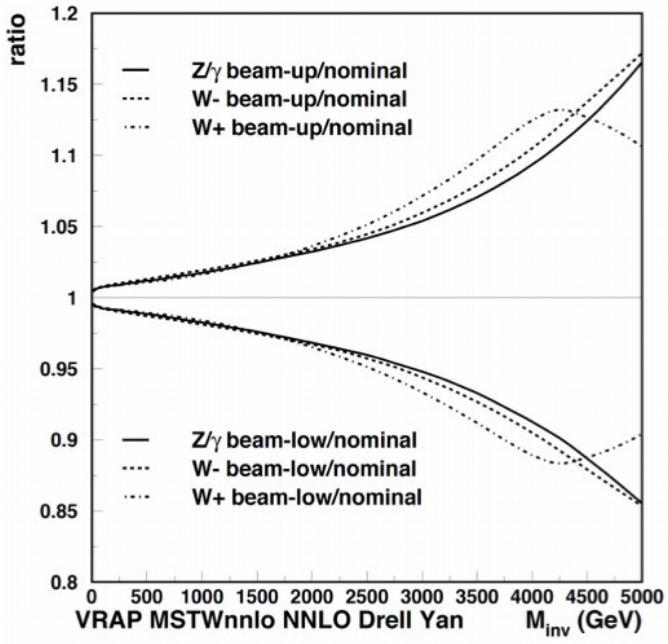

Figure 5.10: Experimental uncertainty due to LHC beam energy and effect on vector boson production rate.

5.2.5 Uncertainties Due to Monte Carlo Statistics

The limited MC statistics are taken into account as a source of systematic uncertainty. This uncertainty is considered for all background and signal samples. As similar to the treatment of other systematic uncertainties, shifted distributions are provided and by comparing them to the nominal ones, uncertainties due to the limited MC statistics are quantified.

Table 5.2: Quantitative summary of the systematic uncertainties taken into account for the expected number of events in the non-resonant dimuon analysis. Values are provided at three relevant benchmark dimuon masses of 1 TeV (2 TeV) [3 TeV]. NA indicates that the uncertainty is not applicable.

Source	Dimuons	
	Signal	Background
Normalization	4.0% (4.0%) [4.0%]	NA
PDF Variation	< 0.1% (< 0.1%) [0.1%]	5.0% (12.0%) [17.0%]
PDF Choice	NA	1.0% (6.0%) [12.0%]
α_S	NA	1.0% (3.0%) [4.0%]
EW Corrections	NA	1.0% (3.0%) [3.0%]
Photon-Induced	NA	6.5% (9.5%) [10.5%]
Efficiency	3.0% (6.0%) [9.0%]	3.0% (6.0%) [9.0%]
Scale/Resolution	1.0% (4.0%) [10.0%]	1.0% (4.0%) [10.0%]
Beam Energy	1.0% (3.0%) [3.0%]	2.0% (3.0%) [3.0%]
Statistical	3.0% (3.0%) [3.0%]	0.5% (0.5%) [0.5%]
Total	6.0% (9.3%) [14.7%]	9.2% (18.7%) [27.5%]

5.3 Summary of Systematic Uncertainties

Theoretical and experimental systematic uncertainties considered in this analysis have been described above. For each systematic uncertainty that is applied on the SM background, shifted histograms (reconstructed events weighted by the relevant uncertainty) of the DY process and nominal histograms are produced to be used in the statistical treatment. On the other hand, systematic uncertainties for the signal processes are parametrized as a function of a parameter of interest. Therefore, shifted and nominal signal parameterizations are fed into the limit calculation. All sources of systematic uncertainty are quantitively summarized in Table 5.2 at three benchmark dimuon mass values of 1 TeV, 2 TeV, and 3 TeV. A summary of systematic uncertainties is presented separately for forward and backward events in Table 5.3.

Table 5.3: Quantitative summary of the systematic uncertainties separated into those for forward and backward events. The uncertainties are taken into account for the expected number of events in the non-resonant dimuon analysis. Values are provided at three relevant benchmark dimuon masses of 1 TeV (2 TeV) [3 TeV]. NA indicates that the uncertainty is not applicable.

Source	Dimuon Channel Signal	
	Forward	Backward
Normalization	4.0% (4.0%) [4.0%]	4.0% (4.0%) [4.0%]
PDF Variation	$< 0.1\%$ ($< 0.1\%$) [0.1%]	$< 0.1\%$ ($< 0.1\%$) [0.1%]
PDF Choice	NA	NA
α_S	NA	NA
EW Corrections	NA	NA
Photon-Induced	NA	NA
Efficiency	3.0% (6.0%) [9.0%]	3.0% (6.0%) [9.0%]
Scale/Resolution	1.0% (4.0%) [10.0%]	1.0% (4.0%) [10.0%]
Beam Energy	1.0% (3.0%) [3.0%]	1.0% (3.0%) [3.0%]
Statistical	3.0% (3.0%) [3.0%]	3.0% (3.0%) [3.0%]
Total	6.0% (9.3%) [14.7%]	6.0% (9.3%) [14.7%]
Source	Dimuon Channel Background	
	Forward	Backward
Normalization	NA	NA
PDF Variation	4.0% (8.5%) [14.5%]	6.0% (15.0%) [19.0%]
PDF Choice	1.0% (6.0%) [12.0%]	1.0% (6.0%) [12.0%]
α_S	1.0% (3.0%) [4.0%]	1.0% (3.0%) [4.0%]
EW Corrections	1.0% (3.0%) [3.0%]	1.0% (3.0%) [3.0%]
Photon-Induced	5.0% (7.5%) [8.0%]	9.5% (13.5%) [14.0%]
Efficiency	3.0% (6.0%) [9.0%]	3.0% (6.0%) [9.0%]
Scale/Resolution	1.0% (4.0%) [10.0%]	1.0% (4.0%) [10.0%]
Beam Energy	2.0% (3.0%) [2.0%]	2.0% (3.0%) [3.0%]
Statistical	0.5% (0.5%) [0.5%]	0.5% (0.5%) [0.5%]
Total	7.6% (15.6%) [25.1%]	11.9% (22.9%) [30.2%]

CHAPTER 6

STATISTICAL ANALYSIS

This chapter begins with the discussion of the Bayes' Theorem. Then the methods that are used to check consistency between data and the SM expectation are discussed. Finally, the expected and observed limit setting procedures using a Bayesian approach and the limit inputs are described.

6.1 Bayesian Analysis

There are two separate approaches that can be followed when performing a statistical analysis: one can follow a frequentist approach or a Bayesian approach. The frequentist approach focuses on the probability of observing a certain set of data given a hypothesis. This approach treats data as random and restricts probabilities to outcomes of repeatable measurements. Bayesian statistics focuses on the probability of the hypothesis, given the data. This approach treats data as fixed and a hypothesis as random (the hypothesis might be true or false, with some probability between 0 and 1). The main idea of Bayesian statistics is to use subjective probability to quantify degree of belief in different models [101].

In this analysis, the observed event yields are compared to the expected event yields for different new physics model parameters. The significance of any observed excess is assessed using a Bayesian approach. In the absence of a signal, 95% C.L. lower exclusion limits are set on that parameter.

Bayes' Theorem was published by Thomas Bayes in 1763. Suppose A and B represent two outcomes to which probabilities are to be assigned. These may be

outcomes of a repeatable observation or hypotheses for which a degree of belief needs to be stated. As long as the probability of B, $P(B)$, is nonzero, the conditional probability of A given B, $P(A|B)$, can be defined as:

$$P(A|B) = \frac{P(A \cap B)}{P(B)}, \tag{6.1}$$

where $P(A \cap B)$ represents the probability that A and B are both true. Since A and B are arbitrary labels, as long as the probability of A, $P(A)$, is nonzero, the equation can be rewritten by reversing the labels:

$$P(B|A) = \frac{P(B \cap A)}{P(A)}, \tag{6.2}$$

whereas $P(B \cap A)$ represents the probability that B and A are both true. Since "A and B" is the same with "B and A", their probability equations are set equal and solved in order to obtain Bayes' Theorem:

$$P(A \cap B) = P(B \cap A), \qquad \text{which gives} \qquad \frac{P(A|B)}{P(A)} = \frac{P(B|A)}{P(B)}, \tag{6.3}$$

Hence, Bayes' Theorem is defined as:

$$P(A|B) = \frac{P(B|A)P(A)}{P(B)}. \tag{6.4}$$

where $P(A|B)$ is known as the "posterior probability" of A given B, $P(B|A)$ is known as the "likelihood" and can also be written as $\mathcal{L}(B|A)$. The likelihood is multiplied by $P(A)$, called the "prior probability", which reflects the degree of belief before any measurements are performed. In Bayesian analysis, there is no rule specified for prior probabilities. They might be based on previous measurements, physical intuition, etc. Generally, in physics analysis, uniform prior probabilities are used not because

they represent real prior judgements but because they provide a convenient point of reference. Integrating $P(B|A)$ over all values of A, in order to normalize $P(A|B)$ to unity, determines the constant of proportionality $1/P(B)$. Thus, P(B) in this equation is a normalization constant.

In the context of new physics searches, in a given bin, A denotes the number of expected events, also often written as μ, and B is the number of observed events, represented by n.

The number of expected events in a given search region is

$$\mu = n_s(\Theta, \nu) + n_b(\nu), \tag{6.5}$$

where Θ represents a set of parameters that defines a given model or hypothesis. In the CI analysis, Θ corresponds to the energy scale Λ and interference parameter η_{ij}, whereas in the ADD analysis it corresponds to a string scale M_S and specific formalism (GRW, Hewett, or HLZ). The quantity $n_s(\Theta, \nu)$ is the number of events predicted by the CI or ADD signal for a particular choice of model parameter Θ, whereas $n_b(\nu)$ is the total number of background events. In both cases ν represents the set of nuisance parameters that account for systematic uncertainties on the number of respective signal and background events.

Since the number of observed events follows a Poisson distribution, the likelihood of observing n events in one mass bin can be written as:

$$\mathcal{L}(n \mid \Theta, \nu) = \frac{\mu^n e^{-\mu}}{n!}. \tag{6.6}$$

Unlike the ADD analysis which is performed in a single mass bin, the CI analysis is performed in 12 separate bins correspond to a choice of two different $\cos\theta^*$ and 6 different mass bins since the background and the signal are not as clearly distinguished as they are in the ADD case. Consequently, Eq. (6.6) needs to be expanded to include

N_{bins} invariant mass bins. It can simply be written by taking the product of the Poisson probabilities for each mass bin k:

$$\mathcal{L}(n \mid \Theta, \nu) = \prod_{k=1}^{N_{bins}} \frac{\mu_k^{n_k} e^{-\mu_k}}{n_k!}. \tag{6.7}$$

According to Bayes' theorem, the posterior probability density function for the parameter Θ given n observed events is:

$$\mathcal{P}(\Theta \mid n, \nu) = \frac{1}{\mathcal{Z}} \mathcal{L}(n \mid \Theta, \nu) P(\Theta, \nu), \tag{6.8}$$

where $\mathcal{Z}$ normalizes the posterior probability density function. $P(\Theta, \nu)$ is the prior probability function and it depends on the new physics parameter Θ and the nuisance parameters $P(\Theta, \nu)$.

In order to marginalize the nuisance parameters and obtain a marginalized likelihood $\mathcal{L}_{\mathcal{M}}$, each Poisson distribution is convolved with a Gaussian probability distribution.

$$\mathcal{L}(n \mid \Theta, \nu) = \prod_{k=1}^{N_{bins}} \frac{\mu_k^{n_k} e^{-\mu_k}}{n_k!} \prod_{i}^{N_{sys}} Gaus(0, 1, \nu_i). \tag{6.9}$$

A multi-dimensional integral over the probability functions of the nuisance parameters is performed. As a result, the dependence on nuisance parameters is removed.

$$\mathcal{L}_{\mathcal{M}}(n \mid \Theta) = \int \mathcal{L}(n \mid \Theta, \nu_1, \nu_2, \nu_3, ...) d\nu_1 d\nu_2 d\nu_3 .... \tag{6.10}$$

After integrating out the nuisance parameters by taking the correlation of these parameters across all mass bins into account, the posterior can be rewritten as:

$$\mathcal{P}(\Theta \mid n) = \frac{1}{\mathcal{Z}} \mathcal{L}_{\mathcal{M}}(n \mid \Theta) P(\Theta) \tag{6.11}$$

The prior probability $P(\Theta)$ is chosen flat in either $1/\Lambda^2$ or $1/\Lambda^4$ in the CI analysis, or in $1/M_s^4$ or $1/M_s^8$ in the ADD analysis. In the absence of a signal, 95% C.L. limits are then found by performing the integration over the posterior and solving for Θ_{lim}:

$$\int_0^{\Theta_{lim}} \mathcal{P}(\Theta \mid n) d\Theta = 0.95, \tag{6.12}$$

where Θ is chosen as $1/\Lambda^2$ or $1/\Lambda^4$ in the CI analysis, $1/M_s^4$ or $1/M_s^8$ in the ADD analysis. The calculations given above are performed with the Bayesian Analysis Toolkit (BAT) [102], which uses a Markov Chain Monte Carlo (MCMC) technique to integrate over the nuisance parameters.

6.2 Consistency Check Between Data and SM

In order to check the consistency between the data and the SM expectation, the log-likelihood ratio (LLR) between the signal+background and pure background hypotheses obtained in the data is compared to the results of pseudo-experiments. The log-likelihood ratio is the log of the ratio between the likelihood computed for the signal+background hypothesis and the likelihood for the background hypothesis only. It is the best discriminant between two hypotheses (in this case between signal+background and background-only hypotheses) according to the Neyman-Pearson Lemma.

To construct the background-only likelihood for the data, Eq. (6.7) is used by taking μ_k as the number of SM-only events from simulation and n_k as the number of observed events, in each mass bin k. The same calculation is done for each of the pseudo-experiments by pulling out the value of n_k from the Poisson-distributed background-only function. For the SM expectation, 1000 pseudo-experiments are performed. The signal+background likelihood is constructed by taking μ_k as the number of signal+background events and evaluated at the Λ ($M_{\rm S}$) value that maximizes the

likelihood for the CI (ADD) analysis. The background-only likelihood is chosen as the likelihood at Θ=0. Then the negative log-likelihood ratio is calculated for the data and for each of the pseudo-experiments. The p-value is derived by taking the ratio of the integral from the value of the log-likelihood in data to infinity relative to the total integral of the pseudo-experiments. The p-value corresponds to the probability of observing a fluctuation in the pseudo-experiments that is as or more signal like than that seen in data, when assuming only the SM background:

$$\text{p-value} = P(LLR_{PE} \geq LLR_{data} \mid \text{SM only}). \tag{6.13}$$

The common convention in particle physics is that a p-value $< 1.35 \times 10^{-3}$ corresponds to evidence for a signal, whereas a p-value $< 2.87 \times 10^{-7}$ is considered a "discovery". These values are the one-sided integrals of the tails of a unit Gaussian distribution beyond $+3\sigma$ and $+5\sigma$, respectively.

6.3 Bayesian Limit Setting

6.3.1 Choice of Prior

The prior probability function can be written as $P(\Theta|\nu) = P(\Theta)P(\nu)$ and $P(\Theta)$ is chosen as flat in Θ. $P(\nu)$ is taken as a set of normalized Gaussian distributions each corresponding to one of the systematic uncertainties considered in this analysis. The posterior dependence on ν is integrated out with 100000 iterations of the MCMC.

The choice of prior is performed by studying the relative impact of the interference and pure CI terms in Eq. (1.43) that defines the differential cross section of the CI process. The relative impact of these terms depends on both the dilepton mass and Λ. The term with $1/\Lambda^2$ is the interference term and becomes increasingly dominant when the DY and new physics contributions are of similar magnitudes and its impact is maximum when both contributions are equal. When $\Lambda \to \infty$, the cross section

looks like DY-only. The term with $1/\Lambda^4$, on the other hand, denotes the pure CI contribution. It is dominant at high mass since the DY contribution decreases more quickly than the CI contribution. Hence, there is no special reason for choosing any of these terms over the other one so both of them are used. Therefore, for the CI analysis, priors flat in either $1/\Lambda^2$ or $1/\Lambda^4$ are chosen and the limits are provided with both priors.

In the ADD analysis, as similar to the CI case, a role of both interference and new physics terms is studied. Unlike the situation with the CI case, interference effects between the DY and virtual KK graviton processes are small due to the dominance of gluon-induced over quark-induced dilepton production by virtual KK gravitons. Nevertheless, priors flat in either $1/M_S^4$ or $1/M_S^8$ are chosen in the ADD analysis.

6.3.2 Limit Setting Procedure

Since signal samples are generated for only five benchmark Λ (M_S) values for the CI (ADD) analysis, counting events in each search bin is performed only for these Λ (M_S) values. These are not enough for posterior calculations since for any random value of Λ (M_S), the total number of expected events (N^{exp}) is not available.

For the construction of the posterior for an arbitrary Θ value, it is necessary to fit the available numbers of expected events at fixed Θ values. The fits are performed according to the theoretical dependence of the differential cross section as a function of the parameter of interest, according to Eqs. (6.14) and (6.15) for the CI and ADD models, respectively.

$$N^{exp}(\Lambda) = c_0 + \frac{c_1}{\Lambda^2} + \frac{c_2}{\Lambda^4}, \tag{6.14}$$

$$N^{exp}(M_{\mathrm{S}}) = d_0 + \frac{d_1}{M_{\mathrm{S}}^4} + \frac{d_2}{M_{\mathrm{S}}^8}. \tag{6.15}$$

These fits are performed in each signal mass-$\cos\theta^*$ bin (12 search bins in total) for the CI analysis and in a single mass bin for the ADD analysis.

When $\Lambda \to \infty$ or $M_S \to \infty$ (so $\Theta \to 0$), N^{exp} corresponds to the number of SM-only events. Thus, the constant c_0 or d_0 gives the SM expectation. In the ADD analysis, $N^{exp}(\Theta = 0)$ is obtained using an ADD signal sample with a very high M_S value, 50 TeV. For such a high value of M_S, the dilepton mass spectrum does not deviate from the pure DY prediction.

Examples of signal parameterizations can be found in Figs. 6.1 and 6.2 for the CI and ADD analyses, respectively. A complete set of parameterizations is included in Appendix D. As seen from the signal parameterization for the CI search, DY+CI events are fitted and the non-DY background is not included here. Next section discusses in more detail the way in which these parameterizations are used in the statistical analysis.

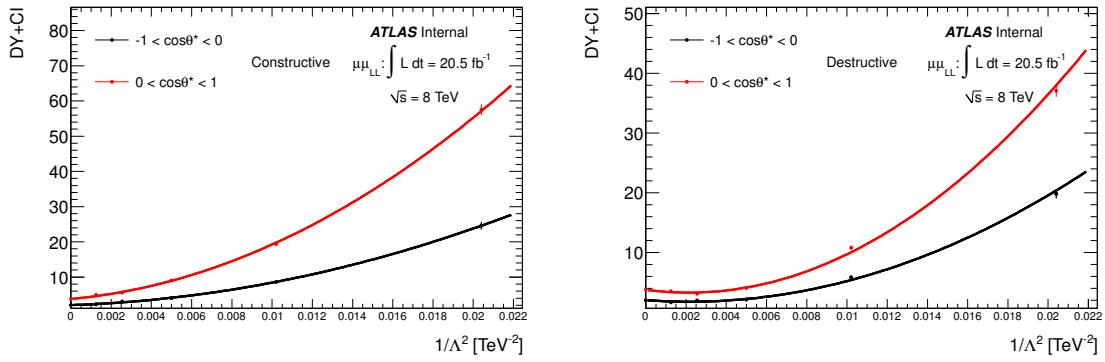

Figure 6.1: Number of DY+CI events in each of the $\cos\theta^*$ bin in the mass bin from 1200 GeV to 1800 GeV for the contact interaction LL model as a function of $1/\Lambda^2$ for the constructive (destructive) interference case is shown on the left (right).

The fit functions are then used to calculate the likelihood:

$$\mathcal{L}(n \mid \Theta) = \prod_{k=1}^{N_{bins}} \frac{N_k^{exp}(\Theta)^{n_k} \cdot e^{-N_k^{exp}(\Theta)}}{n_k!}. \tag{6.16}$$

Finally, the posterior probability is calculated by taking the prior probability as flat in either $1/\Lambda^2$ or $1/\Lambda^4$ for the CI model and in either $1/M_S^4$ or $1/M_S^8$ for the ADD model. The limit is set on Θ according to the Bayesian method.

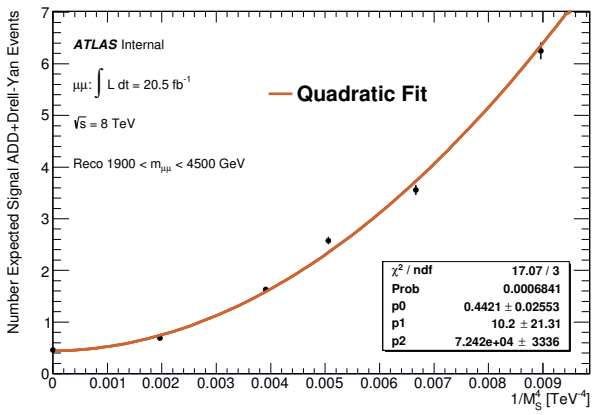

Figure 6.2: Number of expected events in a single mass bin from 1900 GeV to 4500 GeV for the GRW formalism as a function of $1/M_S^4$.

When calculating the observed limit, n_k is the number of observed events and N_k^{exp} is the total number of expected events for signal and background processes in each mass bin k. The likelihood is calculated many times with a corresponding variation in the number of expected events via Eq. (6.14) (Eq. (6.15)) for the CI (ADD) model, whereas n_k is always the same for a given search bin. Using the distribution of these likelihood values as a function of Θ and using Eq. (6.12), the observed limit is calculated.

When calculating the expected limit, only the events from simulation are used, as opposed to using data in the observed limit calculation. Thus, for the expected limit calculation, n_k is the number of SM background events and N_k^{exp} is the number of signal+background events. By taking steps in Θ and following the same procedure used in the observed limit calculation, a limit value is calculated. Due to the uncertainty on the SM background, this limit calculation is repeated 1000 times by pulling out a value of n_k for a given bin each time from the Poisson-distributed function of background-only events. Therefore, 1000 limits are obtained as a result of performing 1000 pseudo-experiments (as opposed to having only one observed limit). The expected limit is set by taking the median of these limit values, then converting

this value to the limit on the parameter of the new physics model chosen (Λ in CI analysis, M_S in ADD analysis).

6.3.3 Inputs for the Limit Calculation

In this analysis, the limit calculation is performed using BAT. Inputs for the limit calculation, that are fed into BAT are:

- Signal parameterizations are provided in order to obtain the number of DY+CI events at any value of Θ chosen.
- The number of SM-only events in each search bin defined is provided.

Adding the expected number of pure signal events obtained from the signal parameterizations to the number of SM-only events, the total number of expected events is obtained.

Systematic uncertainties that are incorporated in the likelihood are calculated in BAT. Inputs which are provided to BAT for the calculation of systematic uncertainties are discussed below:

- Signal parameterizations including DY+CI processes are shifted by each of the systematic uncertainties relevant for the signal processes. Using the ratio between shifted and nominal signal parameterizations, BAT assessed the systematic uncertainties in terms of Θ.
- Since the impact of systematic uncertainties in the non-DY contribution is negligible, only the systematic uncertainties in the DY contribution are taken into account (except for the MC statistics uncertainty). Therefore, the number of DY-only events as well as the number of DY-only events shifted by each of the relevant systematic uncertainties are provided.

- The systematic uncertainty due to the limited MC statistics is applied to all SM backgrounds as opposed to the other uncertainties applied only to the DY background. In order to quantify its impact on the signal, event counts that are shifted by their statistical uncertainty are fitted and the shifted signal parameterizations are obtained. These are then compared to the nominal parameterization.

CHAPTER 7

RESULTS

This chapter presents the results for the contact interaction and ADD large extra dimension searches. The combination of limits with the electron channel is also discussed.

7.1 Contact Interaction Search Results

For the CI search, results are presented using a search in both invariant mass and $\cos\theta^*$. In order to check consistency between data and the SM expectation, as discussed in Section 6.2, 1000 SM-like pseudo-experiments are generated. The log-likelihood ratios calculated both for data and the SM background are compared to each other. Distributions of the negative log-likelihood ratio for all pseudo-experiments and also for the observed results are shown in Fig. 7.1 for the LL CI model. Same distributions for the LR and RR CI model can be found in Figs. E.1 and E.2 of Appendix E, respectively.

Good agreement is observed between the data and expected background yields. This can be seen from Tables 4.3 and 4.4 for different signal regions.

The most significant deviation from the expected background is seen with a p-value of 8% in the LL model with destructive interference given the $1/\Lambda^2$ prior. A full list of p-values is shown in Table E.1 of Appendix E.

Since no significant excess of data is observed above the SM background, the analysis proceeds by setting expected and observed 95% C.L. lower exclusion limits on Λ. The results are provided for both choices of priors: $1/\Lambda^2$ and $1/\Lambda^4$ priors. In order

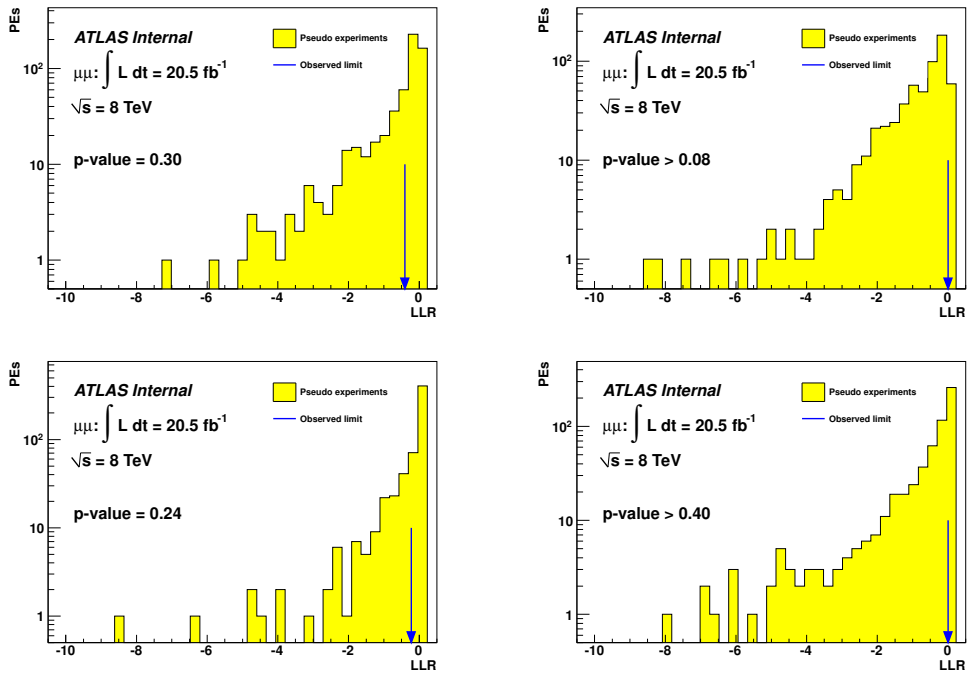

Figure 7.1: Expected and observed negative log-likelihood distributions for the LL contact interaction model, for constructive (plots on the left) and destructive interference (plots on the right). All systematic uncertainties are taken into account, and a uniform positive prior in $1/\Lambda^2$ ($1/\Lambda^4$) for the plots on the top (bottom) is used with the 2D search approach.

to compute expected limits, a set of 1000 pseudo-experiments are performed. The median of these pseudo-experiments is taken to be the expected limit. The expected limit distributions are shown in Fig. 7.2 for the LL CI model. Same distributions for the LR and RR CI model can be found in Figs. E.3 and E.4 of Appendix E, respectively.

The posterior distributions from which the observed limits are calculated are shown in Fig. 7.3 for the LL CI model. Same distributions for the LR and RR CI model can be found in Figs. E.5 and E.6 of Appendix E, respectively.

The resulting expected and observed limits are presented in Table 7.1 and also displayed graphically in Fig. 7.4. These limits are the most stringent to date. The CMS experiment recently quoted the lower limits on Λ for the LL CI model, using the 2012 data at $\sqrt{s} = 8$ TeV, corresponding to an integrated luminosity of 20.6 fb^{-1} in

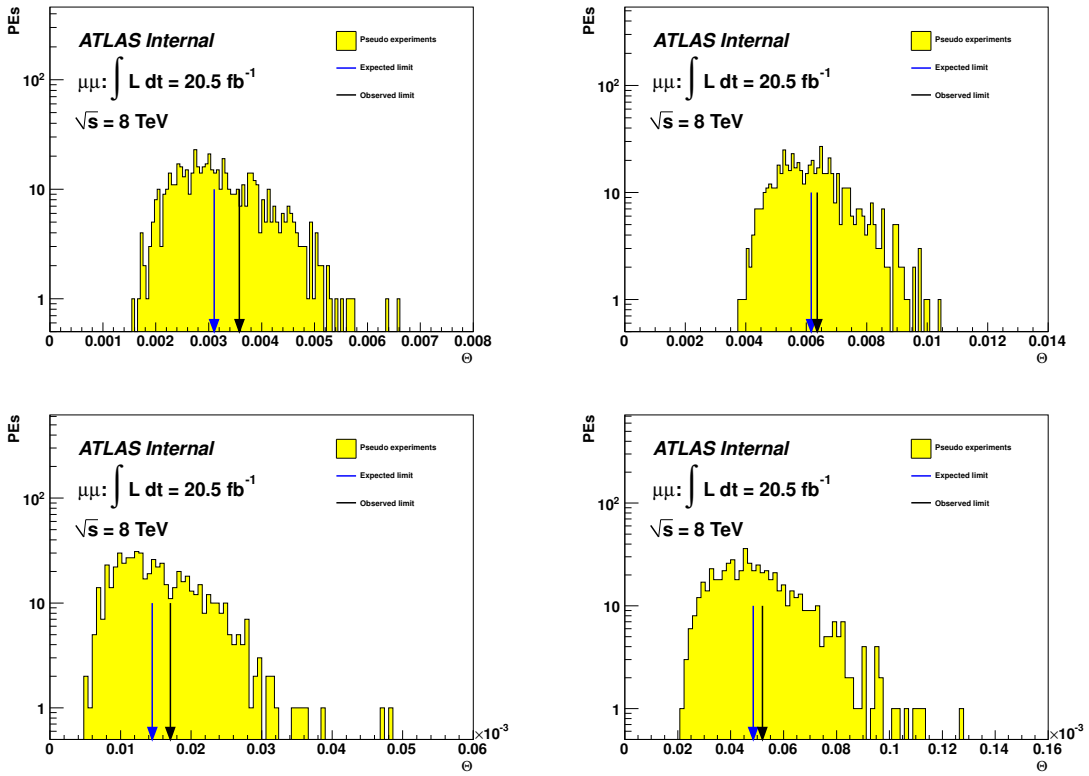

Figure 7.2: Distribution of expected limit values from pseudo-experiments for the LL contact interaction model, for constructive (plots on the left) and destructive (plots on the right) interference. A uniform positive prior in $1/\Lambda^2$ ($1/\Lambda^4$) for the plots on the top (bottom) is used. All systematic uncertainties are taken into account. These results are derived using the 2D search approach. The blue arrow indicates the median limit and the black arrow shows the observed limit.

the dimuon channel [39]. These observed (expected) lower limits are 15.2 TeV (16.9 TeV) for constructive interference and 12.0 TeV (13.0 TeV) for destructive interference whereas the lower limits from the analysis presented here are 16.7 TeV (18.0 TeV) for constructive interference and 12.5 TeV (12.7 TeV) for destructive interference. Thus, the limits from this analysis are ∼1 TeV stronger than the limits from the CMS experiment.

In this analysis, angular information is added for the first time in a search at the LHC. Different chirality models for the CI is also studied for the first time in addition to the LL CI model which is always considered as a benchmark model for CI searches.

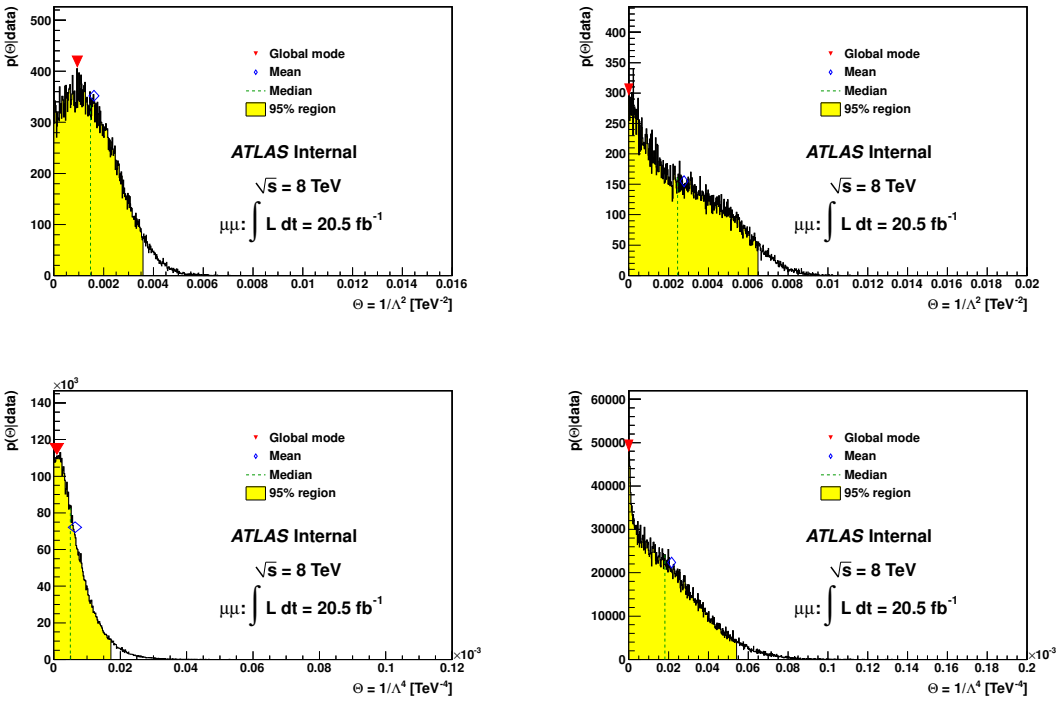

Figure 7.3: Posterior distributions for the LL contact interaction model, for constructive (plots on the left) and destructive (plots on the right) interference. A uniform positive prior in $1/\Lambda^2$ ($1/\Lambda^4$) for the plots on the top (bottom) is used. All systematic uncertainties are taken into account. These results are derived using the 2D search approach.

Limits are approximately 3 TeV stronger for the LR model comparing to the limits for the LL and RR models, which is as expected since the sensitivity gain from the angular information is the largest for the LR model. Also, limits become weaker with a prior flat in $1/\Lambda^4$. The decrease in the expected limit is approximately 2 TeV and 1 TeV for constructive and destructive cases, respectively.

7.2 Large Extra Dimensions Search Results

For the ADD search, results are presented using a single mass bin from 1900 to 4500 GeV. As for the CI analysis, consistency between data and the SM expectation is checked by performing 1000 SM-like pseudo-experiments. The log-likelihood ratios calculated both for data and the SM background are compared to each other. Distri-

Table 7.1: Expected and observed 95% C.L. lower exclusion limits on Λ for the LL, LR, and RR contact interaction search using a uniform positive prior in $1/\Lambda^2$ or $1/\Lambda^4$. Limits are shown for both the constructive and destructive interference cases.

Expected and observed lower limits on Λ [TeV]							
Channel	Prior	Left-Left		Left-Right		Right-Right	
		Const.	Destr.	Const.	Destr.	Const.	Destr.
Expected	$1/\Lambda^2$	18.0	12.7	21.6	16.3	17.7	13.0
Observed		16.7	12.5	20.5	14.9	16.5	12.7
Expected	$1/\Lambda^4$	16.2	12.0	19.8	15.3	16.2	12.1
Observed		15.6	11.8	19.0	14.3	15.4	11.9

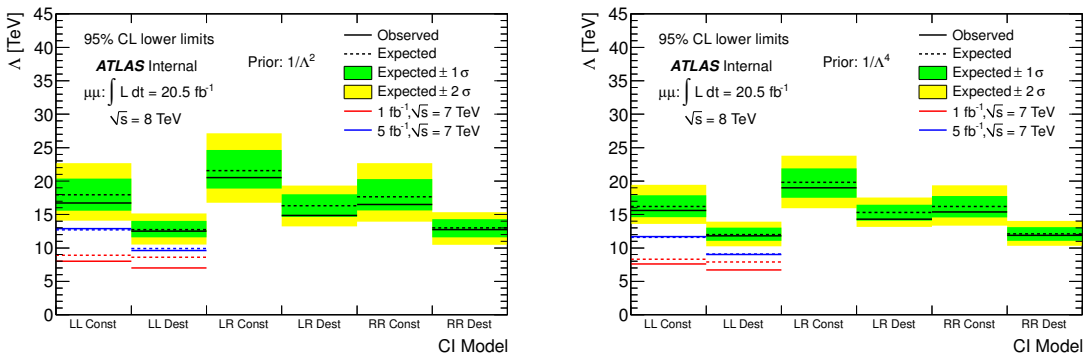

Figure 7.4: Summary of 95% C.L lower exclusion limits on Λ for the dimuon contact interaction search, using a positive prior in $1/\Lambda^2$ (left) and in $1/\Lambda^4$ (right). Previous ATLAS search results are also presented for comparison. Exclusion limits were previously only set on the LL model.

butions of the negative log-likelihood ratio for all pseudo-experiments and also for the observed results are shown in Fig. 7.5 for the GRW formalism. Same distributions for the HLZ n=2 formalism can be found in Fig. E.7 of Appendix E.

In the ADD search, as seen from Table 4.5, the number of expected events is 0.54 whereas the number of observed events is 0. The most significant excess is observed with a p-value of 6% in the GRW formalism for the $1/M_S^4$ prior whereas for the $1/M_S^8$

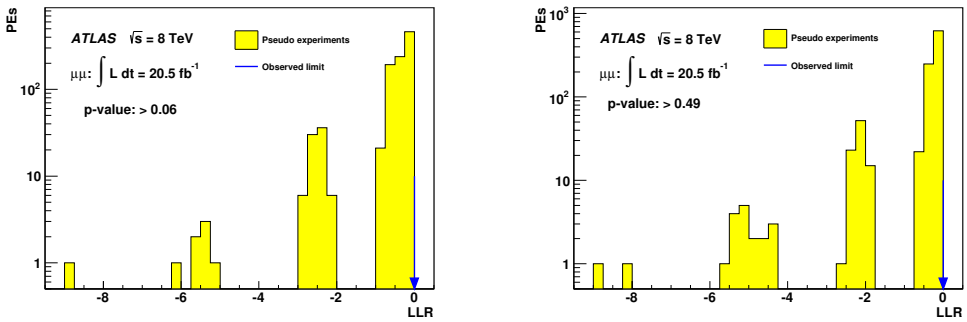

Figure 7.5: Negative log-likelihood distribution resulting from pseudo-experiments with fluctuations on the number of expected SM-only events for the ADD model with GRW formalism with a uniform positive prior in $1/M_S^4$ (left) and $1/M_S^8$ (right).

prior the derived p-value is 49%. These values indicate that there is no significant evidence for new physics in the ADD signal region and thus 95% C.L lower exclusion limits are set on the string scale M_S. The results are provided both $1/M_S^4$ and $1/M_S^8$ priors. In order to compute expected limits, a set of 1000 pseudo-experiments are performed. The median of these pseudo-experiments is taken to be the expected limit. The expected limit distributions are shown in Fig. 7.6.

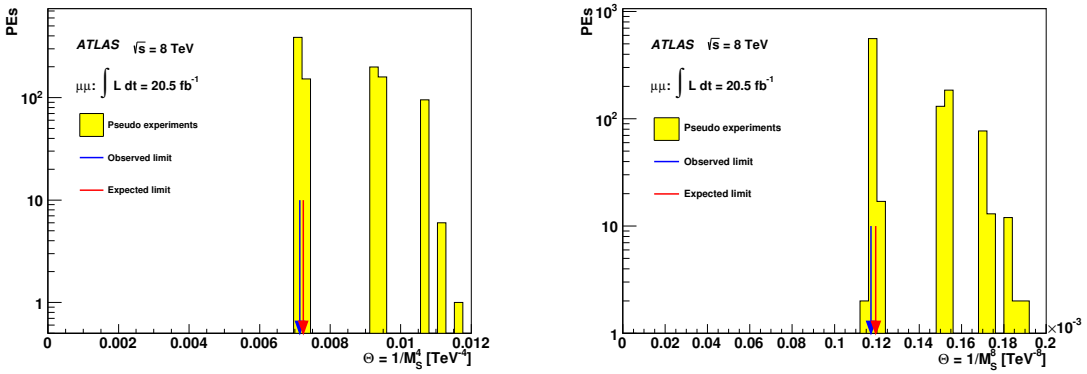

Figure 7.6: Distribution of expected limit values from pseudo-experiments in the muon channel for the GRW ADD model assuming a $1/M_S^4$ (left), and $1/M_S^8$ (right), uniform positive prior. The results take all systematic uncertainties into account. The red arrow indicates the median limit.

The observed limits in the ADD search are well within the range of expected limits. The corresponding posterior distributions are shown in Fig. 7.7 for the GRW

formalism. Same distributions can be found for the HLZ n=2 formalism in Fig. E.8 of Appendix E.

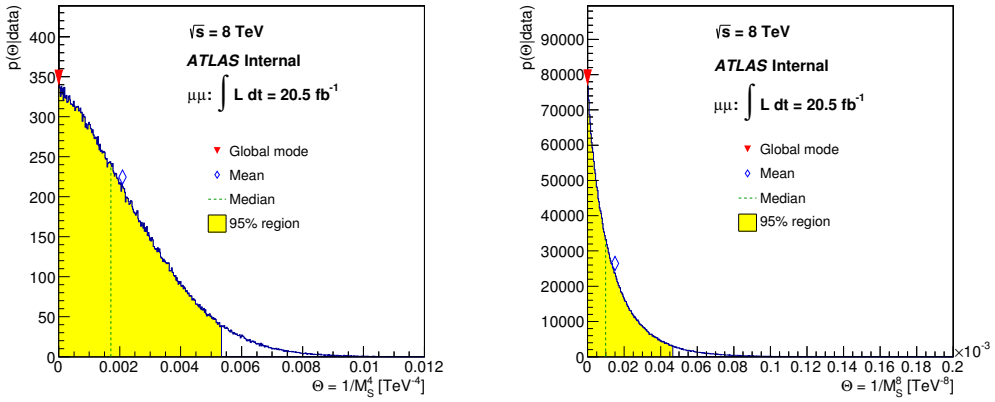

Figure 7.7: Posterior pdf distributions for the GRW ADD model, with a uniform positive prior in $\Theta = 1/M_S^4$ (left) and $\Theta = 1/M_S^8$ (right).

The results are obtained using the GRW formalism. These results are then translated into the HLZ and Hewett formalisms using Eq. (1.47). For the special case of HLZ with n=2, which has a different dependence on the dilepton mass than the other models, conversion of GRW results is not trivial to perform. Thus, dedicated MC samples are generated and subjected to the same analysis and statistical interpretation as the GRW formalism. All results are presented in Table 7.2 and are also displayed graphically in Fig. 7.8. These limits are the most stringent to date. The recent observed (expected) limits from the CMS experiment [54, 55] are 3.64 (3.65) TeV for the GRW formalism whereas in the analysis presented here observed (expected) limits are calculated as 3.73 (3.72) TeV. Thus, the limits are stronger than those from the CMS Collaboration. Using a prior flat in $1/M_S^8$ rather than in $1/M_S^4$ weakens the limits by approximately 0.2 TeV.

Table 7.2: Expected and observed 95% CL lower exclusion limits on M_S including systematic uncertainties, for ADD signal in the GRW, Hewett and HLZ formalisms.

Expected and Observed Limit on M_S [TeV]									
Channel	Prior	GRW	Hewett	HLZ					
				n= 2	n=3	n=4	n=5	n=6	n=7
Expected	$1/M_S^4$	3.7	3.3	3.4	4.4	3.7	3.4	3.1	3.0
Observed		3.7	3.3	3.4	4.4	3.7	3.4	3.1	3.0
Expected	$1/M_S^8$	3.5	3.1	3.1	4.2	3.5	3.2	3.0	2.8
Observed		3.5	3.1	3.1	4.2	3.5	3.2	3.0	2.8

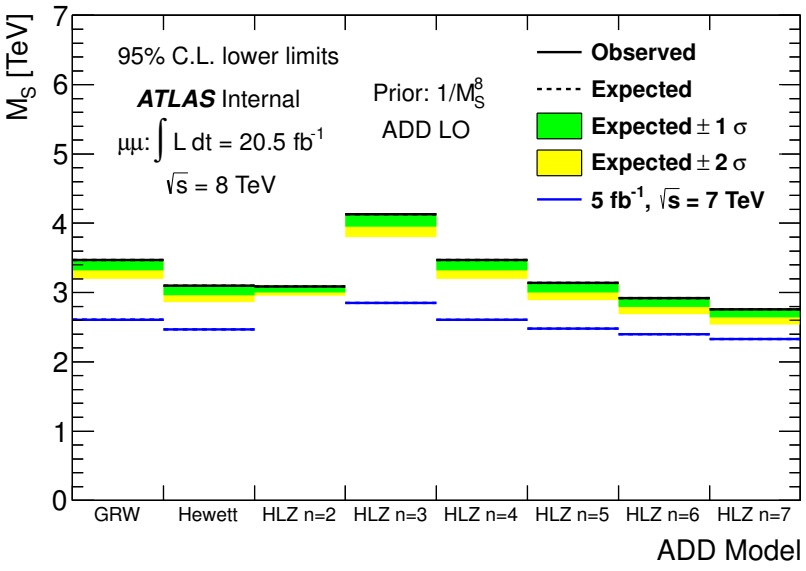

Figure 7.8: Summary of 95% C.L lower exclusion limits on M_S for the dimuon ADD large extra dimensions search, using a positive prior in $1/M_S^8$. Previous ATLAS search results are also presented for comparison. Exclusion limits were not previously set on the HLZ n=2 ADD model.

7.3 Combination of Limits with the Electron Channel

Assuming lepton universality, limits obtained for the muon channel are combined with the results for the electron channel both for CI and ADD searches. The likelihood given in Eq. (6.7) can be rewritten when channel combinations are considered:

$$\mathcal{L}(n \mid \Theta, \nu) = \prod_{l=1}^{N_{channel}} \prod_{k=1}^{N_{bin}} \frac{\mu_{lk}^{n_{lk}} e^{-\mu_{lk}}}{n_{lk}!}, \tag{7.1}$$

where, n_{lk} is the number of events observed in data, and μ_{lk} is the total number of expected events (signal plus background), both in mass bin k and channel l. According to Bayes' theorem, the posterior probability for the parameter Θ given n observed events is then calculated according to Eq. (6.8). When integrating out the nuisance parameters, systematic uncertainties that must be treated as correlated or uncorrelated between two channels are taken into account by the BAT. Sources of systematic uncertainties that are treated as correlated are: PDF, electroweak K-factor, photon-induced, beam energy and Z/γ^* cross section. All other sources are treated as uncorrelated.

Good agreement is observed between the data and expected background predictions in both CI and ADD searches. The derived p-values are included in Table E.2 and E.3 of Appendix E for the CI and ADD analyses, respectively. In neither case is the deviation significant. The expected and observed 95% C.L. lower exclusion limits are set on the parameter of interest in each search, with the resulting limits for the CI and ADD searches presented in Tables 7.3 and 7.4 respectively, including conversions to other formalisms. These results are also displayed graphically in Figs. 7.9 and 7.10 for the CI and ADD analyses, respectively. These limits are the most stringent to date. The CMS experiment recently released the combined observed lower limits on Λ for the LL model, using the 2012 data at $\sqrt{s} = 8$ TeV, corresponding to an integrated luminosity of 20.6 (19.7) fb^{-1} for the dimuon (dielectron) channel [39]. These observed lower limits are 16.9 TeV for constructive interference and 13.1 TeV for destructive interference in the dilepton channel whereas in the analysis presented here combined observed limits are calculated as 21.6 TeV for constructive interference and 17.2 TeV for destructive interference. Therefore, the combined CI limits calculated

in this analysis for the LL model are much stronger ($\sim$4 TeV) than the ones obtained by the CMS Collaboration.

In the ADD search, numbers of expected events are 0.54 in the muon channel and 0.61 in the electron channel whereas in both channels numbers of observed events are 0. This small number of expected SM background events in the ADD search, which is due to the high mass threshold chosen, leads to similar expected and observed exclusion limits within the separate channels. Thus, a large fraction of the pseudo-experiments return a result of zero expected events so the median value that is taken as the expected limit gives also zero expected events. For the combined dilepton channel, the total number of expected SM background events is large enough that a wider range of limits is obtained in the ensemble of pseudo-experiments and the slight data deficit translates into stronger observed limits (4.2 TeV) than expected (4.0 TeV). The most recent observed (expected) limit on M_{S} that the CMS experiment announced is 4.01 (4.00) TeV. Again in the combined case, stronger limits comparing to the ones from the CMS experiment are quoted.

Table 7.3: Expected and observed 95% C.L. lower exclusion limits on Λ for the LL, LR, and RR contact interaction search using a uniform positive prior in $1/\Lambda^2$ or $1/\Lambda^4$. The dielectron, dimuon, and combined dilepton channel limits are shown for both the constructive and destructive interference cases.

Expected and observed lower limits on Λ [TeV]							
Channel	Prior	Left-Left		Left-Right		Right-Right	
		Const.	Destr.	Const.	Destr.	Const.	Destr.
Exp: ee	$1/\Lambda^2$	19.1	14.0	22.0	17.4	19.0	14.2
Obs: ee		20.7	16.4	25.2	19.2	20.2	16.6
Exp: ee	$1/\Lambda^4$	17.4	13.0	20.1	16.3	17.2	13.1
Obs: ee		18.6	14.7	22.2	17.7	18.3	14.9
Exp: $\mu\mu$	$1/\Lambda^2$	18.0	12.7	21.6	16.3	17.7	13.0
Obs: $\mu\mu$		16.7	12.5	20.5	14.9	16.5	12.7
Exp: $\mu\mu$	$1/\Lambda^4$	16.2	12.0	19.8	15.3	16.2	12.1
Obs: $\mu\mu$		15.6	11.8	19.0	14.3	15.4	11.9
Exp: $\ell\ell$	$1/\Lambda^2$	21.4	14.7	24.8	18.5	21.0	15.0
Obs: $\ell\ell$		21.6	17.2	26.3	19.0	21.1	17.5
Exp: $\ell\ell$	$1/\Lambda^4$	19.1	13.8	23.1	17.6	19.1	14.2
Obs: $\ell\ell$		19.6	15.4	23.8	17.8	19.3	15.6

Table 7.4: Expected and observed 95% C.L. lower exclusion limits on M_S, using a uniform positive prior in $1/M_S^4$ or $1/M_S^8$. The dielectron, dimuon, and combined dilepton channel limits are shown for ADD signal in the GRW, Hewett and HLZ formalisms.

Expected and observed lower limits on M_S [TeV]									
Channel	Prior	GRW	Hewett	HLZ					
				$n=2$	$n=3$	$n=4$	$n=5$	$n=6$	$n=7$
Exp: ee	$1/M_S^4$	4.0	3.5	3.6	4.7	4.0	3.6	3.3	3.1
Obs: ee		4.0	3.5	3.6	4.7	4.0	3.6	3.3	3.1
Exp: ee	$1/M_S^8$	3.7	3.3	3.1	4.4	3.7	3.4	3.1	3.0
Obs: ee		3.7	3.3	3.1	4.4	3.7	3.4	3.1	3.0
Exp: $\mu\mu$	$1/M_S^4$	3.7	3.3	3.4	4.4	3.7	3.4	3.1	3.0
Obs: $\mu\mu$		3.7	3.3	3.4	4.4	3.7	3.4	3.1	3.0
Exp: $\mu\mu$	$1/M_S^8$	3.5	3.1	3.1	4.2	3.5	3.2	3.0	2.8
Obs: $\mu\mu$		3.5	3.1	3.1	4.2	3.5	3.2	3.0	2.8
Exp: $\ell\ell$	$1/M_S^4$	4.0	3.6	3.9	4.8	4.0	3.6	3.4	3.2
Obs: $\ell\ell$		4.2	3.8	4.2	5.0	4.2	3.8	3.6	3.4
Exp: $\ell\ell$	$1/M_S^8$	3.8	3.4	3.5	4.6	3.8	3.5	3.2	3.1
Obs: $\ell\ell$		4.0	3.6	3.7	4.7	4.0	3.6	3.4	3.2

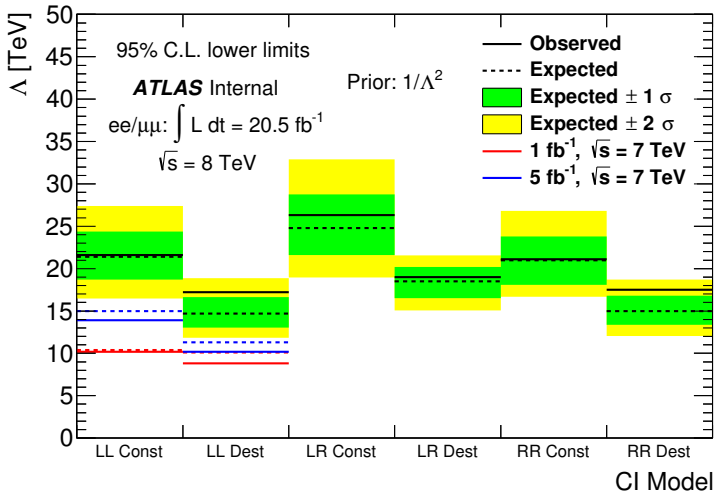

Figure 7.9: Summary of 95% C.L lower exclusion limits on Λ for the combined dilepton contact interaction search, using a positive prior in $1/\Lambda^2$. Previous ATLAS search results are also presented for comparison. Exclusion limits were previously only set on the LL model.

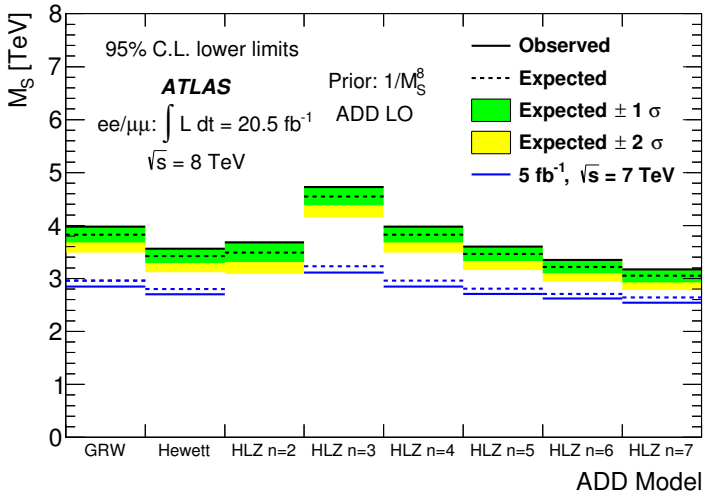

Figure 7.10: Summary of 95% C.L lower exclusion limits on M_S for the dimuon ADD large extra dimensions search, using a positive prior in $1/M_S^8$. Previous ATLAS search results are also presented for comparison. Exclusion limits were not previously set on the HLZ n=2 ADD model.

CHAPTER 8

CONCLUSIONS

A search for contact interactions and large extra dimensions has been performed in dimuon events produced in LHC proton-proton collisions at $\sqrt{s} = 8$ TeV. The data sample corresponds to an integrated luminosity of 20.5 fb^{-1} of pp collisions recorded with the ATLAS detector. For the first time in ATLAS, the angular distribution ($\cos\theta^*$) of the muon pair was used in addition to the invariant mass as a discriminating variable when searching for evidence for $qq\mu\mu$ contact interactions. Again for the first time in ATLAS, left-right and right-right chirality models of contact interactions are studied in addition to the left-left contact interaction model. No significant deviation from the Standard Model is observed either in contact interaction or the ADD large extra dimension searches. Therefore, 95% C.L. lower bounds are set on the parameter of interest in these models (Λ and M_S for the CI and ADD models, respectively). These limits represent the strongest exclusion limits to date on these models.

APPENDIX A

MONTE CARLO SAMPLES

A.1 Background Samples

A list of all DY, diboson and top MC samples used in this analysis are shown in Tables A.1, A.2 and A.3, respectively.

Table A.1: POWHEG+PYTHIA 8 Drell-Yan Monte Carlo samples used in the analysis. The first column gives the process, the second column gives the mass range in which the Drell-Yan process was simulated. For each sample the cross section times branching ratio with which the POWHEG generator produced the sample, and the number of produced events are given. In last column, the integrated luminosity $\int$ L.dt $= N_{evt}/(\sigma B)$ of each sample is given.

Process	$m_{\ell\ell}$ [GeV]	σB [pb]	N_{evt} [k]	$\int$ L.dt [fb^{-1}]
$Z \to \ell\ell$	> 60	1.109×10^{3}	10000	9.01
$Z \to \ell\ell$	250 – 400	5.492×10^{-1}	100	1.82×10^{2}
$Z \to \ell\ell$	400 – 600	8.966×10^{-2}	100	1.11×10^{3}
$Z \to \ell\ell$	600 – 800	1.510×10^{-2}	100	6.62×10^{3}
$Z \to \ell\ell$	800 – 1000	3.750×10^{-3}	100	2.67×10^{4}
$Z \to \ell\ell$	1000 – 1250	1.293×10^{-3}	100	7.73×10^{4}
$Z \to \ell\ell$	1250 – 1500	3.577×10^{-4}	100	2.80×10^{5}
$Z \to \ell\ell$	1500 – 1750	1.123×10^{-4}	100	8.90×10^{5}
$Z \to \ell\ell$	1750 – 2000	3.838×10^{-5}	100	2.61×10^{6}
$Z \to \ell\ell$	2000 – 2250	1.389×10^{-5}	100	7.20×10^{6}
$Z \to \ell\ell$	2250 – 2500	5.226×10^{-6}	100	1.91×10^{7}
$Z \to \ell\ell$	2500 – 2750	2.017×10^{-6}	100	4.96×10^{7}
$Z \to \ell\ell$	2750 – 3000	7.891×10^{-7}	100	1.27×10^{8}
$Z \to \ell\ell$	≥ 3000	5.039×10^{-7}	100	1.99×10^{8}

Table A.2: Diboson Monte Carlo samples used in the analysis. The first column gives the physics process and the second gives the mass range in which the diboson processes were simulated. For each sample, the cross section times branching ratio with which the HERWIG generator produced the sample and also σB at NLO which was used for the normalization are given. The number of produced events and the efficiency (ϵ_G) with which the sample was filtered are also included. In last column, the integrated luminosity $\int$ L.dt $= N_{evt}/(\sigma B)$ of each sample is given.

Process	$m_{\ell\ell}$ [GeV]	σB [pb]		ϵ_G [%]	N_{evt} [k]	$\int$ L.dt [fb^{-1}]
		Herwig	NLO			
$WW \to \ell X$	-	3.25×10^1	5.68×10^1	38.21	2500	2.01×10^2
$ZZ \to \ell X$	-	4.69	7.36	21.17	250	2.52×10^2
$WZ \to \ell X$	-	1.20×10^1	2.15×10^1	30.55	1000	2.73×10^2
$WW \to \mu\nu\mu\nu$	400-1000	0.38	0.66	0.75	10	3.51×10^1
$WW \to \mu\nu\mu\nu$	≥ 1000	0.38	0.66	0.01	10	2.63×10^3
$ZZ \to \mu\mu$	400-1000	0.35	0.54	0.001	10	2.86×10^4
$ZZ \to \mu\mu$	≥ 1000	0.35	0.54	0.00003	10	9.52×10^5
$WZ \to \mu\mu$	400-1000	0.46	0.83	0.003	10	7.25×10^3
$WZ \to \mu\mu$	≥ 1000	0.46	0.83	0.0001	10	2.17×10^5

Table A.3: Top Monte Carlo samples used in the analysis. The first column gives the physics process. For each sample, the cross section times branching ratio with which the MC@NLO generator produced the sample and also σBr at NNLO which was used for the normalization are given. The number of produced events and the efficiency (ϵ_G) with which the sample was filtered are also included. In last column, the integrated luminosity $\int$ Ldt $= N_{evt}/(\sigma B)$ of each sample is given.

Process	σB [pb]		ϵ_G [%]	N_{evt} [k]	$\int$ L.dt [fb^{-1}]
	MC@NLO	NNLO			
$t\bar{t} \to \ell X$	2.08×10^2	2.53×10^2	54.26	1.5×10^4	1.32×10^2
$Wt \to X$	2.07×10^1	2.24×10^1	100.00	0.2×10^4	9.67×10^1

A.2 Signal Samples

A list of all DY+CI signal MC samples used in this analysis is shown in Tables A.4, A.5, and A.6 for the LL, LR, and RR CI model respectively. The columns from left to right show: model, parameter value, mass bin, cross-section, number of generated events, and corresponding integrated luminosity.

Table A.4: PYTHIA 8 Monte Carlo samples for all DY+CI signal samples in LL model.

CI Model	Λ [TeV]	$m_{\ell\ell}$ [GeV]	σB [fb]	N_{evt} [k]	$\int$ L.dt [fb^{-1}]
LL	$\Lambda^- = 7$	300 – 600	3.03×10^2	20	6.60×10^1
		600 – 1200	4.51×10^1	10	2.22×10^2
		$\geq$ 1200	1.13×10^1	10	8.81×10^2
LL	$\Lambda^- = 10$	300 – 600	2.73×10^2	20	7.31×10^1
		600 – 1200	2.65×10^1	10	3.77×10^2
		$\geq$ 1200	3.81	10	2.62×10^3
LL	$\Lambda^- = 14$	300 – 600	2.62×10^2	20	7.64×10^1
		600 – 1200	2.03×10^1	10	4.93×10^2
		$\geq$ 1200	1.58	10	6.33×10^3
LL	$\Lambda^- = 20$	120 – 300	9.50×10^3	20	2.10
		300 – 600	2.57×10^2	20	7.78×10^1
		600 – 1200	1.83×10^1	10	5.47×10^2
		$\geq$ 1200	0.95	10	1.05×10^4
LL	$\Lambda^- = 28$	300 – 600	2.55×10^2	20	7.85×10^1
		600 – 1200	1.74×10^1	10	5.74×10^2
		$\geq$ 1200	0.74	10	1.35×10^4
LL	$\Lambda^+ = 7$	300 – 600	2.43×10^2	20	8.23×10^1
		600 – 1200	2.65×10^1	10	3.77×10^2
		$\geq$ 1200	8.13	10	1.23×10^3
LL	$\Lambda^+ = 10$	300 – 600	2.43×10^2	20	8.23×10^1
		600 – 1200	1.70×10^1	10	5.89×10^2
		$\geq$ 1200	2.16	10	4.63×10^3
LL	$\Lambda^+ = 14$	300 – 600	2.47×10^2	20	8.10×10^1
		600 – 1200	1.57×10^1	10	6.39×10^2
		$\geq$ 1200	0.77	10	1.30×10^4
LL	$\Lambda^+ = 20$	120 – 300	9.47×10^3	20	2.11
		300 – 600	2.50×10^2	20	8.02×10^1
		600 – 1200	1.59×10^1	10	6.29×10^2
		$\geq$ 1200	0.55	10	1.82×10^4
LL	$\Lambda^+ = 28$	300 – 600	2.51×10^2	20	7.96×10^1
		600 – 1200	1.63×10^1	10	6.14×10^2
		$\geq$ 1200	0.54	10	1.85×10^4

Table A.5: Pythia 8 Monte Carlo samples for all DY+CI signal samples in LR model.

CI Model	Λ [TeV]	$m_{\ell\ell}$ [GeV]	σB [fb]	N_{evt} [k]	$\int$ L.dt [fb^{-1}]
LR	$\Lambda^- = 7$	300 – 600	3.27×10^2	20	6.12×10^1
		600 – 1200	6.40×10^1	10	1.56×10^2
		$\geq$ 1200	2.00×10^1	10	5.00×10^2
LR	$\Lambda^- = 10$	300 – 600	2.81×10^2	20	7.13×10^1
		600 – 1200	3.11×10^1	10	3.21×10^2
		$\geq$ 1200	6.06	10	1.60×10^3
LR	$\Lambda^- = 14$	300 – 600	2.62×10^2	20	7.62×10^1
		600 – 1200	2.15×10^1	10	4.66×10^2
		$\geq$ 1200	2.07	10	4.83×10^3
LR	$\Lambda^- = 20$	120 – 300	9.46×10^3	20	2.11
		300 – 600	2.58×10^2	20	7.75×10^1
		600 – 1200	1.85×10^1	10	5.39×10^2
		$\geq$ 1200	1.07	10	9.35×10^3
LR	$\Lambda^- = 28$	300 – 600	2.53×10^2	20	7.91×10^1
		600 – 1200	1.74×10^1	10	5.74×10^2
		$\geq$ 1200	0.76	10	1.32×10^3
LR	$\Lambda^+ = 7$	300 – 600	2.58×10^2	20	7.76×10^1
		600 – 1200	4.47×10^1	10	2.23×10^2
		$\geq$ 1200	1.74×10^1	10	5.73×10^2
LR	$\Lambda^+ = 10$	300 – 600	2.43×10^2	20	8.23×10^1
		600 – 1200	2.16×10^1	10	4.63×10^2
		$\geq$ 1200	4.68	10	2.14×10^3
LR	$\Lambda^+ = 14$	300 – 600	2.46×10^2	20	8.13×10^1
		600 – 1200	1.68×10^1	10	5.96×10^2
		$\geq$ 1200	1.40	10	7.14×10^3
LR	$\Lambda^+ = 20$	120 – 300	9.50×10^3	20	2.10
		300 – 600	2.49×10^2	20	8.04×10^1
		600 – 1200	1.61×10^1	10	6.23×10^2
		$\geq$ 1200	0.72	10	1.39×10^4
LR	$\Lambda^+ = 28$	300 – 600	2.49×10^2	20	8.02×10^1
		600 – 1200	1.62×10^1	10	6.16×10^2
		$\geq$ 1200	0.58	10	1.72×10^4

Table A.6: Pythia 8 Monte Carlo samples for all DY+CI signal samples in the RR model.

CI Model	Λ [TeV]	$m_{\ell\ell}$ [GeV]	σB [fb]	N_{evt} [k]	$\int$ L.dt [fb^{-1}]
RR	$\Lambda^- = 7$	300 – 600	3.04×10^2	20	6.58×10^1
		600 – 1200	4.47×10^1	10	2.24×10^2
		≥ 1200	1.11×10^1	10	8.98×10^2
RR	$\Lambda^- = 10$	≥ 1200	3.72	10	2.69×10^3
RR	$\Lambda^- = 14$	≥ 1200	1.53	10	6.54×10^3
RR	$\Lambda^- = 20$	≥ 1200	0.93	10	1.08×10^4
RR	$\Lambda^- = 28$	≥ 1200	0.73	10	1.37×10^4
RR	$\Lambda^+ = 7$	300 – 600	2.39×10^2	20	8.36×10^1
		600 – 1200	2.66×10^1	10	3.76×10^2
		≥ 1200	8.39	10	1.18×10^3
RR	$\Lambda^+ = 10$	≥ 1200	2.24	10	4.46×10^3
RR	$\Lambda^+ = 14$	≥ 1200	0.81	10	1.23×10^4
RR	$\Lambda^+ = 20$	≥ 1200	0.57	10	1.75×10^4
RR	$\Lambda^+ = 28$	≥ 1200	0.54	10	1.85×10^4

APPENDIX B

PDF EIGENVECTORS

The asymmetric uncertainties calculated by the VRAP program for each PDF eigenvector are shown in Figs. B.1, B.2 and B.3.

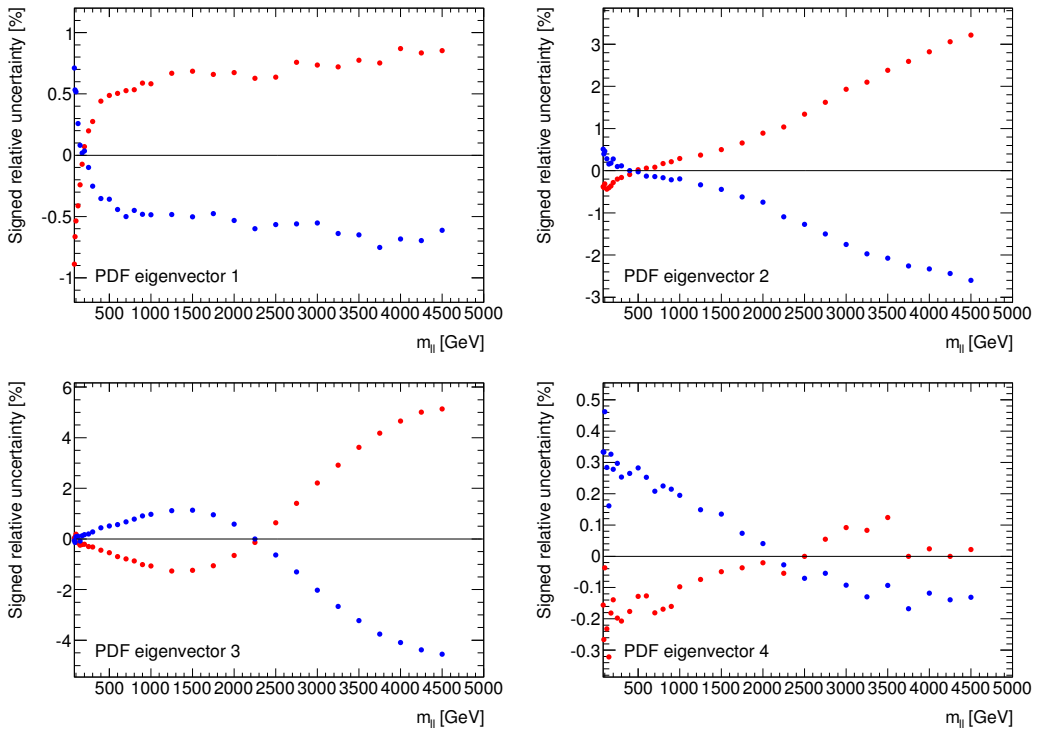

Figure B.1: Asymmetric uncertainty on the Drell-Yan cross section as a function of $m_{\ell\ell}$ due to each PDF eigenvector taken separately. Here eigenvectors 1 to 6 are shown.

The effect of the PDF variation uncertainty on the reconstructed dimuon invariant mass is shown for each bundle separately in Fig. B.4.

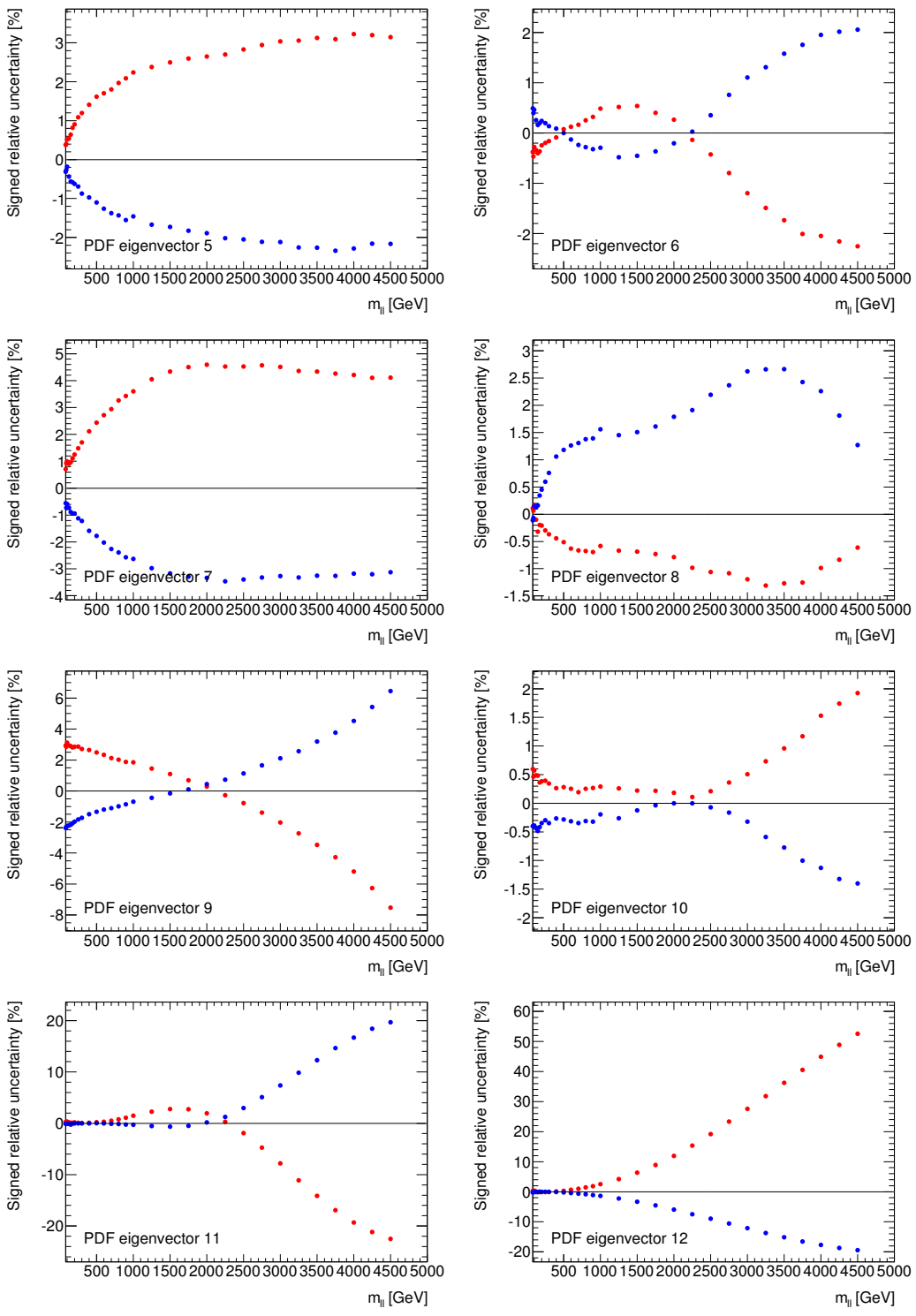

Figure B.2: Asymmetric uncertainty on the Drell-Yan cross section as a function of $m_{\ell\ell}$ due to each PDF eigenvector taken separately. Here eigenvectors 7 to 12 are shown.

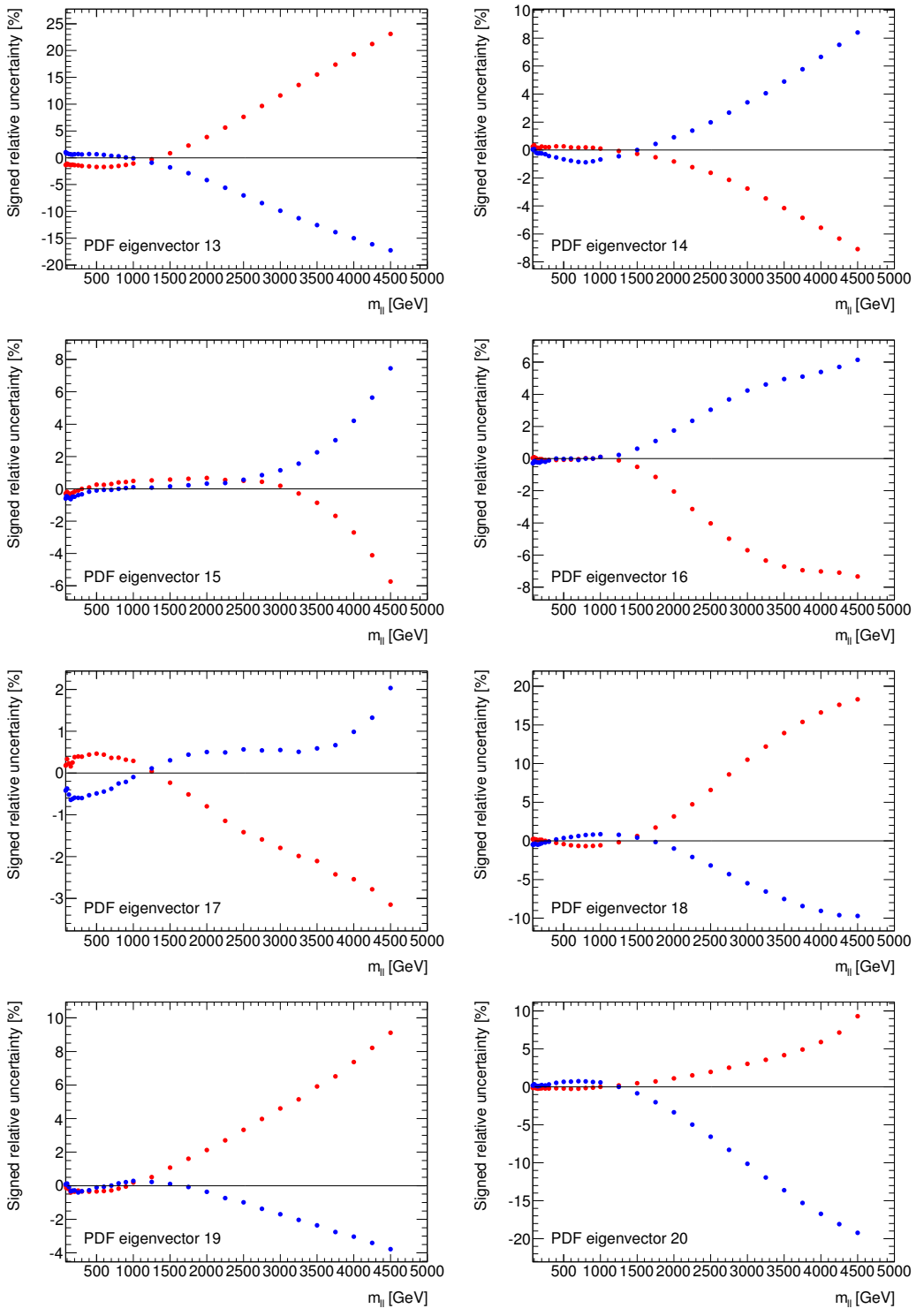

Figure B.3: Asymmetric uncertainty on the Drell-Yan cross section as a function of $m_{\ell\ell}$ due to each PDF eigenvector taken separately. Here eigenvectors 13 to 20 are shown.

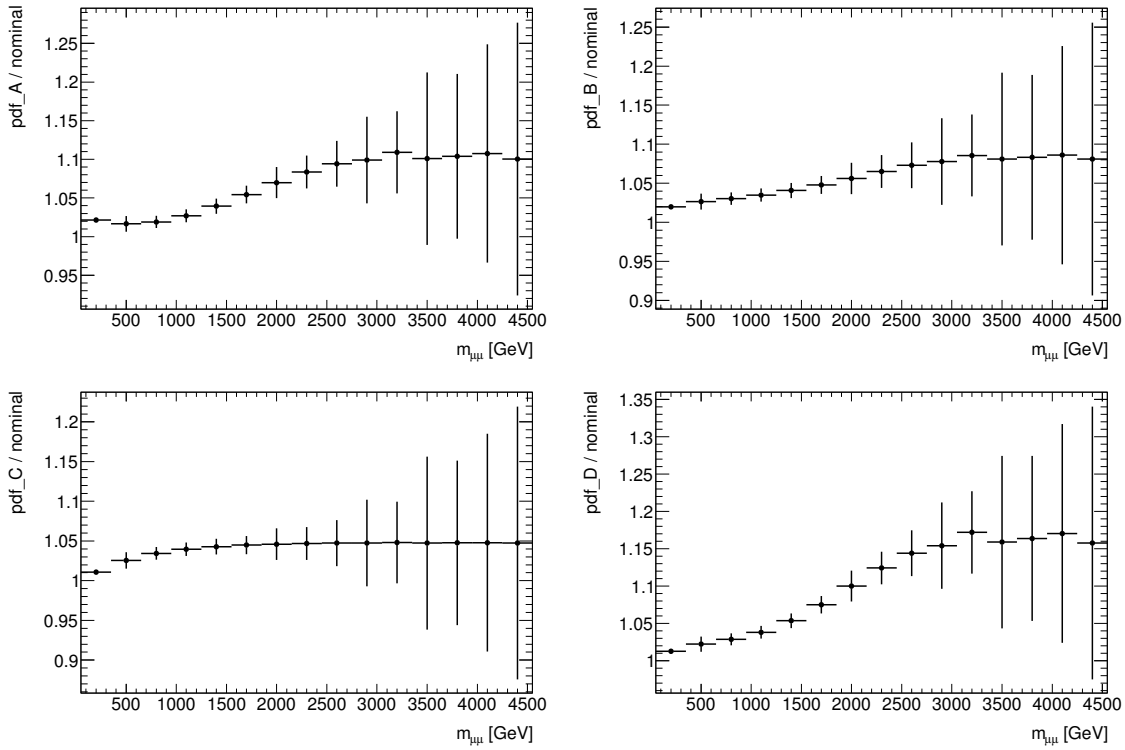

Figure B.4: The effect of the uncertainty due to the PDF variation on the reconstructed dimuon mass shown for each bundle separately.

APPENDIX C

OPTIMIZATION OF LOWER MASS CUT IN THE ADD MODEL

For the ADD analysis, a one bin search is performed above an invariant mass threshold and below 4500 GeV. The lower bound in invariant mass ($m_{\mu\mu}^{min}$) of the search region is selected by calculating the expected limit on M_S as a function of the lower mass threshold. The lower edge of the single mass bin is varied from 1000 GeV to 2200 GeV in 100 GeV steps and the expected limits are calculated. For the limit calculation, for each mass cut, the number of expected events for each benchmark M_S is counted and expressed as a function of $1/M_S^4$ or $1/M_S^8$. To provide more values of N^{exp} than could be obtained from the limited number of ADD MC samples, a fit of the number of expected events in each bin is performed according to the Eq. (6.14). These fits are shown in Fig. C.1 as a function of $1/M_S^4$ for two possible minimum mass cuts: 1300 and 1900 GeV as an illustration.

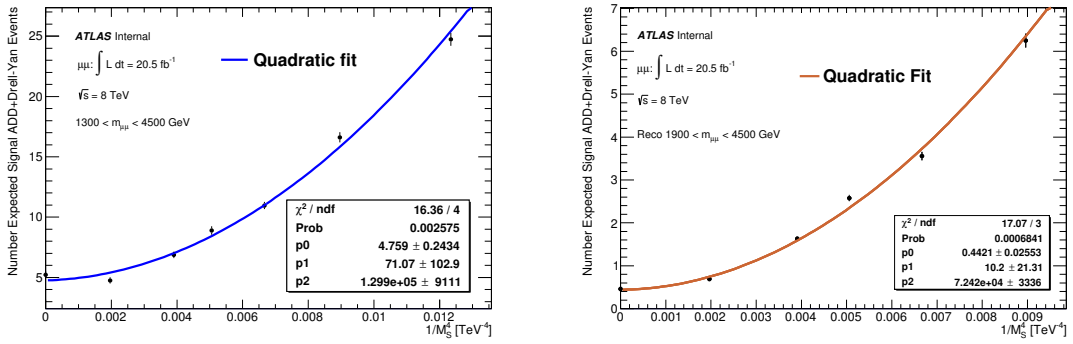

Figure C.1: Number of expected events as a function of $1/M_S^4$ for minimum mass mass cuts of 1300 GeV (left) and 1900 GeV (right) in the muon channel.

Then the expected limit is calculated as explained in Section 6.3.2 by performing 1000 pseudo-experiments for each lower mass cut chosen, using both the $1/M_S^4$ and $1/M_S^8$ priors. Among the varied lower mass values, the one which gave the highest expected limit is chosen as a lower mass cut in the ADD analysis.

In order to determine the optimal value of $m_{\mu\mu}^{min}$, two definitions of the limit on M_S is used; the mean and the median of the expected limit distribution. Due to the high mass cuts that are applied, the statistics in the single bin is low, which leads to the discreteness of expected limit distributions. Thus, if the median definition is used, the limit value can change quickly as the median jumps from one value to another. To avoid this behavior the limit is taken to be the mean of the expected limit distribution. The resulting limits are shown in Fig. C.2 using $1/M_S^4$ prior.

Considering the expected limits, using both the $1/M_S^4$ and $1/M_S^8$ priors, the lower cut is chosen to be 1900 GeV and used for setting observed limits using both choices of prior.

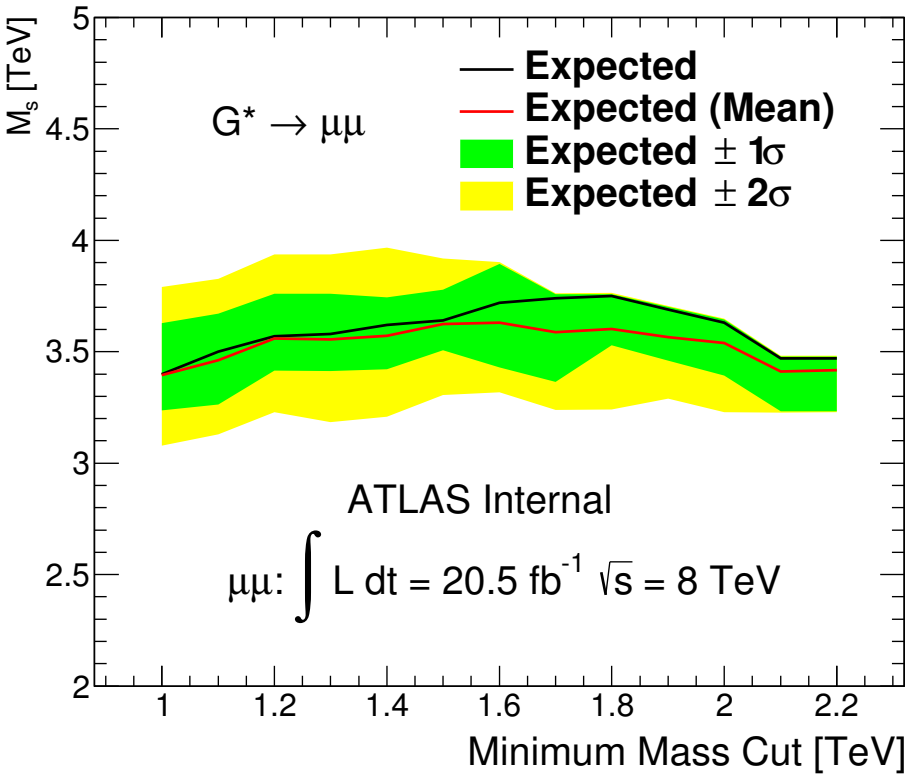

Figure C.2: Expected (black) and mean (red) limit on M_{S} in the ADD GRW model determined as a function of minimum mass cut ($m_{\mu\mu}^{min}$) used to define the search region using a $1/M_{\mathrm{S}}^4$ prior.

APPENDIX D

ADDITIONAL PARAMETERIZATIONS

This section displays all signal parameterizations used in the CI search.

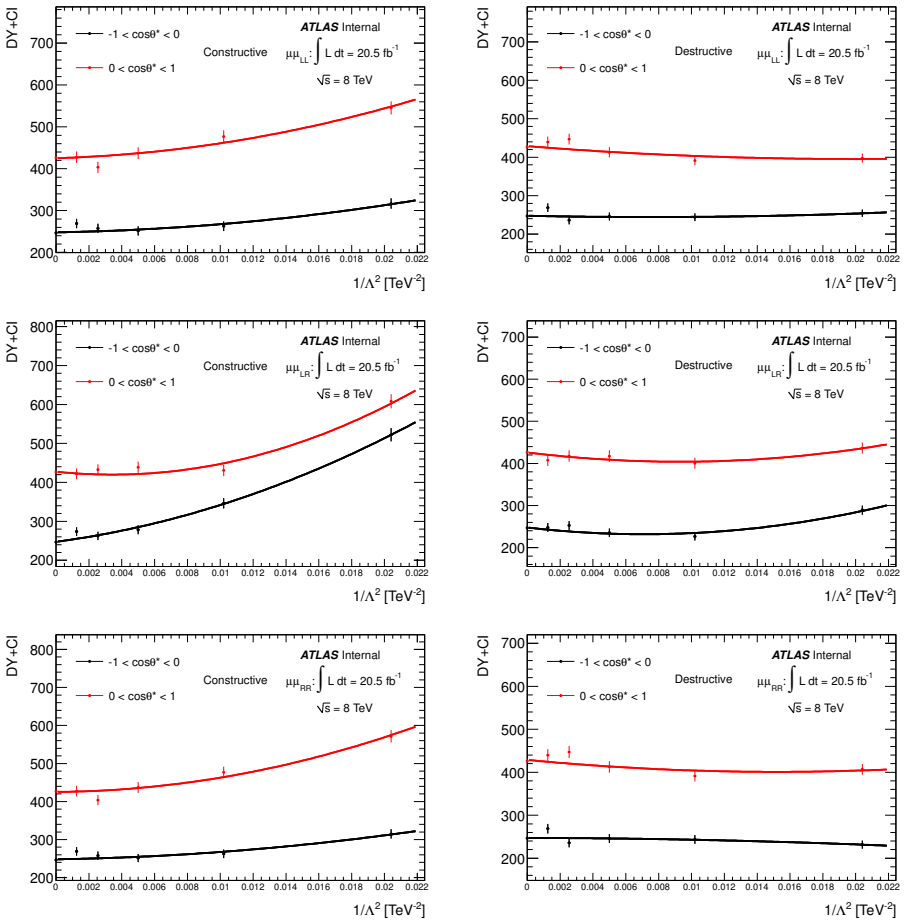

Figure D.1: Number of expected events in each of the $\cos\theta^*$ bins in the mass bin from 400 GeV to 550 GeV for the constructive (left plots) and destructive (right plots) interference cases of the contact interaction LL (top plots), LR (middle plots), RR (bottom plots) models as a function of $1/\Lambda^2$. Benchmark Λ values are shown as points and the lines represent the results of the fit.

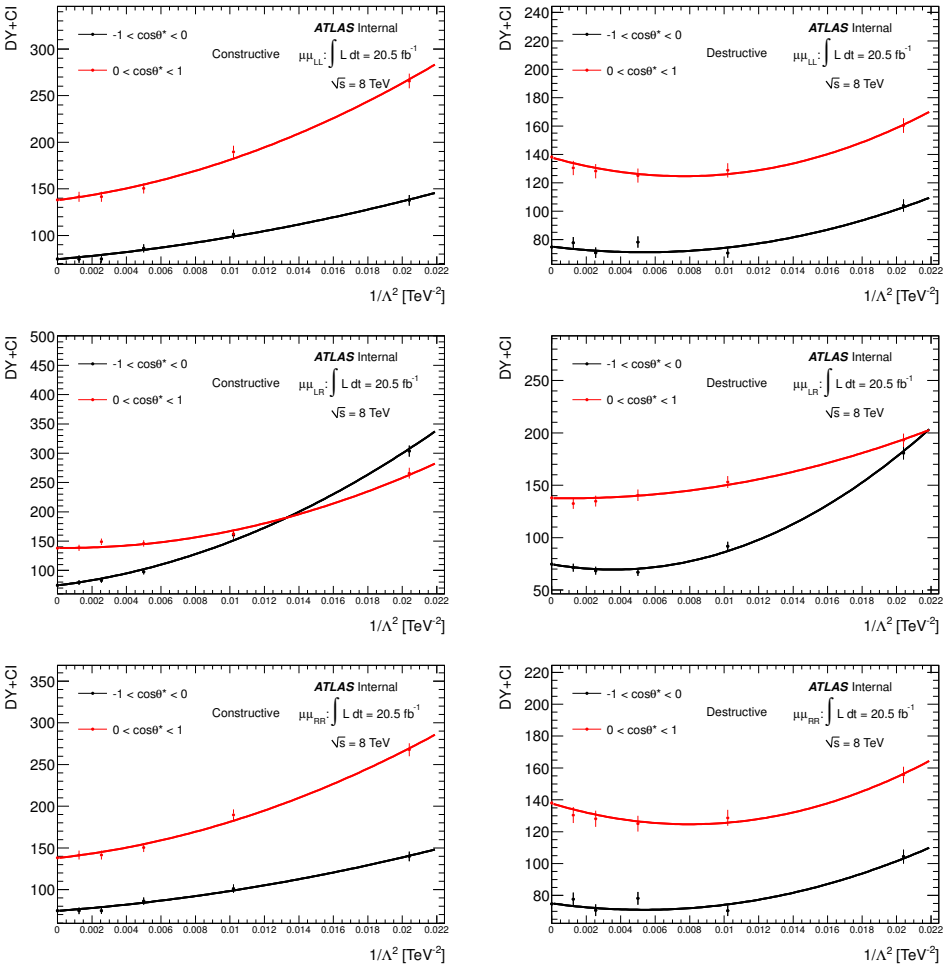

Figure D.2: Number of expected events in each of the $\cos\theta^*$ bins in the mass bin from 550 GeV to 800 GeV for the constructive (left plots) and destructive (right plots) interference cases of the contact interaction LL (top plots), LR (middle plots), RR (bottom plots) models as a function of $1/\Lambda^2$. Benchmark Λ values are shown as points and the lines represent the results of the fit.

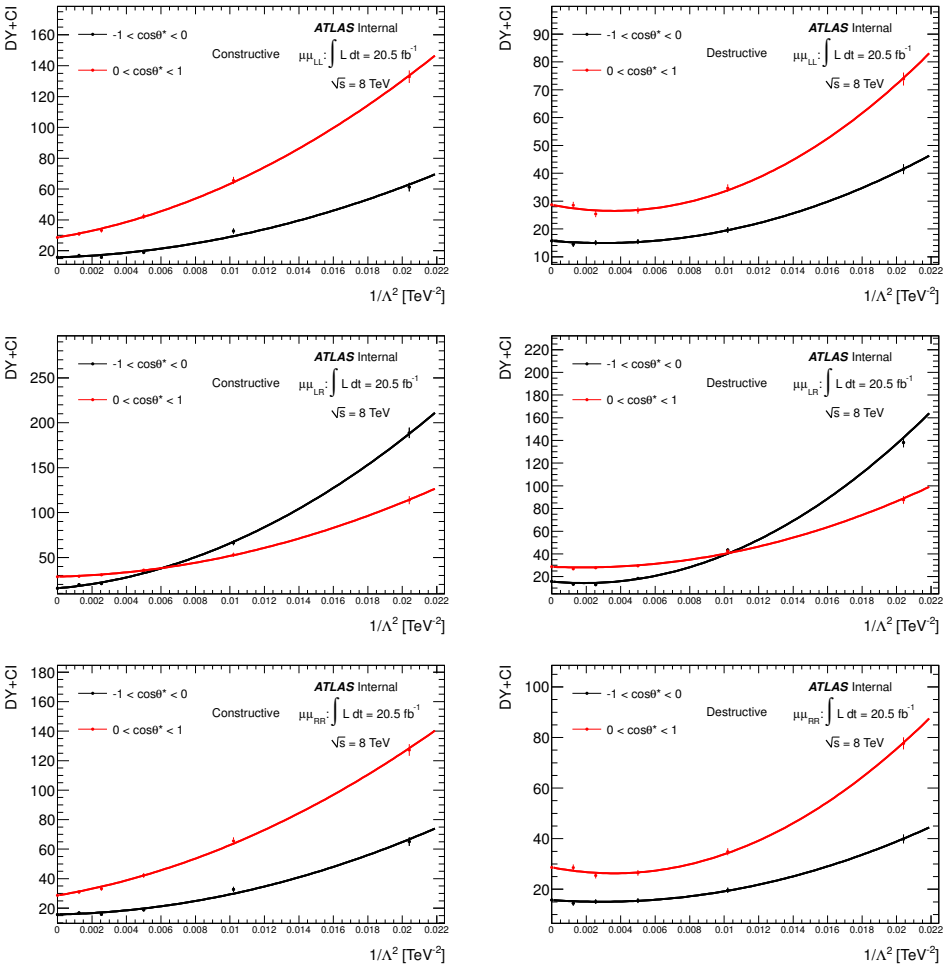

Figure D.3: Number of expected events in each of the $\cos\theta^*$ bins in the mass bin from 800 GeV to 1200 GeV for the constructive (left plots) and destructive (right plots) interference cases of the contact interaction LL (top plots), LR (middle plots), RR (bottom plots) models as a function of $1/\Lambda^2$. Benchmark Λ values are shown as points and the lines represent the results of the fit.

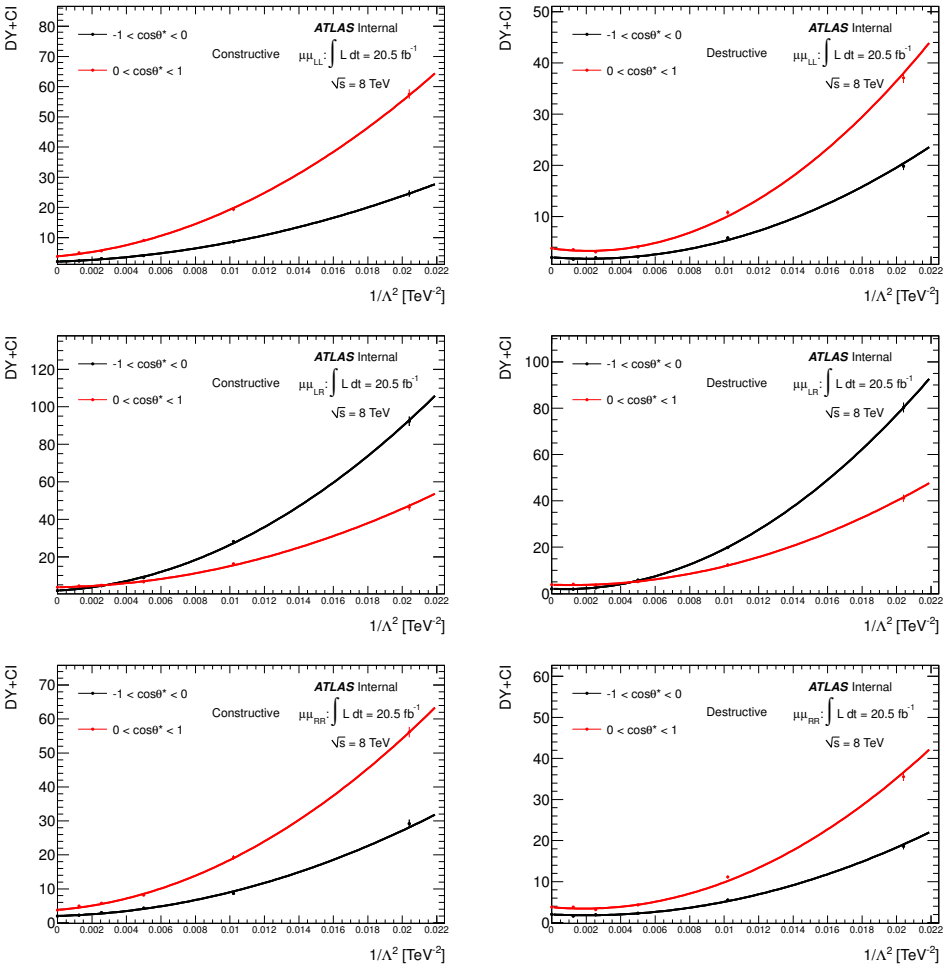

Figure D.4: Number of expected events in each of the $\cos\theta^*$ bins in the mass bin from 1200 GeV to 1800 GeV for the constructive (left plots) and destructive (right plots) interference cases of the contact interaction LL (top plots), LR (middle plots), RR (bottom plots) models as a function of $1/\Lambda^2$. Benchmark Λ values are shown as points and the lines represent the results of the fit.

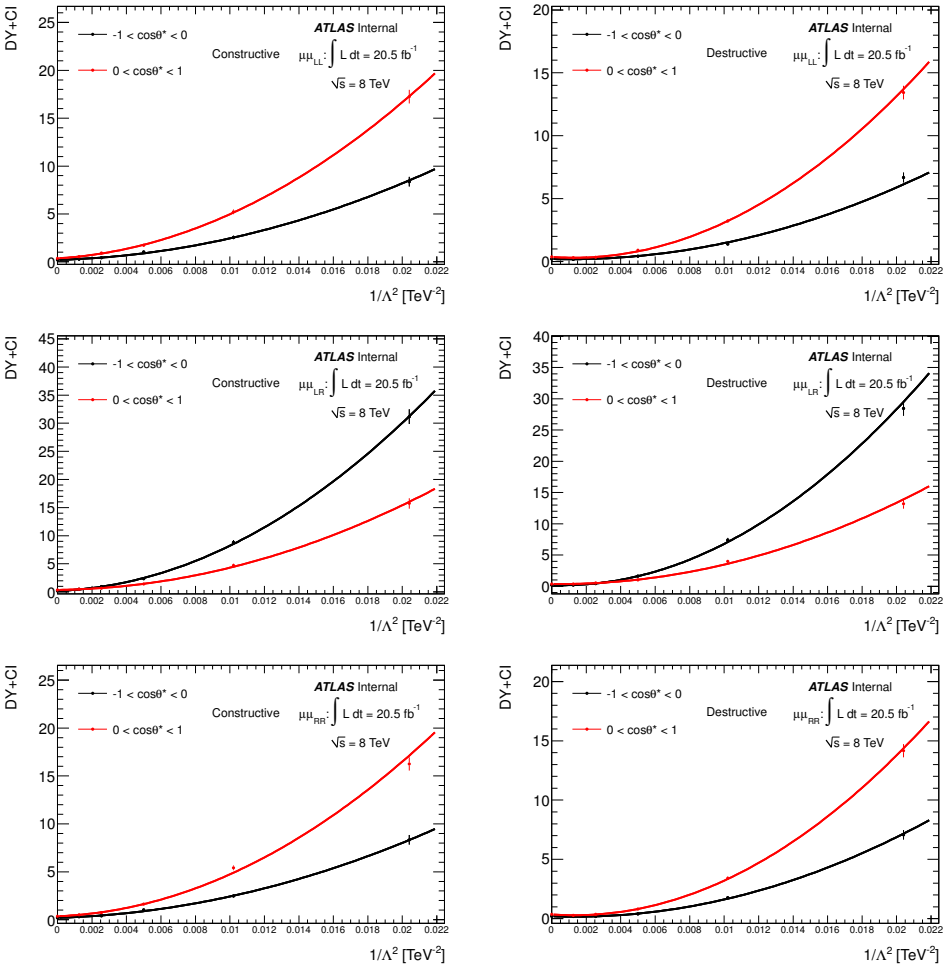

Figure D.5: Number of expected events in each of the $\cos\theta^*$ bins in the mass bin from 1800 GeV to 3000 GeV for the constructive (left plots) and destructive (right plots) interference cases of the contact interaction LL (top plots), LR (middle plots), RR (bottom plots) models as a function of $1/\Lambda^2$. Benchmark Λ values are shown as points and the lines represent the results of the fit.

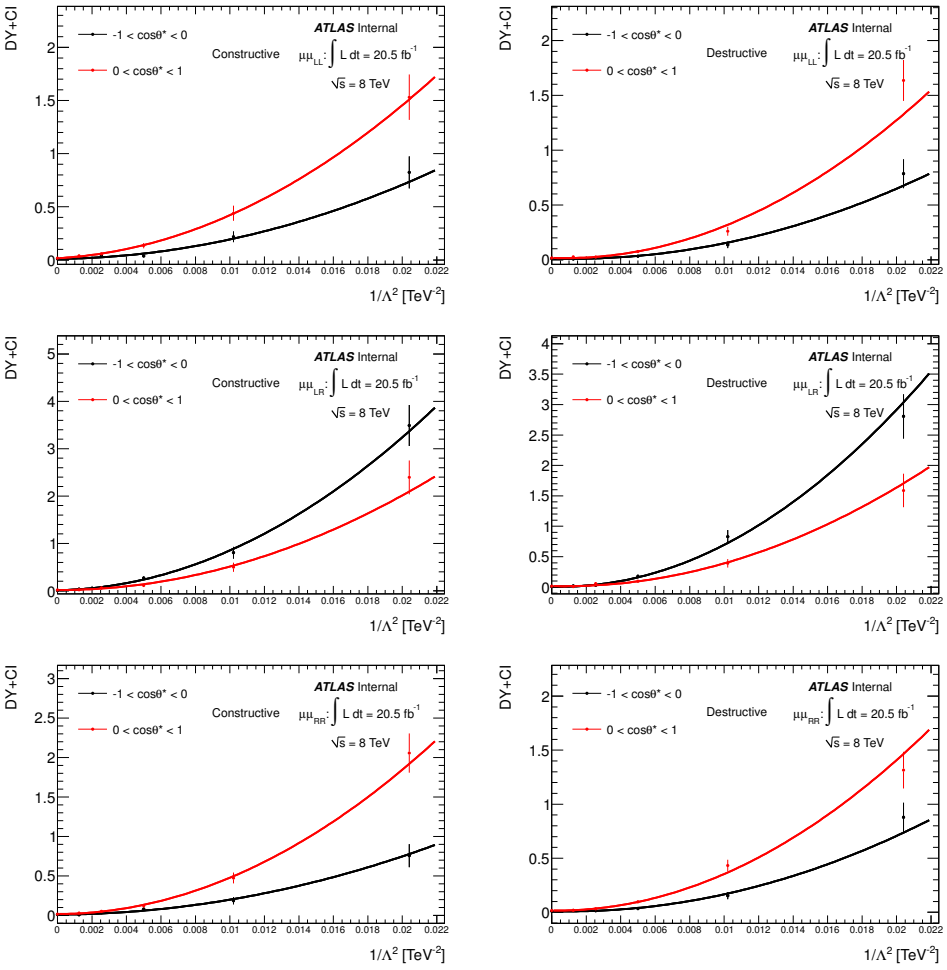

Figure D.6: Number of expected events in each of the $\cos\theta^*$ bins in the mass bin from 3000 GeV to 4500 GeV for the constructive (left plots) and destructive (right plots) interference cases of the contact interaction LL (top plots), LR (middle plots), RR (bottom plots) models as a function of $1/\Lambda^2$. Benchmark Λ values are shown as points and the lines represent the results of the fit.

APPENDIX E

SUPPLEMENTAL RESULTS

E.1 Supplemental CI Results

Distributions of the negative log-likelihood ratio for all pseudo-experiments and also for the observed results are shown in Figs. E.1 and E.2 for the LR and RR CI models, respectively.

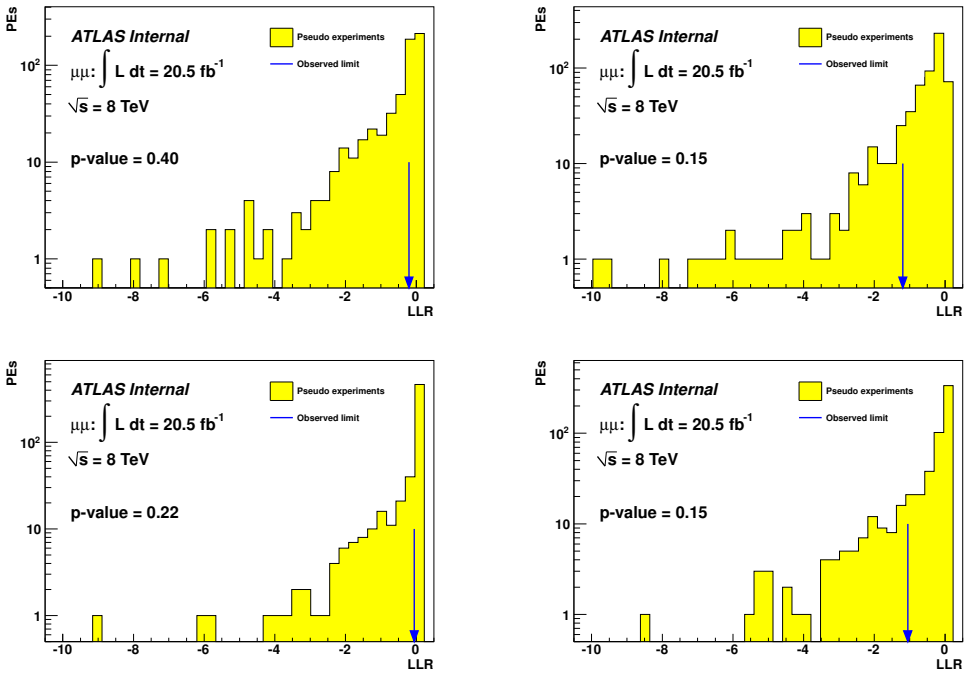

Figure E.1: Expected and observed negative log-likelihood distribution for the LR contact interaction model, for the constructive (plots on the left) and destructive interference (plots on the right). All systematic uncertainties are taken into account, and a uniform positive prior in $1/\Lambda^2$ ($1/\Lambda^4$) for the plots on the top (bottom) is used with the 2D search approach.

A full list of p-values for the contact interaction search is shown in Table E.1.

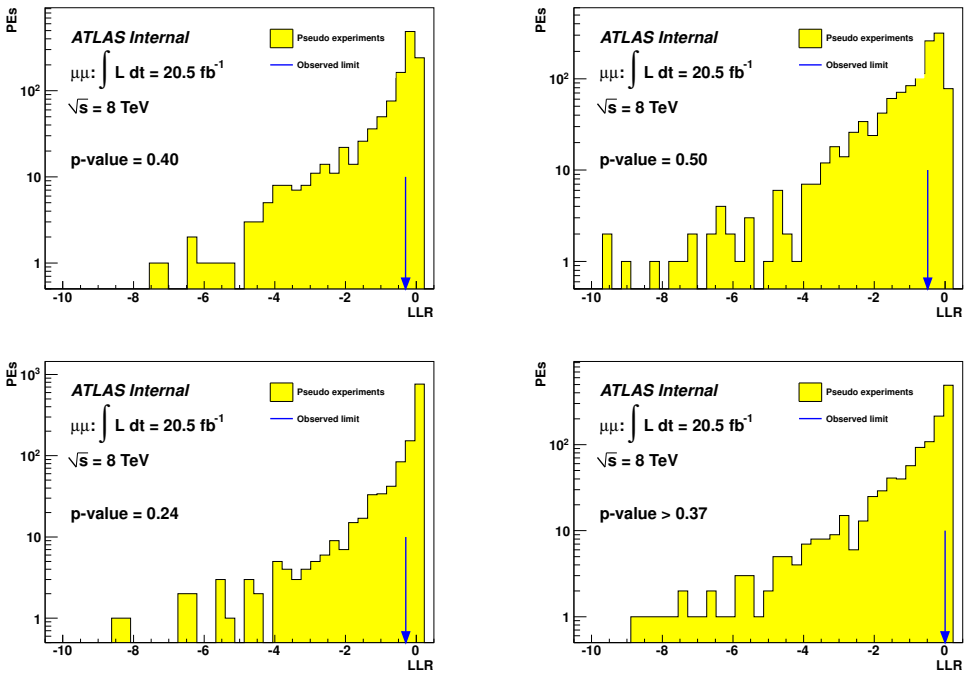

Figure E.2: Expected and observed negative log-likelihood distribution for the RR contact interaction model, for the constructive (plots on the left) and destructive (plots on the right) interference. All systematic uncertainties are taken into account, and a uniform positive prior in $1/\Lambda^2$ ($1/\Lambda^4$) for the plots on the top (bottom) is used with the 2D search approach.

Table E.1: Derived p-values for the contact interaction search in all of the parameter space considered. This includes the LL, LR, and LR model, constructive and destructive interference, as well as assuming a uniform positive prior of either $1/\Lambda^2$ or $1/\Lambda^4$. All systematic uncertainties are taken into account and the 2D search approach is used.

p-value [%]	$1/\Lambda^2$		$1/\Lambda^4$	
	Constructive	Destructive	Constructive	Destructive
Left-Left	31	8	24	40
Left-Right	40	15	22	15
Right-Right	40	50	24	37

The expected limit distributions are shown in Figs. E.3 and E.4 for the LR and RR CI models, respectively.

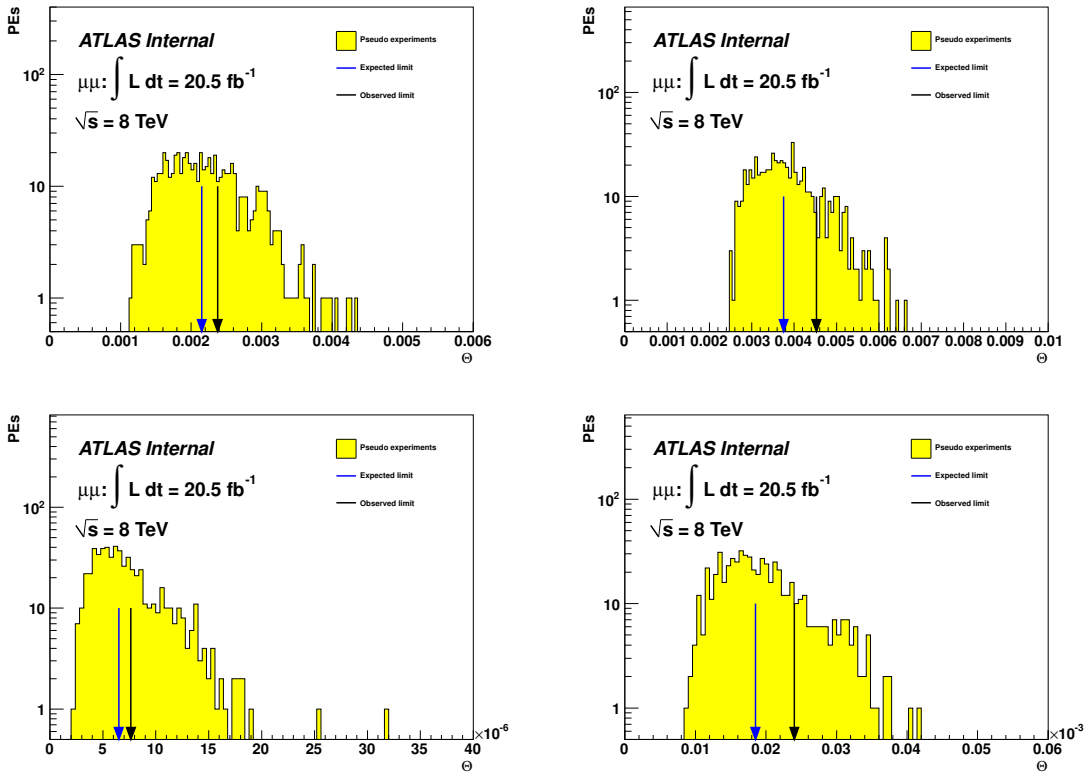

Figure E.3: Distribution of expected limit values from pseudo-experiments for the LR contact interaction model, for constructive (plots on the left) and destructive (plots on the right) interference. A uniform positive prior in $1/\Lambda^2$ ($1/\Lambda^4$) for the plots on the top (bottom) is used. All systematic uncertainties are taken into account. These results are derived using the 2D search approach. The blue arrow indicates the median limit and the black arrow shows the observed limit.

The posterior distributions from which the observed limits are calculated are shown in Figs. E.5 and E.6 for the LR and RR CI models, respectively.

E.2 Supplemental ADD Results

Distributions of the negative log-likelihood ratio for all pseudo-experiments and also for the observed results are shown in Fig. E.7 for the HLZ n=2 formalism.

The posterior distributions for the HLZ n=2 ADD model is shown in Fig. E.8.

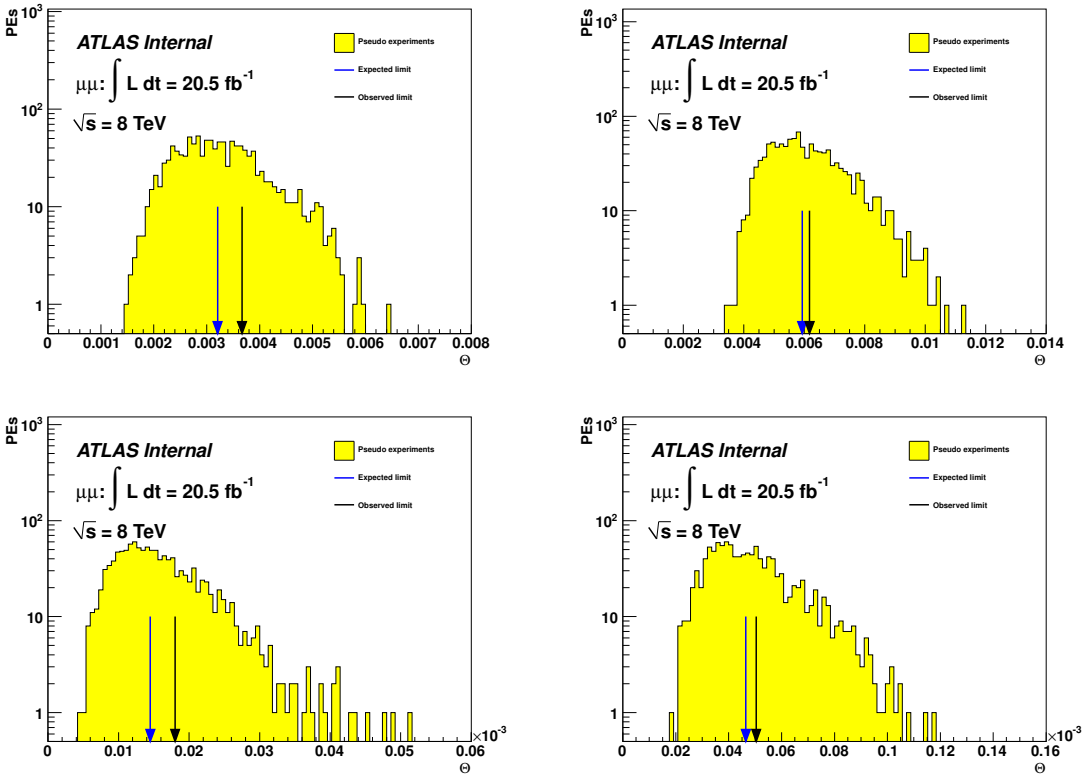

Figure E.4: Distribution of expected limit values from pseudo-experiments for the RR contact interaction model, for constructive (plots on the left) and destructive (plots on the right) interference. A uniform positive prior in $1/\Lambda^2$ ($1/\Lambda^4$) for the plots on the top (bottom) is used. All systematic uncertainties are taken into account. These results are derived using the 2D search approach. The blue arrow indicates the median limit and the black arrow shows the observed limit.

E.3 Combined Channel Results

The derived p-values calculated for the dimuon, dielectron and combined dilepton channels are shown in Tables E.2 and E.3 for the CI and ADD models, respectively.

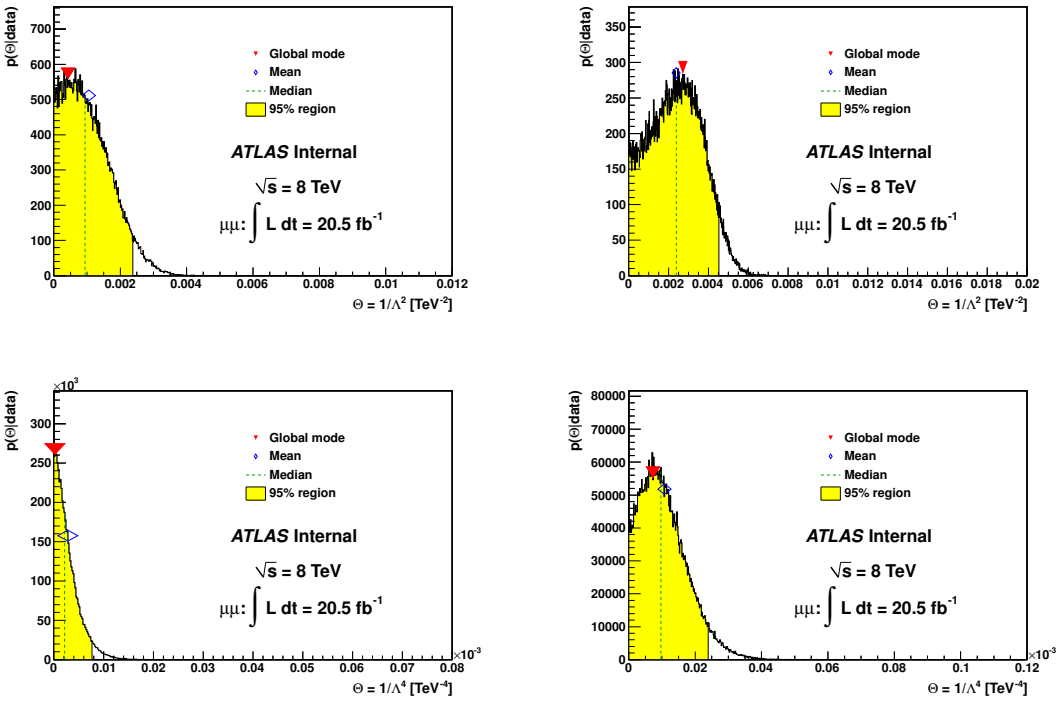

Figure E.5: Posterior distributions for the LR contact interaction model, for constructive (plots on the left) and destructive (plots on the right) interference. A uniform positive prior in $1/\Lambda^2$ ($1/\Lambda^4$) for the plots on the top (bottom) is used. All systematic uncertainties are taken into account. These results are derived using the 2D search approach.

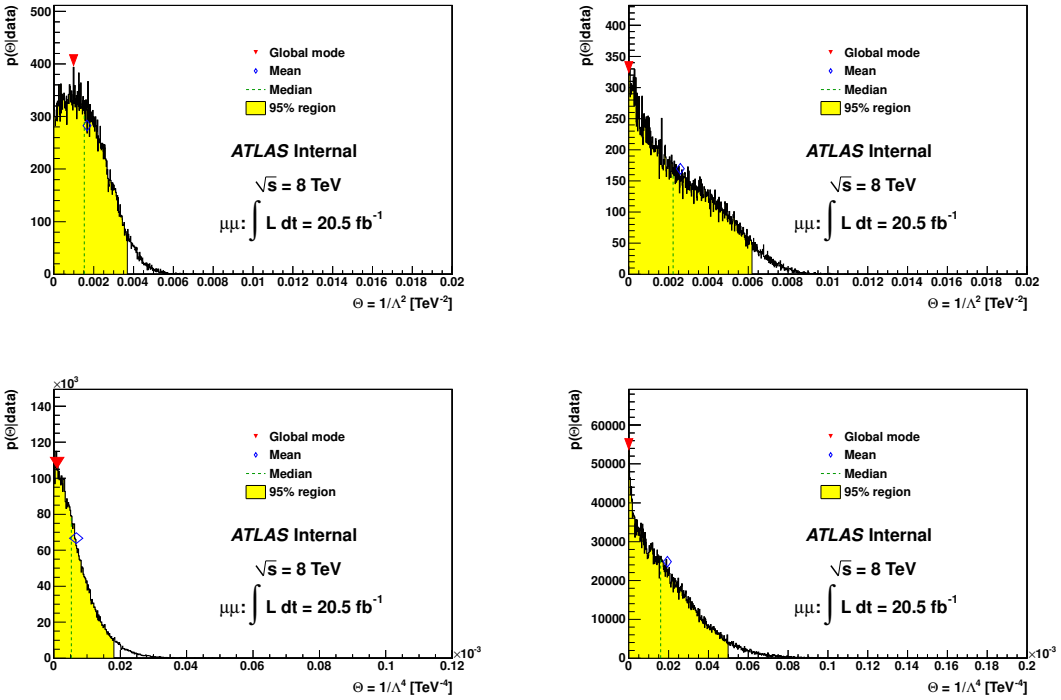

Figure E.6: Posterior distributions for the RR contact interaction model, for constructive (plots on the left) and destructive (plots on the right) interference. A uniform positive prior in $1/\Lambda^2$ ($1/\Lambda^4$) for the plots on the top (bottom) is used. All systematic uncertainties are taken into account. These results are derived using the 2D search approach.

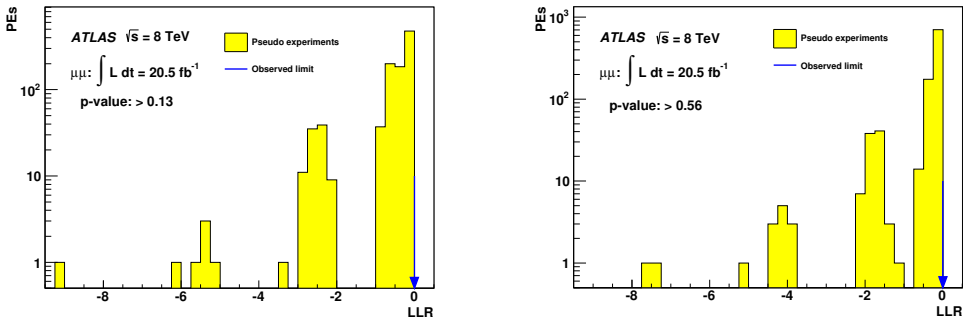

Figure E.7: Negative log-likelihood distribution resulting from pseudo-experiments with fluctuations on the number of expected SM-only events for the ADD model with the HLZ n=2 formalism with a uniform positive prior in $1/M_S^4$ (left) and $1/M_S^8$ (right).

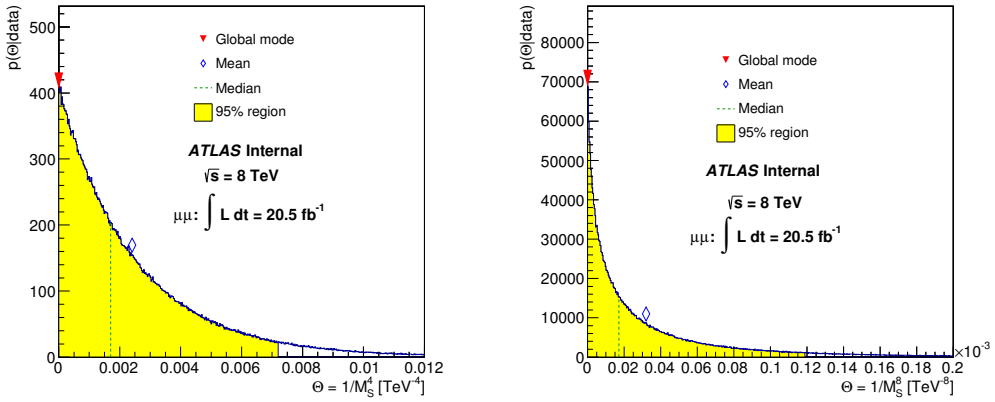

Figure E.8: Posterior pdf distributions for the HLZ n=2 ADD model, with a uniform positive prior in $\Theta = 1/M_S^4$ (left) and $\Theta = 1/M_S^8$ (right).

Table E.2: Derived p-values for the contact interaction search in all of the parameter space considered. This includes the LL, RR, and LR model, constructive and destructive interference, as well as assuming a uniform positive prior of either $1/\Lambda^2$ or $1/\Lambda^4$. Results are presented for the electron, muon, and combined channel using the 2D search approach, with all systematic uncertainties taken into account.

p-value [%]	$1/\Lambda^2$		$1/\Lambda^4$	
	Constructive	Destructive	Constructive	Destructive
LL: ee	58	60	76	58
LR: ee	35	36	85	62
RR: ee	35	68	75	62
LL: $\mu\mu$	31	8	24	40
LR: $\mu\mu$	40	15	22	15
RR: $\mu\mu$	40	50	24	37
LL: $\ell\ell$	20	63	64	54
LR: $\ell\ell$	59	31	72	43
RR: $\ell\ell$	42	84	67	51

Table E.3: Derived p-values for the GRW ADD search assuming a uniform positive prior of either $1/M_S^4$ or $1/M_S^8$. Results are presented for the electron, muon, and combined channel, with all systematic uncertainties taken into account.

p-value [%]	$1/M_S^4$	$1/M_S^8$
ee	50	55
$\mu\mu$	6	49
$\ell\ell$	7	51

BIBLIOGRAPHY

[1] D. Griffiths, *Introduction to Elementary Particles* (1987).

[2] W. Pauli, *Open letter to the Radioactivity Group at the Regional Meeting at Tübingen, Zürich*, December 4, 1930.

[3] E. Fermi, *Versuch einer theorie der β-strahlen / Towards the theory of β-rays*, Nuovo Cim. 11, 1 (1934); Z. Phys. 88, 161 (1934).

[4] T. D. Lee, and C. N. Yang, *Question of parity conservation in weak interactions*, Phys. Rev. 104, 254 (1956).

[5] R. P. Feynman, and M. Gell-Mann, *Theory of the fermi interaction*, Phys. Rev. 109, 193 (1958).

[6] http://warwick.ac.uk/fac/sci/physics/current/teach/module_home/px435/weak.pdf

[7] S. D. Drell, and T. M. Yan, *Massive lepton-pair production in hadron-hadron collisions at high energies*, Phys. Rev. Lett. 25, 316 (1970).

[8] G. Grossi, *Measurement of the Z/γ^* forward-backward asymmetry in muon pairs with the ATLAS experiment at the LHC*, Journal of Physics: Conference Series 383 (2012) 012005.

[9] N. Cabibbo, *Unitary symmetry and leptonic decays*, Phys. Rev. Lett. 10, 531 (1963).

[10] S.L. Glashow, J. Iliopoulos, and L. Maiani, *Weak interactions with lepton-hadron symmetry*, Phys. Rev. D 2, 1285 (1970).

[11] J.J. Aubert et. al., *Experimental observation of a heavy particle j*, Phys. Rev. Lett. 33, 1404 (1974).

[12] M. Kobayashi, and T. Maskawa, *Progress of Theoretical Physics 49*, 2 (1972).

[13] K. Nakamura et. al., *Review of particles physics: The CKM quark-mixing matrix*, Journal of Physics G 37, 075021 (2010).

[14] E. Eichten, K. Lane, and M. Peskin, *New tests for quark and lepton substructure*, Phys. Rev. Lett. 50, 811 (1983).

[15] I. D'Souza and C. S.Kalman, *Preons; Models of leptons, quarks and gauge bosons as composite objects*, (World Scientific, Singapore) 1992.

[16] N. Arkani-Hamed, S. Dimopoulos, and G. R. Dvali, *The hierarchy problem and new dimensions at a millimeter*, Phys. Lett. B 429, 263 (1998).

[17] G. F. Giudice, R. Rattazzi, and J. D. Wells, *Quantum gravity and extra dimensions at high-energy colliders*, Nucl. Phys. B 544, 3 (1999).

[18] J. Hewett, *Indirect collider signals for extra dimensions*, Phys. Rev. Lett. 82, 4765 (1999).

[19] T. Han, J. Lykken, and R.-J. Zhang, *Kaluza-Klein states from large extra dimensions*, Phys. Rev. D 59, 105006 (1999).

[20] K. McFarland, *Neutral currents and strangeness of the nucleon from the NuTeV experiment* , Eur. Phys. J. A 24, 161 (2005).

[21] SLAC E158 Collaboration, P. L. Anthony *et al.*, *Precision measurement of the weak mixing angle in Moller scattering*, Phys. Rev. Lett. 95, 081601(2005).

[22] ALEPH Collaboration, S. Schael *et al.*, *Fermion pair production in e^+e^- collisions at 189209 GeV and constraints on physics beyond the standard model*, Eur. Phys. J. C 49, 411 (2007).

[23] DELPHI Collaboration, J. Abdallah *et al.*, *Measurement and interpretation of fermion-pair production at LEP energies above the Z resonance*, Eur. Phys. J. C 45, 589 (2006).

[24] DELPHI Collaboration, J. Abdallah *et al.*, *A study of $b\bar{b}$ production in e^+e^- collisions at $\sqrt{s}$ =130-207 GeV*, Eur. Phys. J. C 60, 1 (2009).

[25] L3 Collaboration, M. Acciarri *et al.*, *Search for manifestations of new physics in fermion pair production at LEP*, Phys. Lett. B 489, 81 (2000).

[26] OPAL Collaboration, G. Abbiendi *et al.*, *Tests of the standard model and constraints on new physics from measurements of fermion-pair production at 189-209 GeV at LEP*, Eur. Phys. J. C 33, 173 (2004).

[27] H1 Collaboration, F. Aaron *et al.*, *Search for contact Interactions in $e^{\pm}p$ Collisions at HERA*, Phys. Lett. B 705, 52 (2011).

[28] ZEUS Collaboration, S. Chekanov *et al.*, *Search for contact interactions, large extra dimensions and finite quark radius in ep collisions at HERA*, Phys. Lett. B 591, 23 (2004).

[29] CDF Collaboration, K. Abe *et al.*, *Limits on quark-lepton compositeness scales from dileptons produced in 1.8 TeV pp^- collisions*, Phys. Rev. Lett. 79, 2198 (1997).

[30] CDF Collaboration, T. Affolder *et al.*, *Search for quark-lepton compositeness and a heavy W' boson using the $e\nu$ channel in pp^- collisions at $\sqrt{s}$ = 1.8 TeV*, Phys. Rev. Lett. 87, 231803 (2001).

[31] CDF Collaboration, A. Abulencia *et al.*, *Search for $Z' \to e^+e^-$ using dielectron mass and angular distribution*, Phys. Rev. Lett. 96, 211801 (2006).

[32] D0 Collaboration, B. Abbott *et al.*, *Measurement of the high-mass Drell-Yan cross section and limits on quark-electron compositeness scales*, Phys. Rev. Lett. 82, 4769 (1999).

[33] D0 Collaboration, V.M. Abazov *et al.*, *Measurement of dijet angular distributions at $\sqrt{s}$ = 1.96 TeV and searches for quark compositeness and extra spatial dimensions*, Phys. Rev. Lett. 103, 191803 (2009).

[34] ATLAS Collaboration, *Search for new physics in dijet mass and angular distributions in pp collisions at $\sqrt{s}$ = 7 TeV measured with the ATLAS detector*, New J. Phys. 13, 053044 (2011).

[35] ATLAS Collaboration, *Search for contact interactions in dilepton events from pp collisions at $\sqrt{s}$ = 7 TeV with the ATLAS detector*, Phys. Lett. B 712, 40 (2012).

[36] ATLAS Collaboration, *Search for contact interactions and large extra dimensions in dilepton events from pp collisions at $\sqrt{s}$ = 7 TeV with the ATLAS detector*, Phys. Rev. D 87, 015010 (2013).

[37] CMS Collaboration, *Search for quark compositeness with the dijet centrality ratio in pp collisions at $\sqrt{s}$ = 7 TeV*, Phys. Rev. Lett. 105 262001 (2010).

[38] CMS Collaboration, *Measurement of the inclusive jet cross section in pp collisions at $\sqrt{s}$ = 7 TeV*, Phys. Rev. Lett. 107 132001 (2011).

[39] CMS Collaboration, *Search for contact interactions in dilepton mass spectra in pp collisions at $\sqrt{s}$ = 8 TeV*, CMS-PAS-EXO-12-020, https://cds.cern.ch/record/1708245/, (2014).

[40] L3 Collaboration, M. Acciarri *et al.*, *Search for extra dimensions in boson and fermion pair production in e^+e^- interactions at LEP*, Phys. Lett. B 470, 281 (1999).

[41] L3 Collaboration, M. Acciarri *et al.*, *Search for low scale gravity effects in e^+e^- collisions at LEP*, Phys. Lett. B 464, 135 (1999).

[42] DELPHI Collaboration, P. Abreu *et al.*, *Measurement and interpretation of fermion-pair production at LEP energies of 183 and 189 GeV*, Phys. Lett. B 485, 45 (2000).

[43] DELPHI Collaboration, P. Abreu *et al.*, *Determination of the $e^+e^- \to \gamma\gamma(\gamma)$ cross-section at centre-of-mass energies ranging from 189 GeV to 202 GeV*, Phys. Lett. B 491, 67 (2000).

[44] OPAL Collaboration, G. Abbiendi *et al.*, *Multi-photon production in e^+e^- collisions at $\sqrt{s}$ = 181-209 GeV*, Eur. Phys. J. C 26, 331 (2003).

[45] OPAL Collaboration, G. Abbiendi *et al.*, *Tests of the standard model and constraints on new physics from measurements of fermion-pair production at 189 GeV at LEP*, Eur. Phys. J. C 13, 553 (2000).

[46] H1 Collaboration, C. Adloff *et al.*, *Search for compositeness, leptoquarks and large extra dimensions in eq contact interactions at HERA*, Phys. Lett. B 479, 358 (2000).

[47] D0 Collaboration, V. M. Abazov *et al.*, *Search for large extra spatial dimensions in the dielectron and diphoton channels in pp collisions at* $\sqrt{s}$ *= 1.96 TeV*, Phys. Rev. Lett. 102, 051601 (2009).

[48] D0 Collaboration, V. M. Abazov *et al.*, *Search for large extra spatial dimensions in dimuon production with the D0 detector*, Phys. Rev. Lett. 95, 161602 (2005).

[49] ATLAS Collaboration, *Search for extra dimensions using diphoton events in 7 TeV proton-proton collisions with the ATLAS detector*, Phys. Lett. B 710, 538 (2012).

[50] ATLAS Collaboration, *Search for extra dimensions in diphoton events using proton-proton collisions recorded at* $\sqrt{s}$ *= 7 TeV with the ATLAS detector at the LHC*, New J. Phys. 15, 043007 (2013).

[51] CMS Collaboration, *Search for large extra dimensions in dimuon and dielectron events in pp collisions at* $\sqrt{s}$ *= 7 TeV*, Phys. Lett. B 711, 15 (2012).

[52] CMS Collaboration, *Search for large extra dimensions in the diphoton final state at the Large Hadron Collider*, J. High Energy Phys. 1105, 85 (2011).

[53] CMS Collaboration, *Search for signatures of extra dimensions in the diphoton mass spectrum at the Large Hadron Collider*, Phys. Rev. Lett. **108**, 111801 (2011).

[54] CMS Collaboration, *Search for extra dimensions in dimuon events in pp collisions at* $\sqrt{s}$ *= 8 TeV*, CMS-PAS-EXO-12-027, https://cds.cern.ch/record/1523261/ (2014).

[55] CMS Collaboration, *Search for large extra spatial dimensions in dielectron production with the CMS detector*, CMS-PAS-EXO-12-031, https://cds.cern.ch/record/1523280/ (2014).

[56] T. Sjöstrand, S. Mrenna and P. Skands, *A Brief Introduction to PYTHIA 8.1*, JHEP05 (2006) 026, Comput. Phys. Comm. 178 (2008) 852.

[57] P. Golonka and Z. Was, *PHOTOS Monte Carlo: A precision tool for QED corrections in Z and W decays*, Eur. Phys. J. C45 (2006) 97107.

[58] G. Corcella *et al.*, *HERWIG 6: an event generator for hadron emission reactions with interfering gluons* JHEP 01, 010 (2001).

[59] S. Alioli, P. Nason, C. Oleari, and E. Re, *A general framework for implementing NLO calculations in shower Monte Carlo programs: the POWHEG BOX*, JHEP 1006 043 (2010).

[60] S. Frixione and B. Webber, *Matching NLO QCD computations and parton shower simulations*, JHEP 0206, 029 (2002).

[61] T. Gleisberg *et al.*, *Event generation with SHERPA 1.1*, JHEP 02, 007 (2009).

[62] L. Evans and P. Bryant, *LHC Machine*, JINST 3, S08001 (2008).

[63] Document EDMS 973073, *Interim Summary Report on the Analysis of the 19th September 2008 Incident at the LHC*, CERN, 15 October 2008.

[64] ATLAS Collaboration, *The ATLAS experiment at the CERN Large Hadron Collider*, JINST 3, S08003 (2008).

[65] ATLAS Muon Collaboration, *ATLAS Muon Spectrometer Technical Design Report*, CERN/LHCC/97-22, 1997.

[66] A. Yamamoto, Y. Makida, R. Ruber, Y. Doi, T. Haruyama, F. Haug, H. ten Kate, M. Kawai, T. Kondo, Y. Kondo, J. Metselaar, S. Mizumaki, G. Olesen, O. Pavlov, S. Ravat, E. Sbrissa, K. Tanaka, T. Taylor, H. Yamaoka, *The ATLAS Central Solenoid*, Nuclear Instruments and Methods in Physics Research A 584, 53-74, (2008).

[67] A. Dudarev, J. J. Rabbers, C. P. Berriaud, S. Junker, R. Pengo, S. Ravat, L. Deront, E. Sbrissa, G. Olesen, M. Arnaud, J.-M. Rey, P. Vedrine, F. Broggi, G. Volpini, A. Foussat, Ph. Benoit, V. Stepanov, A. Olyunin, I. Shugaev, N. Kopeykin, and H. H. J. ten Kate, *First full-size ATLAS barrel toroid coil successfully tested up to 22 kA at 4 T*, IEEE Trans. Appl. Supercond., Vol 15, No. 2, 1271-1274 (2005).

[68] S. Hassani, L. Chevalier, E.Lancon, J-F. Laporte, R. Nicolaidou, A. Ouraou, *A muon identification and combined reconstruction procedure for the ATLAS detector at the LHC using the (MUONBOY, STACO, MuTag), reconstruction packages*, NIM A572 77-79 (2007) .

[69] Th. Lagouri, et al., *A muon identification and combined reconstruction procedure for the ATLAS detector at the LHC at CERN*, IEEE Trans. Nucl Sci. 51 3030-3033 (2004) .

[70] ATLAS Collaboration, *Preliminary results on the muon reconstruction efficiency, momentum resolution, and momentum scale in ATLAS 2012 pp collision data*, ATLAS-CONF-2013-088, http://cds.cern.ch/record/1580207/, (2013).

[71] ATLAS Computing Group, *ATLAS Computing Technical Design Report*, CERN-LHCC-2005-022, (2005).

[72] S. Agostinelli *et al.*, *GEANT4 - a simulation toolkit*, Nucl. Instrum. Meth. A 506, 250 (2003);

[73] A. Nairz, on behalf of the ATLAS Collaboration, *ATLAS distributed computing: experience and evolution*, ATL-SOFT-PROC-2013-006, http://cds.cern.ch/record/1605418/, (2013).

[74] H. Lai, M. Guzzi, J. Huston, Z. Li, P. Nadolsky, J. Pumplin, and C.-P. Yuan, *New parton distributions for collider physics*, Phys.Rev. D82 074024 (2010).

[75] Y. Li and F. Petriello, *Combining QCD and electroweak corrections to dilepton production in FEWZ*, Phys. Rev. D86 (2012) 094034.

[76] A. Martin, W. Stirling, R. Thorne, and G. Watt, *Parton distributions for the LHC*, Eur.Phys.J. C63 (2009) 189285.

[77] A. Martin, W. Stirling, R. Thorne, and G. Watt, *Uncertainties on alpha(S) in global PDF analyses and implications for predicted hadronic cross sections*, Eur.Phys.J. C64 (2009) 653680.

[78] A.D. Martin, R.G. Roberts, W.J. Stirling, and R.S. Thorne, *Parton distributions incorporating QED contributions*, Eur. Phys. J. C39 (2005) 155-161.

[79] J. Pumplin *et al.*, *New generation of parton distributions with uncertainties from global QCD analysis*, JHEP 0207, 012 (2002).

[80] ATLAS Collaboration, *Single and diboson production cross sections in pp collisions at* $\sqrt{s} = 7$ *TeV*, ATL-COM-PHYS-2010-695 (2010).

[81] J.M. Butterworth *et al.*, *Multiparton interactions in photoproduction at HERA*, Z. Phys. C 72, 637 (1997).

[82] M. Cacciari, M. Czakon, M. Mangano, A. Mitov, and P. Nason, *Top-pair production at hadron colliders with next-to-next-to-leading logarithmic soft-gluon resummation*, Phys. Lett. B710 (2012) 612622.

[83] P. Baernreuther, M. Czakon, and A. Mitov, *Percent Level Precision Physics at the Tevatron: First Genuine NNLO QCD Corrections to* $q\bar{q} \to t\bar{t} + X$, Phys.Rev.Lett. 109 (2012) 132001.

[84] M. Czakon and A. Mitov, *NNLO corrections to top-pair production at hadron colliders: the all-fermionic scattering channels*, JHEP 1212 (2012) 054.

[85] M. Czakon and A. Mitov, *NNLO corrections to top pair production at hadron colliders: the quark-gluon reaction*, JHEP 1301 (2013) 080.

[86] M. Czakon, P. Fiedler, and A. Mitov, *The total top quark pair production cross-section at hadron colliders through* $O(\alpha_S^4)$, Phys. Rev. Lett. 110 (2013) 252004.

[87] M. Czakon and A. Mitov, *Top++: A Program for the Calculation of the Top-Pair Cross-Section at Hadron Colliders*, arXiv:1112.5675 [hep-ph].

[88] M. L. Mangano, M. Moretti, F. Piccinini, R. Pittau, and A. D. Polosa, *ALPGEN, a generator for hard multiparton processes in hadronic collisions*, JHEP 07, 001 (2003).

[89] ATLAS Collaboration, *Muon Momentum Resolution in First Pass Reconstruction of pp Collision Data Recorded by ATLAS in 2010*, ATLAS-CONF-2011-046 (2011).

[90] ATLAS Collaboration, *Preliminary results on the muon reconstruction efficiency, momentum resolution, and momentum scale in ATLAS 2012 pp collision data*, ATLAS-CONF-2013-088 (2013).

[91] ATLAS Collaboration, http://atlas.web.cern.ch/Atlas/GROUPS/PHYSICS/MUON/PublicPlots/2012/June/index.html.

[92] Analysis Software Group, *Extended Pileup Reweighting*, https://twiki.cern.ch/twiki/bin/viewauth/AtlasProtected/ExtendedPileupReweighting.

[93] ATLAS Collaboration, *Improved luminosity determination in pp collisions at $\sqrt{s}$ = 7 TeV using the ATLAS detector at the LHC*, Eur. Phys. J. C (2013) 73:2518.

[94] J. C. Collins and D. E. Soper, *Angular distribution of dileptons in high-energy hadron collisions*, Phys. Rev. D 16, 2219 (1977).

[95] C. Anastasiou, L. Dixon, K. Melnikov, and F. Petriello, *High precision QCD at hadron colliders: Electroweak gauge boson rapidity distributions at NNLO*, Phys. Rev. D 69 (2004) 094008.

[96] M. R. Whalley, D. Bourilkov, R. C. Group *The Les Houches Accord PDFs (LHAPDF) and Lhaglue*, arXiv:hep-ph/0508110.

[97] J. Gao, et al., *The CT10 NNLO global analysis of QCD*, Phys. Rev. D 89, (2014) 033009.

[98] R.D. Ball, et al., *Parton distributions with LHC data*, Nucl. Phys. B 867, 244 (2013).

[99] S. Alekhin, J. Bluemlein, S.O. Moch, *ABM11 PDFs and the cross section benchmarks in NNLO*, PoS LL2012, 016 (2012).

[100] A. Cooper-Sarkar, *PDF fits at HERA* PoS EPS-HEP2011, 320 (2011).

[101] Glen Cowan, *Data analysis: Frequently Bayesian*, PHYSICS TODAY, Vol. 60, Issue 4, Page 82-83 (2007).

[102] A. Caldwell, D. Kollar, and K. Kröninger, *BAT - The Bayesian Analysis Toolkit*, Computer Phys. Commun. 180, 2197 (2009).